Washington University in St. Louis

Washington University Open Scholarship

McKelvey School of Engineering Theses & Dissertations

McKelvey School of Engineering

Winter 12-15-2018

Mechanisms of Calcium Phosphate Mineralization on Biological Interfaces and their Engineering Applications

Doyoon Kim
Washington University in St. Louis

Follow this and additional works at: https://openscholarship.wustl.edu/eng_etds

Part of the Chemical Engineering Commons, Chemistry Commons, and the Environmental Engineering Commons

Recommended Citation

Kim, Doyoon, "Mechanisms of Calcium Phosphate Mineralization on Biological Interfaces and their Engineering Applications" (2018). *McKelvey School of Engineering Theses & Dissertations*. 398.
https://openscholarship.wustl.edu/eng_etds/398

This Dissertation is brought to you for free and open access by the McKelvey School of Engineering at Washington University Open Scholarship. It has been accepted for inclusion in McKelvey School of Engineering Theses & Dissertations by an authorized administrator of Washington University Open Scholarship. For more information, please contact digital@wumail.wustl.edu.

WASHINGTON UNIVERSITY IN ST. LOUIS

Department of Energy, Environmental & Chemical Engineering

Dissertation Examination Committee:
Young-Shin Jun, Chair
John Fortner
Daniel Giammar
Jill D. Pasteris
Stavros Thomopoulos

Mechanisms of Calcium Phosphate Mineralization on Biological Interfaces and their Engineering Applications

by
Doyoon Kim

A dissertation presented to
The Graduate School
of Washington University
in partial fulfillment of the
requirements for the degree
of Doctor of Philosophy

December 2018

St. Louis, Missouri

© 2018, Doyoon Kim

Table of Contents

List of Figures

List of Tables

Acknowledgments

First, I would like to thank to the Lord for everything.

I would like to express my deepest gratitude to my Ph.D. advisor, Professor Young-Shin Jun for giving me a great opportunity and being a great mentor during my graduate studies. Her encouragements always motivate me a lot. I am deeply indebted to Dr. Daniel Giammar, Dr. John Fortner, Dr. Jill Pasteris, and Dr. Stavros Thomopoulos for taking the time to serve on my committee and providing excellent advice and suggestions to push my research to the next level. Especially, I thank Dr. Pasteris for her inspiring discussion during the Biomineralization Group meeting and Dr. Thomopoulos for our wonderful collaboration works. I would also like to thank Dr. Byeongdu Lee at Argonne National Laboratory for his collaboration, patience, and assistance during work at the Advanced Photon Source.

I am grateful to all the former and current members of Environmental NanoChemistry Laboratory, especially Dr. Yandi Hu, Dr. Yang Yi, Dr. Jessica Ray, Dr. Chelsea Neil, Dr. Qingyun Li, Dr. Yujia Min, Dr. Haesung Jun, Dr. Lijie Zhang, Xuanhao Wu, Deoukchen Ghim, Zhenwei Gao, Yaguang Zhu, Albern Tan, Eunyoung Jang, Ping I Chou, Prof. Yongfang Rao, Prof. Youn Sang Kim, and Dr. Xuyang Liu. You are the best friends, mentors, and collaborators. I also thank to all of my research mentees, including Tong Wu, Melanie Cohen, and Inhyeong Jeon. I learned a lot from you while I was mentoring you.

This work would not have been possible without the financial support of Washington University's Faculty Startup and the National Science Foundation's Program (DMR-1608545). I would like to thank Prof. James Ballard for his sincere supports.

I would like to express my deepest gratitude and appreciation for my parents and brother for their endless love and support. Most importantly, I thank my loving wife, Jee-young, for making my life beautiful.

Doyoon Kim

Washington University in St. Louis

December 2018

ABSTRACT OF THE DISSERTATION

Mechanisms of Calcium Phosphate Mineralization on Biological Interfaces and their Engineering Applications

By
Doyoon Kim

Doctor of Philosophy in Energy, Environmental & Chemical Engineering
Washington University in St. Louis, 2018
Professor Young-Shin Jun, Chair

All living organisms utilize phosphorus (P) as an essential component of their cell membranes, DNA and RNA, and adenosine triphosphate. Bones, in addition to bearing loads, play an important role in balancing P levels in our bodies. In bones, a network of collagen templates and calcium phosphate (CaP) nanocrystals builds hierarchical levels, from nano- to macroscale. Within this architecture, the thermodynamic properties of CaP minerals are influential. Despite the importance of nucleation, growth, and crystallization in collagen structures for tissue development, little kinetic study of these processes has been conducted due to the limited *in situ* techniques for monitoring these nanoscale reactions in organic templates. In this dissertation, utilizing synchrotron-based *in situ* measurement techniques, kinetic aspects of collagen mineralization (i.e., nucleation, growth, and crystallization of CaP) were evaluated at multiple-length scales. Based on the kinetic observations, I sought a better understanding of the physicochemical properties of bones, and how they provide thermodynamic advantages for CaP mineralization.

First, I evaluated the nucleation kinetics and pathways for CaP minerals in collagen and their phase transformation from amorphous species to crystalline plates, using *in situ* small-angle X-ray scattering (SAXS). Collagen mineralization without an extrafibrillar nucleation inhibitor, polyaspartic acid (pAsp), led initially to spherical aggregates of CaP in the entire extrafibrillar space (extrafibrillar mineralization, EM). With time, the spherical aggregates transformed into plates at the outermost surface of the collagen matrices, preventing intrafibrillar mineralization (IM). However, mineralization with pAsp led directly to the formation of intrafibrillar CaP plates with a spatial distribution gradient through the depth of the matrix. We also experimentally obtained nucleation energy barriers to IM and EM by combining *in situ* SAXS observations and the modified classical nucleation theory. The addition of pAsp increases interfacial energies between nuclei and mineralization fluids. In contrast, the confined gap spaces inside collagen fibrils lower the energy barrier by reducing the reactive surface area of nuclei, decreasing the surface energy penalty for IM. The confined gap geometry, therefore, guides the 2D morphology and structure of bioapatite and changes the nucleation pathway by reducing the total energy barrier.

Next, we examined the influence of nanoscale nucleation on microscale CaP distribution in highly organized collagen matrices extracted from chicken tibia bones, and consequently on the matrices' mechanical properties. The matrices were mechanically loaded during mineralization to understand the physicochemical responses of collagen, which are different from biological responses. We found that cyclic strain increased acellular nucleation rates by 33% compared to nucleation under static strain. The enhanced transport of mineralization fluids under cyclic strain delivers more nucleation precursors into the matrices, increasing the elastic modulus, strength, and resilience. To easily mimic the microenvironment generated by cyclic strain for engineering applications, we also applied pulsed electric stimulations. Low amplitude pulsed stimulation through the cathode enhanced the transport of ionic body fluid components, leading to successful mineralization of the inner surface of tube-like collagen scaffolds through a microscale channel.

Finally, we expanded our knowledge obtained from the biomineralization studies to an environmental remediation strategy. We proposed a sustainable P management strategy for nutrient-rich aqueous environments, inspired by bones' ability to balance P in the human body. By seeding reactive CaP nuclei with an engineered crystalline structure in calcium alginate beads, we were able to control the energy barriers to CaP nucleation and manage an environmental aqueous P concentration as a function of pH. The CaP seeded beads effectively immobilized aqueous P in their macroscale organic/mineral networks, which have the potential to be reused as a slow-release fertilizer.

Our findings illuminate the importance of nanoscale nucleation reactions, macroscale mineral distributions, and macroscale mechanical properties. The findings also provide new insights into designing biomaterials with hierarchical structures. By improving the engineered control of properties of highly organized collagen matrices, and using cyclic strain condition and pulsed electrical stimulations, we can improve bone-fracture healing. Furthermore, designing CaP–organic composites provides promising solutions for environmental remediation. We expect that the bioinspired principles can also be applied to other fields of engineering requiring knowledge of chemistry at organic–mineral interfaces.

Chapter 1. Introduction

Phosphorus (P), one of the most essential elements of all living organisms, is a main component of cell membranes, DNA and RNA, and adenosine triphosphate (ATP), which is a central molecule in the energy system.[1] About 80 wt % of P in the human body is stored in bones, mainly as a calcium phosphate (CaP) mineral called bioapatite, which is a biologically produced analog of hydroxyapatite (HA, $Ca_5(PO_4)_3OH$).[2,3] Bones mainly function as structural supports by building networks of collagen templates and bioapatite nanocrystals with different hierarchical levels of organization, from nano- to macroscale.[4] CaP nucleation is an initial stage of collagen mineralization, and the kinetics of nucleation, and consequent growth, and crystallization are determined by many biological and physicochemical factors in bones.[5-7] The thermodynamic properties of bioapatite, controlled by this hierarchical architecture, are responsible for maintaining the P balance in body fluid.[2] Therefore, evaluating the kinetics and thermodynamic properties of bioapatite mineralization within collagen templates at multiple-length scales is essential to understanding the mechanisms of bone formation, preventing bone-related diseases, and developing new biomaterials.[8-10]

This study evaluates the nucleation, growth, and crystallization of CaP during collagen mineralization, and explores the chemical and mechanical properties of CaP mineral/organic composites for use in engineering applications. Recent advances in *in situ* analytical methods, including synchrotron-based *in situ* X-ray analyses, can be used as non-destructive approaches to characterize newly formed particles in soft organic templates.[11] Collagen mineralization is examined as a process of building the hierarchical structure of bones, connecting nanoscale nucleation to microscale mineral distribution to macroscale properties. This study also extends what we learned from fundamental studies to engineering applications. For example, the principles of collagen mineralization will be practically useful in designing better biomaterials with enhanced mechanical properties and biocompatibility. They can also contribute to developing new strategies for faster bone fracture healing. Furthermore, principles underlying biomineralization are practically helpful in other fields of research. For example, by learning how bioapatite maintains P balance in human body, we will be able to better manage P-abundant aqueous systems to prevent eutrophication and to recover P as a renewable resource.

In the Introduction, recent studies on CaP biomineralization are reviewed to understand the nucleation, growth, and crystallization pathways of CaP minerals (**Chapter 1.1**). The role of collagen structure on CaP biomineralization is then discussed (**Chapter 1.2**). Next, the influence of nanoscale CaP nucleation on macroscale properties of tissue-level constructs is considered (**Chapter 1.3**). Lastly, the specific research objectives and tasks of this study are described in **Chapter 1.4**.

1.1 Nucleation, Growth, and Crystallization of Calcium Phosphate Minerals

1.1.1 Classical Nucleation Theory

The formation of solids by crystallization from aqueous solution is an essential process in many natural phenomena, including bone mineralization, and its principles are widely used in various industrial applications, such as the synthesis of nanoparticles and pharmaceutical compounds.[11-13] The most fundamental step of crystallization, nucleation, is the formation of the first nuclei from solute precursors, such as atoms, ions, or (macro-)molecules, in aqueous systems.[14] Since the 1930s when its first concept was derived by Becker and Döring,[15] classical nucleation theory (CNT) has been widely used as the theoretical framework to describe nucleation processes during biomineralization.[12-14] CNT assumes that nucleation through monomer-by monomer attachment is thermodynamically driven by the free energy change per molecule (ΔG), which is the sum of the bulk ($-\Delta G_b$) and surface (ΔG_s) terms (Figure 1.1). A typical ΔG profile shows a maximum (i.e., an energy barrier, ΔG_n) at a critical radius (r_c), then decreases with increasing radius (r).

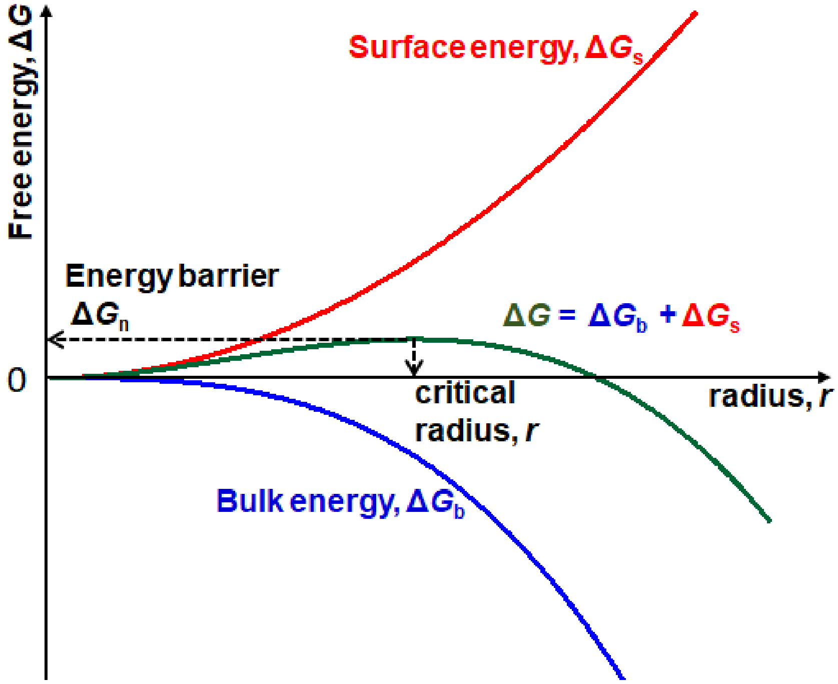

Figure 1.1 Schematic illustration of the size-dependent energetics of nuclei within the framework of classical nucleation theory. Adapted from Ref. 13.

The nucleation rate (J) can be expressed with ΔG_n in its exponential term, as written in Eq. 1.1, where k_B is the Boltzmann constant, T is the Kelvin temperature, and A is the kinetic factor. The kinetic factor A can be expressed in more complicated terms, including its activated energy, which is critically determined by the temperature. Because most bone mineralization studies were conducted a constant temperature around 37°C, A is considered as an incorporated pre-exponential factor in this study. More consideration of the kinetic factors in CNT can be found elsewhere.[16]

$$J = A\exp\left(-\frac{\Delta G_n}{k_B T}\right) \quad \text{Eq. 1.1}$$

For the formation of a spherical nucleus, ΔG_b and ΔG_s are defined in Eq. 1.2, deriving r_c (r at $\frac{d\Delta G}{dr} = 0$) and ΔG_n(ΔG at $r = r_c$) as written Eq. 1.3 and 1.4, respectively. By applying Eq. 1.4 to Eq. 1.1, J can be expressed as a function of the supersaturation (σ) and interfacial energy between a nucleus and mineralization solution (α) as written in Eq. 1.5. Here, σ is given as ln(IAP/K_{sp}), where IAP is the ion activity product and K_{sp} is the solubility product. Additionally, v_m is the volume per molecule of nucleus.

$$\Delta G = -\Delta G_b + \Delta G_s = -\left\{\frac{\left[\left(\frac{4}{3}\right)\pi r^3\right]}{v_m}\right\} k_B T\sigma + 4\pi r^2\alpha \quad \text{Eq. 1.2}$$

$$r_c = \frac{2v_m\alpha}{k_B T\sigma} \quad \text{Eq. 1.3}$$

$$\Delta G_n = \frac{16\pi v_m^2\alpha^3}{3k_B^2T^2\sigma^2} \quad \text{Eq. 1.4}$$

$$J = A\exp\left(-\frac{16\pi v_m^2\alpha^3}{3k_B^3T^3\sigma^2}\right) \quad \text{Eq. 1.5}$$

From Eq. 1.5, a linear relationship between ln(J) and 1/σ^2 is derived (Eq. 1.6). The fitting of the linear slope (B) can provide α values from experimentally obtained J at different σ values (Eq. 1.7).[13,17-19]

$$\ln(J) = \ln(\text{A}) - \left(\frac{16\pi v_m^2\alpha^3}{3k_B^3T^3}\right)\frac{1}{\sigma^2} = \ln(A) - B\,\frac{1}{\sigma^2} \quad \text{Eq. 1.6}$$

$$\alpha = \left(\frac{3Bk_B^3T^3}{16\pi v_m^2}\right)^{\frac{1}{3}} \quad \text{Eq. 1.7}$$

1.1.2 Non-Classical Nucleation Pathways via Formation of Prenucleation Clusters

In recent studies of biomineralization, researchers have reported nucleation pathways which cannot be fully described by CNT. One of the most noticeable findings regarding non-classical nucleation pathways is the existence of prenucleation clusters (PNCs), which are known as solute precursors to phases forming from both under- and supersaturated homogeneous solution.[12,20] The difference between classical and non-classical nucleation pathways is illustrated in Figure 1.2, showing that the aggregation and condensation of PNCs often leads to nucleation of an amorphous phase which can later transform to crystalline phases.[20,21]

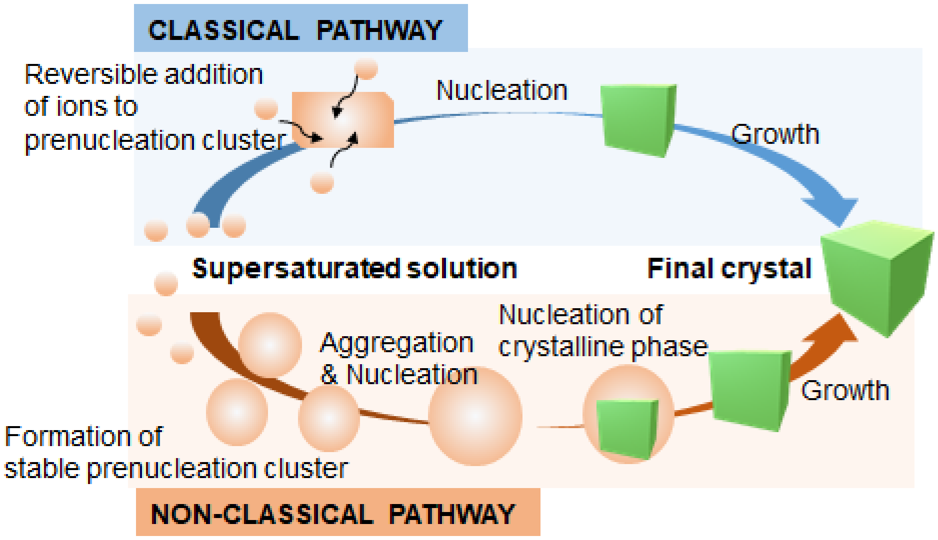

Figure 1.2 Schematic illustration of classical and non-classical pathways of calcium carbonate nucleation suggested by Gebauer *et al.*[20] Adapted from Ref. 21.

Even before the importance of these clusters in nucleation was highlighted about a decade ago,[20,21] nucleation of ACP had been reported in the 1970's by Posner and co-workers.[22,23] Based on analyses of ACP using radial distribution functions based on X-ray diffraction (XRD) and chemical analyses, they suggested clusters of $Ca_9(PO_4)_6$, later named Posner's clusters, would form in solution and aggregate to nucleate ACP. This suggested pathway was well-consistent with the non-classical pathway via the aggregation of PNCs, as shown in Figure 1.2. Posner's clusters were further supported by experimental evidence from later studies,[24,25] observing small clusters whose sizes are comparable to the theoretical values of Posner's clusters (9.5 Å). For example, small clusters of 0.7–1.0 nm were detected by an intensity-enhanced dynamic light scattering technique[24] and by dynamic light scattering photometry[25] in different types of simulated body fluids (SBFs). The hydrodynamic diameter of CaP clusters was relatively stable at ~1 nm, unlike other types of clusters. For example, the size of calcium carbonate clusters ranges between 10 and 30 nm, and their size changes easily over time in SBFs.[25]

Using high-resolution cryogenic temperature transmission electron microscopy (cryo-TEM), recent studies have successfully visualized stable PNCs during the early stage of CaP nucleation.[8,26] Dey *et al*. showed cryo-TEM images captured at five nucleation stages of crystalline apatite, beginning with loose aggregation of PNCs in an SBF solution (stage 1).[26] They estimated the averaged diameter of PNCs as 0.9 ± 0.2 nm. The PNCs were further aggregated at a monolayer surface as an organic substrate (stage 2) and then densified (stage 3) to nucleate spherical ACP particles (stage 4) before crystallization (stage 5).

More recently, from cryo-TEM observations, Habraken *et al*. reported the same nucleation pathway of CaP in an SBF with excess tris-buffer (2-amino-2-hydroxymethylpropane-1,3-diol).[8] Supported by analyses using *in situ* atomic force microscopy (AFM), and computational results from *ab initio* calculation, they concluded that the PNC are soluble ion association complexes $[Ca(HPO_4)_3]^{4-}$. The aggregated form of these complexes takes up Ca^{2+} ions from solution to be precipitated as ACP. The combination of the complexes was revealed to significantly lower the nucleation energy barrier. The authors introduced a term, the elimination of excess free energy,

ΔG_{EX} to incorporate this decrease in ΔG, which can be expressed as an extended CNT model as described in Eq. 1.8, where N is the number of complexes forming the particle.

$$\Delta G = -\Delta G_b + \Delta G_s - N\Delta G_{EX} \qquad \text{Eq. 1.8}$$

1.1.3 Elongated Growth of CaP for the Development of Biomaterials

Many CaP biomineralization studies show that amorphous and spherical CaP nuclei transform to plate-like CaP crystals in both biomimetic conditions[8,26,27] and animal samples.[6,28] Recent molecular dynamics simulations have introduced interesting results showing how organic molecules in body fluid solutions, such as non-collagenous proteins, control the morphology and crystallinity.[29-31] For example, Yang *et al*., suggested that the preferential crystal growth directions of HA can be determined by changes in the interfacial energy of the (001), (100), and (110) faces of HA, accomplished by the adsorption of two phosphorylated acidic amino sequences in bone sialoprotein.[29] Similarly, adsorption of small acidic molecules, such as phosphoserine and citrate,[30,31] or even carbonate ions,[32] were suggested to mediate the growth of apatite to form bone-like apatite minerals. Therefore, to better understand how the morphology of bioapatite is controlled in physiologic conditions, more tissue observations and kinetic studies in biomimetic conditions are needed.

1.2 Collagen as a Biological Template for Heterogeneous CaP nucleation

1.2.1 Fibrillar Collagen Structures as Biological Templates for Bone Mineralization

The recent findings about nucleation, growth, and crystallization described in **Chapter 1.1** have broadened our understanding of the formation of CaP minerals in biomimetic solutions, such as SBFs. However, these mineralization behaviors are different when CaP forms within the fibrillar collagen structure, which serves as a biological template. We poorly understand how the physicochemical properties of collagen are related to CaP mineralization.

The Hodge–Petruska model offers a relatively simple but widely accepted description for the packing of collagen molecules in bone.[33,34] Briefly, triple helix type I collagen molecules pack together in a quarter stagger array to form microfibrils. The molecules are stacked end-to-end, with approximately 40 nm of space between them and approximately 27 nm of overlapped area. This arrangement forms a regular pattern of gap channels within which mineral can nucleate for intrafibrillar mineralization (IM). Orgel and colleagues demonstrated a three-dimensional super-twist and a more complex collagen packing structure, a finding supported by a synchrotron-based electron density map.[35,36] Alexander *et al*. developed a steric model to describe the three-dimensional arrangements of apatite relative to collagen, based on a scanning transmission electron microscopy (STEM) analysis of Ca and C distribution in bone tissues.[33] Their model was effectively used to estimate the packing density of bioapatite within the collagen gap region, which is an important parameter in predicting the mechanical properties of collagen fibrils in the mineralization process. Collagen fibrils consist of collagen molecules self-assembled in a hierarchical manner to form a matrix, which becomes a hierarchical structure with several levels. In this section, we mostly focus on nucleation at this microfibril level to gain a nanometer-scale view of collagen mineralization. Its consequences for higher level structures will be discussed in **Chapter 1.3**.

1.2.2 Collagen as a Substrate for Heterogeneous CaP Nucleation

To explain how the interfacial energy and nucleation barrier decrease in the presence of a substrate, a heterogeneous nucleation model in CNT has often been adopted.[11,13] With an assumption of hemispherical particle formation on a flat substrate, ΔG in Eq. 1.2 can be modified as below,[13] where α_{lc}, α_{sc}, and α_{ls} are the interfacial energies between the liquid-substrate, substrate-crystal, and liquid-substrate, respectively.

$$\Delta G = -\left\{\frac{\left[\left(\frac{2}{3}\right)\pi r^3\right]}{v_m}\right\} k_B T\sigma + \pi r^2(2\alpha_{lc} + \alpha_{sc} - \alpha_{ls}) \qquad \text{Eq. 1.9}$$

We can simplify the terms in the brackets by defining the effective interfacial energy, α':

$$\alpha^{'} = \alpha_{lc}(1 - \frac{(\alpha_{ls} - \alpha_{sc})}{2\alpha_{lc}}) \qquad \text{Eq. 1.10}$$

Then, we can utilize the CNT relationships in Eq. 1.3–1.7 as they are, by simply replacing α with α'. The morphology (or contact angle) of a nucleus is highly influenced by the structural match between the nucleus and the substrate. This influence can be incorporated into CNT by using an interfacial correlation function, whose information can be found in a recent study by Jung *et al*.[37]

Collagen has also been reported to serve as a substrate promoting heterogeneous CaP nucleation.[38-40] For example, Koutsoukos and Nancollas reported α' = 105 mJ m^{-2} for heterogenous HA nucleation on collagen.[40] With an improved measurement technique using *in situ* AFM, Habraken *et al*. also reported a similar value of α' = 90 mJ m^{-2},[8] which is about one half of the value for homogeneous nucleation in bulk solution (α = 180 mJ m^{-2}).[41] Although these studies provided meaningful information, limitations still exist for evaluating nucleation behaviors in the complex collagen structure. For example, AFM is a surface characterization tool, thus it cannot not fully analyze CaP particles embedded in the collagen structure. In addition, a more careful consideration of collagen geometry than the flat substrate assumption is needed to properly account for the influence of the confinement of nuclei in gap regions. These aspects will be further discussed in the following chapters.

1.2.3 Intrafibrillar Mineralization versus Extrafibrillar Mineralization

Non-collagenous proteins (NCPs), which are abundant in circulating body fluids, are known to mediate IM in physiological systems. The mechanisms of IM, designed to successfully mimic the biomineralization process, are the subject of a number of hypotheses. These include processes involving a polymer-induced liquid-precursor (PILP), in which stable pre-nucleation clusters (PNCs) form and penetrate the gap regions.[42] Using polyaspartic acid (pAsp) as a replacement for NCP, *in vitro* studies have supported this hypothesis.[43-45] Nudelman *et al*. captured important moments, using cryo-TEM, during intrafibrillar CaP formation within a single collagen fibril. Their images show that amorphous calcium phosphate (ACP) particles transport into the gap channels in the presence of pAsp.[27] However, the authors suggested that the role of NCP may be limited to the inhibition of EM, because a similar process was observed using one of the NCPs, fetuin, which is too large to diffuse into the gap region.[46] The role of C-terminal ends at the border between the overlap and gap regions can be important because their net negative charges can attract ACP. However, this cannot fully explain how ACP can be transported into the central areas of the collagen fibrils, rather than accumulating near the entry of the C-terminus. A more likely mechanism to explain this phenomenon is the transport of PILP-initiated ACP by capillary action.[43,44]

While the role of NCPs in IM is still controversial, a recent study emphasized the role of collagen structure over NCP.[47] Mineralization of intrafibrillar spaces of dense collagen matrices was achieved in the absence of any NCP, by seeding calcium phosphate nuclei within the collagen fibrils during the preparation of the matrix. Even so, a number of unresolved questions remain. For example, if PILP formation is not the dominant mechanism for IM, how can NCP control this process? How are ACP nuclei, formed at the edge of the collagen fibril, transported into the central area of the fibrils? How does the mineralization process of a single collagen fibril differ from that of a dense collagen matrix? How do fibrillar structures of collagen influence mineralization behaviors? To properly answer these questions, more nanoscale evaluation of CaP nucleation in collagen is required.

Although IM has been highlighted in recent studies about nanoscale collagen mineralization, CaP crystals are also found in the unconfined extrafibrillar spaces of collagen (extrafibrillar mineralization, EM) as an aggregate without a specific orientation.[48,49] It is interesting to note that two clearly distinct mineralization behaviors occur in the same body fluid condition, which emphasizes the importance of fibrillar collagen structure in controlling mineral distribution. By evaluating the different nucleation behaviors of CaP during EM and IM, we will be able to understand the role of collagen in CaP nucleation for the construction of bones and how EM and IM compete for calcium and phosphate precursors in body fluids.

The difficulty of performing *in situ* measurements makes an accurate examination of CaP nucleation and growth within collagen matrix challenging. Conventional techniques, such as high-resolution TEM (HRTEM), Raman spectroscopy, and X-ray diffraction (XRD), require *ex situ* sample preparation that likely alters the physiochemical properties of the collagen and nanometer-scale inorganic nuclei. Moreover, real-time measurements and matrix-level observations are not possible with these techniques due to the sample treatment procedures and regulated environment needed in the instrument for cryogenic imaging. Synchrotron-based *in situ* X-ray scattering techniques can be a promising option to overcome the difficulties. In aqueous system, these techniques can provide time-resolved information about newly formed particles, such as their morphologies, nucleation rates, and crystallinities, minimizing the physicochemical properties of particles and substrates. More discussion on heterogeneous nucleation of nanoparticles in an aqueous system using *in situ* observation tools (Figure 1.3) can be found in our review article.[11]

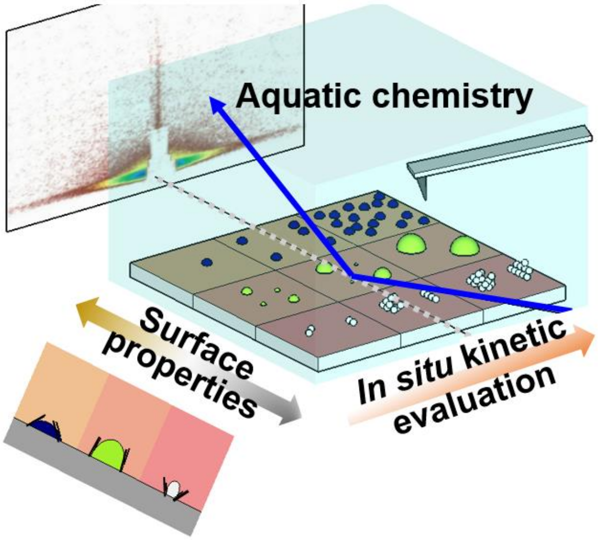

Figure 1.3 *In situ* experimental approaches for nanoparticle observations in real-time: X-ray scattering and atomic force microscopy.[11] Copyright 2016 American Chemical Society.

1.2.4 Confined Nucleation of CaP minerals in Collagen

One of the noticeable differences between IM and EM is the nanoscale confinement effect resulting from the dimensions of the collagen gap region. The confined nucleation and growth of mineral phases, such as mineral formation in porous structures, are of interest in many biological and geochemical processes and engineering applications.[50-53] Minerals formed under confinement exhibit physicochemical properties, such as their melting point or crystal polymorphism, which are distinct from their bulk phase counterparts.[52,54,55] For example, the solubilities of the minerals can be altered by the curvature of edge surfaces created by confinement. To predict solubility changes from confinement, the modified Kelvin equation has been used (Eq. 1.11).[56]

$$\frac{S_r}{S_0} = \exp\left(\frac{2\alpha V}{RTr}\right) \qquad \text{Eq. 1.11}$$

In this equation, S_r and S_0 are the solubilities in confined space and the solubility of bulk, respectively. V is the molecular volume in $m^3\ mol^{-1}$, and R is the gas constant. Depending on the wettability or chemical affinity, the sign of r can be either positive (convex nucleus) or negative (concave nucleus), leading to increased or decreased solubility, respectively.[57,58]

Because the collagen gap spaces provide confined nucleation sites (~40 nm long and 2 nm high), many researchers have evaluated CaP nucleation in the confined porous structure. For example, HA crystals nucleated in 25–300 nm pores showed a higher degree of orientation than those formed in bulk solution,[59,60] as commonly observed in bioapatite in bones and teeth.[61] However, we know little about how nanoscale confinement affects the nucleation of calcium phosphate minerals (CaP) in more physiologically relevant systems, leaving open the question of why nature chose confined collagen gap spaces for bone mineralization.

1.3 Macroscale Mechanical Properties Controlled by Nucleation at Nanoscale

1.3.1 Hierarchical Structures of Bone

In bone, the combination of a relatively compliant component (collagen) with relatively stiff inclusions (mineral crystals) provides a wide range of tissue-level mechanical properties. Investigating CaP crystal formation on collagen at the nanoscale (i.e., at the earliest stages of nucleation) is crucial for understanding how the mineral stiffens collagen while exhibiting a remarkable range of mechanical properties, such as elastic modulus and toughness. Bone's excellent mechanical properties are related to its hierarchical structures and nanoscale organization of bioapatite minerals and protein templates. Nanomechanical heterogeneities are produced by this hierarchical arrangement produces, enabling high energy dissipation and resistance to fracture.[62]

The structural hierarchy of bone was firstly suggested to have five levels, and nowadays, it was extended to even nine levels.[63] Reznikov *et al.* introduced a scheme showing the hierarchical organization of bone, from level I (components: collagen, bioapatite, NCPs, and etc.) to level IX (organ: whole bone) as shown in Figure 1.4.[4] With the advances in technologies, more structural information will become available.

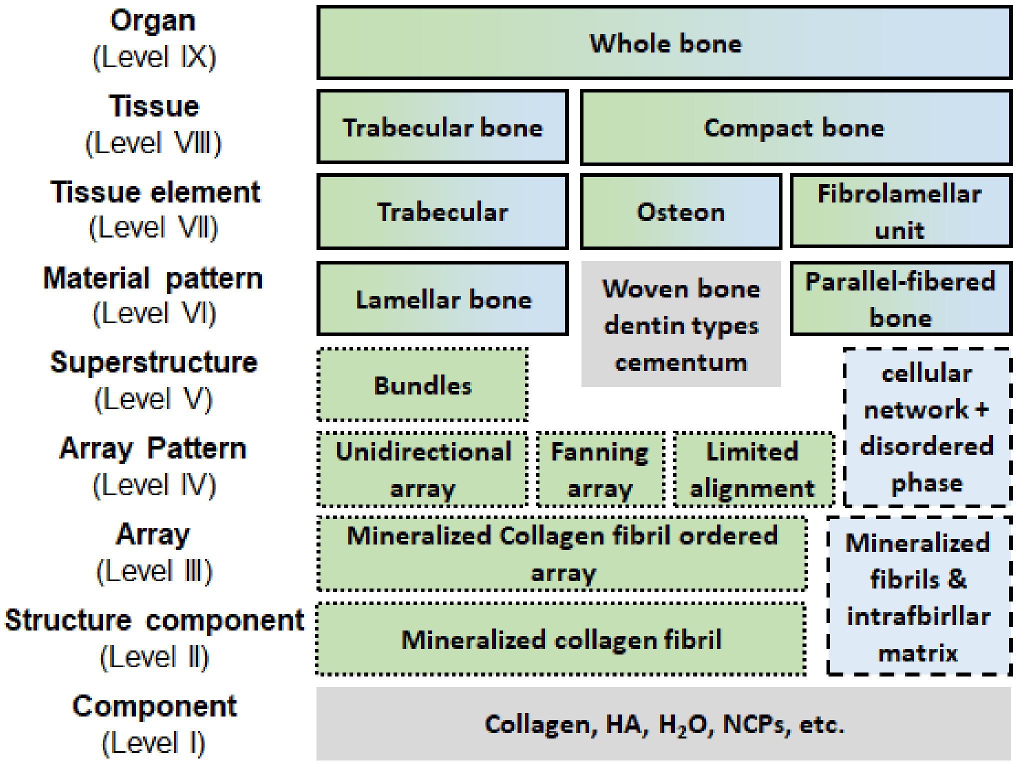

Figure 1.4 Hierarchical organization of bone, suggested by Reznikov *et al*. Adapted from Ref. 4. Materials in level II–V can be divided into ordered material (green dotted box) and the disordered material (blue dashed box). At level VI, these two materials combine (Solid box).

1.3.2 Multiscale Analyses: From Nanoscale Nucleation to Macroscale Mechanical Properties

Traditionally, bulk parameters, such as the total Ca contents or porosities, have been used as parameters to predict the strength and elastic modulus of bone.[64,65] However, recent studies have emphasized that the specific arrangements of minerals relative to collagen strongly determine mechanical properties at the tissue-level, such the strength and toughness.[66,67] Therefore, multi-scale analyses are important to fully understand bone's hierarchical structure, from nanoscale nucleation to mechanical properties at macroscale. Reznikov *et al*. emphasized the importance of the association of the mineral phase with collagen in bones' paradoxical increase of both stiffness and toughness with mineralization.[5] They observed, based on 3D reconstruction of STEM images, that curved nanocrystal rods merge laterally to form platelets, which further organize into stacks with approximately 2 nm of separation. These stacks of platelets, single platelets, and single rods coalesce into larger polycrystalline aggregates, ultimately spanning adjacent fibrils continuously to achieve cross-fibrillar mineralization. The fractal-like organization is self-assembled to form a hierarchical structure, yet we do not fully understand the contributions of individual components to the mechanical properties of bones.

Recently, full-atomistic calculations of the 3D molecular structure of collagen were performed by Nair *et al*., simulating the mechanical properties of mineralized collagen matrix at different mineral densities.[10] Under tensile loading, the mineral crystals within collagen gap regions carried up to four times the stress of the collagen fibrils. Collagen, on the other hand, predominantly determined matrices' deformation response. These findings revealed that the combination of collagen and mineral was able to able to achieve superior energy dissipation and fracture resistance characteristics beyond the simple summation of individual components.

Liu *et al*. successfully simulated stiffening of collagen fibril along the mineralization (a lower hierarchical level), and connected this fibril-level model with higher hierarchical levels to estimate mineralization-dependent mechanics at the tissue-level.[9] Interestingly, the nucleation site, whether in the gap region or on the external surface, was revealed as an important factor governing the stiffness of collagen, highlighting the importance of the interaction between nanoscale reactions and macroscale mechanical properties. These articles clearly show that nanoscale nucleation needs to be understood as a process of building a hierarchical structure. More experimental studies, utilizing multi-scale analytical tools, are required to connect nanoscale nucleation and macroscale mechanical properties.

1.4 Research Objectives and Hypothesis

As discussed in **Chapter 1.1–1.3**, CaP biomineralization has been evaluated by researchers from many disciplines, including chemistry, geochemistry, mineralogy, materials science, and mechanical and biomedical engineering. Thanks to their efforts, significant advances have been achieved during recent decades. However, the complexity of hierarchical nano/organic composite systems still makes it challenging to fully understand the mechanisms of CaP nucleation and crystallization and their practical applications.

The purposes of this study were to provide new thermodynamic and kinetic information about CaP nucleation, growth, and phase transformation in organic matrices, and to provide engineering solutions, using the obtained information, to biomedical and environmental problems. To achieve these goals, we importantly utilized multidisciplinary approaches, including synchrotron based in *situ* X-ray analyses for nanoscale observation and tensile mechanical testing. In addition to suggesting practical application of the findings from fundamental aspects of CaP biomineralization, in a leap of scale, the obtained knowledge was applied to develop a new environmental remediation strategy. The ability of CaP minerals to balance aqueous P concentrations will inspire better management of P balances in aqueous systems disrupted by the excessive inflow of P from human activities. To achieve these research goals, five specific objectives were established, as described below, followed by their significances and hypotheses.

Objective 1: Investigate kinetics and pathways of calcium phosphate nucleation for collagen mineralization

Significance & Hypothesis: Non-classical nucleation pathways were suggested for CaP biomineralization in aqueous environments simulating body fluid conditions. However, CaP nucleation pathways within collagen fibrils have not been fully understood due to the complexity of collagen/CaP composites and the lack of proper analytical tools to monitor the nucleation kinetics. To achieve **Objective 1**, I utilized state of the art synchrotron-based X-ray analyses for collagen matrices, which could overcome the limitations of conventional *ex situ* measurements. Using *in situ* measurements in real-time, X-ray analyses better illuminated the effects of solution chemistries on CaP mineralization on/in collagen matrices, with minimal alterations of sample properties. We hypothesized that we could separately evaluate the nucleation behaviors during IM and EM utilizing pAsp. I determined the nucleation and growth rates of CaP during the development of IM and EM, in addition to the kinetics of phase transformation. The kinetic information revealed the mechanisms behind bone mineralization by illuminating the factors controlling the spatial and temporal distribution of CaP during IM and EM.

Objective 2: Examine the thermodynamics of confined nucleation in collagen gap regions during intrafibrillar mineralization

Hypothesis & Significance: Collagen matrices have hierarchical pore-structures consisting of micrometer scale extrafibrillar pore structures and nanoscale gap channels within the fibrils. Both extrafibrillar and intrafibrillar mineralization behaviors have been reported in different environments. However, it is not fully understood how intrafibrillar mineralization is achieved. From **Objective 1**, we evaluated the different pathways for IM and EM. The different nucleation pathways indicated that different nucleation energy barriers exist for the pathways. To achieve **Objective 2**, I evaluated J at different σ of SBF solutions during IM and EM separately. Then, utilizing CNT as described in Eqs. 1.1–1.7, the α and ΔG_n values for CaP mineralization of collagen were evaluated. We hypothesized that 2D growth enforced in the confined gap spaces would provide less surface energy penalty. However, a proper model still needs to be developed to address this aspect.

Objective 3: Evaluate the influence of mechanical bonding applied to collagen during CaP nucleation and analyze the resulting mechanical properties of the structure at the tissue-level.

Hypothesis & Significance: After understanding the kinetic and thermodynamic properties of CaP nucleation in collagen, we evaluated how nucleation influences mechanical properties at the tissue-level. To achieve **Objective 3**, collagen matrices with different extents of IM and EM were examined. The contribution of IM to elastic modulus increase would be more significant than that of EM due to a better contact with porous surfaces. Cyclic strain, which mimics human walking motion, was applied as an efficient approach to increase the extent of IM. Based on the observations, a better structure-functional relationship model was developed. A more accurate prediction of the mechanical effects of biomineralization on collagen matrices will guide tissue engineering efforts for mineralized tissue substitutes.

Objective 4: Utilize pulsed electric stimulation to enhance collagen mineralization

Hypothesis & Significance: Development of a faster bone regeneration strategy is still challenging. One difficulty is that the dense fibrillar structure of collagen limits diffusion of precursor molecules into the inner matrix zones. To overcome this problem, I applied electrical stimulation, which is known to improve *in vivo* development of skeletal muscles and bone fracture healing in the clinical setting. However, the mechanism of action remains unclear, inhibiting its practical application. In particular, how the electric fields interact with the CaP nuclei formed inside the gap regions is unknown. I hypothesized that pulsed stimulation could enhance diffusion of precursor molecules within the dense fibrillar matrix. The research findings provide new insight for the study of IM, beyond the chemical and biological components.

Objective 5: Develop a sustainable environmental P management strategy utilizing biomineralization principles

Hypothesis & Significance: The global P cycle has been interrupted significantly during recent decades due to the increasing anthropogenic sources. To recover P from eutrophic environments and re-use it as a valuable resource, it is essential to develop a better P management plan. To achieve **Objective 5**, I utilized bioinspired principles of bone mineralization to control P levels in aqueous environments. Although CaP minerals, such as hydroxyapatite, show very low solubility at neutral pH, a huge nucleation barrier inhibits their precipitation, keeping the P concentration higher than its equilibrium condition. I hypothesized that the nucleation barrier can overcome by embedding reactive seed CaP nuclei in calcium alginate beads, which simulates CaP mineralization in collagen proteins.

1.5 Dissertation Overview

To realize the five objectives described above, five tasks were completed, with each task corresponding to an objective. The dissertation and five tasks are illustrated in Figure 1.5.

Task 1, regarding evaluation of nucleation kinetics and pathways, is addressed in **Chapter 2**. To evaluate the kinetics and pathways of CaP nucleation during EM and IM, we conducted *in* *situ* small-angle X-ray scattering (SAXS) and wide-angle X-ray diffraction (WAXD) analyses. To separately evaluate EM and IM, we added 10 mg L^{-1} pAsp in SBF solution. **Task 1** is addressed in **Chapter 2**.

Task 2, regarding confined nucleation in collagen gap regions for IM, is addressed in **Chapter 3**. To evaluate interfacial energies between nuclei and SBF solutions and their consequent nucleation energy barriers, we evaluated nucleation rates at different supersaturation indices of SBFs with respect to CaP minerals. In this task, a modified CNT model was developed to better evaluate thermodynamic parameters from experimental data. **Task 2** is addressed in **Chapter 3**.

Task 3, regarding the relationship between nanoscale nucleation and macroscale mechanical properties, is addressed in **Chapter 4**. Collagen samples demineralized from chicken tibia bones were re-mineralized under different mechanical loading conditions. The mechanical properties of re-mineralized collagen samples were evaluated for elastic modulus by a uniaxial tensile test. The correlation between nucleation behaviors and elastic modulus increase was evaluated using a tissue-level model. **Task 3** is addressed in **Chapter 4**.

Task 4, regarding enhancing collagen mineralization using pulsed electric stimulation, is addressed in **Chapter 5**. We applied pulsed electric stimulation, which mimics bioelectricity generated in human body. The stimulation was applied either through a cathode or an anode. The results were compared with continuous electric stimulation. The potential damage of pulsed application was also examined. **Task 4** is addressed in **Chapter 5**.

Task 5, regarding the development of a sustainable environmental P management plan, is addressed in **Chapter 6**. To reduce the nucleation energy barrier for CaP mineralization in P-rich aqueous environments, we embedded reactive nuclei in calcium alginate beads. Then the beads were utilized for P removal, and the beads after P recovery were evaluated for use as a slow-release fertilizer. We explored the crystalline degree of seed minerals and P removal and release efficiency. **Task 5** is addressed in **Chapter 6**.

In **Chapter 7**, the major conclusions and implications of the current work are summarized, and future directions are recommended.

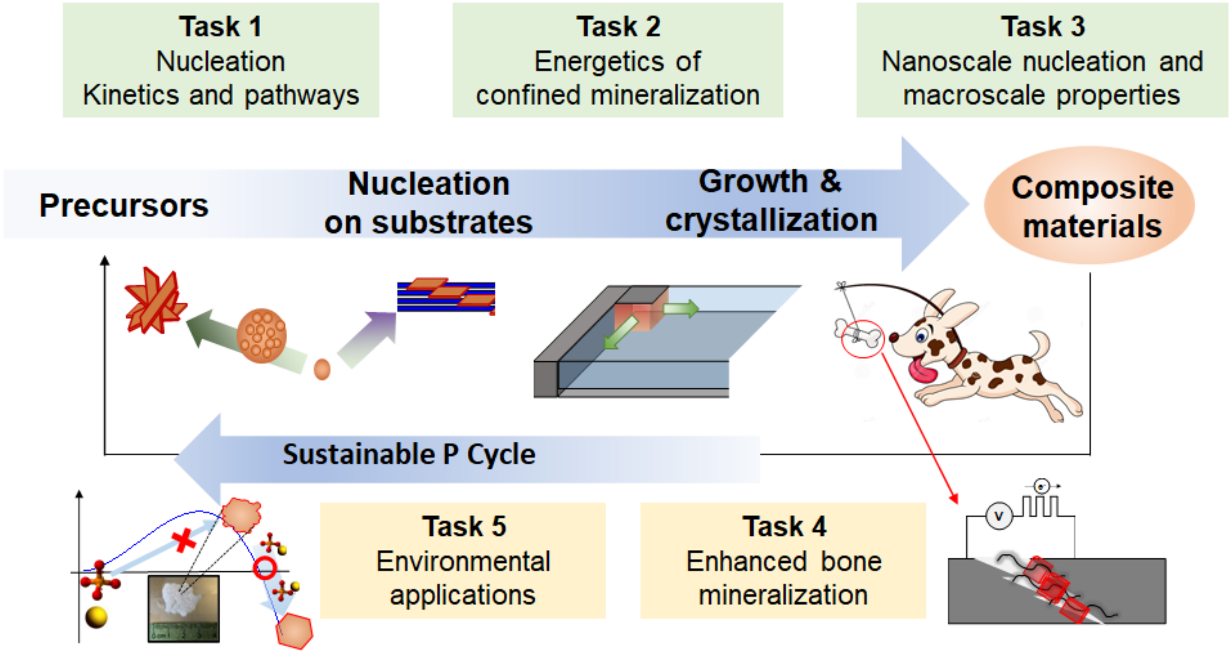

Figure 1.5 Overview and tasks of the dissertation.

Reprinted with permission from [Doyoon Kim, Byeongdu Lee, Stavros Thomopoulos, and Young-Shin Jun, *In Situ* Evaluation of Calcium Phosphate Nucleation Kinetics and Pathways during Intra- and Extrafibrillar Mineralization of Collagen Matrices. *Crystal Growth & Design*, 2016, 16(9), 5359–5366. DOI: 10.1021/acs.cgd.6b00864]. Copyright [2016] American Chemical Society.

Chapter 2. Investigation of Calcium Phosphate Nucleation Kinetics and Pathways for Collagen Mineralization

Portions of this chapter have been published in *Crystal Growth & Design* in 2016, DOI: 10.1021/acs.cgd.6b00864.

2.1 Overview

New pathways for CaP biomineralization, which are distinct from the classical view of nucleation, have been suggested recently. However, CaP nucleation pathways within collagen fibrils have not been fully understood owing to the complexity of collagen/CaP composites. Moreover, the lack of proper analytical tools to monitor the nucleation *in situ* has limited the thorough evaluation of kinetics for the pathways. Using *in situ* SAXS, we examined the nucleation and growth of CaP within collagen matrices. We revealed that nucleation sites within collagen fibrils determined the kinetics and pathways for CaP nucleation and its phase transformation, from amorphous species to crystalline plates, during the biomineralization process. Further, we elucidated how a nucleation inhibitor, pAsp, governs mineralization kinetics and pathways at multiple length scales. Mineralization without pAsp led initially to spherical aggregates of CaP in the entire extrafibrillar space. With time, the spherical aggregates transformed into plates at the outermost surface of the collagen matrix, preventing intrafibrillar mineralization inside. However, mineralization with pAsp led directly to the formation of intrafibrillar CaP plates with a spatial distribution gradient through the depth of the matrix. The results illuminate mineral nucleation kinetics and real-time nanoparticle distributions within organic matrices in solutions containing body fluid components. Because the macroscale mechanical properties of collagen matrices depend on their mineral content, phase, and arrangement at the nanoscale, this study contributes to better design and fabrication of biomaterials for regenerative medicine.

2.2 Introduction

Mammalian mineralized tissues are natural composites of fibrillar collagen proteins[34,35] and CaP nanocrystals.[2,6,68] The combination of a compliant component (collagen) with relatively stiff inclusions (CaP crystals) provides a wide range of tissue-level mechanical properties.[9,10,33] This range includes stiff (but brittle) tooth enamel, made mostly of mineral,[2,6] and partially mineralized tendon-to-bone attachments with high toughness.[9,69,70] Type I collagen molecules self-assemble into a fibril with a periodic 67 nm banded pattern.[34,35] There are 40 nm gap zones between neighboring collagen molecules, providing nucleation sites for IM.[27,68,71] Stabilization of PNCs is essential to IM by inhibiting CaP nucleation in extrafibrillar spaces (EM).[8,27,72,73] In addition to physiologically existing NCPs, such as fetuin,[27,72] pAsp has been shown to promote IM during the in vitro mimicking of collagen mineralization.[27,43,71] Controlling the nucleation sites and kinetics using EM inhibitors, such as pAsp, can be an effective approach to achieving targeted mechanical properties of both individual collagen fibrils at the nanometer scale and tissue constructs at the millimeter scale.

Previous nanoscale observations relied on snapshot images of debris[43] or selected cross sections from matrices[47] or individual fibrils,[27] typically focusing on late *in vitro* mineralization events. These studies required extensive sample preparation procedures prior to imaging or were limited to cryogenic sample environments,[27,43,47] and so could not fully explore the *in situ* kinetics of nucleation and growth of CaP, which involve a dynamic sequence of morphological changes with phase transformations. The phase transformations include amorphous CaP phases as important intermediate products.[8,23,26,28,74,75] To understand the mineralization of tissue-level scaffolds, the spatial distribution of CaP within millimeter-sized collagen matrices needs to be evaluated from the nanoscale, as mineral crystals nucleate and grow within collagen fibrils,[27] through the macroscale, where mineral crystals are widely distributed in the extrafibrillar spaces between collagen fibrils arranged within the matrix.[47,49] Prior approaches have not provided continuous real-time information on the spatial distribution of CaP within a collagen matrix over these length scales. Without *in situ* kinetic evaluation of mineral nucleation and growth, and of the spatial distribution of the mineral crystals at multiple length scales, a precise design of CaP-stiffened collagen matrices cannot be achieved.

Studies utilizing synchrotron X-ray techniques have revealed important aspects of bone and bioengineered materials.[23,76-80] Recent studies have provided full 3D reconstruction of collagen fiber orientation in human trabecular bone and tooth, using SAXS with tensor tomography.[81,82] However, in situ nucleation kinetics during collagen mineralization have not been evaluated despite their importance in governing the chemical and mechanical properties of organic-nanocrystal composites. Here, using SAXS, we provide *in situ* investigations[17,83] of CaP development (i.e., its morphology and distribution) within reconstituted collagen matrices under the influence of pAsp, which controls the nucleation kinetics of CaP in extrafibrillar space.[27,42,71] This evaluation of the temporal development of CaP demonstrates different pathways for intra- and extrafibrillar mineralization. The macroscale spatial distributions of CaP nanocrystals in different stages emphasize the role of the extrafibrillar spaces of the collagen matrices in transport of nucleation and growth precursors during tissue mineralization.

2.3 Materials and Methods

2.3.1 Preparation of Samples

Collagen matrices were reconstituted based on a previously published method.[84] Type I collagen (C857, calf skin lyophilized, Elastin Products Company, Inc.) was dissolved in 0.5 mM HCl (12 mg ml^{-1}) by magnetic stirring, followed by degassing under vacuum for 4 days. Collagen samples were maintained at 4°C during this process. Then the collagen solution was placed in a specially designed PTFE frame with a #1 cover glass on one side, and the frame was placed for an hour in TES buffered saline (5.5, 6.32, and 3.4 g l^{-1} of TES, NaCl, and Na_2HPO_4, in deionized water, pH 7.5 at 37°C). The frame was then stored in deionized water overnight to remove excess salt, and the opposite side was capped with another glass. The cover glass held the solution and collagen, and also allowed X-ray penetration during the X-ray scattering analysis. The frame was 2 mm thick in the direction of the X-ray path. The collagen matrices were 10 mm wide and 5 mm high. The cover glasses were 3 mm taller than the matrices, to contain sufficient SBF to prevent collagen dehydration during the X-ray scattering analysis (Figure 2.1a). To reconstitute the lyophilized collagen in a well-controlled shape with uniform thickness for the SAXS evaluations, a collagen fibrillar density of 12 mg ml^{-1} was used. With this collagen fibrillar density, we were able to observe both intra and extrafibrillar mineralization behaviors clearly in the mineralization solution.

In addition, thin collagen films were prepared on glass slides to simulate the reaction occurring at the outermost surface of collagen matrices, which were not analyzed from sections cut along the *z*-direction. To prepare a film, a droplet (0.1 ml) of dissolved collagen (12 mg ml^{-1} of collagen in 0.5 mM HCl) was evenly dispersed on a glass slide (1×1 cm^2) using a spin coater (Laurell WS-650MZ-23NPP, 5000 rpm for 30 s). Then the slide was placed in the TES buffered saline for an hour to polymerize collagen fibrils. The prepared film on glass was stored in deionized water, as was done for collagen matrices. CaP structures formed during the collagen mineralization were compared with synthetic hydroxyapatite sample (ACROS Organics™).

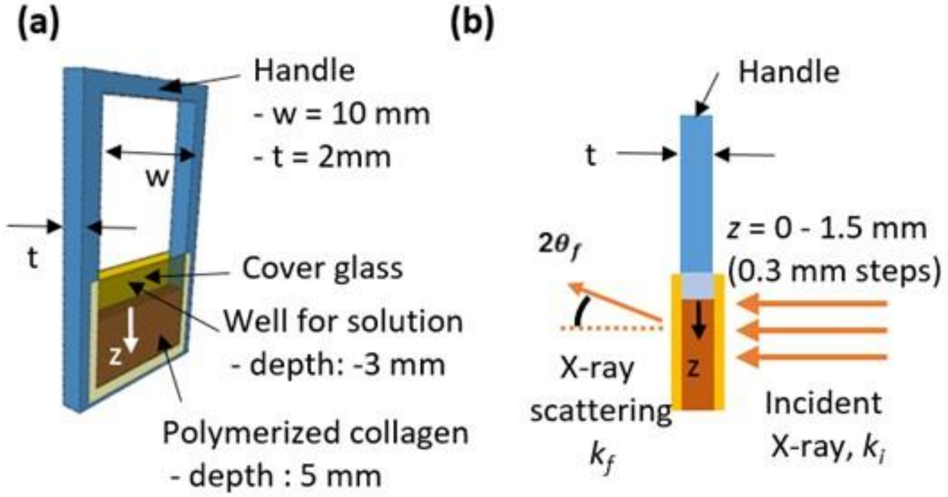

Figure 2.1 (**a**) Design of custom-made sample frame containing collagen matrix between two cover glasses, with an indication of the *z*-direction. (**b**) Experimental setup for SAXS measurements. k_i and k_f are the incident and scattered wave vectors, respectively, and $2\theta_\mathrm{f}$ is the exit angle of the X-rays. SAXS measurements were taken at different positions of the matrix along the *z*-direction from 0 (the interface between the SBF and collagen matrix) to 1.5 mm, with 0.3 mm steps.

2.3.2 Simulated Body Fluid and the Flow-through Reactor

Simulated body fluid and the flow-through reactor. A simulated body fluid proposed by Kokubo *et al*. (1×SBF) is commonly used because of its similarity in ionic components to human body plasma.[85,86] To conduct our experiments within a reasonable time, we used an SBF with three times higher concentrations of calcium and phosphate ions (3×SBF) as an experimental solution. The ionic compositions of 1×SBF, 3×SBF, and human blood plasma are listed in Table 2.1. American Chemical Society grades of NaCl (7.996 g, BDH Chemicals), $NaHCO_3$ (0.350 g, BDH

Chemicals), KCl (0.224 g, BDH Chemicals), $MgCl_2 \cdot 6H_2O$ (0.305 g, EMD Millipore), 1 M HCl (40 ml, BDH Chemicals), Na_2SO_4 (0.071 g, Alfa Aesar), tris(hydroxymethyl)aminomethane (Tris, 6.057 g, Alfa Aesar) were added to 900 ml of deionized water (18.2 MΩ-cm). Either 0 or 10 mg of polyaspartic acid, pAsp (sodium salt, Mw: 5,000 Da, LANXES) was added to the solution, depending on the experimental condition. The solution was equally separated into two 500 ml polyethylene bottles, then either 0.684 g of $K_2HPO_4 \cdot 3H_2O$ (Alfa Aesar) or 0.834 g of $CaCl_2$ (Alfa Aesar) was added to each bottle. Both solutions were adjusted to pH 7.25 using 1 N HCl, and the volumes of the solutions were adjusted to 500 ml with deionized water.

Table 2.1. Ionic components of simulated body fluids and human blood plasma.

Solution	Na^+	K^+	Mg^{2+}	Ca^{2+}	Cl^-	HCO^{3-}	HPO_4^{2-}	SO_4^{2-}
1×SBF[2]	142.0	5.0	1.5	2.5	147.8	4.2	1.0	0.5
3×SBF	142.0	9.0	1.5	7.5	157.8	4.2	3.0	0.5
Human blood plasma[3]	142.0	5.0	1.5	2.5	103.0	27.0	1.0	0.5

* The pH of the 3×SBF was adjusted to 7.25 with 50 mM of Tris ($(CH_2OH)_3CNH_2$) and 1 N HCl.

For the collagen mineralization, the two solutions, separately contained in 60 mL syringes, were continuously flowed into reactor at 0.11 ml min^{-1} per syringe, using a syringe pump. To prevent any precipitation prior to the experiment, the two solutions were combined just before the reaction (Figure 2–S1a). The volume of the solution in the reactor was 12.5 ml, giving 57 min of residence time. A hot plate maintained the reactor at 37±1°C. Homogeneous nucleation in 3×SBF containing either 0 or 10 mg l^{-1} pAsp was not significant enough to be detectable by SAXS.

In this study, to better evaluate the different nucleation kinetics and pathways during both mineralization processes and to thoroughly investigate this complex system, we simplified the system to use one type and concentration of pAsp (10 mg l^{-1} of 5,000 Da pAsp). The addition of 10 mg l^{-1} pAsp effectively controlled mineralization patterns during the 15 h period in our experimental setup; therefore, we used this concentration throughout the study. The concentration of pAsp used here was within the ranges of previous studies evaluating the influence of pAsp on CaP mineralization: 10 mg l^{-1} was used in a study by Nudelman *et al*. for their cryogenic observations of collagen fibrils;[27] 50 mg l^{-1} was used by studies by Jee *et al*. on the biomimetic mineralization of collagen utilizing the PILP process;[43,44] 1–100 mg l^{-1} was used by Cantaert *et al*., to study the effect of pAsp on CaP precipitation in confined structures utilizing track-etch (TE) membrane pores.[60] Furthermore, we did test 100 mg l^{-1} pAsp; however, we were not able to monitor the nucleation behaviors properly due to its slow mineralization kinetics. The influences of other types of nucleation inhibitors were not tested for a similar reason. For example, fetuin, one of the most well-known NCPs, stimulates IM, while simultaneously forming extrafibrillar CaP.[27] Therefore, the use of the fetuin would not provide separate CaP nucleation pathways for IM and EM. In addition, we expect that changes in concentration and molecular weight of pAsp may alter the nucleation kinetics; however, we do not expect that those changes will lead to totally different nucleation pathways. Based on this study, future work can systematically evaluate the effects of molecular weights and concentrations of pAsp, or other types of nucleation inhibitors, such as non-collagenous proteins.

2.3.3 *In Situ* X-ray Scattering Data Collection and Analysis

SAXS data were collected at the Advanced Photon Source (APS, Sector 12-ID-B, Figure 2–S1b) at Argonne National Laboratory (Argonne, IL, USA).[17,83] At intervals of 5, 9.5, and 15 h, frames were immediately moved to the SAXS sample stage and scanned from $z = 0-1.5$ mm depth of the matrix (Figure 2.1b). The distance from the sample to the SAXS detector was 3.6 m, which provided a range of 0.0017−0.53 $Å^{-1}$ for the scattering vector, q. For each scan, the sample was exposed to a 14 keV X-ray beam for 1 s. The size of the beam was 150 μm (perpendicular to the z-direction) × 40 μm (parallel to the z-direction). Two different lateral positions were scanned at each time for duplicated samples; therefore, a total of four scattering patterns were obtained for each condition and position. Control SAXS intensities were acquired for unmineralized scenarios and used to define the background intensity (Figure 2–S2). Similarly, *in situ* WAXD analysis was conducted at APS sector 11-ID-B to identify the CaP phases during collagen mineralization ($q > 0.6$ $Å^{-1}$). Samples were exposed to a 58.66 keV X-ray beam (size: 300 μm × 300 μm) for 5 min for the data collection. The detailed procedures for the SAXS/WAXD data analyses are described in Section 2.7.1 Additional Experimental Section.

2.3.4 *Ex Situ* Analyses of Collagen Mineralization

Thin sections (100 nm) of the matrices were prepared for TEM analysis. Matrices were fixed in 100 mM cacodylate buffer containing 2% paraformaldehyde and 2.5% glutaraldehyde. The matrices were rinsed in a cacodylate buffer solution and then fixed with 1% osmium tetroxide in the buffer solution for 1 h. After dehydration in successive ethanol baths (30, 50, 70, 90, and 95 % for 15 min each, and 100% for 15 min × 3 times), samples were embedded in epoxy resin and thin sections were prepared using an ultramicrotome (EM UC7, Leica). Uranyl acetate and Reynold’s lead citrate were used for staining before the analysis. For TEM imaging without staining, treatments using osmium tetroxide, uranyl acetate, and lead citrate were omitted during the sample preparation. Two different instruments were used for TEM imaging. A JEOL 1200 EX II was operated at 100 kV, and a JEOL JEM-2100F was operated at 200 kV for higher resolution images.

Collagen matrices and films were placed in an ethanol bath for 5 h to remove excess ions, then stored at 4^{o}C until *ex situ* analyses by Raman spectroscopy and SEM equipped with energy-dispersive X-ray spectroscopy (EDX). Additionally, matrices were frozen in liquid nitrogen and cut into ~1 mm thick sections for the analysis along the *z*-direction (Figure 2–S5a). These sections were air-dried on either glass slides, for Raman spectroscopy, or on SEM specimen stubs covered with carbon tape, for SEM imaging. Using a 50× objective lens, Raman spectra were collected (inVia Raman spectrometer, Renishaw plc) at each position, with corresponding optical images. A spectral range from 100 to 3,700 Δcm^{-1} was used, and simultaneously detected with a spectral resolution of 1.13 Δcm^{-1}, using 514 nm laser excitation focused on the sample surface. Samples dried on the SEM stubs were sputter-coated with Au-Pd under Ar at 0.2 mbar (Cressington 108) to increase conductivity, then imaged with a 10 kV electron accelerating voltage at a 5−6 mm working distance (FEI Nova NanoSEM 230).

Fluorescence correlation spectroscopy (FCS) was used to evaluate the extrafibrillar pore structures of the matrices by measuring the diffusion time of rhodamine 6G (R6G).[87] We used an inverted design confocal laser scanning microscope (Zeiss Axiovert 200M) equipped with a 40× water immersion lens and a 514 nm argon laser. Fluorescence intensities were collected for 30 s × 10 times, and then the diffusion time, τ_D, was evaluated by analyzing correlation curves.[88] The procedures for the FCS data analyses are also described in Section 2.7.1 Additional Experimental Section.

2.4 Results and Discussion

2.4.1 SAXS Analysis of CaP Development within Collagen Matrices

An overview of the influence of pAsp on CaP development can be seen from invariant values, *Q*, which are proportional to the total volume of newly formed CaP particles with the same morphology and structure at a given time.[83,89] Q is expressed as $Q = (\frac{1}{2\pi^2}) \int q^2 I(q) dq$, where $I(q)$ is the scattering intensity at the scattering vector, q.[90] As shown in Figure 2.2a, for mineralized collagen matrices without pAsp (MC0p), Q increased monotonically up to 15 h, without any variation in the spatial distribution at z = 0.3−1.5 mm. However, the outermost surface of the matrix (z = 0) showed Q values at 15 h more than twice as high as those of other positions, with a statistically significant difference (Figures 2.2b and 2–S3a). In contrast, CaP formation was strongly hindered until 9.5 h in the matrices mineralized with the addition of 10 mg L^{-1} pAsp (MC10p) as a nucleation inhibitor.[27,91] With pAsp, interestingly, a clear gradient in CaP distribution, with statistically significant differences, was observed throughout the depth of the matrix at 15 h, demonstrating a direct relationship between the proximity of the SBF−matrix interfaces and CaP formation (Figures 2.2c and 2–S3b).

The intensities at high q for 15 h of mineralization showed typical SAXS patterns for plate-like objects (the slope at q around 0.01−0.1 $Å^{-1}$ is about −2, Porod scattering appears at q above 0.2 $Å^{-1}$),[8,92] both for samples mineralized with pAsp (at all z–positions) and without pAsp (only at z = 0). These data can be fit using a specific form factor and size distribution function (Supporting Information eqs. 2–S4−7). In the MC0P system, a population of plates was observed only at the SBF−MC0p interface (z = 0) at 15 h (Figure 2.3a), showing a sudden, but significant, volume fraction of plates at that location (V_{pl}, Figure 2.4b). Contrarily, populations of plates developed at all z-positions of the MC10p samples at 15 h, with decreasing V_{pl} along the z-direction (Figures 2.3b and 2.4b). The morphology of these plates (a thickness of 1.5 nm and mean diameter of 40 nm) was comparable to widely accepted dimensions for apatite crystals in mature bone (~2.1 × 30 × 40 nm^3).[9,73]

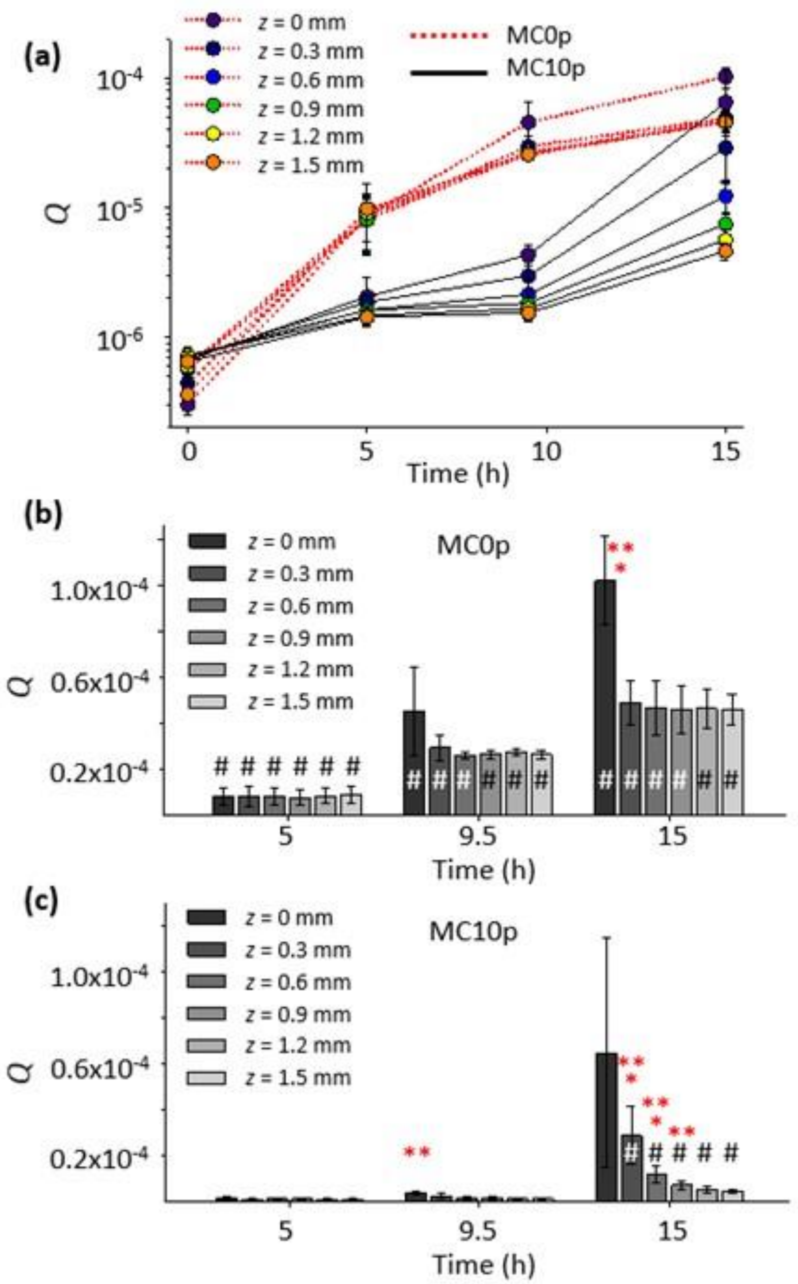

Figure 2.2 (**a**) Spatiotemporal development of CaP within collagen matrix, observed from the SAXS invariant, *Q*. The background intensity from unmineralized collagen matrices was subtracted from the SAXS intensities. (**b, c**) Statistical analysis of *Q* values from MC0p and MC10p, using a three-factor analysis of variance and post hoc *t* tests. The asterisk symbols * and ** indicate that an averaged *Q* has a significant difference ($p < 0.05$) compared to the next and second next *z*-positions, respectively. A sharp symbol # indicates a significant difference compared to a measurement at previous time interval.

A similar thickness, though slightly thinner than that of crystals in mature bone, was reported from a SAXS pattern of octacalcium phosphate-like plates (∼1.4 nm),[15] and most bone crystals observed were less than 2 nm thick.[2,93] In our observations, CaP plates developed from both MC0p and MC10p had almost identical thicknesses, and the thickness of plates was uniform along the *z*-directions of MC10p. Another population of spheres, following Porod's law (P ≈ 4), was also observed in MC10p samples, demonstrating that this population was not formed by aggregation of smaller precursors but consisted of individual compact spherical particles (Figures 2.3b and 2–S3d,e).

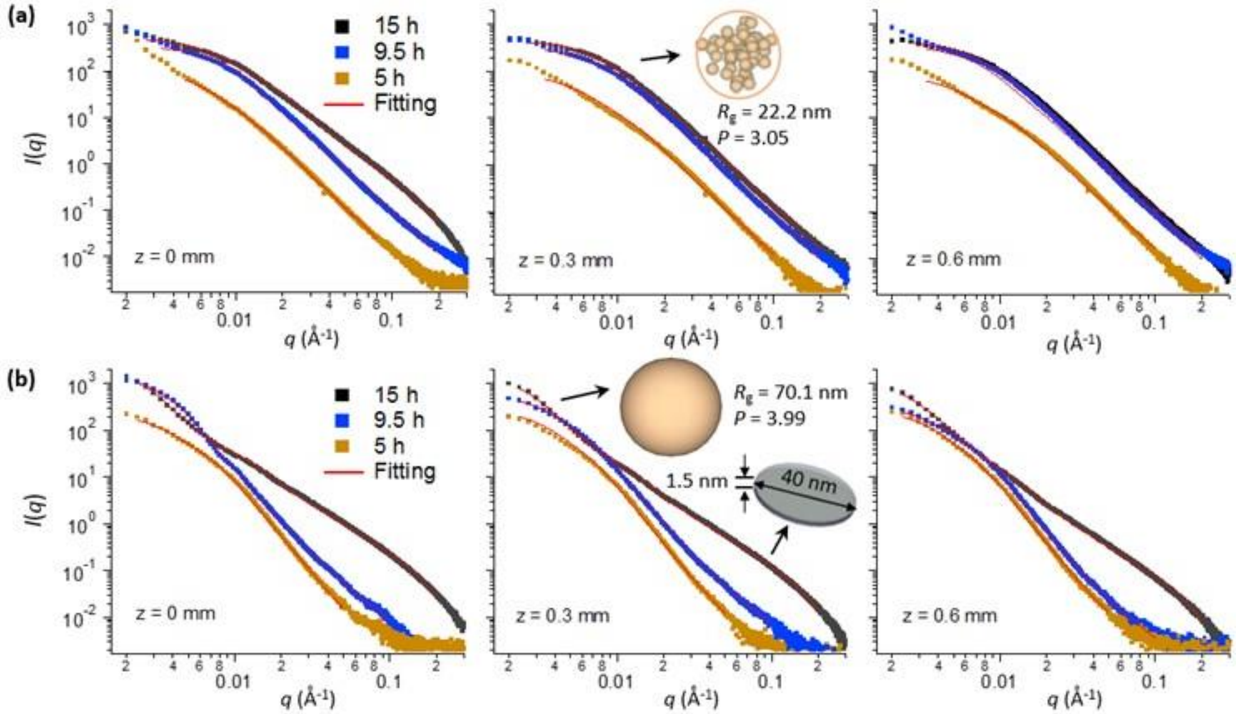

Figure 2.3 SAXS patterns from collagen matrices and their fittings. SAXS patterns from MC0p (a) and MC10p (b) over time at $z = 0-0.6$ mm, and their fittings. The SAXS patterns fit one or two CaP populations with morphologies of spherical aggregates, compact spheres, or plates. For example, the SAXS pattern at $z = 0.3$ mm of MC0p at 15 h fits spherical aggregates ($R_g = 22.2$ nm and $P = 3.05$), and the corresponding pattern of MC10p fits a combination of compact spheres ($R_g = 70.1$ nm and $P = 3.99$, at small q) and plates (diameter = 40 nm with a standard deviation of 0.15 in lognormal distributions and thickness = 1.5 nm, at large q).

In addition, V_{sp} was significantly lower in MC10p samples than in MC0p samples, without showing a clear increasing trend over time until the development of plate-like crystals (Figure 2.4a). The three different populations of particles with dissimilar morphologies and size ranges observed by *in situ* SAXS analysis in this study show that CaP developments in intra- and extrafibrillar spaces undergo different pathways, although both pathways include 1.5 mm thick plates at 15 h. The following discussion describes how those pathways are determined by the nucleation inhibitor, pAsp, and how they consequently influence the mineralization patterns of tissue-level constructs.

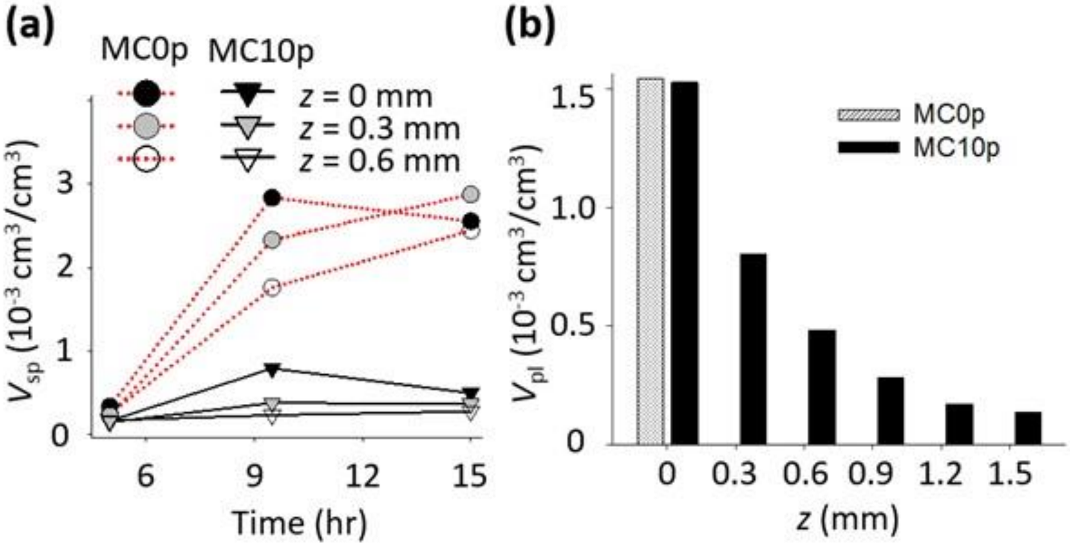

Figure 2.4 (**a**) Volume fractions of CaP populations with spherical morphologies, V_{sp}, at 5−15 h and (**b**) volume fractions of plate-like shapes, V_{pl}, at 15 h, determined from fittings of SAXS patterns. No plate-like shape particles were identified from MC0p below 0.3 mm. The volume fractions of each particle population were estimated by calibrating $I(q)$ using a glassy carbon reference sample.

2.4.2 Distinctively Different Pathways for CaP Mineralization in the Intra- and Extrafibrillar Spaces of Collagen Matrices

A TEM image of thin sections of MC0p indicated that CaP developed primarily in extrafibrillar spaces. At 15 h of mineralization, aggregated thin plates (dashed circle and inset image in Figure 2.5a) were imaged near $z = 0$, around unmineralized collagen fibrils (black arrow in Figure 2.5a) showing brighter contrast than the embedding epoxy resin. On the other hand, CaP development with 10 mg L^{-1} pAsp (MC10p) represents an IM-dominant system, showing darker contrasts from collagen fibrils than the surrounding epoxy resin (white arrow in Figure 2.5b). The different mineralization patterns resulting from pAsp were also evaluated from the thin collagen films on glass slides after 15 h of mineralization (Figure 2.6). This process simulated reactions at the outermost surface of the matrices ($z = 0$), which were not imaged from thin sections cut along the z-direction. In the absence of pAsp, the collagen surface was mostly covered with micrometer scale spheres, consisting of a number of nanoscale plates (Figure 2.6a).

The Raman spectra from these spheres is similar to that of synthetic hydroxyapatite, with a clear phosphate peak at $\Delta 960$ cm^{-1} (the P−O band for apatite, Figure 2.6d). This peak indicates CaP formed during the mineralization without pAsp (Figure 2.6a), but the spectrum does not include peaks from collagen fibrils. On the other hand, individual fibrils were clearly mineralized by the addition of 10 mg L^{-1} pAsp (Figure 2–6b, the atomic percentages of Ca and P by SEM-EDX were 21.4% and 16.6%, respectively) losing their periodic patterns shown in the unmineralized fibrils (Figures 2.5c and 2.6c). In Raman spectra, peaks indicating both apatite (at $\Delta 960$ cm^{-1} for the P−O band) and collagen (at $\Delta 2941$ cm^{-1} for the C−H band) clearly appeared (Figure 2.6d). Similar Raman spectra have been frequently reported from partially mineralized tendons or bone samples.[69,70] Ca/P molar ratios of EM and IM in this study were 1.19 and 1.29.

Those numbers are slightly lower than the theoretical value of octacalcium phosphate (1.33), which are expected to appear during the early stage CaP development process.[8]

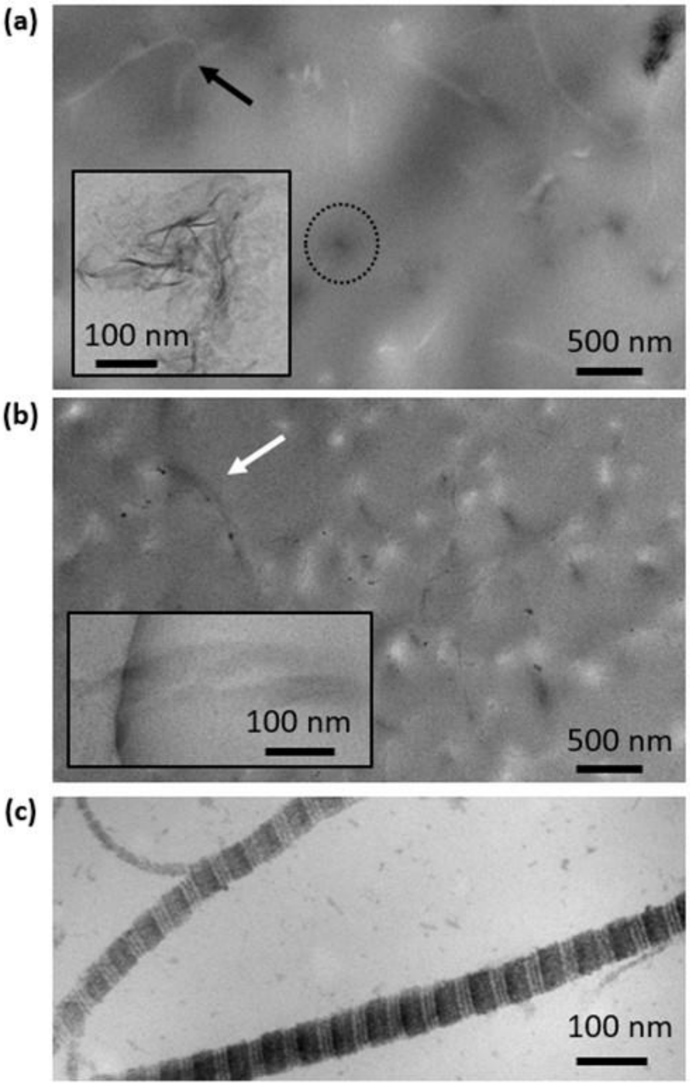

Figure 2.5 TEM images of thin sections of collagen matrices. (**a**) Near the outer surface of a MC0p sample at 15 h. The black arrow indicates an unmineralized collagen fibril. The dashed circle surrounds an aggregate of extrafibrillar CaP plates. The inset is a high-resolution image of extrafibrillar CaP plates, corresponding to the features in the circle. (**b**) Near the outer surface of the MC10p at 15 h. The higher magnification inset is taken from a neighboring area. Collagen fibrils, indicated with a white arrow, are mineralized, showing darker contrast than the surrounding epoxy resin. No staining was applied to collagen fibrils for (**a**) and (**b**) because precipitates from staining cannot easily be distinguished from CaP particles formed within the matrices. (**c**) Stained unmineralized collagen fibrils demonstrated a clear banding pattern of collagen fibrils.

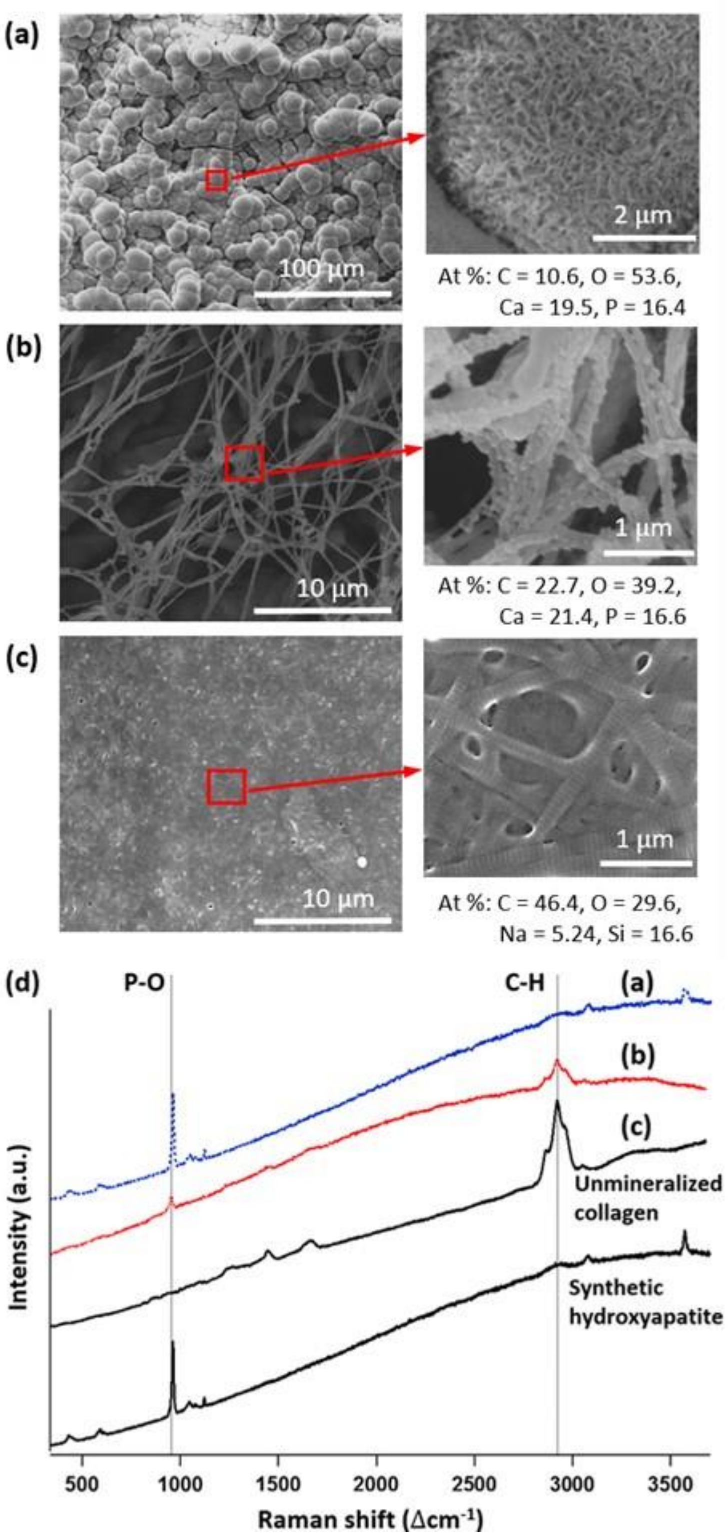

Figure 2.6 (**a**−**c**) SEM images of collagen films on glass. (**a**) Mineralized for 15 h in 3×SBF without pAsp. (**b**) Mineralized for 15 h in 3×SBF with 10 mg L^{-1} pAsp. (**c**) Unmineralized collagen. (**d**) Raman spectra of (**a**−**c**) and synthetic hydroxyapatite for comparison.

On the basis of *ex situ* observations (Figures 2.5 and 2.6), we concluded that the addition of 10 mg L^{-1} pAsp effectively controlled the IM and EM patterns. This control allowed us to evaluate the nucleation kinetics and pathways for both mineralization processes separately, using in situ SAXS observations. To better evaluate the different nucleation kinetics and pathways during both mineralization processes and to thoroughly investigate this complex system, we simplified the system to use one type and concentration of pAsp (10 mg L^{-1} of 5000 Da pAsp).

From the SAXS analyses during EM (MC0p), we found a CaP population of spherical aggregates (Figure 2.3a, $P \approx 3$) as intermediate products. This finding is consistent with a CaP nucleation pathway without collagen fibrils in the absence of nucleation inhibitors, as observed in recent cryogenic studies of CaP formation.[8,26] These studies showed that amorphous CaP spheres formed via aggregation and densification of PNCs before transformation into plate-like morphologies with increased crystallinity. The diameters of the densified aggregates in prior reports were 30−80 nm,[8,26] consistent with the SAXS results of the current study ($R_g = 20.5-32.3$ nm, equivalent to a diameter = 52.9−83.4 nm, Figure 2–S3f). A decreasing pattern in R_g over time can be evidence of the CaP pathway of the densification of ionic clusters as nucleation precursors.

During the CaP development with pAsp (MC10p), plate-like crystals (akin to the shape of bone apatite crystals) formed without an intermediate phase of spherical aggregates (between 9.5 and 15 h, Figure 2.3b), and this showed that the pathway of CaP development for IM is clearly distinguished from that for EM. This new finding also indicates that CaP transformation to plates for IM is much faster (once nucleation occurs) than for EM. In the absence of pAsp, it took 15 h for the transformation of spherical aggregates to plates in the extrafibrillar spaces, and this transformation was observed only at the top surface of the matrix (Figure 2.3a). Therefore, the inhibition of CaP nucleation at the extrafibrillar spaces by pAsp allows the nucleation in the intrafibrillar spaces, and during this IM process, CaP takes a new pathway, which is faster in its transformation but slower in nucleation than EM process.

Similarly, *in situ* WAXD data show that crystalline structure of CaP developed faster in MC10p than in MC0p (Figure 2.7). The WAXD pattern clearly shows peaks (corresponding to the (002), (211), and (112) faces of hydroxyapatite) developed in MC10p after 20 h. When CaP developed in the extrafibrillar structure (MC0p), only the (002) peak appeared, indicating that more amorphous or poorly crystalline states persisted for a longer period. This finding supports our SAXS observation that the morphological transformation from spherical aggregates to plates in MC0p was maintained for a relatively longer period (compared to the direct development of plates after the incubation time in MC10p) and was limited to only the outermost surface.

On the other hand, the spherical population observed for MC10p (Compact spherical particles, $P \approx 4$) does not seem to be directly related to plates, due to its large size ($R_g = 47-71$ nm, Figure 2–S3f) and much lower V_{sp} than V_{pl} (Figure 2.4a,b). Instead, CaP spheres might develop from aqueous Ca-pAsp complexation in the extrafibrillar space.[72] However, the SAXS patterns that are fitted to compact spheres had minimal influence on the fitting of plate-like crystals (Figure 2–S3d), validating that plate-like CaP developed without any intermediate products.

In situ SAXS and WAXD observations indicate that nanoscale evaluations of amorphous CaP phase are critical to thoroughly understand the kinetics and pathways of CaP nucleation and its phase transformation. This study highlights the importance of *in situ* X-ray scattering applications for future studies on the early stage collagen mineralization.

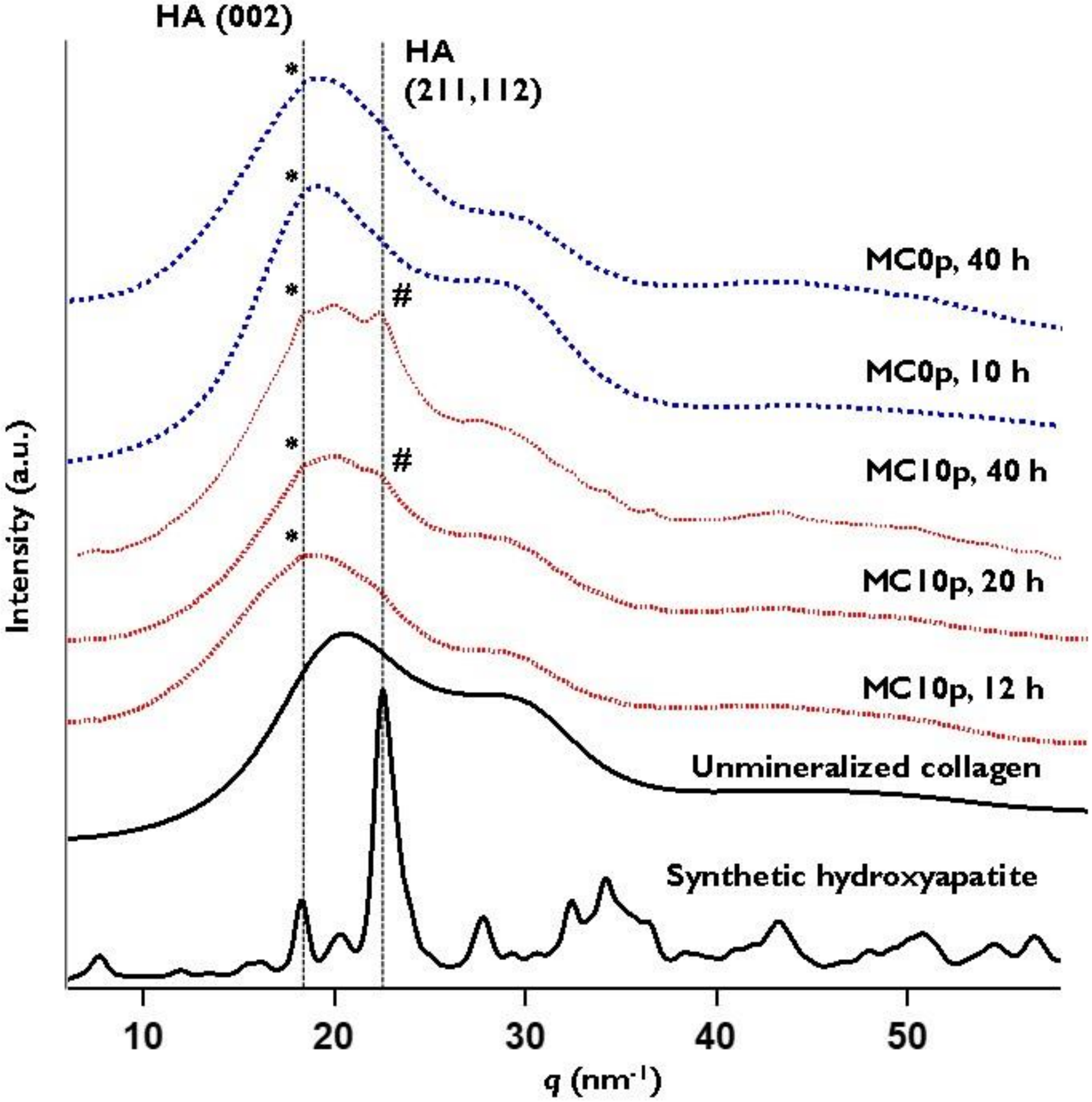

Figure 2.7 WAXD patterns from mineralized collagen matrices at *z* = 0–0.3 mm and from synthetic HA. Until 10–12 h, a peak of WAXD intensity appeared only at *q* ~ 18.25 nm^{-1}, which corresponds to the (002) face of HA (d-spacing: 3.442 Å, indicated as *) from both MC0p and MC10p. After 20 h, more peaks matching with HA appeared distinctively only from MC10p, including one at *q* ~ 22.5 nm^{-1} for the (211) and (112) faces of HA (d-spacing: 2.813 and 2.778 Å, respectively, indicated as #).

2.4.3 Macroscale Spatial Distribution of CaP Nanocrystals

Despite the importance of collagen fibrillar structure on tissue mineralization, as suggested in recent studies,[47,59,60] the role of extrafibrillar space, which can be an important entryway for molecules required for the CaP mineralization, has been neglected in most studies. Therefore, researchers have often not connected the implications from *in vitro* findings to those found *in vivo*. The spatial distribution of CaP as a function of the distance from the SBF−matrix interface explored in this study is especially important for understanding how molecules, such as PNCs or Ca^{2+} ions, are delivered from the SBF to the inside of the matrix to form CaP plates. The occupation of extrafibrillar pores with CaP (Figures 2.5a and 2.6a) could influence the transport of those molecules within the matrix by limiting their diffusion.[87]

To examine this possibility, the diffusion time, τ_D, of rhodamine 6g (R6G) was evaluated using fluorescence correlation spectroscopy (Figure 2.8a). τ_D at $z = 0$ was about three times higher than at other positions in MC0p at 15 h, indicating that a diffusion of molecules decreased, especially at the SBF−matrix interface, and further prevented nucleation precursors from penetrating into the deeper positions of the matrix. The increased diffusion time corresponds to the SAXS observation that the increase in scattering intensity from MC0p became mild at $z = 0.3-1.5$ mm (Figure 2.2a). In consequence, a thin layer of aggregated plates formed on the outer surface of MC0p in a later stage, as clearly imaged using TEM (Figures 2.8b and 2–S4a,b,c). These aggregated plates filled the extrafibrillar space less than 0.2 mm deep from the top surface, but they were scarcely observed at deeper *z*-positions. This layer could be a diffusion barrier for the further nucleation in deeper positions of MC0p. Ex situ analyses of matrices' sections using SEM and Raman spectroscopy demonstrated that IM was not achieved in MC0p even after the additional 23 h mineralization period, showing clearly distinguishable features between the extrafibrillar CaP layer and collagen matrix (Figure 2–S5 and Table 2–S1).

On the other hand, the increase in τ_D after mineralization in MC10p was relatively low compared to MC0p (Figure 2.8a), demonstrating that neither the occupation of extrafibrillar spaces by CaP crystals nor the influence of the intrafibrillar CaP plate on the extrafibrillar space was significant, allowing scattering intensities to increase with relatively steep slopes at low *z* positions of MC10p (Figure 2.2a). Therefore, CaP plates can form more deeply in the matrices even at *z* = 1.5 mm (Figure 2.4b). The extrafibrillar CaP crystals in MC10p were visible only at the later stage, showing elongated morphologies in the micrometer scale (Figures 2.8c and 2–S4d,e,f). Unlike in MC0p, extrafibrillar CaP crystals were not severely aggregated (corresponding to different *P* values for spherical populations in MC0p and MC10p, Figure 2–S3e) and did not significantly occupy the extrafibrillar spaces except for a few areas at *z* = 0 (Figure 2.8c).

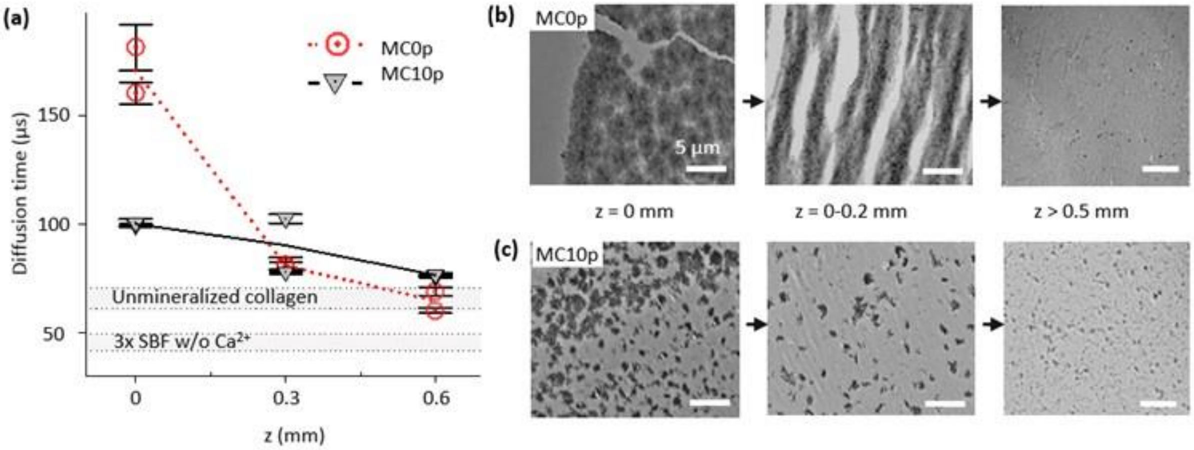

Figure 2.8 Reduced diffusion of R6G during the early stage (within 15 h) of EM results in a nucleation barrier in a later stage of mineralization (after additional 23 h). (**a**) Diffusion times of R6G into MC0p and MC10p at different depths after 15 h. The average and standard deviation were obtained from 10 measurements at each scanning position. Two different positions were scanned at the same depth. Diffusion times in unmineralized collagen matrix and SBF without Ca^{2+} are also indicated as gray regions for the comparison. (**b, c**) Spatial distributions of CaP within MC0p (**b**) and MC10p (**c**) systems at the late stage were influenced by the reduced diffusion of molecules required for the CaP mineralization from SBF solution into the deeper positions of the matrices. After an initial 15 h of mineralization, for *in situ* SAXS analysis, TEM images were taken after an additional 23 h incubation in 3×SBF. Scale bars are 5 μm.

2.4.4 Kinetic Control of CaP Nucleation for Tissue-Level

The proposed mechanisms of CaP development in collagen matrices are described in Figure 2.9. In the absence of a nucleation inhibitor, spherical aggregates form in extrafibrillar spaces, in a fashion similar to CaP developing in solution.[8,26] Initially, CaP precursors, such as PNCs or other ionic Ca and P species, move freely within the matrix through the relatively large extrafibrillar spaces, nucleating in the extrafibrillar spaces with little *z*-position dependency. This population of spherical aggregates grows continuously, filling the extrafibrillar spaces while reducing the diffusion of precursors penetrating deeper into the matrix. Over time, spherical aggregates continuously bond with Ca^{2+} from the solution and transform into crystalline plates,[15] but this dominantly occurs only at the solution−matrix interface (Figure 2.4b). These aggregated plates eventually become dense enough to create a diffusion barrier at the later stage (Figure 2.7b), inhibiting the transport of precursors to the inside of the matrix and preventing further mineralization throughout its depth.

In the presence of a nucleation inhibitor (representing the physiologically relevant case), the nucleation of CaP in extrafibrillar spaces is kinetically restricted by aqueous complexation of Ca^{2+} ions with inhibitors. Thus, PNCs or other CaP precursors can be continuously supplied to collagen gap channels before they are consumed for EM or blocked by a diffusion barrier. The confined space of narrow gap channels (40 nm wide, but less than 2 nm high)[2,33,35] does not allow for the formation of large aggregates; hence, nuclei can directly grow as plates without the intermediate step of spherical aggregates, as observed in MC0P. When ionic precursors do not form aggregated clusters due to the inhibition by pAsp, the activation energy barrier for creating new surfaces for nucleation of CaP in extrafibrillar spaces cannot be overcome easily.[8] Therefore, about 9.5 h of induction time was required before the initial development of CaP plates. Once nucleation occurs within the gap channels, however, CaP nuclei strongly attract precursors and begin to grow into plates. This pathway results in a faster morphological transformation (Figure 2.3) and crystallization (Figure 2–S4) than the pathway with intermediate spherical aggregates in the absence of pAsp. The consumption of precursors by nuclei for IM cause the delivery of fewer precursors to deeper *z*-positions; therefore, intrafibrillar CaP plates develop with a gradual spatial distribution.

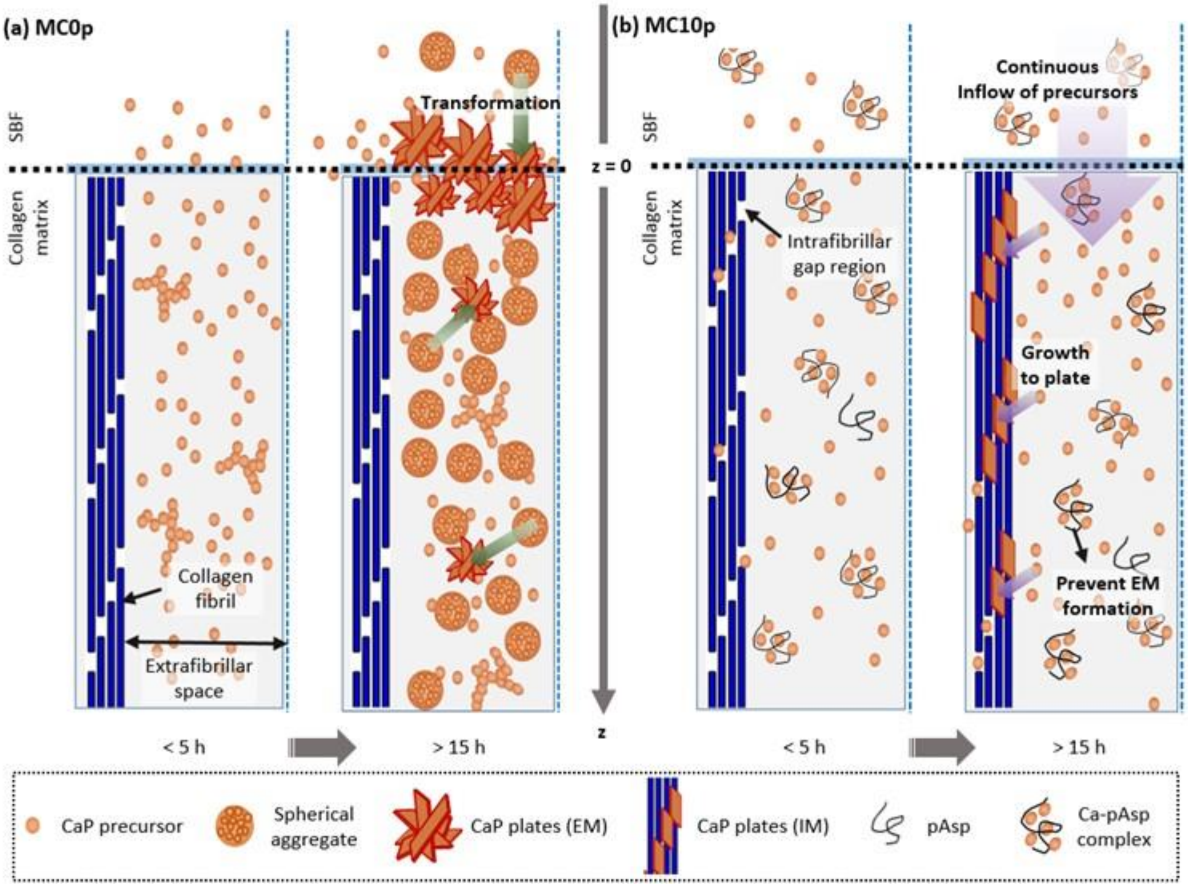

Figure 2.9 Mechanisms of (**a**) EM within collagen matrices in the absence of pAsp (MC0p) and (**b**) IM of collagen fibrils in the presence of pAsp (MC10P).

2.5 Conclusions

In summary, we evaluated the kinetics of mineralization of collagen matrices at nano- through macroscales, using in situ SAXS analysis. The evolution of CaP's morphology and its volume size distribution were separately determined during nucleation and growth within intra- and extrafibrillar spaces. The findings of this study revealed that the pathways and kinetics of CaP development during intrafibrillar mineralization are distinctively different from those during extrafibrillar CaP mineralization. In the absence of nucleation inhibitors, improper control of CaP nucleation kinetics brought significant CaP populations of spherical aggregates into the extrafibrillar spaces. This highlights the importance of including nucleation inhibitors for recreating physiologically relevant mineralization of collagen-based matrices.[27,71]

In situ SAXS measurement at the different *z*-positions utilized in this study has a number of practical benefits. For example, we were able to detect unexpected layers that clearly formed at the outermost surface ($z = 0$), which disrupts the preparation of biomaterials with a uniform mineral distribution in macroscale. The quantitative information showing gradual development of plate-like crystals along the *z*-positions can be adapted to evaluate the kinetic parameters, such as the diffusion coefficients of precursor molecules for the nucleation of biominerals in biological templates. Furthermore, because the distribution of CaP mineral relative to collagen, at both nano and macroscales, dictates the mechanics of the tissue,[7,8] the current results provide guidance for proper mineralization of scaffolds for creating *in vitro* model systems and for developing constructs for regenerative medicine.

2.6 Acknowledgments

The authors acknowledge the Biomineralization discussion group at Washington University in St. Louis, consisting of J. D. Pasteris, G. Genin, T. Daulton, A. Deymier, A. G. Schwartz, J. Lipner, and J. Boyle for helpful discussions. We thank J. Ballard for carefully reviewing the manuscript. The project was mainly supported by Y.S.J.'s faculty startup fund at Washington University and partially supported by the National Science Foundation (DMR-1608545 and DMR-1608554) and the National Institutes of Health (U01 EB016422). The Nano Research Facility, Institute of Materials Science & Engineering, Molecular Microbiology Imaging Facility, Confocal Microscopy Facility, and Soft Nanomaterials Laboratory at Washington University in St. Louis provided their facilities for the experiments. Use of the Advanced Photon Source (sector 12-ID-B and 11-ID-B) at Argonne National Laboratory was supported by the U.S. Department of Energy, Office of Science, Office of Basic Energy Sciences, under Contract No. DE-AC02-06CH11357.

2.7 Supporting information for Chapter 2

2.7.1 Additional Experimental Section

***In situ* X-ray scattering data collection and analysis**. SAXS data were collected at the APS, Sector 12-ID-B at Argonne National Laboratory (Argonne, IL, USA).[17,83] At intervals of 5, 9.5, and 15 h, frames were immediately moved to the SAXS sample stage and scanned within 5 min. By vertically moving the sample stage, each sample was scanned from $z = 0$, where the collagen matrix and simulated body fluid contact each other, to $z = 1.5$ mm depth of the matrix (Figure 2–S1b). The distance from the sample to the SAXS detector was 3.6 m, which provided a range of 0.0017–0.53 $Å^{-1}$ for the scattering vector, q. For each scan, the sample was exposed to a 14 keV X-ray beam for 1 s. The size of the beam was 150 μm (perpendicular to the z-axis) × 40 μm (parallel to the z-axis). Two different lateral positions were scanned at each time for duplicated samples; therefore, a total of four scattering patterns were obtained for each condition and position.

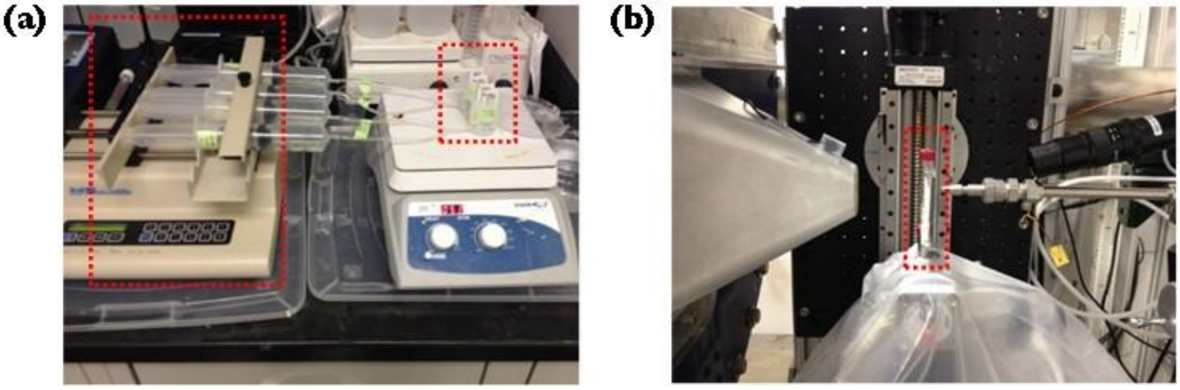

Figure 2–S1 Experimental setup for collagen mineralization and SAXS measurements. (**a**) Mineralization of collagen matrices occurred within the frames in a flow-through reaction system (left dashed box: a syringe pump providing two different reaction conditions simultaneously; right dashed box: two testing frames per each condition). (**b**) The SAXS setup at the Advanced Photon Source sector 12-ID-B, Argonne National Laboratory (dashed dox: testing frame, viewed from the side, as in Figure 2.1b).

The 2D scattering intensity counted by the detector (2M Pilatus) was averaged over the *q* range along the radial direction to produce 1-dimensional scattering intensities *I*(*q*). Silver behenate powder was used as the *q* calibration standard. *I*(*q*) was normalized by the incident beam intensities and calibrated using a reference glassy carbon standard sample, thus SAXS intensities collected from different measurements could be compared each other. The SAXS intensities were corrected by subtracting the averaged intensity of unmineralized collagen matrices (at 0 h) as a background (Figure 2–S2).

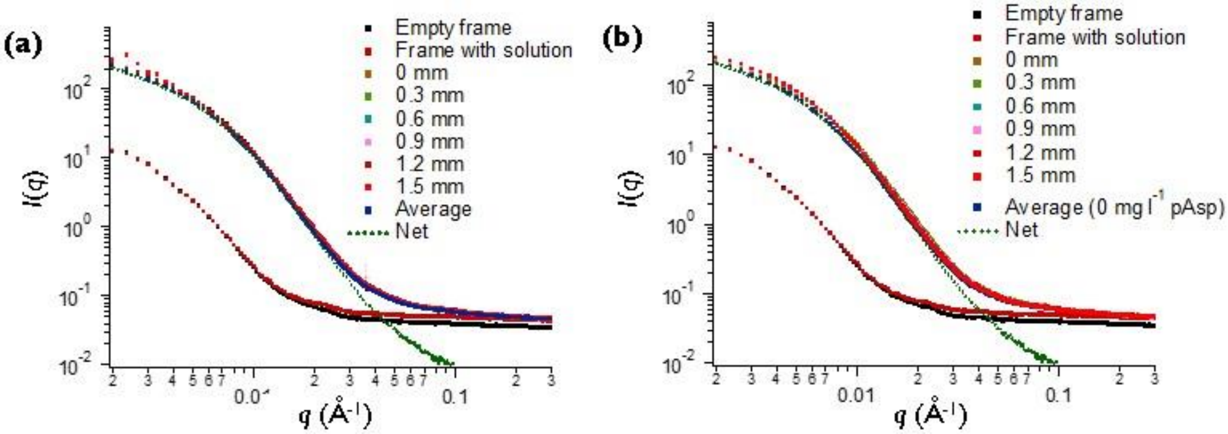

Figure 2–S2 Background SAXS intensities (**a**) SAXS intensities were measured for an empty frame with cover glass, a frame filled with 3×SBF solution with no Ca^{2+} ions, and a frame with an unmineralized collagen matrix at *z* = 0–1.5 mm. Before the analysis, unmineralized collagen matrices were stored overnight in 3×SBF solutions with no Ca^{2+} ions. There was little difference in SAXS intensities for unmineralized collagen at different *z*-positions. The net intensity (green dotted line) indicates the scattering from collagen, and was obtained by subtracting scattering of solution and frames (Frame with solution) from unmineralized collagen matrix (Average). (**b**) The addition of 10 mg l^{-1} pAsp in SBF did not affect the intensities of the unmineralized matrix. The averaged values of intensities from unmineralized collagen at *z* = 0–1.5 mm (**a**) were used as the background intensity for all analyses of SAXS intensities in the subsequent experiments.

Total particle volume was estimated from the linear relationship with invariant values, Q, as shown in eq. 2–S1. Integration was conducted within a limited q range of 0.0017–0.2 Å^{-1}, due to the relatively high noise in larger q regions.

$$Q = \left(\frac{1}{2\pi^2}\right) \int q^2 I(q) dq \qquad \text{eq. 2–S1}$$

The Modelling II tool of the IRENA package written in IGOR Pro (WaveMetrics Inc.) was provided by APS and used for the data analysis to fit the SAXS pattern. The equations used in the fitting are summarized below, and more detailed information can be found elsewhere.[94] Absolute volume fractions of CaP particles in collagen matrices were obtained by the fitting of $I(q)$ calibrated on an absolute scale using a reference glassy carbon standard sample.[95] The structural factor was assumed to be 1. Using a two-population model of this Modelling II in the IRENA package, $I(q)$ can be evaluated as a sum of spherical and platy calcium phosphate (CaP) populations. In the absence of collagen fibrils, the spherical CaP was reported to appear as a precursor to crystalline apatite at the initial stage of nucleation.[8,26] A unified level tool was for the evaluation of spherical populations with fractal dimensions and a fitting tool using form factor was used for considering platy shape particle population in the Modelling II. First, spherical populations with fractal dimensions can represent the aggregation behavior during particle formation. In this model, $I(q)$ can be expressed as eq. 2–S2.[90,94]

$$I(q) = G \exp\left(-\frac{q^2 R_g^2}{3}\right) + B(q^*)^{-P}. \qquad \text{eq. 2–S2}$$

where, $q^* = \frac{q}{[\mathrm{erf}(\frac{q R_g}{\sqrt{6}})]^3}$, R_g is the radius of gyration, and B is the constant prefactor specific to the type of power-law scattering. A power-law scattering exponent P can be evaluated from the slope of log(I) vs. log(q) at high q. For typical monodisperse spheres following Porod's law, P = 4. For P = 1–3, particles are considered to have mass fractal structures with fractal dimensions, D_f, equal to P. Spherical aggregates typically show D_f ~ 3.[90,92] The exponential prefactor, G, can provide volume fractions of the particles from the eq. 2–S3.

$$G = n\, r_e^2 \Delta\rho^2 V^2, \qquad \text{eq. 2–S3}$$

where n is the number concentration of particles and V is the volume of a particle ($V = (\frac{2{,}000\,\pi^2}{243} R_g^6)^{\frac{1}{2}}$). r_e and Δρ represent the classical electron radius (2.818 fm) and the difference in electron densities between particles and the medium, respectively. Therefore, from the fitting parameters of G, and R_g, the particle volume fractions of a spherical CaP population, V_{sp}, can be evaluated by n multiplied by V.

For fitting the plate CaP population with thickness, t, another fitting tool using a built-in form factor (a unified disk, eq. 2–S4)[96] and a size distribution function in the Modelling II package was used.

$$|F(q,R)|^2 = A + G1\, exp^{-\frac{q^2 R_g 1^2}{3}} + \frac{B1}{q*^4} \qquad \text{eq. 2–S4}$$

where R is the radius of the plate, $\mathrm{A} = exp^{-\frac{q^2 R_g 2^2}{3}} + \frac{2}{R^2 {Q_{SV}}^2}\, e^{-\frac{(1.1 R_g 1)^2 q^2}{3}}$, $q *= \frac{q}{[\mathrm{erf}(\frac{q\, R_g 1}{\sqrt{6}})]^3}$, $\mathrm{B1} = 4\frac{t+R}{R^3 t^2}$, $\mathrm{G1} = 2\frac{t^2}{3R^2}$, $R_g 1 = \frac{\sqrt{3}\, t}{2}$, and $R_g 2 = \sqrt{(\frac{R^2}{2} + \frac{t^2}{12})}$. Then, SAXS intensity was calculated by a summation over a discrete size histogram with eq. S5:

$$I(q) = r_e^2 |\Delta\rho|^2 \sum_i |F(q,R_i)|^2 V(R_i) f(R_i) \Delta R_i \qquad \text{eq. 2–S5}$$

In eq. S5, the subscript i includes all bins in the size distribution, and ΔR_i is the width of bin i. $V(R)$ is the particle volume, and $f(R)$ is the volume size distribution, which can be related to the number size distribution by

$$f(R) = V(R) n P(R), \qquad \text{eq. 2–S6}$$

where $P(R)$ is the probability of occurrence of a scatter of radius R. For the lognormal distribution,

$$P(R) = \frac{1}{\sigma R\sqrt{2\pi}} e^{-\frac{(\ln(R-\mu))^2}{2\sigma^2}}, \qquad \text{eq. 2–S7}$$

where μ is the mean radius in number size distribution, and σ is the standard deviation. For the fitting, μ, σ, and n were first fitted, and then the particle volume fractions of platy CaP population, V_{pl} was obtained by $\sum_i V(R_i) n P(R) \Delta R_i$.

The scattering contrast, $\Delta\rho$, was estimated from difference between the electron densities, ρ, of CaP and water, ($\rho_{\mathrm{CaP}} - \rho_{\mathrm{water}}$). $\rho = \sum C_z f_z$ for all elements, where, C_z is the atomic concentration and f_z is the scattering factor, which is equivalent to the atomic number for SAXS analysis. For the spherical population, CaP was assumed to be amorphous ($Ca_9(PO_4)_6$, known as a Posner's cluster, with a specific gravity of 1.75,[23,74] yielding $\Delta\rho = 1.89 \times 10^{23}$ cm^{-3}. A recent study by Habraken *et al.*[8] estimates the structure of post-nucleation clusters as $[Ca_2(HPO_4)_3]^{2-}$, which provides an almost similar $\Delta\rho$ (1.93×10^{23} cm^{-3}). For the CaP platy population, the structure of CaP is assumed to be a hydroxyapatite crystal ($Ca_5(PO_4)_3OH$ with a specific gravity of 3.16), yielding $\Delta\rho = 6.12 \times 10^{23}$ cm^{-3}. Although hydroxyapatite is known to most closely approximate bone crystals, octacalcium phosphate (OCP) is frequently proposed as the early stage of platy CaP for bone.[8] The assumption that platy particles are OCP ($Ca_8H_2(PO_4)_6{\cdot}5H_2O$, with a specific gravity of 3.16) also provides little change in $\Delta\rho$ (6.22×10^{23} cm^{-3}). Therefore, the errors resulting from assumptions of the structure of spherical and platy particles are expected to be about 4%.

Similarly, *in situ* WAXD data was collected at APS sector 11-ID-B to identify the CaP phases during collagen mineralization. Collagen matrices were exposed to a 58.66 keV X-ray beam for 5 min (2 s × 150 times) during flow-through mineralization reaction. The beam size was 300 μm in both the lateral and vertical dimensions. The 2-dimensional WAXD intensities were counted by a Perkin Elmer amorphous silicon detector, which was 20 cm away from the sample, providing information at q higher than 0.6 Å^{-1}. Then the 2D intensities were averaged over the q range along the radial direction to produce 1D scattering intensities $I(q)$, using FIT2D software provided by the European Synchrotron Radiation Facility. Cerium dioxide was used as the calibration standard.

Fluorescence correlation spectroscopy (FCS) analysis. FCS analysis was used to evaluate the pore structures of the matrices by measuring the diffusion time of rhodamine 6G (R6G). R6G was chosen for its small size (MW = 479.02 g mol^{-1}), photostability, and high fluorescence quantum yield. FCS measurement was performed using an inverted design confocal laser scanning microscope (Zeiss Axiovert 200M) equipped with a 40× water immersion lens. R6G molecules were excited by a 514 nm argon laser. Fluorescence intensities were collected for 30 s × 10 times, then the diffusion time was evaluated by analyzing correlation curves. Two different locations were evaluated from each z-position in each sample. The time shift τ was varied, and the correlation curve was obtained by multiplying the deviation of the average intensity, I, at the time point t, by the deviation at time point $t + \tau$, and then averaging over the whole trace. Finally, the correlation function, $G(t)$, was normalized to the squared average signal.[87,88]

$$G(\tau) = \frac{<I(t)I(t+\tau)>}{<I(t)>^2} - 1 \qquad \text{eq. 2–S8}$$

The diffusion time, τ_D, and number of fluorescent molecules in the detection volume, N, of a given component, i, are commonly fitted with the standard model:

$$G(\tau) = \frac{1}{N}\sum_i \varphi_i \left(1 + \frac{\tau}{\tau_{D,i}}\right)^{-1}\left[1 + \left(\frac{\omega_0}{z_0}\right)^2 \frac{\tau}{\tau_{D,i}}\right]^{-\frac{1}{2}}, \qquad \text{eq. 2–S9}$$

where φ_{i} characterizes the fraction of molecules of the component, and ω_0, and z_0 are Gaussian profiles of the detected volumes in the x-y directions. τ_D can be correlated with the diffusion coefficient, D, using the following equation:

$$\tau_D = \frac{\omega_0^2}{4D}. \qquad \text{eq. 2–S10}$$

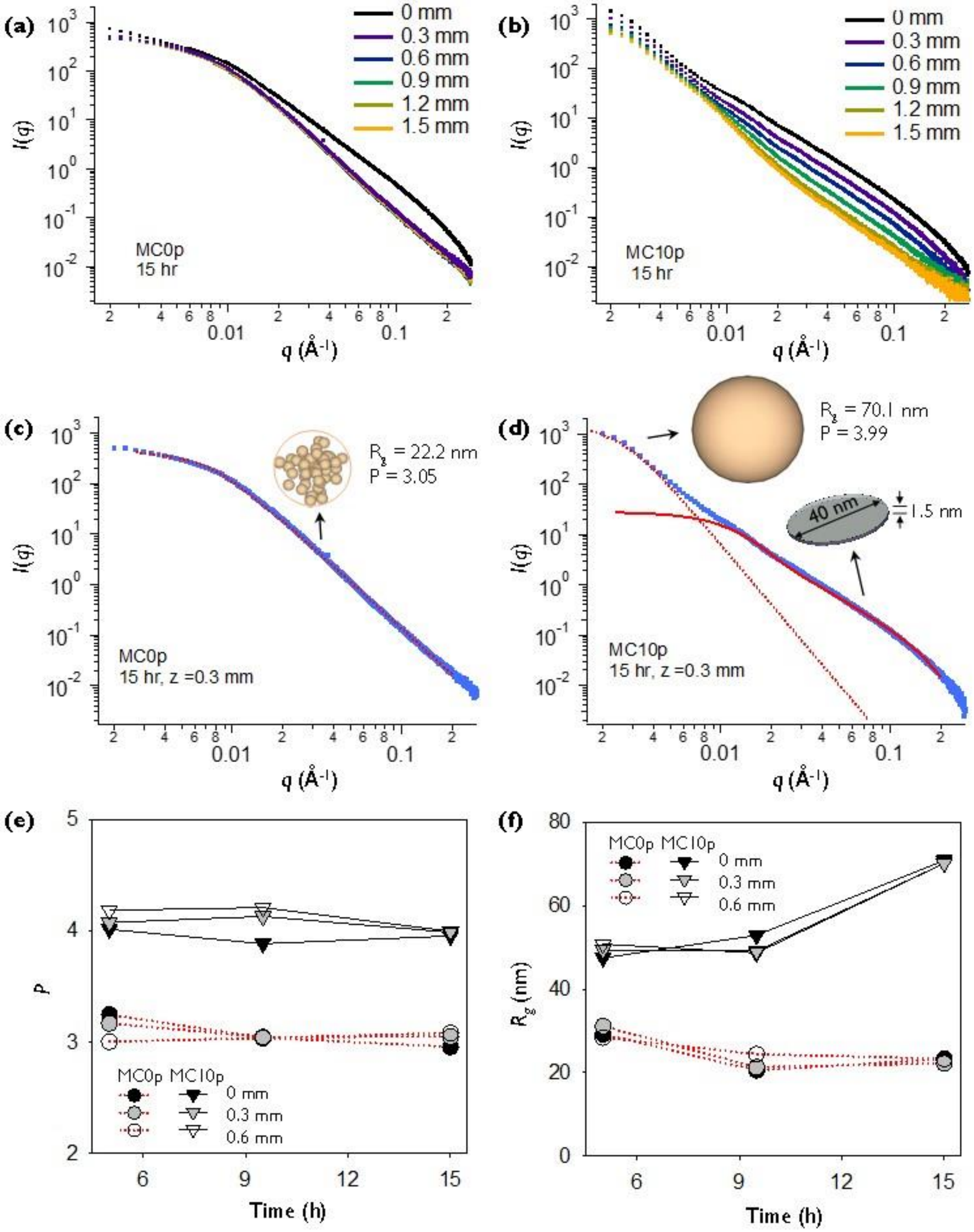

Figure 2–S3 SAXS intensities from mineralized collagen matrices and their fittings. SAXS intensities from MC0p (**a**) and MC10p (**b**) at z = 0–1.5 mm at 15 h of mineralization. (**c**, **d**) Examples of fittings for SAXS intensities at z = 0.3 mm at 15 h (thick blue lines) using a model of two populations of plates

and spheres. (**c**) The fitting of SAXS pattern from MC0p (the red dotted line overlaps with the raw intensity indicated by the blue line) indicated that CaP particles were aggregated spheres (the power-law scattering exponent, P = 3.05) with R_g = 22.2 nm. The contribution of the platy CaP population was minimal. (**d**) The fitting of the SAXS pattern from MC10p shows that populations of plates and spheres co-exist. The SAXS intensity at large q fits 1.5 nm thick plates with a diameter of 40 nm (standard deviation of 0.15 in log-normal distribution). The obtained morphology of plates closely approximates known bone crystalline dimensions. These morphologies were used for fitting the total particle volume fractions of the plate population from other SAXS patterns at different depths and time. Another population of spheres of R_g = 70.1 nm appears at small q, with a P fitting to 3.99, which indicates that particles were typical surface scatter, not formed from aggregation of primary particles or nucleation precursors. (**e**, **f**) P and R_g values for the spherical population fitted from SAXS intensities from MC0p and MC10p at z = 0–0.6 mm over time.

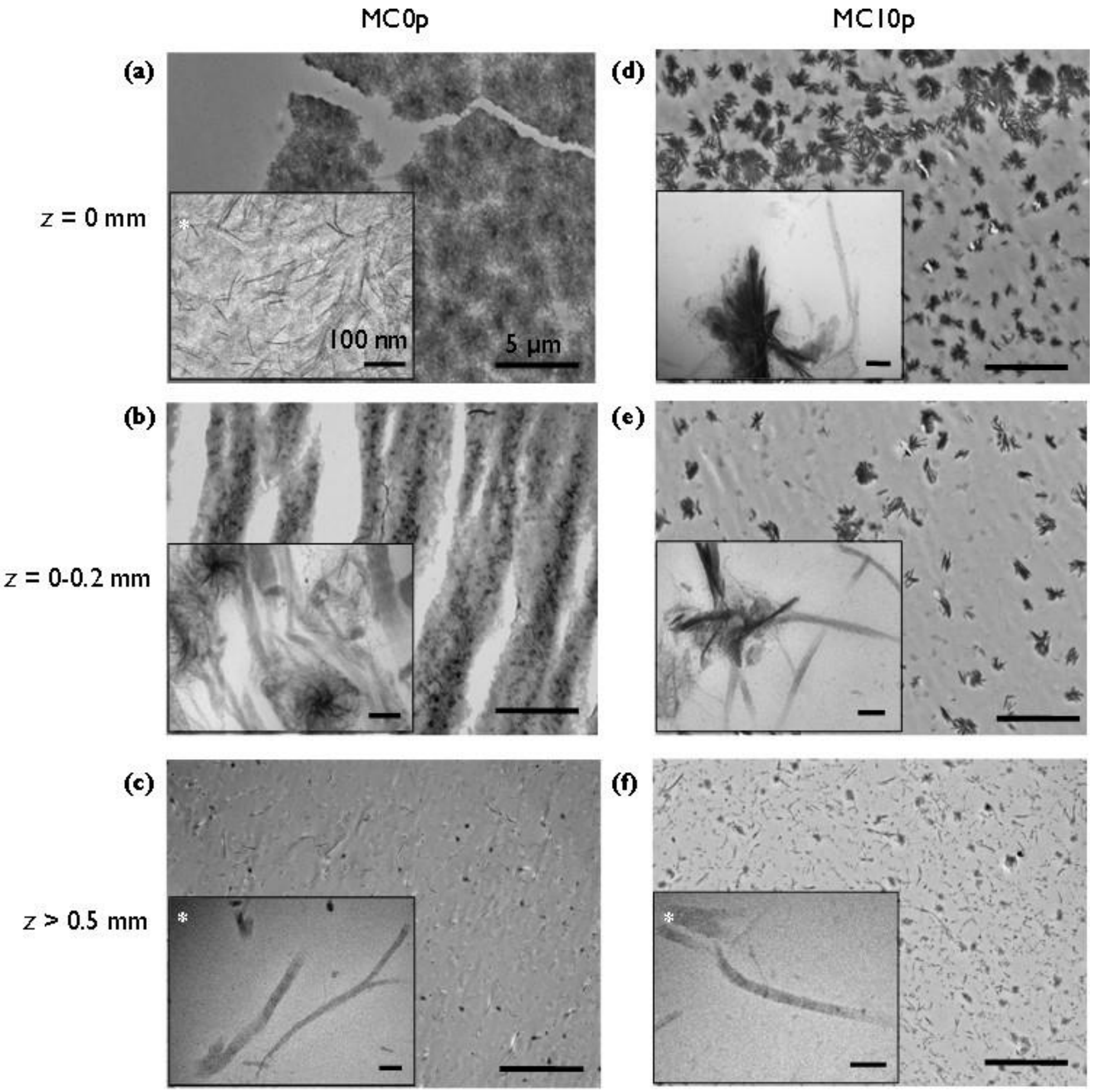

Figure 2–S4 TEM images of stained thin sections of MC0p (**a-c**) and MC10p (**d-f**) at a late stage of mineralization. Samples were prepared after 15 h of mineralization for *in situ* SAXS analysis, followed by an additional 23 h incubation in 3×SBF. Insets are high resolution images corresponding to features in **a-f**. Scale bars in **a-f** are 5 µm, and those in insets are 100 nm. The * symbols indicate that images were taken at an acceleration voltage of 200 kV. Other images were taken at 100 kV. Near the area of the solution–collagen matrix interface, for MC10p samples, banding patterns are nearly absent from collagen fibrils due to intrafibrillar mineralization (the inset in **d**). Banding is still visible in MC0p samples (the inset in **b**). In the interior of the matrices (*z* > 0.5 mm), where few extrafibrillar particles present, collagen fibrils appear similar in both groups, with ambiguity between CaP particles and precipitations of staining molecules (the insets in **c** and **f**).

2.7.2 *Ex situ* analyses of CaP distribution within the collagen matrices at a late stage of mineralization

To better evaluate the CaP distribution within the collagen matrices at a late stage of mineralization, sections cut along the *z*-direction of MC0p and MC10p (Figure 2–S5a) were analyzed using SEM-EDX and Raman spectroscopy. The surface of the MC0p section was mostly covered with a layer of CaP minerals, and collagen matrix was located below and slightly visible through narrow gaps in the mineral layer (Figure 2–S5b). Possibly, the collagen fibrils had shrunk to the bottom during dehydration for sample preparation, while relatively mobile extrafibrillar CaP particles were more densely aggregated on top. The EDX analyses of MC0p sections (Table 2–S1) showed distinctly different characteristics for the mineral layer (Figure 2–S5d,g) and the surface of the collagen matrix without visible particles (Figure 2–S5f). Ca/P ratios from the mineral layer were 1.2–1.38, which are close to that of OCP (1.33). This range is expected to appear during the early stage apatite (Ca/P = 1.67) development process.[8] However, Ca and P were not detected on the surface of the collagen matrix at $z = 0.3$ mm, where no extrafibrillar particles were visible (Figure 2–S5f). This demonstrates that intrafibrillar mineralization was not achieved, even after the additional 23 h of reaction after the initial 15 h experiment.

Unlike the MC0p samples, the surfaces of the MC10p were clearly exposed, rather than entirely covered by a mineral layer (Figure 2–S5c), due to the inhibition of extrafibrillar CaP formation by pAsp. The MC10p surfaces without extrafibrillar CaP particles (indicated as ‘IM’ in Figures 2–S5e,h) clearly showed Ca and P signals, proving that the addition of pAsp promoted intrafibrillar mineralization. There would be little chance that extrafibrillar CaP particles were hidden below the collagen fibrils and detected by the surface sensitive SEM-EDX because most collagen fibrils located below the extrafibrillar CaP layers as shown in Figure 2–6b. Even with more extrafibrillar CaP particles during the mineralization without pAsp, no Ca and P signal was detected from exposed collagen surfaces (Figure 2–S5f). The Ca/P ratios from mineralized collagen matrices (Ca/P = 0.84–1.0) were lower than that of OCP, but similar to that of the amorphous phase (typically less than 1).[8] However, we did not conclude that CaP crystals embedded inside the collagen fibrils are amorphous. SEM-EDX has a low resolution compared to the size of nanoscale intrafibrillar CaP plates, raising the possibility that Ca and P signals were detected from other parts of the collagen matrices. In sum, we found that the Ca/P ratios of the extrafibrillar particles were close to those of OCP or apatite. In the presence of pAsp, the Ca/P ratio in collagen matrices reflected mineralization, while in the absence of pAsp, neither Ca nor P was detected from the collagen surface without extrafibrillar particles (Figure 2–S5f). Thus, it is evident that IM was promoted only with the addition of pAsp.

Raman spectra analyzed from multiple spots throughout the MC10p surface at z = 0.3 mm (Figure 2–S5h) showed a regular pattern characteristic of phosphate peaks at Δ960 cm^{-1} (the P–O band for apatite in the solid box in Figures 2–S5i, j) and collagen peaks at Δ2,941cm^{-1} (the C–H band for collagen in the dotted box in Figure 2–S5i). These spectral patterns are consistent with *Ex situ* evaluations using Raman spectra (by providing the development of P–O banding) and SEM-EDX (by providing Ca/P ratio; estimation of elemental composition in macroscale) in this study can help to identify the CaP phases. However, the direct comparison of the above information with *in situ* WAXD analysis should take a careful approach because the WAXD analysis can provide additional information about the development of each lattice structure of specific mineral (i.e., both short- and long- range order information). As shown in Figure 2.7, only amorphous status of extrafibrillar CaP was observed from MC0p, thus, we conclude that extrafibrillar CaP aggregates, developed during the *in situ* mineralization without pAsp, are mostly amorphous, but they can transform into apatite minerals when further mineralized.

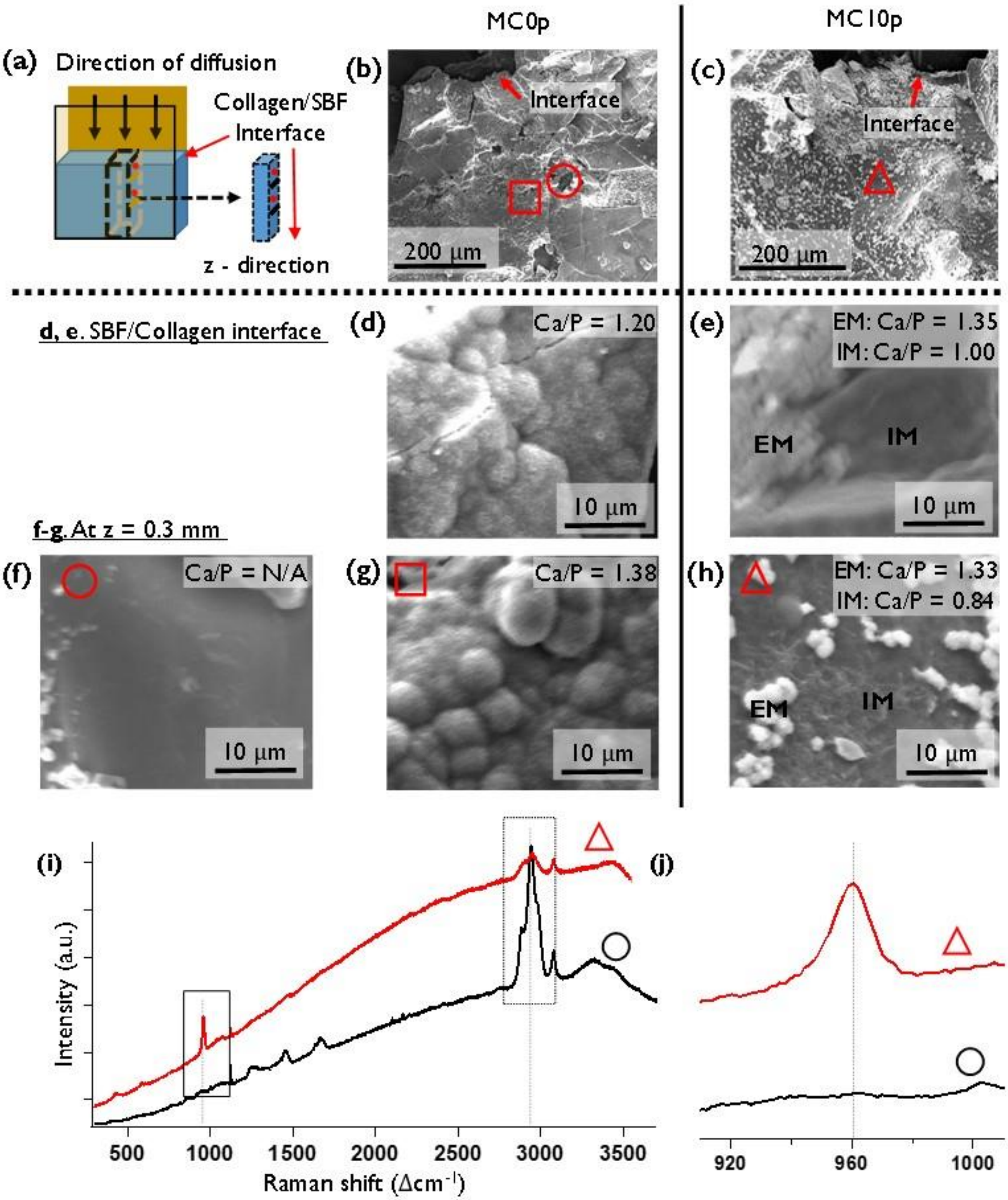

Figure 2–S5 SEM images and corresponding Raman spectra of collagen matrices. Samples were analyzed after 15 h of mineralization for *in situ* SAXS analysis, followed by an additional 23 h incubation in 3×SBF. (**a**) Schematic illustration of sample preparation for evaluating the cross section of the matrices. Samples were frozen in liquid nitrogen before cutting sections. SEM low resolution images of a section of (**b**) MC0p

and (**c**) MC10p. (**d-h**) High-resolution SEM images of selected areas indicated in b and c. Ca/P ratios were evaluated by SEM-EDX. (**d**) A layer of aggregated CaP plates on MC0p at z = 0 mm. (**e**) Mineralized collagen of MC10p at *z* = 0 mm with scattered extrafibrillar CaP. (f) Unmineralized collagen matrix of MC0p at *z* = 0.3 mm (circle in b). (**g**) A layer of aggregated CaP plates on MC0p at z = 0.3 mm (square in **b**). (**h**) Mineralized collagen of MC10p at *z* = 0.3 mm, with a few scattered extrafibrillar CaP (triangle in **c**). EM and IM indicate the extrafibrillar CaP and the surface of mineralized collagen matrix, respectively. (i) Raman spectra of selected positions indicated in b and c. The black and red lines correspond to **f** (circle in **b**) and h (triangle in **c**), respectively. (**j**) Enlarged area of Raman spectra (left box in **i**) showing phosphate-specific peaks at Δ960 cm^{-1}.

Table 2–S1 Atomic ratios of mineralized collagen at different positions on cross sections, from SEM-EDX.

Sample	MC0p			MC10p			
z (mm), Fig. 2–S5[*]	0, **d**	0.3, **f**	0.3, **g**	0, **e**-EM	0, **e**-IM	0.3, **h**-EM	0.3, **h**-IM
C	35.5	69.1	34.3	42.0	64.2	42.4	62.8
N	-	13.3	-	7.4	16.0	9.4	12.9
O	29.4	15.5	36	30.6	16.1	31.6	18.5
Na	10.1	0.7	5.8	2.0	0.6	1.7	1.0
Cl	9.6	1.4	5.7	2.0	1.3	1.6	1.3
Ca	**8.4**	**-**	**10.5**	**9.2**	**1.0**	**7.6**	**1.6**
P	**7.0**	**-**	**7.6**	**6.8**	**1.0**	**5.7**	**1.9**
Ca/P[**]	**1.20**	**N/A**	**1.38**	**1.35**	**1.0**	**1.33**	**0.84**

[*] Figure labels in Fig. 2–S5

[**] Ca/P for OCP and apatite are 1.33 and 1.67, respectively.

Reprinted with permission from [Doyoon Kim, Byeongdu Lee, Stavros Thomopoulos, and Young-Shin Jun, The role of confined collagen geometry in decreasing nucleation energy barriers to intrafibrillar mineralization. *Nature Communications*, 2018, 9, 962. DOI: 10.1038/s41467-018-03041-1]. Copyright [2018] Nature Publishing Group.

Chapter 3. Evaluation of Confined Collagen Structure as a Biological Template

Portions of this chapter have been published in *Nature Communications* in 2018, DOI: 10.1038/s41467-018-03041-1.

3.1 Overview

In **Chapter 2**, we evaluated how calcium phosphate (CaP) nucleation in collagenous structures follows distinctly different patterns in highly confined gap regions (nanoscale confinement) than in less confined extrafibrillar spaces (microscale confinement). The differences in nucleation pathways and kinetics imply that the nucleation energy barriers differ in intrafibrillar and extrafibrillar spaces. Although the mechanism(s) driving these differences are still largely unknown, differences in the free energy for nucleation may explain these two mineralization behaviors. Here, we report experimentally obtained values for the nucleation energy barriers to intra- and extrafibrillar mineralization, using *in situ* X-ray scattering observations and classical nucleation theory. Polyaspartic acid (pAsp), an extrafibrillar nucleation inhibitor, increases interfacial energies between nuclei and mineralization fluids. In contrast, the confined gap spaces inside collagen fibrils lower the energy barrier by reducing the reactive surface area of nuclei, decreasing the surface energy penalty. The confined gap geometry, therefore, guides the two-dimensional morphology and structure of bioapatite and changes the nucleation pathway by reducing the total energy barrier.

3.2 Introduction

The nucleation and growth of mineral phases in porous media are critical for many biologic processes and engineering applications.[50-53] Recent studies have investigated nucleation in confined nanoscale pore spaces,[52,54,55] where the physicochemical properties, such as the melting point or crystal polymorphism,[55] of the minerals formed in the pores are clearly distinct from their bulk phase counterparts. These findings provide a better understanding of biominerals. For example, HA crystals nucleated in the 25–300 nm pores showed stronger orientation than in bulk solution,[59] as commonly observed in bioapatite in bones and teeth.[2,61] However, we know little about how nanoscale confinement affects the nucleation of CaP minerals in more physiologically relevant systems.

Mineralization of the skeleton relies on the nucleation and growth of mineral crystals in both unconfined and confined spaces.[47,59,60] CaP mineralization takes place in nanoscale porous structures created by a unique arrangement of collagen molecules.[33-35] Narrow channel-like gap regions (~40 nm long and ~2 nm high)[10,33,68,73] in type I collagen molecules are known to provide appropriate spaces for IM, forming oriented bioapatite.[33,71,97] Thus, in addition to NCPs in the extracellular matrix,[71,73,98] the collagen fibrillar structure itself has been emphasized as another major factor in IM. Recently, Wang *et al*. reported bonelike bioapatite formation in collagen in vitro within a collagen structure during fibrillogenesis, even without NCPs.[47] Nudelman *et al*. showed that a specific band position in the gap region of collagen with a net positive charge can attract net negatively charged ACP nuclei in the presence of pAsp, which is a well-known substitute for NCPs in biomimetic experiments.[27]

Bioapatite crystals are also found in the unconfined extrafibrillar spaces of collagen (EM) as aggregate without a specific orientation.[48,49] Our previous work showed that the pathways and kinetics of bioapatite formation during IM and EM were distinct from each other.[99] The nucleation pathway for EM included aggregation and densification of prenucleation clusters to form spherical ACP as an intermediate product. A similar pathway was reported to occur in biomimetic environments, but without confinement.[8,14,26] On the other hand, such an intermediate stage did not appear in the IM pathway for in vitro collagen mineralization, suggesting a direct formation of plate-like particles, as reported in our previous study.[99] Despite the absence of an intermediate step, the kinetics for IM were, however, slower than for EM, due to the nucleation inhibiting effect of pAsp.[8,99]

Despite experimental evidence of different nucleation patterns in IM and to EM, the mechanism(s) behind these processes remain unclear. The differences in nucleation pathways and kinetics imply that the nucleation energy barriers differ in EM and IM. For example, the formation of prenucleation clusters. which was observed only during EM,[99] reduces the energy barrier to ACP nucleation,[8] while the intermediate stage did not appear during IM. Therefore, a higher nucleation barrier is expected for IM than EM. However, in most in vitro collagen mineralization studies, IM is more favored than EM in the presence of nucleation inhibitors.[27,44,99] Thus far, no study has separately evaluated the nucleation energy barriers for the two mineralization patterns to the best of our knowledge, so it is unclear how the confined collagen gap region contributes to overcoming the high nucleation energy barrier to IM.

Here, we present experiments using SAXS analysis to examine CaP nucleation rates during EM and IM in simulated body fluids (SBF) with or without pAsp (Figure 3.1 and Table 3.1). These data allow us to evaluate the nucleation energy barriers for IM and EM separately by applying the principles of classical nucleation theory (CNT).[11,13,17,19,28–31] To better determine nucleation patterns in the confined gap region, a new model was developed with an assumption of plate-like nuclei formation. Based on the CNT analysis, EM occurs initially in SBF solutions, due to their lowest nucleation energy barrier. The addition of pAsp kinetically inhibits EM formation; instead, it leads nucleation to occur dominantly in the narrow collagen gap regions, despite the increased interfacial energy there. In these highly confined spaces, nuclei grow in 2D, limiting the reactive surface area for nucleation and decreasing the surface energy contribution to the barrier. With this observation, we provide an explanation for how the highly confined spaces of the fibrillar collagen structure foster biomineralization.

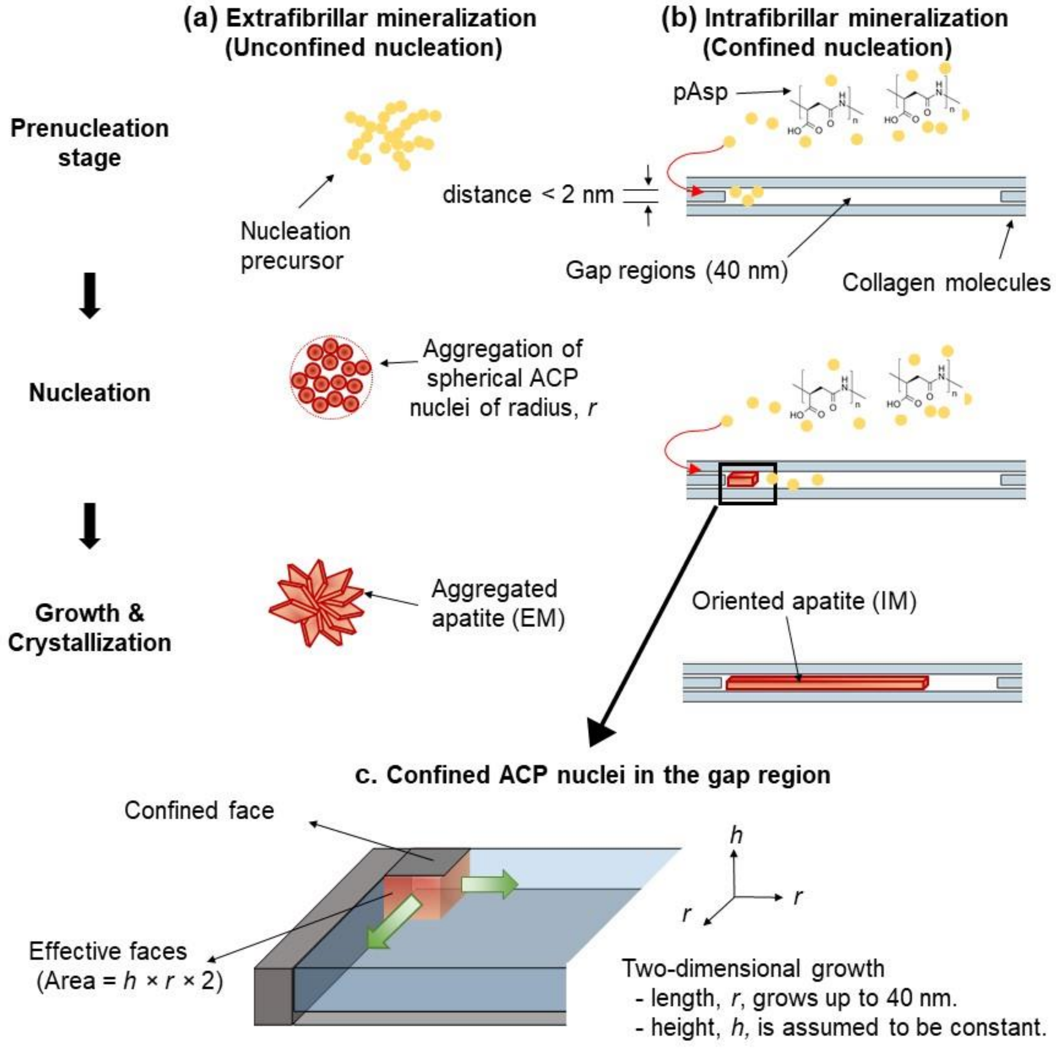

Figure 3.1 Schematic illustration of two different nucleation models for collagen mineralization. (**a**) Extrafibrillar nucleation in unconfined space. (**b**) intrafibrillar nucleation in a confined gap region. (**c**) Geometry of confined amorphous calcium phosphate (ACP) nuclei in the gap region.

3.3 Materials and Methods

3.3.1 Preparation of Collagen Matrices

Type I collagen (C857, calf skin lyophilized, Elastin Products Company, Inc.) was used to reconstitute collagen matrices.[84,99] Collagen was carefully dissolved in 0.5 mM HCl (12 mg ml^{-1}) at 4°C with magnetic stirring, followed by degassing under vacuum at 4°C for 4 days. The dissolved collagen solution was placed in two holes (3 mm in diameter) in a specially designed PTFE frame with a thickness of 2.38 mm (Figure 3.2a). A #1 cover glass was attached on one side of the frame to support the collagen solution during polymerization in TES buffered saline (5.5, 6.32, and 3.4 g l^{-1} of TES, NaCl, and Na_2HPO_4, in deionized water, pH 7.5) at 37±1°C. The frame was then stored in deionized water overnight to remove excess salt. Based on our previous study described in Chapter 2, the reconstituted collagen with a fibrillar density of 12 mg ml^{-1} was optimal for observing both intrafibrillar and extrafibrillar mineralization with SAXS. AFM imaging revealed ~67 nm periodicity of the collagen, confirming that the nanoscale confinement distribution in the fibrils was comparable to native type I collagen (Figure 3–S2a,b). In addition, the well-controlled shape and uniform thickness of the collagen matrix allowed for quantification of the nucleation rates using *in situ* SAXS at different time intervals.

3.3.2 Preparation of Simulated Body Fluid Solutions

SBF solutions were prepared using the method proposed by Kokubo *et al*.[86] to mimic major ionic compounds in human body plasma.[85] American Chemical Society grades of NaCl (7.996 g, BDH Chemicals), $NaHCO_3$ (0.350 g, BDH Chemicals), KCl (0.224 g, BDH Chemicals), $MgCl_2 \cdot 6H_2O$ (0.305 g, EMD Millipore), 1 M HCl (40 ml, BDH Chemicals), Na_2SO_4 (0.071 g, Alfa Aesar), and tris(hydroxymethyl)aminomethane (Tris, 6.057 g, Alfa Aesar) were added to 900 ml of deionized water (18.2 MΩ-cm). Either 0 or 10 mg of pAsp (sodium salt, Mw: 5,000 Da, LANXES) was added to the solution, depending on the experimental condition. Then the solution was equally separated into two 500 ml polyethylene bottles, and either 0.604–0.684 g of $K_2HPO_4 \cdot 3H_2O$ (Alfa Aesar) or 0.974–1.103 g of $CaCl_2 \cdot 2H_2O$ (Alfa Aesar) was added to each bottle. The pH of the solutions was adjusted to 7.25 with 1 M HCl, followed by filling up the volume with water to 500 mL. To prevent any precipitation of calcium phosphate minerals prior to the start of the experiment, the two stable solutions containing either Ca^{2+} or HPO_4^{2-} precursors (SBF-Ca or SBF-P) were prepared separately and mixed just before the reaction (Figure 3.2b). The concentrations of Ca and P in the reactor after the two solutions were mixed were 2.65 to 3.0 times higher than in the SBF solution by Kokubo's method (2.65–3.0×SBF). However, the Ca/P molar ratio was constantly fixed to 2.5. The continuous flow-through reaction system (Figure 3.2) allowed maintaining constant concentrations of ionic components and pH in the reactor for each set of experiments (details listed in Table 3.1). The addition of 10 mg l^{-1} pAsp, a nucleation inhibitor for EM, effectively promoted IM for up to 15 h during the mineralization of collagen matrices in the 3.0×SBF[23]. The use of a buffer in the SBF solution was unavoidable in order to maintain the desired pH. This buffer allowed us to use a constant supersaturation value for each SBF solution for the application of CNT. In this study, tris-buffer was used because it has been widely and effectively used for biomimetic CaP synthesis and intrafibrillar collagen mineralization.[23,58,91,99] More details about the potential influence of buffers in physiological solutions were summarized in a recent review paper.[91]

Supersaturation (σ) values of the SBF solutions were calculated for both HA (σ_{HA}) and ACP (σ_{ACP}). The ion activity product of hydroxyapatite (IAP_{HA}) was defined as $(\alpha_{Ca^{2+}})^5(\alpha_{PO_4^{3-}})^3(\alpha_{OH^-})$.[100] The activity of an ionic compound i, α_i, is the product of its activity coefficient, γ_i, and concentration, C_i. We calculated γ_i values at 37°C from the modified Debye–

Hückel equation, $\log \gamma_i = -0.5211\, z_i^2 [\frac{I^{\frac{1}{2}}}{1+I^{\frac{1}{2}}} - 0.3I]$,[100,101] where I is the total ionic strength ($I = \frac{1}{2}\sum C_i z_i$) and z_i is the charge number. To calculate C_i of all the ionic components in SBF solutions, MINEQL+ was used, with consideration of pAsp based on its dissociation and calcium binding constants as reported by Wu and Grant.[102] Using values from the literature,[103,104] we set K_{sp} (HA) = 2.35×10^{-59} and set the molecular volume, v_m (HA) = 2.63×10^{-22} cm^3. σ_{ACP} was calculated based on $Ca_2(HPO_4)_3^{2-}$ ($IAP_{ACP} = (\alpha_{Ca^{2+}})^2(\alpha_{HPO_4^{2-}})^3$) with an estimated K_{sp} (ACP) value of $(6.04 \times 10^{-4})^5$ and v_m (ACP) = 5.0×10^{-23} cm^3, as recently suggested by Habraken *et al.*[8] The concentrations of ionic compounds and calculated σ values are summarized in Table 3.1.

Table 3.1 Concentrations (mM) of ionic components in SBF and human blood plasma.

Solution	Na^+	K^+	Mg^{2+}	Ca^{2+}	Cl^-	HCO^{3-}	HPO_4^{2-}	SO_4^{2-}	σ_{ACP}	σ_{HA}
Reference values										
SBF[86]	142.0	5.0	1.5	2.50	147.8	4.2	1.00	0.5	-3.89	23.32
Human blood plasma[85]	142.0	5.0	1.5	2.50	103.0	27.0	1.00	0.5	-4.10	22.70
Without pAsp										
2.65×SBF	142.0	8.3	1.5	6.63	156.1	4.2	2.65	0.5	0.60	30.57
2.75×SBF	142.0	8.5	1.5	6.88	156.6	4.2	2.75	0.5	0.74	30.84
2.85×SBF	142.0	8.7	1.5	7.13	157.1	4.2	2.85	0.5	0.91	31.09
3.0×SBF	142.0	9.0	1.5	7.5	157.8	4.2	3.0	0.5	1.13	31.47
With 10 mg L^{-1} pAsp										
2.65×SBF	142.0	8.3	1.5	6.63	156.1	4.2	2.65	0.5	0.59	30.56
2.7×SBF	142.0	8.4	1.5	6.75	156.3	4.2	2.70	0.5	0.68	30.69
2.75×SBF	142.0	8.5	1.5	6.88	156.6	4.2	2.75	0.5	0.74	30.84
2.85×SBF	142.0	8.7	1.5	7.13	157.1	4.2	2.85	0.5	0.91	31.09

* pH adjusted to 7.25 with 50 mM of Tris ($(CH_2OH)_3CNH_2$) and HCl.

** σ, values of the SBF solutions were calculated for ACP and HA using MINEQL+ (Ver. 4.6). NCPs and other small acidic molecules exist in human blood plasma, and would influence the σ values. However, in this proof of concept calculation, we limited the input parameters to the major ionic compounds.

3.3.3 *In situ* X-ray Scattering Data Collection and Analysis

In situ SAXS data were collected during the mineralization of collagen at the APS, Sector 12 ID-B. For the collagen mineralization, SBF-Ca and SBF-P were separately placed in 60 ml syringes, then continuously flowed into the reactor at 0.11 ml min^{-1} per syringe, using a syringe pump. The volume of the solution in the reactor was 12.5 ml, giving 57 min of residence time, and maintaining the solution at a pH of 7.25 ± 0.05. A hot plate maintained the reactor at 37 ± 1℃ (Figure 3.2b). Two frames holding two collagen matrices (a total of four samples in a reactor) were placed in the reactor for mineralization and temporarily (~2 min) moved to the SAXS sample stage for analysis (Figure 3.2c). Samples were measured at intervals of 1–3 h during the mineralization, up to 15 h. The distance from the sample to the SAXS detector was 3.6 m, which provided a range of 0.0017–0.53 Å^{-1} for the scattering vector, q. For each scan, the sample was exposed to a 14 keV X-ray beam for 0.1 s. With this experimental setup, we confirmed that homogeneous nucleation in 3×SBF containing either 0 or 10 mg l^{-1} pAsp was not significant enough to be detectable by SAXS for up to 15 h.[23] Therefore, we concluded that the stability of the SBF solution was well maintained during the entire period of *in situ* measurements. The 2D scattering intensity counted by the detector (2M Pilatus) was averaged over the q range along the radial direction to produce 1D scattering intensities $I(q)$. Each obtained $I(q)$ was normalized by the incident beam intensity and calibrated on an absolute scale, using a reference glassy carbon standard sample,[45] and thus SAXS intensities collected from different measurements could be compared. Three different positions of each sample were analyzed, and their average 1D values were used for further analysis. The Modelling II tool of the IRENA package, written in IGOR Pro (WaveMetrics Inc.), was provided by APS and used to fit the SAXS pattern.[94]

In addition to SAXS, *in situ* WAXD analysis was conducted at APS sector 11-ID-B to identify the phases of calcium phosphate minerals formed during collagen mineralization ($q > 0.6$ Å^{-1}). For the data collection, five different positions of samples were exposed to a 58.66 keV X-ray beam for 2 min each.

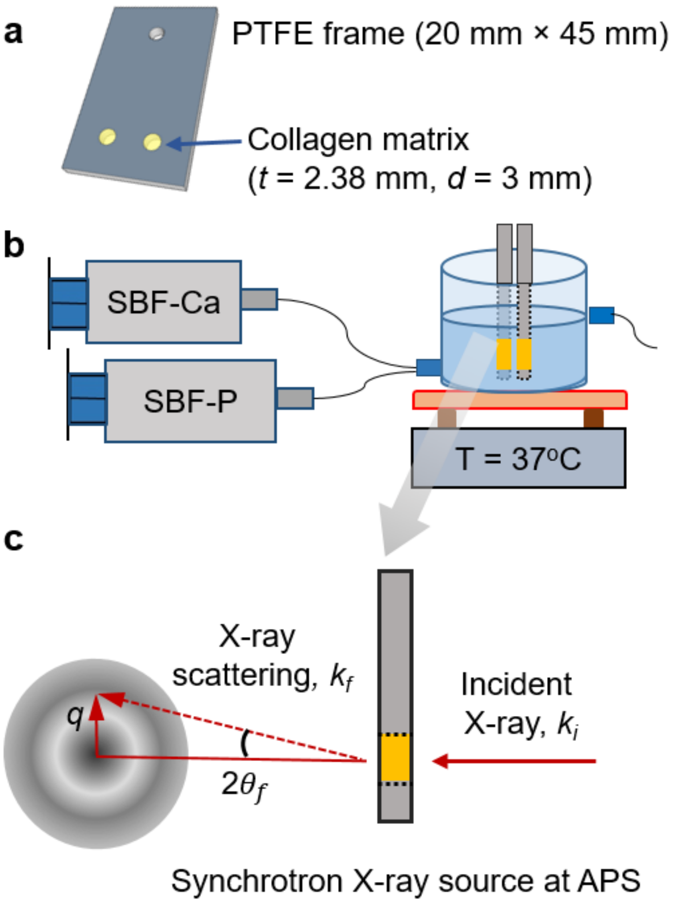

Figure 3.2 Experimental setup for *in situ* SAXS measurements during collagen mineralization. (**a**) Design of a custom-made sample PTFE frame containing two collagen matrices (thickness, $t = 2.38$ mm; diameter, $d = 3$ mm). t was chosen to collect enough scattering intensity signals, and d was chosen to scan multiple positions for averaging the data. (**b**) Mineralization of collagen matrices held in the frame, using a flow-through reaction system on a hot-plate maintaining the reactor at 37±1℃. (**c**) Experimental setup for SAXS measurements. k_i and k_f are the incident and scattered wave vectors, respectively. The scattering vector, q, is given by k_i - k_f, and $2\theta_f$ is the exit angle of the X-rays.

3.3.4 *Ex situ* Sample Analysis

For *ex situ* imaging of the mineralization, thin collagen films were prepared on glass slides to simulate the reaction occurring at the outermost surface of collagen matrices. To prepare a film, a droplet (0.1 ml) of dissolved collagen (12 mg ml^{-1} of collagen in 0.5 mM HCl) was evenly dispersed on a glass slide (1×1 cm^2) using a spin coater (Laurell WS-650MZ-23NPP, 5000 rpm for 30 s). Then the slide was placed in TES buffered saline for an hour to polymerize collagen fibrils. The mineralization of collagen films was also conducted in SBF solutions using the flow-through reaction system, as was done for *in situ* SAXS analysis. After the mineralization, these thin films were fixed in 100 mM cacodylate buffer containing 2% paraformaldehyde and 2.5% glutaraldehyde. The films were then rinsed in a cacodylate buffer solution and dehydrated in successive ethanol baths (30, 50, 70, 90, and 100 % for 15 min each). For SEM imaging and EDX analysis, films were placed in SEM stubs and were sputter-coated with Au-Pd under Ar at 0.2 mbar (Cressington 108) to increase conductivity, then imaged with a 10 kV electron accelerating voltage at a 5−6 mm working distance (FEI Nova NanoSEM 230). EDX was calibrated by using Cu and Al standards with a measurement error of ±1 %.

3.4 Results

3.4.1 CNT Application to Extra and Intrafibrillar Mineralization

CNT has often been adopted to evaluate the interfacial energy between nuclei and a mineralization solution, and to evaluate the nucleation energy barrier.[13,17,19] CNT has provided fundamental knowledge about the nucleation and growth of biominerals, and recent studies have expanded its scope to interpret non-classical nucleation behaviors.[8,14,21,105] A heterogeneous nucleation model in CNT has also been adopted to explain how the interfacial energy and nucleation barrier decrease in the presence of collagen, by assuming the collagen is a flat substrate for hemispherical particle formation.[8,38-40] However, without a proper evaluation of the differences between EM and IM, the role of collagen in nucleation remains elusive. In addition, a careful consideration of collagen geometry is needed to properly account for the influence of the confinement of nuclei in the gap regions on IM.

According to CNT, nucleation through monomer-by-monomer attachment is assumed to be thermodynamically driven by the free energy change per molecule, ΔG. For the formation of a nucleus from a solution, ΔG is given by the sum of the bulk ($-\Delta G_b$) and surface (ΔG_s) terms. A typical ΔG profile shows a maximum (i.e., an energy barrier, ΔG_n) at a critical radius (r_c), then decreases with increasing radius (r). The nucleation rate (J) can be expressed with ΔG_n in its exponential term, $J = A\exp\left(-\frac{\Delta G_n}{k_B T}\right)$, where k_B is the Boltzmann constant, T is the Kelvin temperature, and A is a kinetic factor. For the formation of a spherical nucleus, $\ln(J)$ shows a linear relationship with $1/\sigma^2$. Here, the supersaturation (σ) of the solution is given as $\ln(IAP/K_{sp})$, where IAP is the ion activity product and K_{sp} is the solubility product. In this linear relationship, the fitting of the slope (B), as listed in Table 3.2, can provide the interfacial energy (α) between nuclei and the mineralization solution. We applied this relationship to evaluate α for EM, where nucleation occurs in relatively unconfined macroscale spaces, with the assumption of spherical nuclei formation (Figure 3.1a). This assumption is reasonable because the EM pathway forms spherical ACP nuclei.[8,26,99]

On the other hand, we previously found that plate-like CaP formed in the confined gap region without intermediate spherical ACP.[99] Similar 2D crystallization can occur by the preferential adsorption of small acidic molecules, such as phosphoserine and citrate, on specific faces of apatite nuclei.[30,31] To quantitatively evaluate nucleation in the confined gap region (IM), we developed a model of nucleation in which 2D crystals grow only in the lateral directions with a uniform height (Figure 3.1b). The relevant equations are given in Table 3.2. A plate-like morphology was assumed to better reflect the CNT precept that the nucleus and final crystal have the same crystalline structure. In this model, the surfaces of nuclei confined in the collagen gap region do not allow monomer-by-monomer attachments of precursor molecules for nucleation. Only the exposed surfaces can affect the calculation of ΔG_s (Figure 3.1c).[106] To simulate the reported IM nucleation initiated at the specific band positions near C-terminal ends of the gap region,[14,20,4127,68,107] we assumed that nuclei formed at a corner of the collagen gap region (two edge surface exposure). The nuclei then thermodynamically benefit by minimizing their surface area to form a solid phase in an aqueous solution. In this model, $\ln(J)$ shows a linear relationship with $1/\sigma$, which also provides α (between the edge surfaces of nuclei and the solution) from the fitting of the slope B (Table 3.2). When the confinement effect is considered, the different assumptions about the morphology and effective surfaces of nuclei do not change this linear relationship and consequent ΔG_n values (Section 3.7.1). Therefore, in this study, we mainly evaluated the comparison between confined and unconfined models, instead of exploring other possible scenarios of nucleation occurring in this confined space.

Table 3.2. Derivation of the nucleation energy barrier (ΔG_n) and interfacial energy (α) of the unconfined nucleation model for extrafibrillar mineralization (EM) and the confined nucleation model for intrafibrillar mineralization in the collagen gap region (IM), based on classical nucleation theory.

	Extrafibrillar mineralization (Unconfined nucleation)	**Intrafibrillar mineralization Confined nucleation**
Morphology of nucleus	Sphere	Plate (constant *h*)
Effective surface area exposed to solution	$4\pi r^2$	$2rh$ (two edge surfaces)
Volume	$\frac{4}{3}\pi r^3$	r^2h
$\boldsymbol{\Delta G = \Delta G_b + \Delta G_s}$	$-\left\{\frac{\left[\left(\frac{4}{3}\right)\pi r^3\right]}{v_m}\right\}k_BT\sigma + 4\pi r^2\alpha$	$-\left\{\frac{[r^2h]}{v_m}\right\}k_BT\sigma + 2rh\alpha$
$\boldsymbol{r_c}$ **(at dΔG/dr = 0)**	$\frac{2v_m\alpha}{k_BT\sigma}$	$\frac{v_m\alpha}{k_BT\sigma}$
$\boldsymbol{\Delta G_n}$ **(at $r = r_c$)**	$\frac{16\pi v_m^2\alpha^3}{3k_B^2T^2\sigma^2}$	$\frac{hv_m\alpha^2}{k_BT\sigma}$
$\boldsymbol{J = A \exp(-\Delta G_n / k_BT)}$	$A\exp(-\frac{16\pi v_m^2\alpha^3}{3k_B^3T^3\sigma^2})$	$A\exp(-\frac{hv_m\alpha^2}{k_B^2T^2\sigma})$
ln(*J*)	$\mathbf{ln}(\boldsymbol{A}) - \boldsymbol{B}\frac{\mathbf{1}}{\boldsymbol{\sigma}^{\mathbf{2}}}$ $B = (\frac{16\pi v_m^2\alpha^3}{3k_B^3T^3})$	$\mathbf{ln}(\boldsymbol{A}) - \boldsymbol{B}\frac{\mathbf{1}}{\boldsymbol{\sigma}}$ $B = (\frac{hv_m\alpha^2}{k_B^2T^2})$
α	$(\frac{3Bk_B^3T^3}{16\pi v_m^2})^{\frac{1}{3}}$	$(\frac{Bk_B^2T^2}{hv_m})^{\frac{1}{2}}$

* The effect of confinement on the shape and growth of nuclei for the confined nucleation model is illustrated in Figure 3.1. The morphology of the nucleus changes the parameters in the bulk and surface energy terms (ΔG_b and ΔG_s, respectively). As a result, ln(*J*) shows a linear relationship with $1/\sigma^2$ for unconfined nucleation, but with $1/\sigma$ for fully confined nucleation.

** *r* and *h* are the radius (or length for the confined nucleation model) and height of nuclei. For the volume per molecule of nucleus, v_m, 5×10^{-23} cm^3 and 2.63×10^{-22} cm^3 are used for ACP[8] and for HA,[104] respectively. k_B is the Boltzmann constant (1.38×10^{-23} J K^{-1}). *T* is the temperature of the reactor (310 K). σ is the supersaturation ($\ln(IAP/K_{sp})$), where *IAP* is the ion activity product and K_{sp} is the solubility product. α is the interfacial energy between nuclei and solution.

3.4.2 Extra and Intrafibrillar Mineralization Controlled by pAsp

To evaluate the differences in α and ΔG_n between IM and EM, nucleation rates must be separately measured. The two mineralization behaviors were controlled using pAsp. Our previous study also utilized pAsp in 3×SBF and showed how it controlled these two mineralization behaviors.[99] In the current study, SEM images revealed that the addition of 10 mg l^{-1} pAsp successfully separated EM and IM patterns in a wide range of σ, using 2.65–3.0×SBF solutions (Section 3.7.2).

The differences in nucleation behaviors between EM and IM controlled by pAsp were also apparent in SAXS patterns (Figures 3.3a,b). For example, SAXS intensities in the small q region (< 0.01 Å^{-1}) continuously increased during EM without pAsp over time. The intensity increases in the small q region were mainly caused by the formation of particles larger than 62.8 nm in diameter ($d = 2\pi/q$). Without pAsp, such large particles were observed only as an aggregated form of CaP in the extrafibrillar space (Figure 3–S2c,d). The SAXS patterns in the large q region ($>$ 0.01 Å^{-1}, Figure 3.3a at after 280 min) fit well with plate-like particles with a uniform height of 1.5 nm. The negative slope of 2 between the two extreme regions, at q around 0.01−0.2 Å^{-1}, is evidence of the 2D structure of a plate-like particle.[92,94,108] Thus, we concluded that these patterns represent aggregates of thin apatite crystals, as commonly observed during EM (Figure 3–S2d). On the other hand, during IM with 10 mg l^{-1} pAsp, similar plate-like particles (1.5 nm height) developed without forming an aggregate (little increases of SAXS intensities at small q, Figure 3.3b). This observation indicates that individual plates are separately arranged within the collagen, as expected from IM. Evidence of aggregation during EM can also be found from the negative slope, P, of the Porod regime, $q > 0.2$ Å^{-1}, at the induction period before plate-like particle development. During EM without pAsp, a P value close to 3 (at 192 min, Figure 3.3a) indicates an isometric mass fractal structure, such as a spherical aggregate. This slope is clearly distinct from that of a typical compact object (P = 4), such as appeared during the induction period of IM (at 179 min, Figure 3.3b).[99,108]

Wide-angle X-ray diffraction (WAXD) of samples indicated that very little crystalline structure developed, either because the structure was mostly amorphous or because the nuclei were few and small, at the beginning of both intrafibrillar and extrafibrillar mineralization (Figure 3.3c, < 240 min). However, these patterns developed to HA-like, yet poorly crystalline, crystals at a later stage (> 900 min). In the presence of pAsp (IM case), from the beginning, a slightly higher crystallinity developed from nucleated minerals. In other words, with pAsp, enhanced intensities were observed at q = 1.83, 2.23, and 2.26 $Å^{-1}$ (corresponding to (002), (211) and (112) reflections, respectively), while only a smooth hump appeared around q =1.83 $Å^{-1}$ without pAsp (EM case). These data show that the crystallinity of nuclei developed more slowly during EM than IM, even though the total particle volume in this period, as quantified from the absolute SAXS intensity,[95] was slightly higher for EM. EM essentially undergoes a phase transformation pathway involving an amorphous intermediate product, delaying the transformation to HA-like crystals.[99]

Because amorphous phases were dominant in WAXD patterns at the early stage of mineralization, we assumed that nuclei were amorphous in further studies exploring the interfacial energy relationship. Many previous studies have also hypothesized ACP as a precursor phase of bioapatite in bones.[8,23,27,28,75] However, there remains a possibility of direct formation of crystalline apatite during IM, because a sudden formation of plate-like particles was observed in our recent report.[99] Indeed, the absence of ACP has been reported in studies of young bones[109] and biomimetic nanocrystalline HA.[110] Therefore, we also provided the relationship based on the assumption of HA nuclei, which is comparable to previous reports examining the interfacial energy for HA nucleation.[8,39,40]

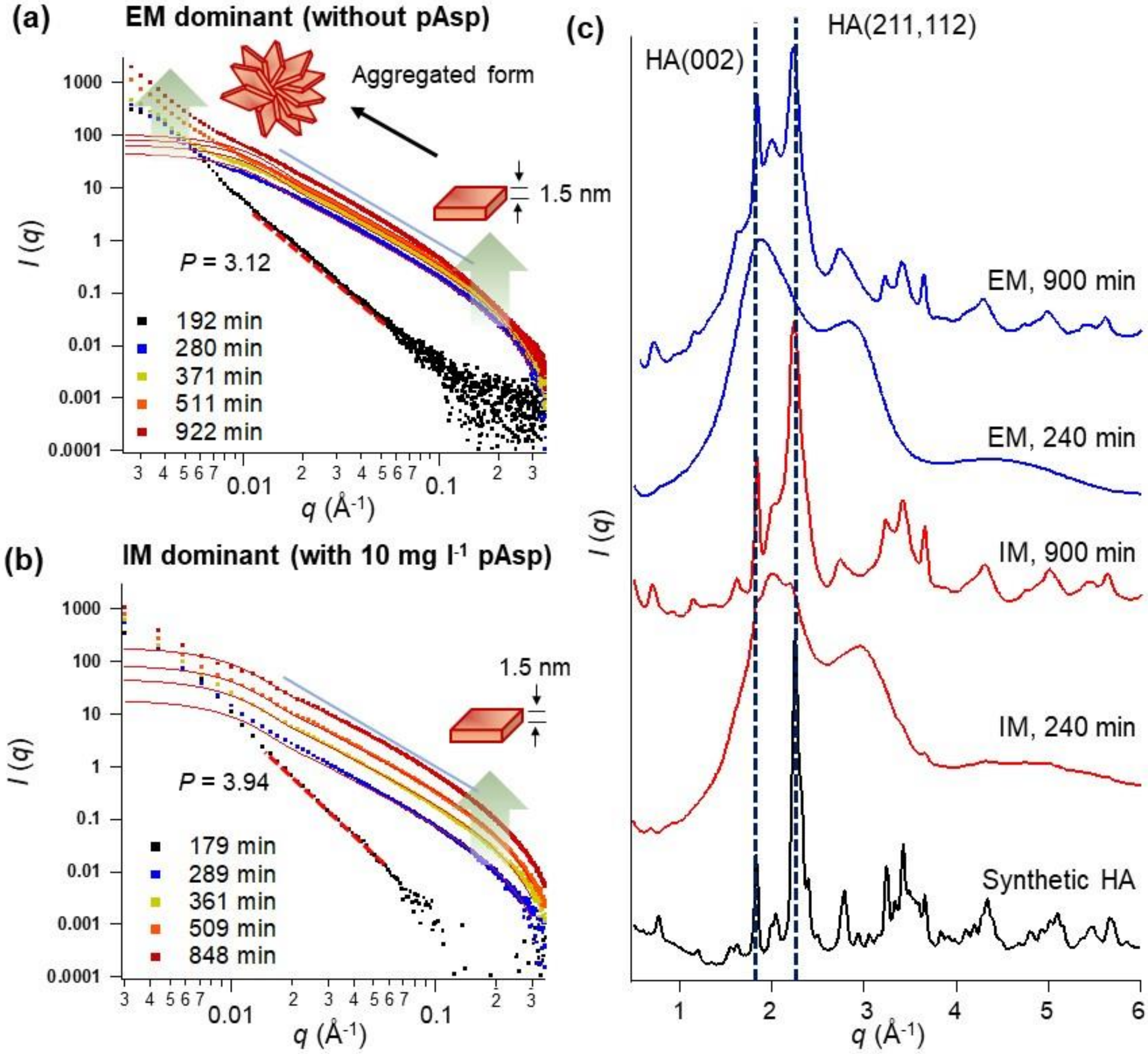

Figure 3.3 *In situ* SAXS/WAXD patterns from collagen matrices during mineralization. Data collected from unmineralized collagen was used for background subtraction. (**a,b**) Small-angle X-ray scattering (SAXS) patterns collected during mineralization without pAsp for extrafibrillar mineralization (EM, **a**) and with pAsp for intrafibrillar mineralization (IM, **b**) in the 2.85 × SBF solution. Red solid lines fit plate-like particles (height: 1.5 nm and length: 40 nm). *P* values are the slopes of the Porod regime at 179 and 192 min, in red dotted lines ($I(q) \propto q^{-P}$). The solid light blue lines show negative slopes of 2 in the log-log plot after the induction time, indicating the 2-dimensional morphology of nuclei. (**c**) Wide-angle X-ray diffraction (WAXD) patterns of CaP formed in collagen matrices at early (240 min) and later (900 min) stages of mineralization. Synthetic HA was analyzed for comparison.

3.4.3 Nucleation Rates Measured by *In situ* SAXS Analysis

SAXS patterns collected at the nucleation stage suggest the formation of plate-like particles for both EM and IM. The invariant value, $Q = \frac{1}{2\pi^2}\int q^2 I(q)dq$, is a quantity proportional to the total particle volume.[110] Therefore, J was determined from the slope of Q vs. time plots during mineralization in different SBF solutions (Figure 3.4a,b), with the assumption of constant morphology and electron density of the nuclei. During EM development without pAsp (Figure 3.4a), Q values increased after 160–290 min of induction (x-intercepts), then reached a plateau around $Q = 4 \times 10^{-5}$ for all SBF solutions. At the SBF–collagen matrix interface, a thin layer of calcium phosphate crystals formed, acting as a diffusion barrier to the molecules required for the mineralization of the inner side of the matrix.[99] Therefore, only the outer surfaces of the collagen matrices could serve as nucleation sites. On the other hand, during IM with pAsp, the milder slopes of Q and longer induction times (230–500 min) than for EM indicate that nucleation was inhibited by pAsp at the early stage.[99] However, the Q values pass through the maximum plateau value obtained from EM, showing continuous and linear increases of Q over 900 min (Figure 3.4b). Because no diffusion barrier formed during IM, the entire volume of the collagen matrices could be mineralized.

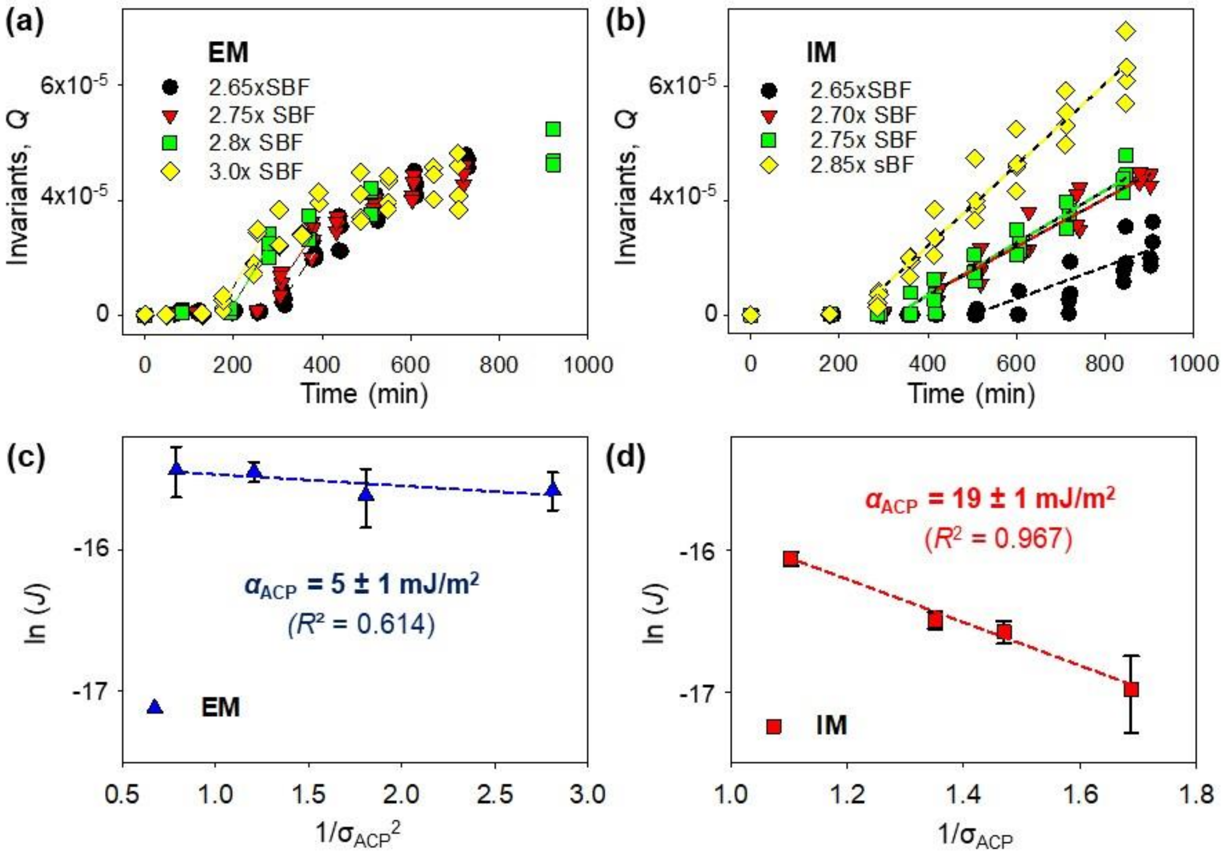

Figure 3.4 Interfacial energy relationships during the nucleation of calcium phosphate within collagen fibrils. (**a,b**) Evolution of the invariant, *Q*, from *in situ* SAXS measurements of collagen matrices in different simulated body fluid (SBF) solutions without pAsp (**a**, representing extrafibrillar mineralization, EM) and with pAsp (**b**, representing intrafibrillar mineralization, IM). The slopes of the dotted lines indicate the nucleation rate, *J*. For the EM case, the initial J values were taken from the maximum slopes between two time intervals. Only *Q* within the range of $q = 0.05–0.3$ Å^{-1} (corresponding to plate-like particles) were calculated. (**c,d**) Interfacial energies for ACP nucleation (α_{ACP}) during EM and IM, calculated from the relationship between J and supersaturation with respect to ACP, α_{ACP} (see Table 3.1 for the equations). Error bars in the symbols indicating ln(*J*) are standard errors of the estimates, obtained from the regressions between *Q* and time (from **a, b**). Error ranges for αACP values for EM and IM are standard errors of the estimates for regressions between ln(J) and $1/\sigma^2$, and between ln(*J*) and $1/\sigma$, respectively.

3.4.4 Interfacial Energies and Energy Barriers for EM and IM

Separately obtained J values for EM and IM were applied to our CNT models for EM ($\ln(J) \propto 1/\sigma^2$, Figure 3.4c) and IM ($\ln(J) \propto 1/\sigma$, Figure 3.4d). In this way, we could quantify the interfacial energies between CaP nuclei and SBF solutions in unconfined extrafibrillar space and confined gap regions. The α value for IM was calculated to be about four times higher than that for EM with respect to ACP ($\alpha_{\mathrm{ACP}} = 19 \pm 1$ mJ m^{-2} for IM vs. 5 ± 1 mJ m^{-2} for EM). Due to this significant difference in α, a small concentration of pAsp could effectively control the nucleation behavior, while not significantly decreasing the σ of the bulk SBF solutions. The amount of pAsp used (10 mg l^{-1}) was equivalent to only 0.072 mM of aspartyl residue;[102] therefore the change in σ by complexation between ionic calcium species and pAsp was less than 5% (Table 3.1). Due to the increased α, ΔG_{n} for ACP nucleation is typically higher for IM than for EM over a wide range of σ (Table 3.1 and Figure 3.5a, red and blue lines), including our experimental range ($\sigma_{\mathrm{ACP}} = 0.60$–$1.13$, Table 3.1). The ratio of the ΔG_{n} for IM over the ΔG_{n} for EM, however, decreases with decreasing supersaturation ($\Delta G_{\mathrm{n,IM}} / \Delta G_{\mathrm{n,EM}} = \frac{3hK_bT\alpha_{IM}^2}{16\pi v_m \alpha_{EM}^3}\sigma = 18.8\sigma$). Eventually, at $\sigma_{\mathrm{ACP}} < 0.05$, $\Delta G_{\mathrm{n,IM}}$ becomes lower than $\Delta G_{\mathrm{n,EM}}$ (Figure 3.5b), making IM more favorable than EM in this σ range. The low supersaturation degree of the body fluid with respect to ACP, therefore, could be an important factor guiding nucleation in the confined gap regions.

Although human blood plasma is highly supersaturated with respect to HA, our thermodynamic calculation shows that it is undersaturated with ACP ($\sigma < 0$, Table 3.1). However, it has been suggested that the concentrations of ionic components, such as Ca^{2+} and $\mathrm{HPO_4}^{2-}$, can increase during fibrillogenesis of the collagen scaffold.[47] The extracellular pH might be higher near the bone-forming zone than in body fluids, because bone serves as a massive reservoir of alkaline materials.[2] Therefore, body fluids might be locally saturated to form ACP. Indeed, aggregated ACP particles were more abundant on the surface of newly forming bones than in other areas in the extracellular space of embryonic chickens.[111] Thus, we expect the actual σ value with respect to ACP near bone-forming zones is slightly higher than zero.

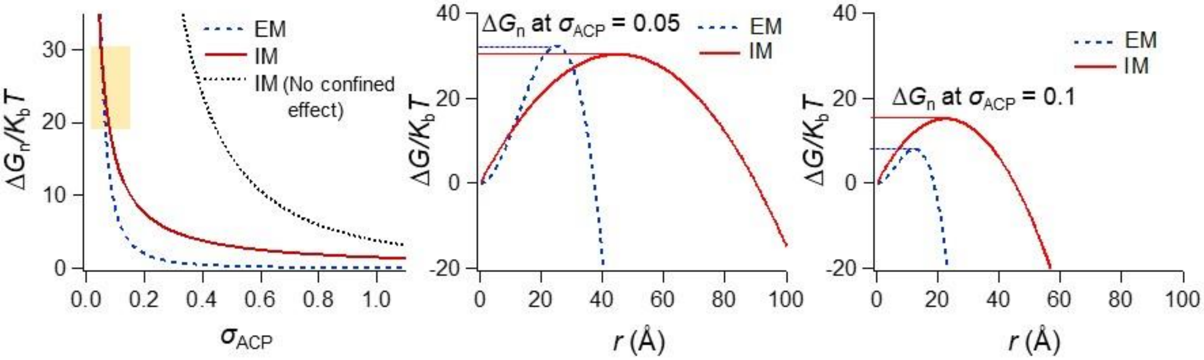

Figure 3.5 Energy barriers to ACP nucleation at different σ_{ACP}. (a) ΔG_n for three different nucleation models: unconfined nucleation without pAsp (representing extrafibrillar mineralization, EM), confined nucleation with pAsp (representing intrafibrillar mineralization, IM), and unconfined nucleation with pAsp (IM with no confined effect). (b,c) ΔG profiles at σ_{ACP} = 0.05 and 0.1 (yellow box in Figure 3.5a)

When the plate-like CaP nucleus is confined to finite thickness, h, its edge surfaces can have a convex curvature, $r = \frac{h}{2}$. The increased solubility of the confined CaP mineral compared to its bulk property can be calculated using the modified Kelvin equation, $\frac{S_r}{S_0} = \exp(\frac{2\alpha V}{RTr})$,[56] where S_r and S_0 are the solubility in confined space and the solubility of bulk, respectively. V is the molecular volume in m^3 mol^{-1}, and R is the gas constant. With a strong wettability of the nucleus or chemical affinity toward the confining walls, the nucleus would have concave edges.[57,112] Then, the Kelvin equation reads $\frac{S_r}{S_0} = \exp(-\frac{2\alpha V}{RTr})$ for negative curvature $-r$. According to the Kelvin equation, the confinement increases solubility by 3% with a convex curvature and decreases it by 2% with a concave curvature (Figure 3.6). The decreased solubility of CaP with a concave edge contributes to reducing ΔG_n and facilitating 2D crystallization in the confined space (Figure 3.7).

For convex edges, the contribution of increased solubility to ΔG_n is not significant, and therefore, confined nucleation is still preferred over nucleation without confinement.

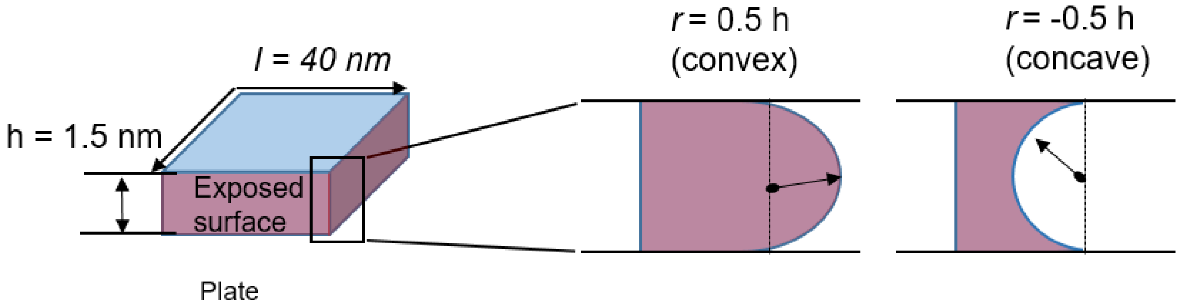

ΔG	$4\pi r^2\alpha - \frac{4}{3}\pi r^3 \frac{RT}{V} ln(\frac{S_r}{S_0})$
$\frac{\Delta G}{dr}$	$8\pi r\alpha - 4\pi r^2 \frac{RT}{V} ln\left(\frac{S_r}{S_0}\right)$
ΔG_n (at $\frac{\Delta G}{dr} = 0$)	$\frac{S_r}{S_0} = \exp(\frac{2\alpha V}{RTr})$
Fraction of exposed surface area	$f = \frac{2lh}{2l^2+4hl}$
Solubility of confined nuclei	$S = S_0(1-f) + S_r f$
$\frac{S}{S_0}$	1.03 (Convex, $r = 0.5$ h)
	0.98 (Concave, $r = -0.5$ h)

Figure 3.6 Exposed surface model to evaluate the solubility of plate-like CaP nucleus in a confined space, using the Kelvin equation. The model assumes that the Kelvin effects on the overall solubility of the nucleus is proportional to the fraction of the plate-like nucleus' surface exposed to the SBF solution. In addition, the two exposed edge surfaces of the plate-like CaP nucleus (red faces of plate; also refer to our confined model in Figure 3.1b) are affected by the Kelvin effect, and because of the curvature created on these surfaces by the confinements (either convex or concave), we can utilize the Kelvin equation for spherical particles.

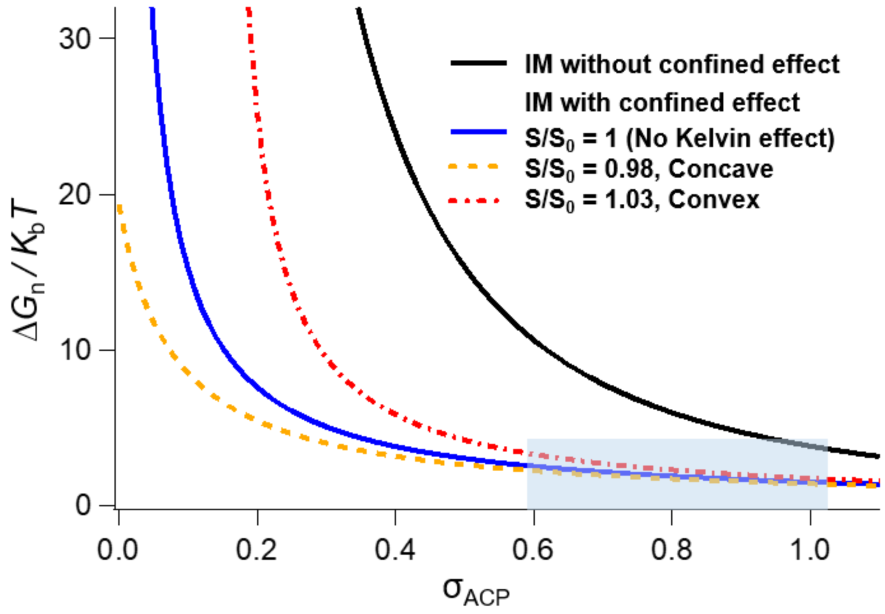

Figure 3.7 Energy barrier, Δ*G*n to amorphous calcium phosphate (ACP) nucleation for intrafibrillar mineralization (IM) at different σ under the influence of the Kelvin effect. The blue highlighted box indicates the experimental range of σ_{ACP} (See also Table 3.1).

By evaluating an IM model with no confined effect, we clearly demonstrate that the confined collagen structure contributes further to reducing the nucleation energy barrier. We assumed that nucleation occurs in the presence of pAsp (using α_{ACP} for IM), but without consideration of the confined collagen geometry (unconfined model). $\Delta G_{n,IM}$ was smaller than ΔG_n for the unconfined IM model ($\Delta G_{n,unconf}$) over the entire σ_{ACP} range, and the difference became larger at lower σ ($\Delta G_{n,unconf} / \Delta G_{n,IM} = \frac{16\pi v_m \alpha_{IM}}{3hK_bT\sigma} = 2.5/\sigma$, Figure 3.5a). We also evaluated α values based on the HA nuclei assumption (α_{HA} = 267 ± 27 (IM) vs. 58 ± 8 (EM) mJ m^{-2}, Figure 3–S4). ΔG profiles for the three cases (EM, IM, and unconfined IM) are shown in Figure 3–S5.

3.5 Discussion

In previous studies, collagen has been examined as a substrate promoting the formation of calcium phosphate crystals via heterogeneous nucleation.[8,11,26] However, the promoted nucleation by collagen is somewhat contradictory to other studies, which suggest that a nucleation inhibitor is required for *in vitro* mineralization in gap regions.[27,99] Our evaluation of ΔG_n for three different scenarios provides a thermodynamic explanation for how the nucleation inhibitor and confined collagen gap combine to drive IM. Without pAsp, EM is the preferred pathway for CaP nucleation over a wide σ range. pAsp is a strong regulator, preventing undesirable nucleation in the extrafibrillar space by increasing α. In an environment where pAsp (or other nucleation inhibitors) are present, nuclei seek nucleation sites with a lower energy barrier. The confined collagen gap region provides such sites for nuclei because the space effectively reduces ΔG_s by minimizing the effective surface area of nuclei.

By separately evaluating the α values for EM and IM, for the first time, we report that this value varies significantly depending on the nucleation site. The α_{HA} values provided by previous studies (90 mJ m^{-2} by Habraken *et al*.[8] and 105 mJ m^{-2} by Koutsoukos and Nancollas,[40] with no distinction between EM and IM) were approximately in the middle of the range of values that we obtained (58 and 267 mJ m^{-2} for EM and IM). Thus, the current approach can be used to identify the contributions of EM and IM in different biomimetic environments, providing new insights into biomaterials with multi-scale pore structures.

The findings can also help identify important mechanisms governing biomineralization, although with significant uncertainties due to the complexity of physiologic systems. The uncertainty is exaggerated for ACP, whose physicochemical properties remain unclear. The α_{ACP} values evaluated in this study are lower (5 and 19 mJ m^{-2} for EM and IM) than in the previous study by Habraken *et al*.[8] (40 mJ m^{-2} for heterogeneous nucleation on a collagen-coated substrate, assuming hemispherical nuclei). Their study used *in situ* atomic force microscopy (AFM) to determine nucleation rates, which could not distinguish between IM and EM, and thus did not account for the confinement in collagen structures. Because AFM is a surface technique, this study might probe mainly the EM on the surface. The complexities of the ionic compounds found in SBF solutions (which would notably be even more complex in physiologic systems) can also influence α. Ionic components, such as Mg^{2+} and HCO_3^-, can make SBF solutions more favorable to forming ACP, although they do not change the σ of the solutions significantly.[91]

To better evaluate the complexity of the physiological system, the roles of NCPs in collagen mineralization should be also carefully examined in future studies. For example, mineralization of collagen may be decreased when NCPs are removed.[113] A recent immunocytochemistry study showed that osteocalcin was present in both gap and overlap regions, while bone sialoprotein was located only at the surface of or outside type I collagen of gastrocnemius tendons extracted from turkeys.[48] Therefore, the type(s) of NCPs and their spatial distributions within or near collagen fibrils may influence calcium phosphate deposition by altering the sequence of amino acid side changes at the nucleation sites.[107] A better understanding of the NCP distributions would provide important insight into how organisms control mineral deposition to meet the specific requirements of mineralized tissues while using the same template, type I collagen. In the current study, we used an idealized model system to simulate one specific role of NCPs: pAsp was added to prevent nucleation of mineral in the bulk solution and allow nucleation of mineral in the confined collagen fibril spaces. This approach allowed us to determine the interfacial energy relationship of the IM-dominant system without the complications that would arise from the use of NCPs, which may have multiple functions during mineralization.

In this study, we evaluate CaP nucleation in the collagen gap regions where the equilibrium CaP solubility is influenced by the confinement. The confinement can also affect other physicochemical properties of CaP and fluid. Based on the literature, these potential differences in the materials' properties in the confined spaces are expected to make the energy barrier for IM even smaller than we estimated.[8,47,107,114] For example, the value of α might be particle size-dependent, and the height of plate-like nuclei is more likely in a range where α is decreasing from the value at its bulk phase.[8,114] Therefore, a smaller ΔG_n is expected if the particle size-dependency is properly considered. It is known that decreasing particle size influences α through two opposing factors: The presence of high-energy sites can increase α, but the structural similarity of the surface and interiors of nanoparticles may decrease it.[114] Although not experimentally proven yet for bioapatite, Habraken *et al*. suggested that a decreasing pattern of α would be valid for nuclei smaller than 3 nm in radius.[8] In our study, the height of plate-like nuclei measured by SAXS was 1.5 nm, and the critical nucleus size for HA nuclei was calculated as less than 1 nm at σ_HA = 22.7 (body plasma condition, Figure 3–S4). Another recent study calculated that the water density in the collagen gap regions was only about 0.7 g cm^{-3}, which would similarly benefit CaP nucleation in this region by reducing the enthalpic penalty for ion desolvation.[107]

By combining *in situ* SAXS measurement and thermodynamic evaluation using CNT, this study clearly shows that collagen fibrils provide nucleation sites for IM with a reduced nucleation energy barrier. These findings provide new insight into bone mineralization occurring in the complex fibrillar collagen structure within a confined space and driven by extracellular proteins. Collagen fibrils were confirmed to play a significant role in biomineralization by controlling nucleation pathways and energy barriers; they do not therefore serve as passive templates.

3.6 Acknowledgments

We acknowledge Dr. Jill Pasteris, Dr. Alix C. Deymier, Dr. Guy Genin, and Dr. Tyrone Daulton for helpful discussions. We thank Prof. James Ballard for carefully reviewing the manuscript. The project was supported by the National Science Foundation (DMR-1608545 and DMR-1608554). The Nano Research Facility and the Institute of Materials Science & Engineering at Washington University in St. Louis provided their facilities for the experiments. Use of the Advanced Photon Source (sectors 12-ID-B and 11-ID-B) at Argonne National Laboratory was supported by the U.S. Department of Energy, Office of Science, Office of Basic Energy Sciences, under Contract No. DE-AC02-06CH11357.

3.7 Supporting information for Chapter 3

3.7.1. Comparison of different confined nucleation models

To evaluate the nucleation energy barrier to intrafibrillar mineralization, classical nucleation theory was applied to the confined nucleation (Table 3.1 and Figure 3.1 in the main text). In this model, we assumed a plate-like nucleus initiated at a corner of the confined gap region of the collagen (two surfaces exposure model, 2M). By comparing this model with other possible scenarios, we found that nucleation energy barrier (ΔG_n) is independent of the morphology nucleus or the effective surface area exposed to the solution, if the top and bottom of the surfaces are confined. As shown in Figure 3–S1, we considered two other possible models: a plate-like nucleus with three surfaces exposed to the mineralization solution (3M), and a disc-like nucleus with a rounded surface (RM). Due to the different geometries of nuclei, ΔG_n for each model has different terms. However, all three models are built based on the confined system leading to a two-dimensional growth, and they show the same relationship between nucleation rate (J) and supersaturation (σ): $\ln(J) = \ln(\mathrm{A}) - B/\sigma$. In this linear relationship, the difference in the morphology and effective surface area of the nucleus are incorporated in the slope term, B. The interfacial energy between the effective surfaces and solution, α, for the three models were reversely related to their effective surface area (ESA).$\mathrm{ESA}_{2\mathrm{M}} : \mathrm{ESA}_{3\mathrm{M}} : \mathrm{ESA}_{\mathrm{RM}} = 1 : 3/2 : \pi$

$$\alpha_{2\mathrm{M}} : \alpha_{3\mathrm{M}} : \alpha_{\mathrm{RM}} = 1 : (4/9)^{1/2} : (1/\pi)^{1/2} = 1 : 0.667 : 0.564$$

However, the decrease in α values was fully compensated for by the increased ESA. Consequently, ΔG_n for the three models has the same value.

$$\Delta G_{\mathrm{n,2M}} : \Delta G_{\mathrm{n,3M}} : \Delta G_{\mathrm{n,RM}} = (\alpha_{2\mathrm{M}})^2 : 9/4\,(\alpha_{3\mathrm{M}})^2 : \pi\,(\alpha_{\mathrm{RM}})^2 = 1 : 1 : 1$$

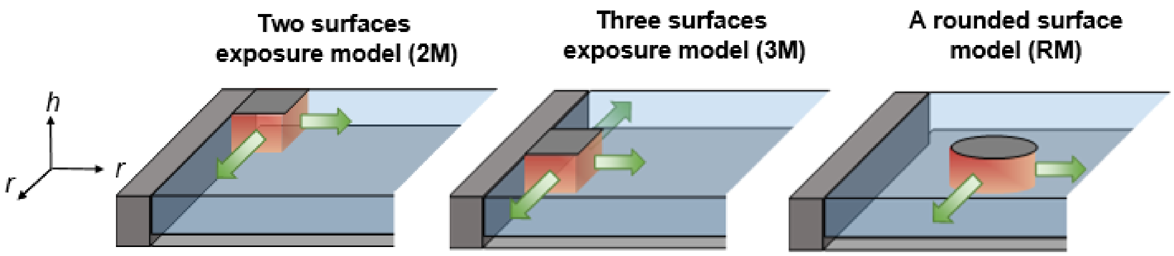

	2M	**3M**	**RM**
Morphology of nucleus	Plate (constant *h*)	Plate (constant *h*)	Disc (constant *h*)
Effective surface area exposed to solution	$2rh$ (two edge surfaces)	$3rh$ (three edge surfaces)	$2\pi rh$ (one edge surface)
Volume	r^2h	r^2h	πr^2h
$\Delta G = \Delta G_b + \Delta G_s$	$-\left\{\frac{[r^2h]}{v_m}\right\}k_BT\sigma + 2rh\alpha$	$-\left\{\frac{[r^2h]}{v_m}\right\}k_BT\sigma + 3rh\alpha$	$-\left\{\frac{[\pi r^2h]}{v_m}\right\}k_BT\sigma + 2\pi rh\alpha$
r_c (at $d\Delta G/dr = 0$)	$\frac{v_m\alpha}{k_BT\sigma}$	$\frac{3v_m\alpha}{2k_BT\sigma}$	$\frac{v_m\alpha}{k_BT\sigma}$
ΔG_n (at $r = r_c$)	$\frac{hv_m\alpha^2}{k_BT\sigma}$	$\frac{9hv_m\alpha^2}{4k_BT\sigma}$	$\frac{\pi hv_m\alpha^2}{k_BT\sigma}$
$J =$ A exp $(-\Delta G_n / k_BT)$	$A\exp(-\frac{hv_m\alpha^2}{k_B^2T^2\sigma})$	$A\exp(-\frac{9hv_m\alpha^2}{4k_B^2T^2\sigma})$	$A\exp(-\frac{\pi hv_m\alpha^2}{k_B^2T^2\sigma})$
ln(*J*)	$\ln(A) - B\frac{1}{\sigma}$ $B = (\frac{hv_m\alpha^2}{k_B^2T^2})$	$\ln(A) - B\frac{1}{\sigma}$ $B = (\frac{9hv_m\alpha^2}{4k_B^2T^2})$	$\ln(A) - B\frac{1}{\sigma}$ $B = (\frac{\pi hv_m\alpha^2}{k_B^2T^2})$
α	$(\frac{Bk_B^2T^2}{hv_m})^{\frac{1}{2}}$	$(\frac{4Bk_B^2T^2}{9hv_m})^{\frac{1}{2}}$	$(\frac{Bk_B^2T^2}{\pi hv_m})^{\frac{1}{2}}$

Figure 3–S1 Comparison of interfacial energy relationships for confined nucleation models with different exposed surfaces. The free energy change per molecule (ΔG) is the sum of the bulk and surface energy terms (ΔG_b and ΔG_s, respectively). A typical ΔG profile shows a maximum (i.e., energy barrier, ΔG_n) at a critical radius (r_c). *r* and *h* are the length and height of nuclei. For the volume per molecule of nucleus, v_m, 5×10^{-23} cm^3 and 2.63×10^{-22} cm^3 are used for ACP[8] and for HA,[103] respectively. k_B is the Boltzmann constant (1.38×10^{-23} J K^{-1}). *T* is the temperature of the reactor (310 K). σ is the supersaturation ($\ln(IAP/K_{sp})$), where *IAP* is the ion activity product and K_{sp} is the solubility product. α is the interfacial energy between nuclei and solution.

3.7.2. Intra- and Extrafibrillar Mineralization Controlled by pAsp

Without pAsp, spherical particles at the outer surface of fibrils were observed on collagen films mineralized in both 2.65× and 2.85×SBF solutions, as shown in scanning electron microscope (SEM) images (Figure 3–S2c,d). In 2.65×SBF, relatively small spheres (Figure 3–S2c, radius, $r = 67.1 \pm 13.4$ nm) were observed at extrafibrillar collagen spaces, showing a low Ca/P molar ratio of around 1.05 as analyzed by energy-dispersive x-ray spectroscopy (EDX). The rough surface texture also indicated that these spheres were aggregates of smaller primary particles (Figure 3–S2c, inset). In 2.85×SBF, microscale aggregates of thin crystals were more frequently observed at the extrafibrillar spaces after 11 hr of mineralization (Figure 3–S2d). These aggregates showed an increased Ca/P molar ratio = 1.62 (Figure 3–S2d, inset). These properties of extrafibrillar spheres formed without pAsp correspond well to an early stage of CaP development under a pathway involving aggregation of prenucleation clusters, which has been observed in environments without nanoscale confinement.[8,26,99] The increase in the Ca/P molar ratio is one characteristic of this pathway, which shows a transition from 0.67 to 1.67 during the transformation from amorphous spheres to aggregates of apatite plates.[8] In all SBF solutions, no P signals were detected from collagen fibrils surrounding extrafibrillar spheres until 18 h, so we excluded the possibility of intrafibrillar mineralization during the *in situ* SAXS measurements for all SBF solutions in the absence of pAsp.

On the other hand, with 10 mg l^{-1} pAsp, collagen fibrils showing clear Ca and P signals (Ca/P atomic ratio of 1.35 and 1.37) were observed in 2.65× and 2.85×SBF solutions, respectively (Figure 3–S2e,f). The periodic banding patterns (~67 nm, Figure 3–S2a,b) disappeared with mineralization by the deposition of bioapatite crystals, which aligned perpendicular to the bands of fibrils.[27] The Ca/P molar ratio obtained from intrafibrillar-mineralized fibrils was relatively constant, at around 1.35, which is somewhat lower than the theoretical value for hydroxyapatite (1.67). Similar Ca/P molar ratios, mainly due to CaP phase transformation from amorphous to crystalline, have been reported for early stage development of intrafibrillar mineralized fibrils.[47,99] With 10 mg l^{-1} pAsp, we did not observe any aggregated extrafibrillar particles of larger size (as shown in Figure 3–S2c,d) in all SBF solutions. Therefore, we assumed that the influence of extrafibrillar mineralization is not significant in the presence of pAsp.

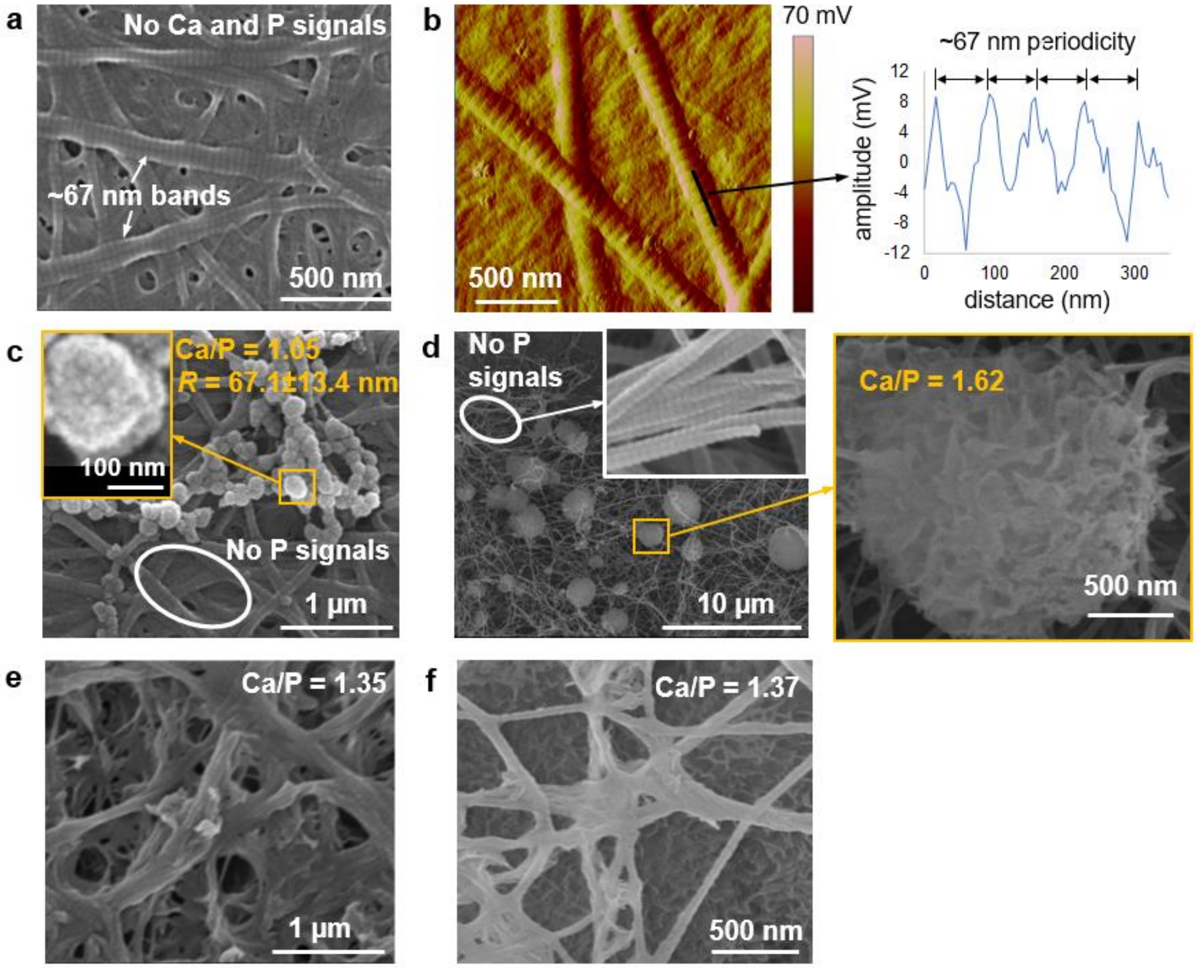

Figure 3–S2 (**a**) Unmineralized collagen thin film imaged by scanning electron microscopy. (**b**) Analysis of unmineralized collagen fibrils using atomic force microscopy. (**c-f**) Scanning electron microscopy images of thin collagen films after mineralization. (**c**) 2.65xSBF without pAsp for 18 h. (**d**) 2.85xSBF without pAsp for 11 h. (**e**) 2.65xSBF with 10 mg l^{-1} pAsp for 14 h. (**f**) 2.85xSBF with 10 mg l^{-1} pAsp for 12 hr. Ca/P molar ratios were analyzed with energy-dispersive X-ray spectroscopy.

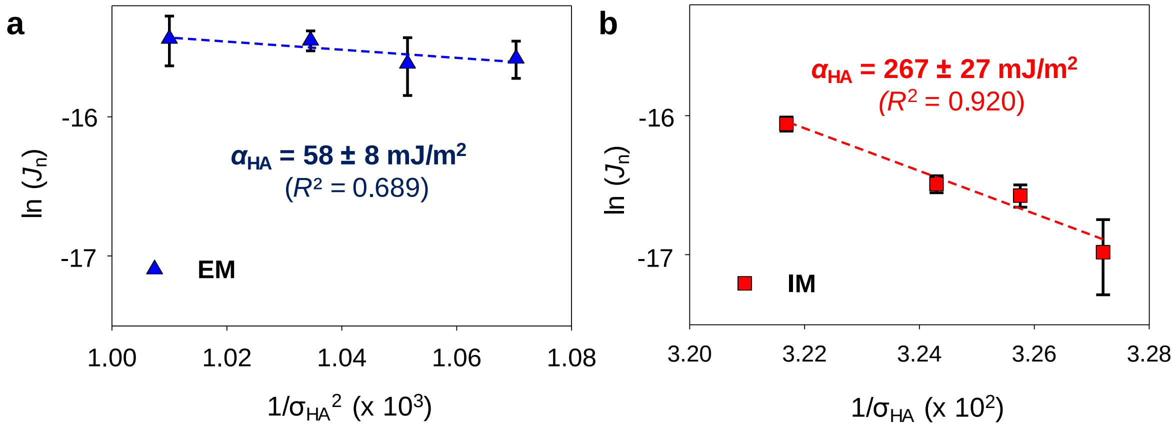

Figure 3–S3 Interfacial energies for HA nucleation, α_{HA}, during EM (a) and IM (b). Error bars in the symbols indicating ln(J) are standard errors of the estimates, obtained from the regression between Q and time (from Figure 3.4a,b in the main text). Error ranges for α_{HA} values for EM and IM are standards errors of the estimates for regressions between ln(J) and $1/\sigma^2$, and between ln(J) and $1/\sigma$, respectively.

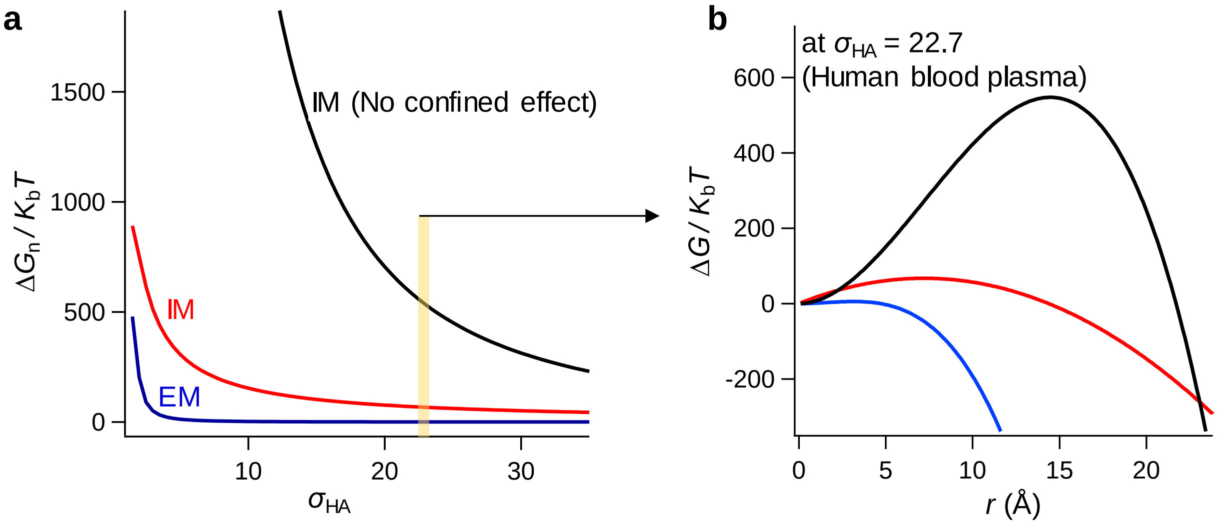

Figure 3–S4 Energy barriers to HA nucleation at different σ_{HA}. (**a**) ΔG_n for three different nucleation models: Unconfined nucleation without pAsp (representing extrafibrillar mineralization, blue line), confined nucleation with pAsp (representing intrafibrillar mineralization, red line), and unconfined nucleation with pAsp (IM calculation with no confinement effect, black line). (**b**) ΔG profiles at σ_{HA} = 22.7, which corresponds to human blood plasma (yellow bar in Figure 3–S4a).

Chapter 4. Consequence of Nanoscale Nucleation in Mechanical Properties: Effects of Cyclic Strain on Collagen

4.1 Overview

The nucleation and crystallization of CaP in collagen is important for bone mineralization because these behaviors critically determine mechanical properties of bones, such as its elastic modulus and toughness. In this chapter, we examine how early stage nucleation behaviors affect mineralization patterns in collagen matrix, and their consequent influence on mechanical properties. While CaP nucleation is essential for bone's mechanical properties, mechanical loading exerted on bone significantly influences CaP nucleation, due to the adaptive response of bone. Although it is commonly believed that moderate exercise enhances bone strength, little is known about how cyclic strain from external loading influences the physicochemical responses of collagen during mineralization.

Here, we show that, compared to the static strain condition, cyclic strain increases acellular nucleation rates by 33% in highly-organized fibrillar collagen matrices. The transport of mineralization fluids by cyclic strain delivers nucleation precursors to the inner surface of the matrix effectively. The inner matrix bioapatite formed under cyclic strain increases the elastic modulus, strength, and resilience more effectively than minerals poorly bonded to collagen surfaces. The results suggest that the spatial distribution of minerals determines tissue-level mechanical properties more critically than the total mineral contents, and that the distribution can be effectively engineered by utilizing cyclic strain. By linking nano- and macro-scale observations with tissue-level mechanical properties, our findings provide new insights into designing biomaterials.

4.2 Introduction

Bones are hierarchical structures that consist mainly of an organic fibrillar template, inorganic mineral, and cells[61]. Collagen, the primary extracellular protein in bone, provides the fibrillar template for bioapatite mineral (an analog of HA).[2,6,115] The nanoscale through microscale organization of collagen fibrils and bioapatite crystals determines the tissue-level mechanical behavior of bones.[2,9,10,33] For example, bovine leg bones have relatively high concentrations of mineral to support high body weight, whereas the high porosity in deer antlers makes them advantageously light and flexible.[64,116] The biologic control of collagen mineralization has been extensively studied, and is largely dictated by, osteoblasts and osteoclasts, which form and resorb bone, respectively.[61] When mineralization is complete, osteoblasts become entrapped by the mineralized collagen matrix and fully differentiate into mature bone cells called osteocytes; these cells are then interconnected by channels called canaliculi, allowing them to communicate with each other to control tissue-level bone properties.[6]

Physiologic mechanical loads are known drivers of bone formation and remodeling[117]. For example, mechanical loading from physical activity increases bone mineral density in young children[118], while reduced mechanical loading from microgravity conditions during space flight decreases the bone mineral density of astronauts[119]. Mechanobiology studies have shown that cells respond to strain-mediated fluid flow under natural cyclic loading environments[120] to increase bone formation rates.[121,122] Piekarski and Munro first suggested that deformations of bones caused by mechanical loading generate fluid flow, thereby promoting nutrient delivery to the osteocytes and removing their waste products.[123] Later studies showed that bone cells response sensitively to fluid shear stress,[120] leading to increased intracellular calcium in bone cells[124] and inhibition of osteoclast formation,[125] and hence to bone formation.

In addition to cell-driven mineralization, recent studies have also emphasized physicochemically-driven mineralization independent of cells.[27,32,47,99,126] For example, Wang *et al*. showed *in vitro* formation of bone-like mineral without any cell activity or non-collagenous proteins[47]. Based on *in situ* observations and a modified version of classical nucleation theory, our previous study revealed that the physical geometry of the collagen gap regions could significantly reduce nucleation energy barriers to intrafibrillar mineralization, emphasizing a more active role for collagen, which previously had underestimated compared to biological factors.[126] Although these findings illuminated acellular bone mineralization mechanisms, it remains unclear if mechanical loading also affects acellular strain-induced mineralization.[120,127,128]

In the current study, we investigated the influence of cyclic strain on the mineralization of densely-packed and highly-organized collagen matrices. We determined the nucleation rates and changes in crystallization of calcium phosphate (CaP) minerals during *in situ* mineralization, using SAXS and WAXD. Our findings showed that, compared to static loading or control (unloaded) conditions, cyclic strain leads to faster nucleation rates with deeper matrix mineralization through increased transport of mineralization fluid. These changes in mineralization patterns led to higher matrix elastic moduli than predicted by a traditional model based on the total mineral volume fraction, highlighting microscale mineral distribution as a key contributor to mechanical properties at the tissue-level. By showing enhanced mineralization and elastic moduli of collagen matrices under cyclic loading, we highlight a new acellular role for physiologic loading in bone health. The findings underscore the importance of mimicking dynamic human motions in designing improved hierarchical biomaterials.

4.3 Materials and Methods

4.3.1 Preparation of Collagen Samples

Tibia bones were separated from fresh chicken legs obtained from local grocery stores. Top and bottom metaphysis and epiphysis of the bones were removed from the tibia using a diamond saw. The soft tissues, bone marrow, and blood were also carefully removed, leaving hollow-shaft like bones. The bone shafts were demineralized in ethylenediaminetetraacetic acid (EDTA) solution (0.1 M, pH 7.4) for 3 weeks under magnetic stirring (130 rpm) at room temperature. The solution was replaced every 2 days. After the demineralization process, soft collagen parts of the bones remained, still in their original shape, and were cut in half longitudinally using scissors. The half-tubular demineralized bones were sectioned on a freezing stage (Physitemp BFS-30MP) using a sledge microtome (Leica 1400) to obtain thin and flat collagen samples with thicknesses < 1mm. Using a razor blade, collagen samples were cut in a uniform shape 0.5 cm wide × 3 cm long for further experiments. The thickness of each sample was measured accurately using a laser scanner (LJ-V700-1, Keyence).

4.3.2 Preparation of Mineralization Solution

Deionized water ($\geq$ 18.2 MΩ-cm), obtained from Barnstead Ultrapure Water System (D11931, Thermo Scientific) and American Chemical Society grade chemicals were used for mineralization. We prepared two separate solutions, containing either calcium (1.838 g L^{-1} of $CaCl_2 \cdot 2H_2O$, Alfa Aesar) or phosphate (1.14 g L^{-1} of $K_2HPO_4 \cdot 3H_2O$, Alfa Aesar) to prevent any precipitation of calcium phosphate minerals prior to the start of the experiment. To mimic major ionic compounds in human body plasma (Gamble, 1967), both solutions contained NaCl (7.996 g L^{-1}, BDH Chemicals), $NaHCO_3$ (0.350 g L^{-1}, BDH Chemicals), KCl (0.224 g L^{-1}, BDH Chemicals), $MgCl_2 \cdot 6H_2O$ (0.305 g L^{-1}, EMD Millipore), 1 M HCl (40 ml L^{-1}, BDH Chemicals), Na_2SO_4 (0.071

g L^{-1}, Alfa Aesar), and tris(hydroxymethyl)aminomethane (Tris, 6.057 g L^{-1}, Alfa Aesar). The solution pH was adjusted to 7.4. In addition, polyaspartic acid (10 mg L^{-1}, sodium salt, MW: 5,000 Da, LANXES) and sodium azide (0.2 g L^{-1}, Amersco) were added to both solutions. Sodium azide was used to minimize any influence caused by microbial activities. In our previous studies, 10 mg L^{-1} pAsp was shown to aid intrafibrillar mineralization of collagen while inhibiting undesirable extrafibrillar mineralization or homogeneous calcium phosphate nucleation in solution[99,126]. Equal volumes of the two solutions were used as the mineralization solution, which provided 2.5× higher calcium and phosphate concentrations than in human body plasma (2.5× SBF, Table 4–S1)[85]. The increased concentrations of these two nucleation precursors allowed us to conduct the experiments within a reasonable time and without significant loss by homogeneous nucleation in solution. Before mixing, the two separate solutions were stored in an incubator at 37°C; after mixing the mineralization solution was maintained at 37°C using a hot plate during mineralization. Fresh solutions were replaced every two hours to minimize changes in concentrations of ionic compounds and pH.

4.3.3 *In situ* X-ray Data Collection during Collagen Mineralization under Strain Conditions

To mineralize collagen samples under strain conditions, we built a stainless steel holder (Figure 4–S1a). During mineralization up to 10 hours, the holder, containing two collagen samples, was placed in 130 mL of the mineralization solution (Figure 4–S1b). This holder was connected to a customized motor-driven BiSlide module (Velmex, Inc.) to control the strain during mineralization. A 3% cyclic strain condition at 0.5 Hz was applied to the collagen samples, mimicking repetitive physiologic weight-bearing forces. In most animal bones, a typical peak functional strain is about 0.2–0.3% ;[129,130] however, the mechanical stresses are amplified significantly in soft-tissue where mineralization is initiated.[131] In this environment, approximately

7% strain can be applied to osteoblasts[129,132]. Samples under static 3% strain and zero strain were separately evaluated for comparison. To collect *in situ* X-ray data, mineralization was conducted at the Advanced Photon Source (APS) at Argonne National Laboratory (Argonne, IL, USA).[11,83,133] Every 2 hours during mineralization, the collagen-loaded sample holder was detached from the BiSlide module and then moved to a specially designed sample stage at Sector 12 ID-B for SAXS measurements (Figure 4–S1c), after which the holder was promptly re-attached to the module for further mineralization. During each measurement, the mineralization reaction was interrupted for less than 5 minutes. The same experiments were repeated for WAXD at Sector 11 ID-B. The procedures for SAXS/WAXD data collections and analyses are described in Section 4.7.1 in detail.

4.3.4 *Ex situ* Imaging

Collagen matrices were fixed in 100 mM cacodylate buffer containing 2% paraformaldehyde and 2.5% glutaraldehyde. The matrices were rinsed in a cacodylate buffer solution and then fixed with 1% osmium tetroxide in the buffer solution for 1 h. After dehydration in successive ethanol baths, samples were embedded in epoxy resin and thin sections were prepared using an ultramicrotome. Uranyl acetate and Reynold’s lead citrate were used for staining before the analysis. Afterwards, the stained sections were imaged using a transmission electron microscopy (JEOL 1200 EX II).

Confocal microscope (ZEISS LSM880) images were obtained from different confocal sections of collagen matrices with 3 µm steps. Samples were exposed to different strain conditions in phosphate buffer saline (PBS) containing 2% of PicroSirius Red F3BA stain solution (Polysciences, Inc) for 10 hr, then rinsed with pure PBS before the confocal imaging.

4.3.5 Mechanical Testing

Uniaxial tensile testing was conducted at the Musculoskeletal Soft Tissue Lab, Washington University in St. Louis. Collagen matrices mineralized under different strain conditions for 10 hr were loaded in a custom mechanical testing machine. These samples were pulled in tension at a rate of 1% elongation per second until failure while tensile stress was monitored. The elastic moduli of the samples were obtained from linear regions of their strain-stress curves.

4.3.6 Statistical Analyses

Quantitative data are given as mean ± standard deviation, and error bars in the bar graphs represent standard errors. The variable n indicates the number of samples analyzed. Neither the experiments nor the outcomes were blinded during the study. Statistical differences were determined using one-way ANOVA with the Tukey HSD post-hoc test with significance considered as $p < 0.05$ (R ver. 3.2.0). We used two-way ANOVA to compare the elastic moduli, strength, and resilience of collagen matrix mineralized in PBF and SBF under different strain conditions.

4.4 Results & Discussion

4.4.1 Nucleation and Crystallization Characteristics during *In situ* Collagen Mineralization

Nucleation and crystallization of CaP minerals in collagen are necessary initial steps for bone mineralization.[27] To provide quantitative kinetic information on nucleation and crystallization,[11,83,133] SAXS and WAXD data were collected during *in situ* collagen mineralization. The setup was designed to test the effect of strain conditions on collagen mineralization in the following groups: 1) control (0% strain), 2) cyclic strain (3% peak strain applied at 0.5 Hz), and 3) static strain (3% strain). The peak physiologic strains experienced by typical mature, fully mineralized, animal bones range from 0.1 to 0.32%[129]; however, the strain levels in immature collagenous tissues at the onset of mineralization are likely an order of magnitude higher[131,134]. Therefore, in the current study, 3% cyclic strain was applied to collagen matrices to replicate the early stages of bone mineralization during development. The collagen matrices were prepared by demineralizing chicken tibias, thereby mimicking the density and alignment of collagen in mineralizing cortical bone[135]. The matrices were mineralized under three strain conditions using a modified simulated body fluid (2.5×SBF, Table 4–S1).

From the SAXS data, we observed that the number of newly formed particles increased over time after 4–6 hours in mineralization solution. The formation of nuclei appeared as increased SAXS intensities in a *q* range of 0.02–0.3 $Å^{-1}$, regardless of the applied strain (Figures 4.1a-c). The background—unmineralized collagen, intensity at 0 hr—subtracted patterns after this initial induction time were relatively uniform for all three conditions and fit well with a disc shape with a thickness of 1.5 nm (Figure 4.1d). This dimension is comparable to bioapatite crystals commonly observed in nature[9,73] and during *in vitro* mineralization.[8,99,126] The uniform shape of nuclei over time indicates that the increasing number of nuclei, not the growth of individual particles, was the dominant reason for the increasing SAXS intensities.[108]

The crystallization of nuclei during *in situ* collagen mineralization was also observed from WAXD measurements. A small peak at 1.83 $Å^{-1}$, indicating the HA (002) face, and a small shoulder at 2.25 $Å^{-1}$, indicating (211) and (112) faces of HA, developed in collagen matrices after 8 hr of mineralization (Figure 4.2a), which is slightly later than the induction time observed from SAXS (4–6 hr). Compared to fresh tibia bones, the development of bioapatite crystallinity, evidence of the early stage of collagen mineralization, continued to show weak peak intensities (Figure 4.2a). Background-subtracted WAXD patterns revealed the mineral crystalline structure as poorly crystalline hydroxyapatite (Figure 4.2b), typical of bioapatite from most animal bones.[6,136] Therefore, both SAXS and WAXD data confirmed that applied strain (cyclic and static) did not affect the morphology (plate-like shape) and crystallinity (poorly crystalline hydroxyapatite) of bioapatite formed during collagen mineralization at this early stage.

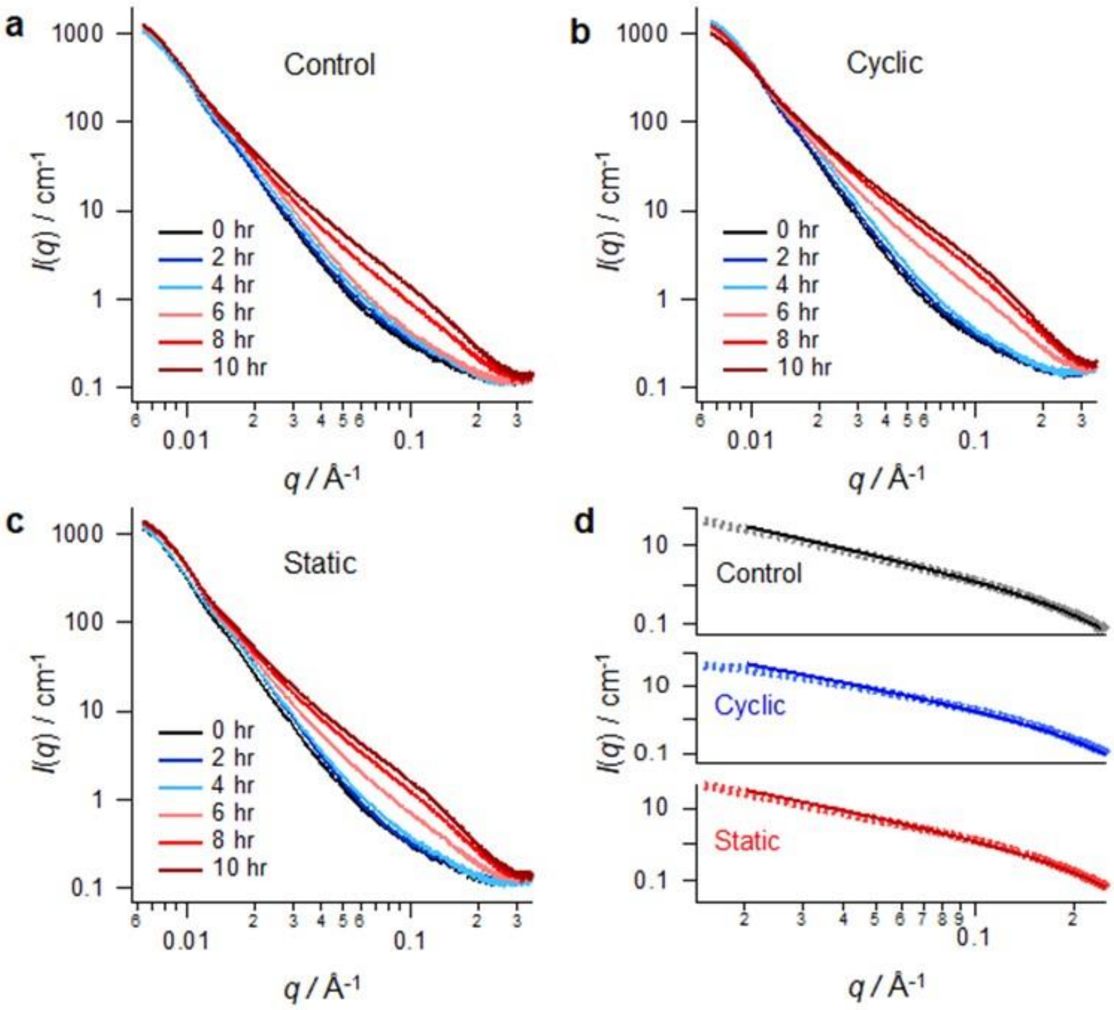

Figure 4.1 SAXS patterns from collagen during mineralization under different strain conditions. (**a-c**) Examples of *in situ* SAXS evolution of collagen samples during 10 hr of mineralization under control condition (**a**, with no strain), cyclic condition (**b**, 3% strain with 0.5 Hz frequency), and static condition (**c**, 3% static strain) conditions. (**d**) Background-(unmineralized collagen, data at 0 hr) subtracted SAXS patterns at 10 hr. The background-subtracted patterns (dotted lines) of all conditions are similar and fit the morphology of bioapatite plates (solid lines, 1.5 nm thick and 40 nm in diameter).

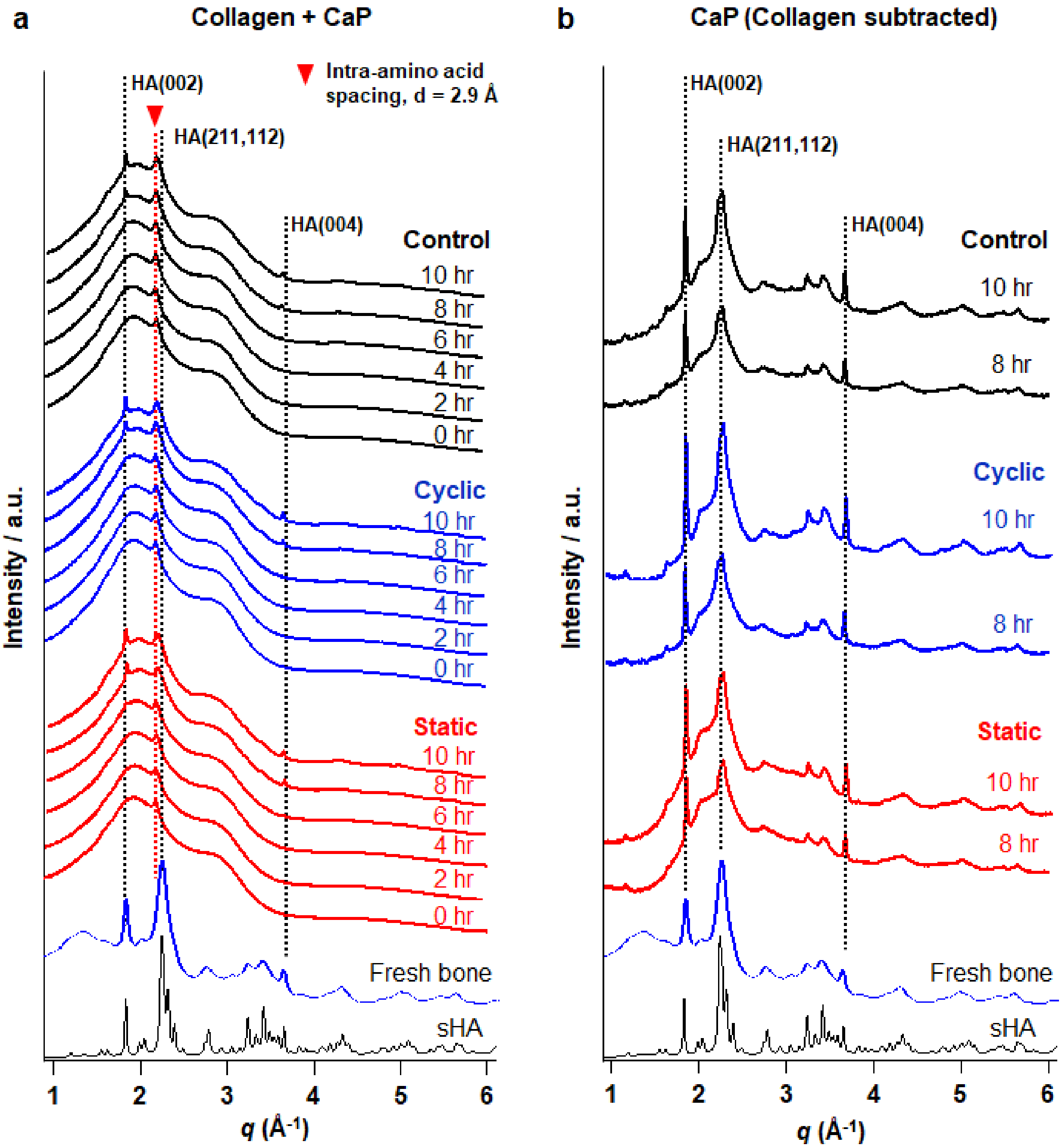

Figure 4.2 WAXD patterns from collagen during mineralization under different strain conditions. Patterns from a synthetic hydroxyapatite (sHA) sample and fresh tibia bone are shown for comparison. (**a**) Raw patterns showing diffraction from both collagen and bioapatite nuclei. (**b**) Background-subtracted patterns showing diffraction only from both bioapatite nuclei.

4.4.2 Cyclic Strain Enhances Calcium Phosphate Nucleation Rates and Matrix Elastic Moduli

Using the morphology and crystalline structure of the calcium phosphate nuclei determined from SAXS and WAXD data, we calculated the mineral nucleation rates and particle volume fractions in collagen matrices using the SAXS invariant value, $Q = \frac{1}{2\pi^2}\int I(q)q^2dq$[95,99]. This value indicates the total scattering amount, and thus could be considered as proportional to particle number concentration, $N_c = \frac{Q}{r_e^2\Delta\rho^2 V}$, when the particle morphology is uniform[17,90]. Here, r_e and V represent the classical electron radius (2.818 fm) and volume of an individual particle, respectively. $\Delta\rho$ is the difference in electron densities between HA and collagen ($\Delta\rho = 5.02\times10^{23}$ cm^{-3}, assuming particles were HA crystals surrounded by collagen molecules[78,99]). From the linear slopes of N_c vs. time plots, nucleation rates normalized to the scanning surface area were obtained for each sample (J_s). Representative results are shown in Figure 4.3a. The results from four different experiments (8 samples per strain condition, all SAXS data analyses are described in Section 4.7.2) showed that, compared to the zero strain condition, J_s under cyclic strain increased by 17% and J_s under static strain decreased by 13% (the difference in J_s between the cyclic and static strain conditions was statistically significant; Figure 4.3b).

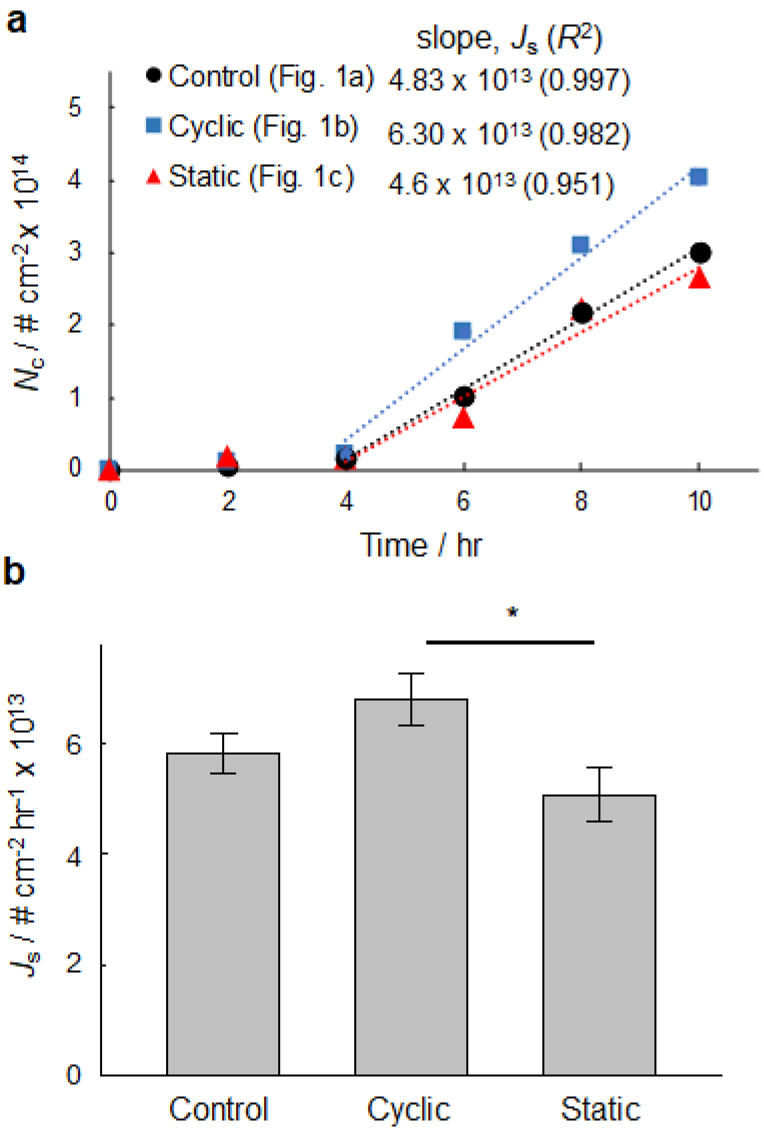

Figure 4.3 The influence of strain conditions on collagen mineralization. (**a**) Slopes of linear regions of number concentrations vs. time plots to evaluate nucleation rates of bioapatite plates (J_s, number of particles per scanning surface area per hour). The data in each plot were obtained from the one time in situ SAXS measurement shown in Figures 4.1a–c. (**b**) Mean and standard errors of Js during collagen mineralization under different strain conditions. Number of samples, $n = 8$ for each condition. * indicates a statistically significant difference ($p < 0.05$, one-way ANOVA with the Tukey HSD post-hoc test) for comparison under the bar.

The mechanical properties of collagen matrices mineralized under different strain conditions in SBF were analyzed and compared to the properties of matrices reacted in phosphate buffer saline (PBS), where no mineralization occurred (Figure 4.4a). Mineralization for 10 hr significantly increased the elastic modulus (E_m) and strength, as determined by two-way ANOVA ($p < 0.05$). Increased resilience by mineralization was also clearly observed ($p = 0.052$). In PBS, the differences in these properties by strain condition were not significant, indicating that neither cyclic nor static strain altered the mechanical properties. Therefore, the combination of mineralization and specific strain conditions determines the properties. Consistent with the increase in J_s, mineralization under cyclic strain increased the E_m of the matrices by 30.9% compared to matrices reacted in PBS under cyclic strain (Figure 4.4a). On the other hand, E_m was slightly higher after mineralization in SBF than in PBS for the control group. The increase in E_m for the static condition was not easily distinguished from unmineralized matrices. In addition to E_m, samples mineralized under cyclic strain showed the highest strength and resilience, and the control group also showed noticeable increases in both properties with mineralization (Figures 4.4b,c). However, the static strain condition does not change the strength and resilience during 10 hr of mineralization, unlike in native bones, where E_m, strength, and resilience all increased with mineralization.[65]

Yield strain was not influenced by either mineralization or strain condition. Because 3% strain is much lower than the yield strain and the strain was applied for only 10 hr before matrices became too brittle (i.e., decrease in yield strain),[65] there was no statistical difference in yield strain after 10 hr of reaction in PBS compared to SBF (20 ± 5% and 21 ± 4%, respectively, Fig. 4d).

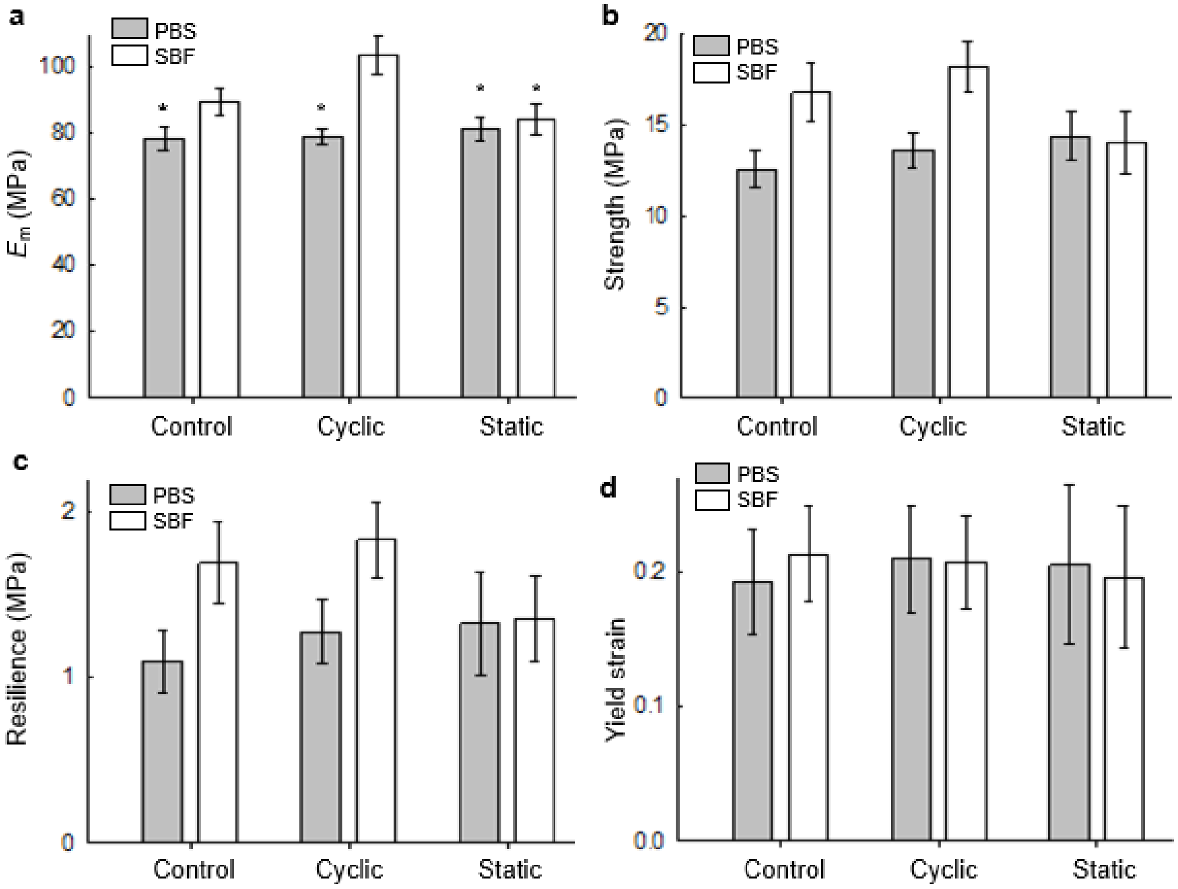

Figure 4.4 Tensile test results of collagen matrices. (**a**) Elastic modulus, E_m, (**b**) strength (**c**) resilience, and (**d**) yield strain. Collagen matrices experienced different strain conditions for 10 hours in PBS (no mineralization, $n = 8$ for each condition) and simulated body fluid (SBF, with mineralization, $n = 9$ for each condition). * indicates a statistically significant difference compared to cyclic-SBF system ($p < 0.05$, two-way ANOVA with the Tukey HSD post-hoc test).

4.4.3 Spatial Distribution of Bioapatite under Strain Conditions

There was no significant difference in the volume fractions of mineral (f_V) among the three strain groups after 10 hr of mineralization. The wide variations in f_v were caused by induction time and sample thickness (Figure 4–S6). These results contrast with the mechanical testing results, which showed that cyclic strain increased E_m more than the other two conditions. The implication is that mineral crystals formed under cyclic loading had morphologies and distributions within collagen matrices that differed from those of the other groups.[9,137,138] Thus, cyclic strain conditions can alter the availability of nucleation sites and subsequent deposition of mineral, leading to more effective increases in E_m, while simultaneously increasing J_s.

According to transmission electron microscopy (TEM) images of sample cross-sections along the long direction (Figure 4.5a), strain conditions affected the spatial distribution of mineral at the sub-micrometer scale, particularly at the surfaces of collagen matrices (Figure 4.5b–c). With f_V less than 1.4% after 10 hr of mineralization (a level that represents the early stages of bone mineralization), the mineralization depth from the outer surface was on the order of ~5 µm for all groups. The mineralization depth was highest in the cyclic strain group compared to the control and static strain groups (mineral demarcated between two dotted lines in bottom row of panels of Figure 4.5). Furthermore, under the control (unstrained) and static strain conditions, loose collections of plate-like minerals formed on the outer surfaces of the collagen matrices (noted by dotted circles in the bottom row of panels of Figure 4.5). Scanning electron microscopy with energy-dispersive X-ray spectroscopy (SEM-EDX) analyses supported the conclusion that a layer of minerals formed on the surfaces of collagen matrices in these groups (Section 4.7.3). This mineral layer is not expected to contribute mechanically to the collagen matrix, but it could act as a diffusion barrier, preventing mineralization of the inner portion of the matrix[99]. Notably, the lowest J_s was observed under static strain (Figure 4.3b), and a clearly negative correlation ($R^2 = 0.78$) was observed between f_V and sample thickness (Figure 4–S6f). The results indicate that the mineral layer created by static strain conditions acted as a diffusion barrier at the outer surface, decreasing J_s and limiting mineralization of the inner portion of the matrix. In contrast, cyclic strain shows higher J_s for thicker samples which have more interior space to allow mineralization (Figure 4.6b). Thus, the application of cyclic strain can be beneficial for mineralizing scaled-up collagen-based biomaterials.[43,47]

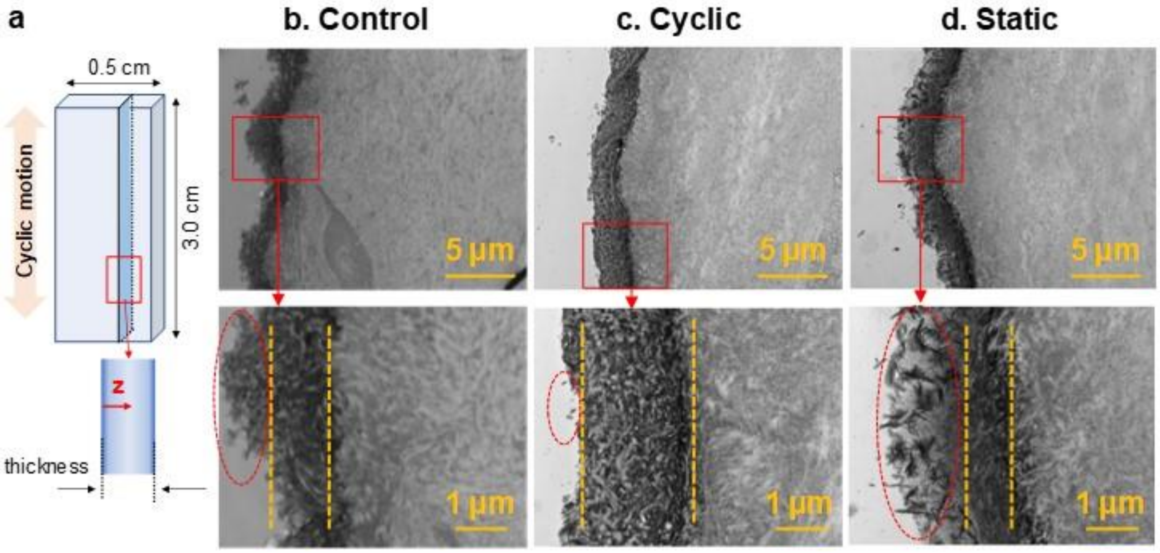

Figure 4.5 Cross-sectional images of collagen matrices. (**a**) Schematic illustration of sample geometry direction of cyclic loading and sectioning plane. (**b–d**) Transmission electron microscope images of cross sections. Bottom panels are higher magnification images of selected areas (red rectangles) from top panels. Dotted circles indicate bioapatite crystals at the outer surface of matrices, and highly mineralized inner matrix areas are indicated between two dotted lines in bottom figures.

4.4.4 Elastic Moduli Affected by Spatial Distribution of Bioapatite

Using a tissue-level model, we evaluated how effectively the bioapatite particles formed in collagen matrices under different strain conditions contribute to E_m. According to Smith *et al*. the relative increase in E_m with mineralization can be formulated by the following relation, where E_un is the elastic modulus of the unmineralized matrix.[139]

$$\frac{E_m}{E_{un}} = \exp(\mathrm{A}\, f_V(1-2f_\mathrm{d})) \qquad \text{(Eq. 4.1)}$$

This equation was derived from Teng's model describing nonlinear bimodular stiffness properties[140]. The effectiveness of particles in load transfer can be expressed as the fraction of debonded particles (f_d). A debonded particle, unlike an intact particle, poorly contacts the surface of the pores, and thus cannot transfer load within the matrix, negatively influencing E_m. Based on the study by Smith *et al.*, showing a decrease in E_m with the formation of poorly bonded apatite mineral in reconstituted collagen[139], it is assumed that E_m decreases when f_d in Eq. 4.1 is larger than 0.5. The constant A is determined by the ratio of the elastic moduli of the particle and the matrix.

We obtained A and f_d values by fitting Eq. 4.1 with reported elastic modulus values for various animal bones in work previously (Table 4–S2).[64,65] The fit resulted in $A = 15.98$, and all the data points are within ±20% of A (Figure 4–S9). We determined f_d to be 0.083, indicating that approximately 92% of bioapatite in bones contributes to increasing E_m. Figure 4.6 compares the experimental data with the model. The data for control samples are located within ±20% of A. Thus, we can expect that their mechanical properties are comparable to those of early-stage animal bones. Interestingly, the increase in E_m by cyclic strain was even higher than the prediction, indicating that applying cyclic mechanical loading can effectively enhance the mechanical properties of collagen-based biomaterials. Conversely, under static strain, the increase in E_m is significantly lower than for other conditions. This result is caused by the formation of debonded particles at the outer surface of the matrix (Figure 4.4d). Therefore, an environment that causes permanent mechanical strain in collagen should be avoided in the synthesis of elastic biomaterials. The differences in observed mineral stiffening behavior, compared to the levels predicted by the model, highlight the importance of the microscale distribution of mineral on the surfaces and within the matrices in defining tissue-level mechanical properties. The results also demonstrate that the spatial distribution of mineral is more important than f_V in determining the mechanical strength of bones, even though f_V has been commonly used in predictions.[64,65] In future biomaterial design studies, f_d from Eq. 4.1 can better quantify the influence of particle formation at undesirable locations.

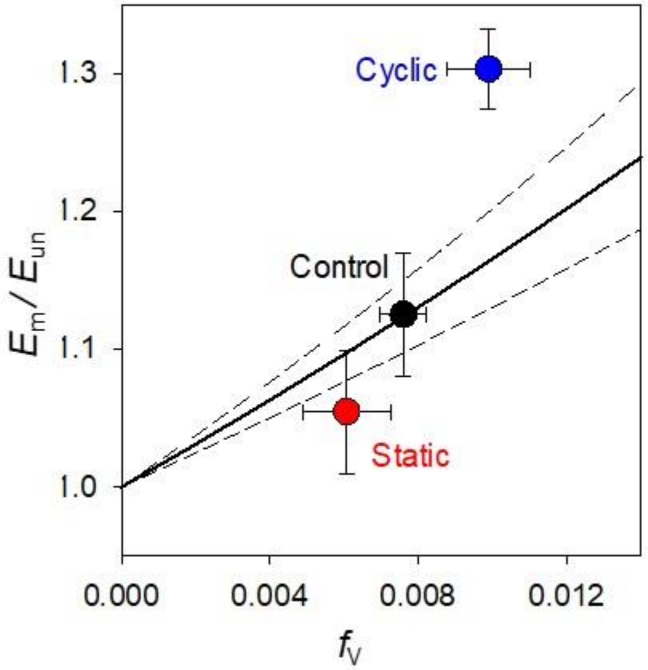

Figure 4.6 Relative increase in E_m by nucleation under different strain conditions. Solid line is Eq. 4.1 with A = 15.98 and f_d = 0.083, based on fitting the equation with data from different animal bones (Figure 4–S9). Dotted lines show an error range of ± 20% of A, where most data were located.

4.4.5 Transport of Calcium Phosphate Precursors in Strain-Mediated flow

Bone's ability to resist fracture is developed by adapting to repeated loading with varying strain magnitude and frequencies.[127] Many previous studies describe how cells in bone modulate their activities based on strain-mediated fluid flow in the lacunar-canalicular spaces[120] (e.g., by enhancing delivery of nutrients or disposing waste products of cell metabolism[128]) or generating strain-generated potentials[141] and fluid shear stress.[142] While these biologic mechanisms have been studied extensively, the role of strain-mediated fluid flow on the chemistry of biomineralization is poorly understood. The enhanced transport of body fluids by cyclic strain may directly influence mineralization, as implied in our cell-free collagen mineralization system. There are many micropores in the extrafibrillar spaces within collagen matrices, allowing for fluid flow under loading that may mimic that seen in lacunar-canalicular spaces.[120] Deformation of these pore spaces under cyclic strain conditions produces pressure gradients that enhance fluid flow, thereby potentially enhancing biomineralization processes.[128,143]

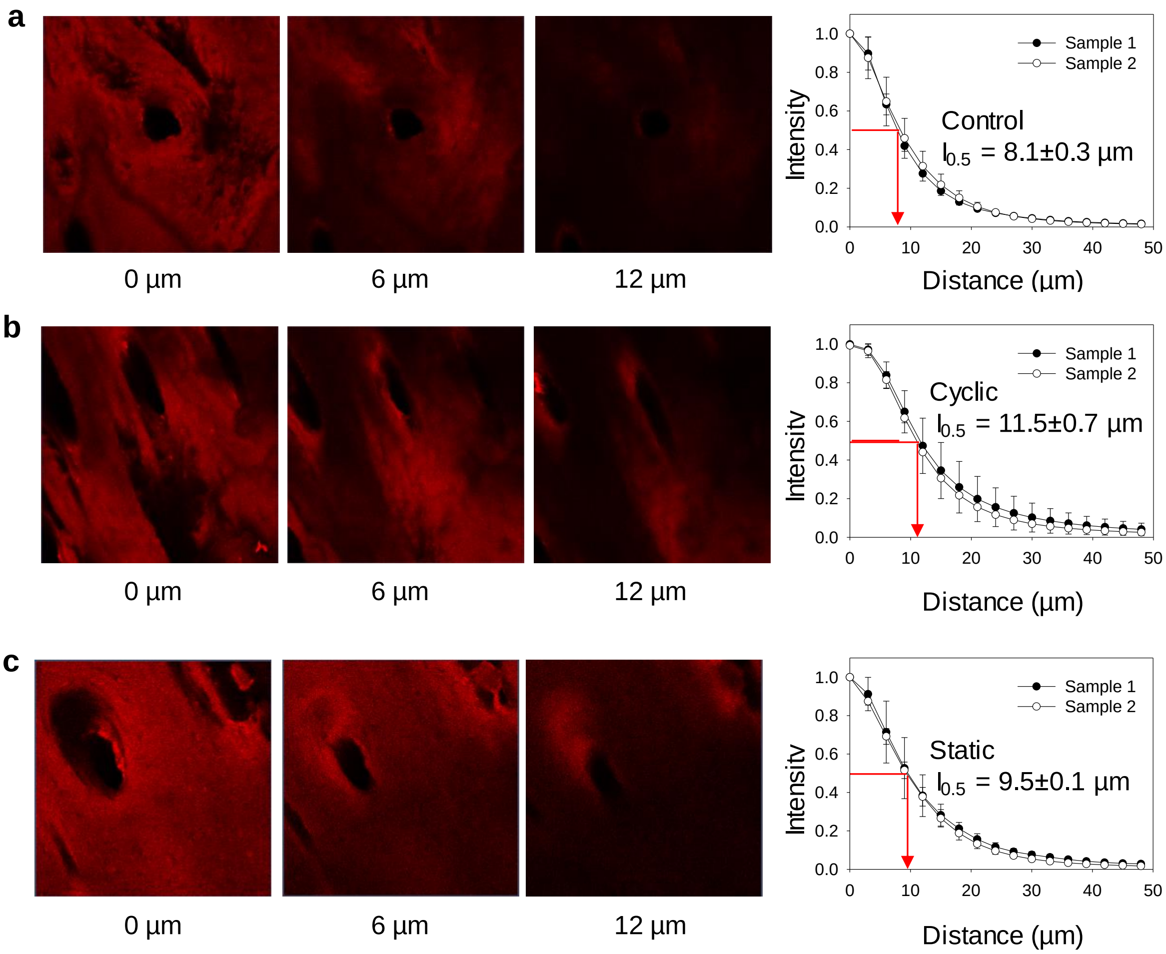

Figure 4.7. Transport of Sirius Red fluorescent dye into collagen matrices. (**a-c**) Microscope images of confocal sections of collagen matrices at z = 0, 6, 12 µm. Samples were experienced different strain conditions (**a**, control; **b**, cyclic strain; and **c**, static strain) in PBS containing Sirius Red for 10 hr. Right plots show red fluorescence intensities at different depths. The intensities were normalized using the intensity at distance = 0 µm to correct for the intensity differences from different coverage areas of collagen. $I_{0.5}$ is the depth position where the intensity reduces to half, obtained from two samples. Error bars are standard deviations from triplicate measurements at different positions from one sample.

Increased fluid flow would increase delivery of precursor molecules, including Ca^{2+}, HPO_4^{2-}, prenucleation clusters, and/or amorphous calcium phosphate,[8,27,99] to deeper sites in the collagen matrices. In this study, the transport of body fluid components into collagen matrices under different strain conditions was evaluated using Sirius Red dye observed under confocal microscopy. This red fluorescent molecule (MW: 1,373 g mol^{-1}; $pK_{a1\text{–}6} < 2$, $pK_{a7,8} > 13$) stains collagen; therefore, counting fluorescence intensity at different depths of collagen indicates how actively the molecules have diffused into the matrix[144]. The results demonstrated a 40% increase in the penetration depth of the staining molecule under cyclic strain conditions compared to control conditions (Figure 4.7). This behavior is consistent with the findings of increased J_s and deeper mineralization depth, which consequently increased the elastic modulus of the matrices after mineralization.

4.5 Conclusions

In this study we evaluated the influence of cyclic strain on the initial stages of bone mineralization, nucleation, and crystallization. The cyclic strain condition, simulating mechanical loading from human walking, increases J_s with deeper inner matrix mineralization within the collagen matrices. These outcomes resulted from the enhanced transport of precursor molecules by strain-mediated flow of mineralization solution, as illustrated in Figure 4.8. The cyclic strain condition significantly influenced the spatial distribution of mineral at the microscale, leading to more inner matrix mineralization. Cyclic mechanical loading effectively overcomes the diffusion barriers created by the extracellular matrix, delivering nucleation precursor molecules to locations within the matrix where nuclei formed (e.g., collagen gap regions). Consequently, mineralization under cyclic strain increased the E_m, strength, and resilience of the collagen matrices more effectively than unloaded or static strain conditions. Minerals that formed in the inner matrix of collagen increase E_m more effectively than particles that formed at the outer surface of the matrix, which cannot transfer load efficiently. On the other hand, the morphology (thickness of bioapatite in nanoscale), crystalline structure (molecular scale), and f_V (macroscale) were not influenced by the cyclic motion, implying the importance of multi-scale analyses for nano-organic composites for tissue engineering. By showing that enhanced collagen mineralization is a physicochemical response of collagen structure to cyclic strain, our findings provide insights into new collagen-based biomaterials.

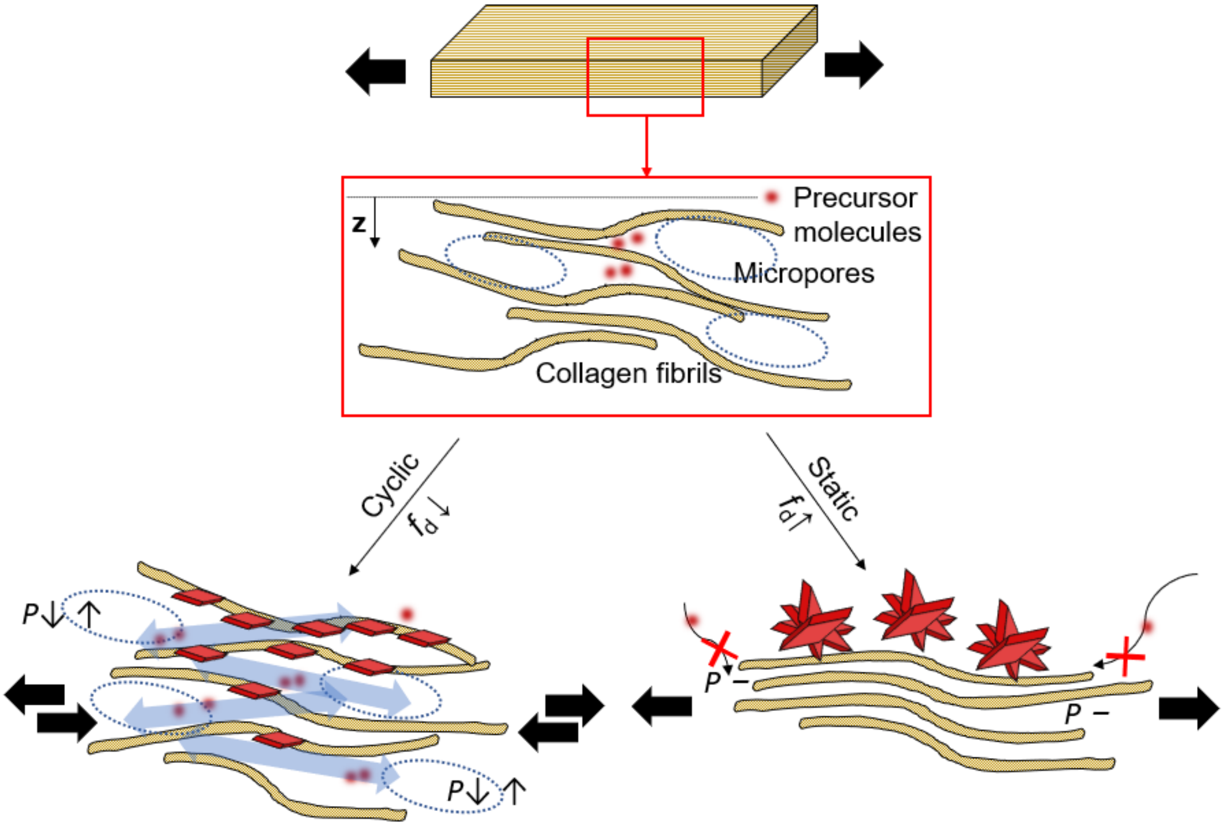

Figure 4.8 Mechanisms of collagen mineralization under strain conditions. Deformation of micropores by cyclic strain generates pressure (P) gradients. Thus, transport of precursor molecules increases along with the flow of mineralization fluid. The static condition only rearranges the micropore structures, without producing P gradients.

4.6 Acknowledgments

The authors acknowledge Dr. Spencer Lake (Musculoskeletal Soft Tissue Lab at Washington University in St. Louis) for providing his facilities for tensile testing and freezing leveling of samples. The Nano Research Facility, the Institute of Materials Science & Engineering, and the Molecular Microbiology Imaging Facility at Washington University in St. Louis provided their facilities for the experiments. We thank Prof. J. Ballard for carefully reviewing the manuscript. The project was supported by the National Science Foundation (DMR-1608545 and DMR-1608554). Use of the Advanced Photon Source (sectors 12-ID-B and 11-ID-B) at Argonne National Laboratory was supported by the U.S. Department of Energy, Office of Science, Office of Basic Energy Sciences, under Contract No. DE-AC02-06CH11357.

4.7 Supporting information for Chapter 4

4.7.1. SAXS and WAXD data Collection and Analysis

SAXS data were collected for collagen matrices during *in situ* calcium phosphate mineralization. The sample holder grip module, connected to the BiSlide machine during mineralization, was designed to be detached easily and loaded on another modularized sample stage for the SAXS measurement (Figure 4–S1a,b). For each SAXS scan, the sample was exposed to a 13.3 keV X-ray beam for 1 second. The sample was scanned five times, moving the sample stage vertically by 0.2 mm per scan. The average intensity value of five scans was taken to represent one position of the sample. The left half and the right half of each sample (total 10 scans) were measured at each time interval (Figure 4–S2). From the obtained 2-dimenstional scattering intensity images, 1-dimensional scattering intensities, $I(q)$, were extracted by averaging the sector along the horizontal direction, which was perpendicular to the fibrillar direction (Figure 4–S2). Therefore, we were able to analyze $I(q)$ to quantify the nucleation rates and to fit the data for obtaining the morphology of newly formed particles without interference by peaks caused by the periodicity (~67 nm) of the collagen gap and hole regions. The distance from the sample to the SAXS detector was 2 m, which provided a range of 0.003–0.5 Å^{-1} for the scattering vector, q. Silver behenate powder was used as the q calibration standard, and $I(q)$ was normalized by the incident beam intensities and calibrated using a reference glassy carbon standard sample.[95] In this way, SAXS intensities collected from different measurements could be compared.

Further SAXS data analyses were conducted using 1-dimensional intensity data. Total particle volume was estimated from the linear relationship with invariant values, $Q = \frac{1}{2\pi^2}\int q^2 I(q)dq$. Due to the relatively high noise in larger q regions, integration was conducted only within a limited q range of 0.005–0.3 Å^{-1}. The Modeling II tool of the IRENA package written in IGOR Pro (WaveMetrics Inc.) was provided by APS and used to fit the SAXS pattern to evaluate the particle morphology and volume fraction. Details about the models used in the package are well described elsewhere.[94]

Similarly, to identify CaP phases during collagen mineralization, *in situ* wide-angle X-ray diffraction (WAXD) data was collected at APS sector 11-ID-B. Every two hours during the mineralization, collagen samples were exposed to a 58.66 keV X-ray beam for 10 seconds, with a 95 cm distance between the sample and detector (Perkin Elmer amorphous silicon detector). Due to the larger beam size (500 μm × 500 μm) and longer exposure time for WAXD than for SAXS, a one-time scan was used to collect the data for one spot. The 2-dimensional intensities were then averaged over the q range along the radial direction to produce 1-dimensional intensities $I(q)$, using GSAS-II.[145] Cerium dioxide was used as the calibration standard.

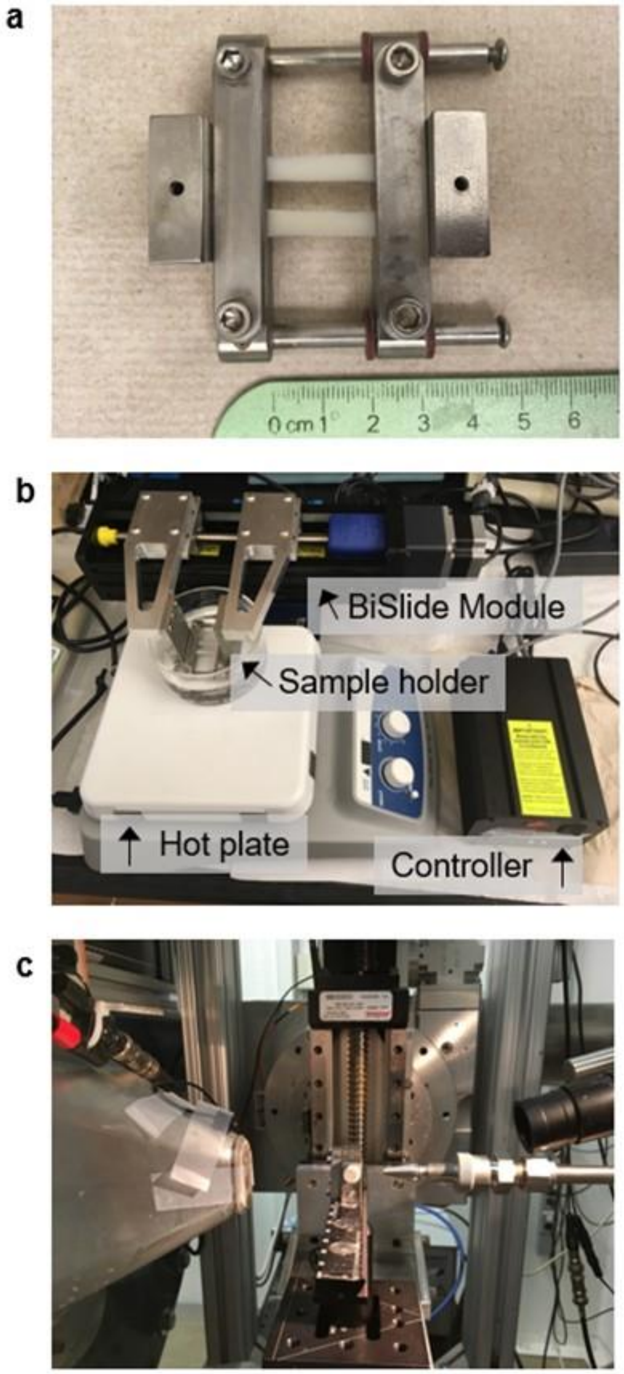

Figure 4–S1 Experimental setup for *in situ* collagen mineralization. (**a**) A custom-made stainless-steel sample holder to grip two collagen samples (3 cm long, 0.5 cm width, and ~ 1 mm thick). The initial distance between the two grips was set to 2 cm. (**b**) A customized BiSlide module to apply stress to samples during mineralization. (**c**) The sample holder placed on the stage for small-angle X-ray scattering measurements at the Advanced Photon Source sector 12-ID-B (Argonne National Laboratory, IL, USA).

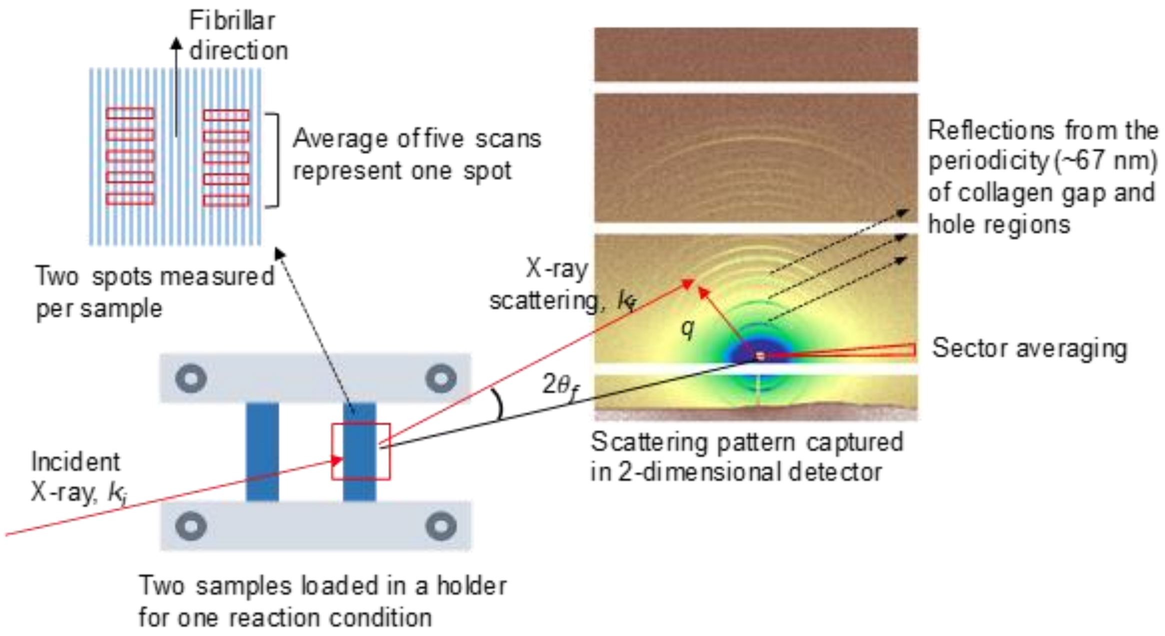

Figure 4–S2 A schematic of SAXS measurement and an example of 2-dimensional intensity data. k_i and k_f are the incident and scattered wave vectors, respectively, and $2\theta_f$ is the exit angle of the X-rays.

Table 4–S1 Concentrations (mM) of ionic components of simulated body fluids and human blood plasma**.**

Solutions	Na^+	K^+	Mg^{2+}	Ca^{2+}	Cl^-	HCO_3^-	HPO_4^{2-}	SO_4^{2-}
SBF[86]	142.0	5.0	1.5	2.5	147.8	4.2	1.0	0.5
2.5×SBF	142.0	8.0	1.5	6.3	155.3	4.2	2.5	0.5
Human blood plasma[85]	142.0	5.0	1.5	2.5	103.0	27.0	1.0	0.5

*The pH of 2.5×SBF was adjusted to 7.4 with 50 mM of Tris ($(CH_2OH)_3CNH_2$) and 1 N HCl.

4.7.2. *In situ* SAXS data analyses

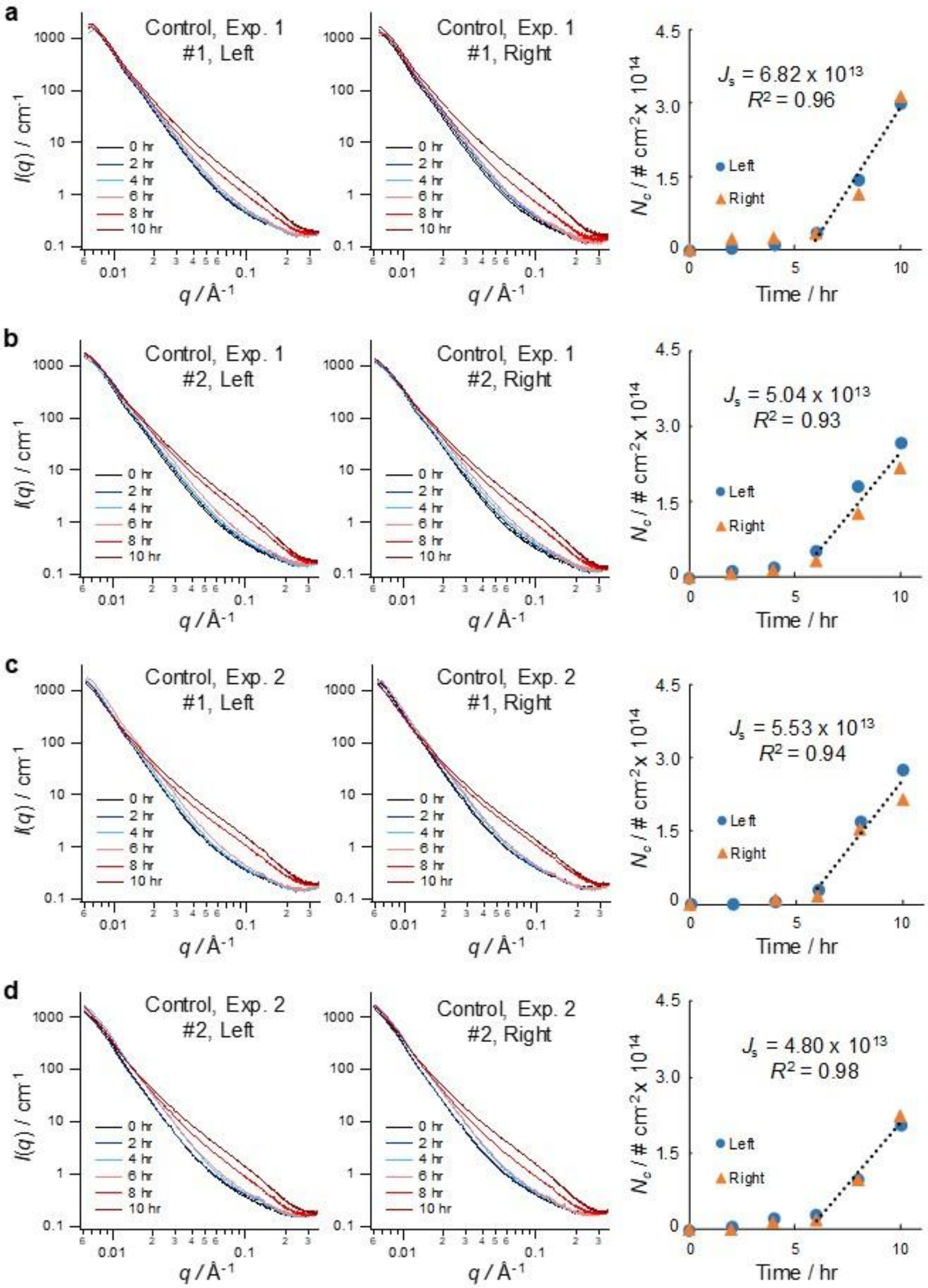

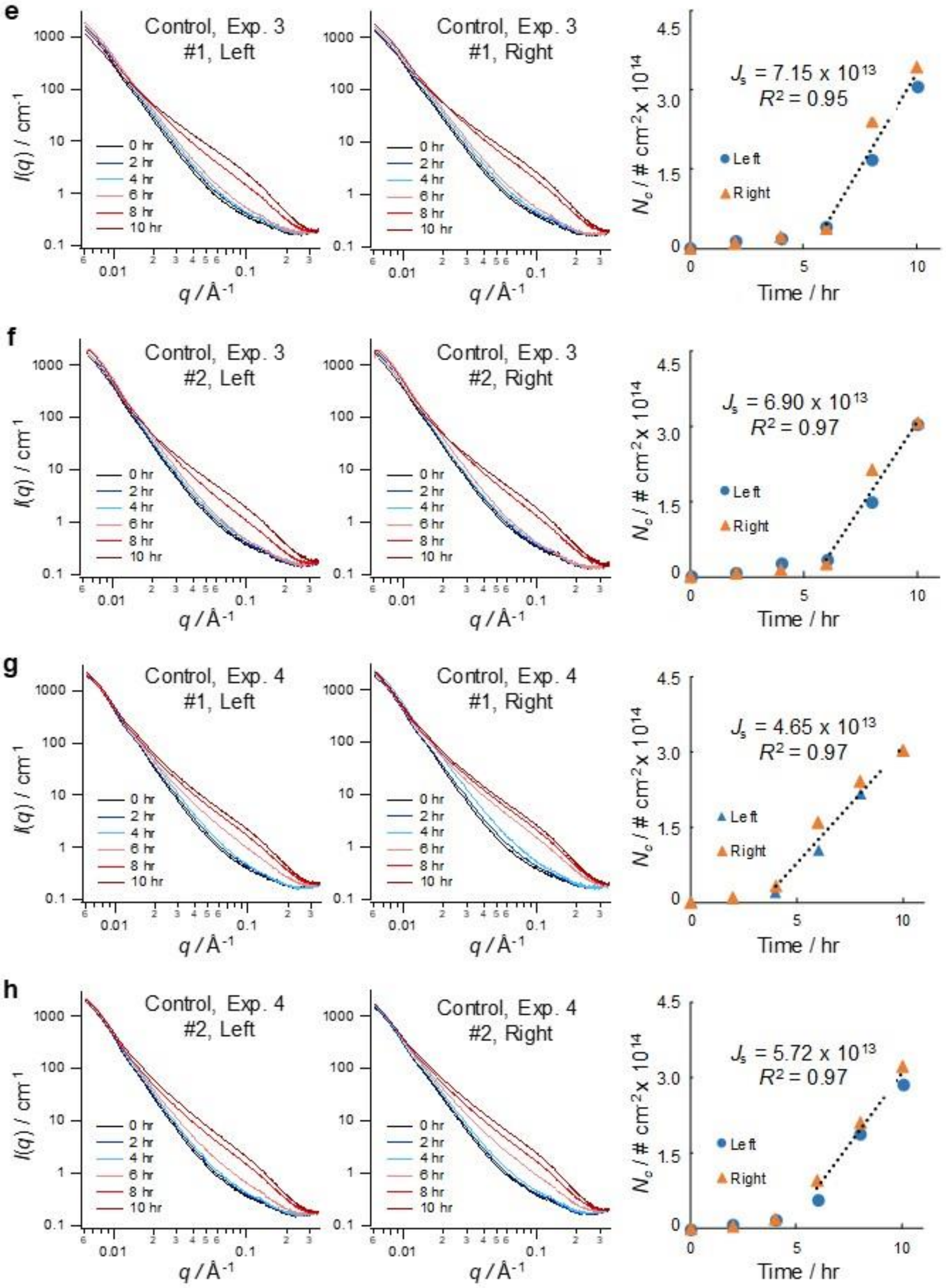

Figure 4–S3 *In situ* SAXS data for collagen mineralization under no strain (control). Four experiments were conducted. Two samples (#1 and #2) were analyzed per experiment, and two positions (left and right sides) were scanned per sample. The linear slopes of the number concentration vs. time plots indicate nucleation rates, J_s.

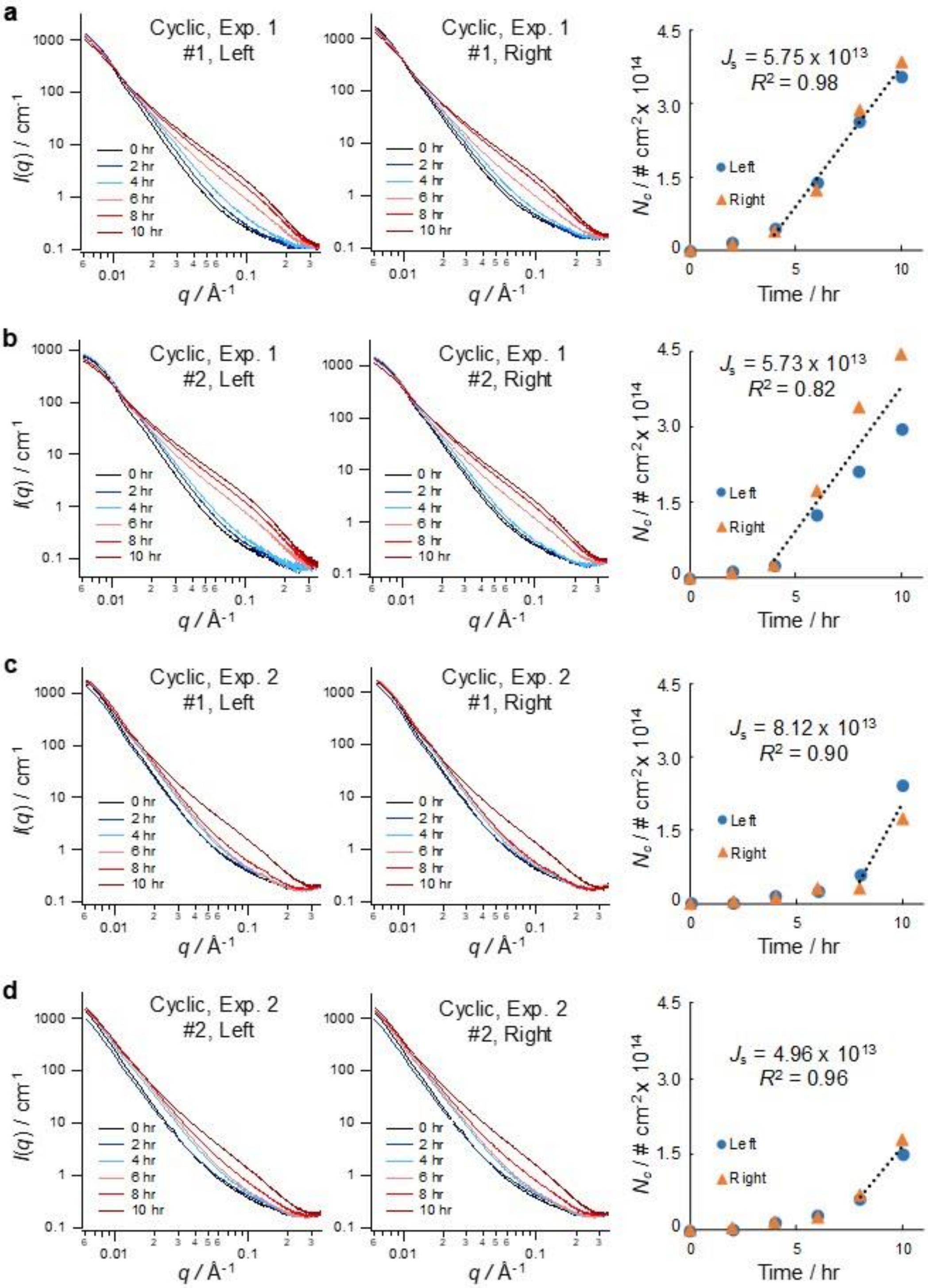a
Cyclic, Exp. 1 #1, Left
Cyclic, Exp. 1 #1, Right
J_s = 5.75 x 10^{13}
R^2 = 0.98
b
Cyclic, Exp. 1 #2, Left
Cyclic, Exp. 1 #2, Right
J_s = 5.73 x 10^{13}
R^2 = 0.82
c
Cyclic, Exp. 2 #1, Left
Cyclic, Exp. 2 #1, Right
J_s = 8.12 x 10^{13}
R^2 = 0.90
d
Cyclic, Exp. 2 #2, Left
Cyclic, Exp. 2 #2, Right
J_s = 4.96 x 10^{13}
R^2 = 0.96
$I(q)$ / cm^{-1}
1000
100
10
1
0.1
q / $Å^{-1}$
6
0.01
2
3
4
5
6
0.1
2
3
0 hr
2 hr
4 hr
6 hr
8 hr
10 hr
N_c / # cm^{-2} x 10^{14}
4.5
3.0
1.5
0
Time / hr
0
5
10
● Left
▲ Right

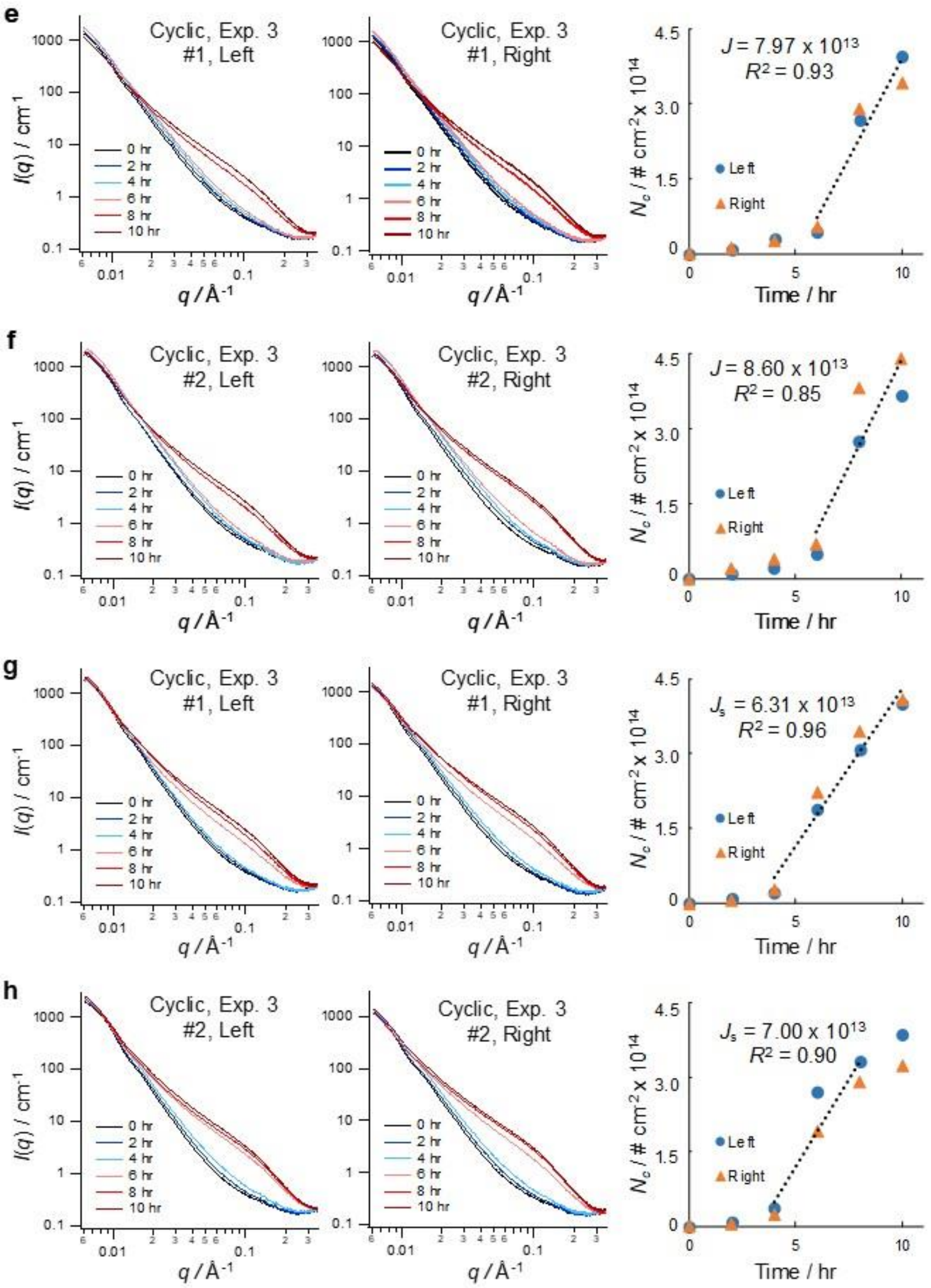

Figure 4–S4 *In situ* SAXS data for collagen mineralization under cyclic strain. Four experiments were conducted. Two samples (#1 and #2) were analyzed per experiment, and two positions (left and right sides) were scanned per sample. The linear slopes of the number concentration vs. time plots indicate nucleation rates, J_s.

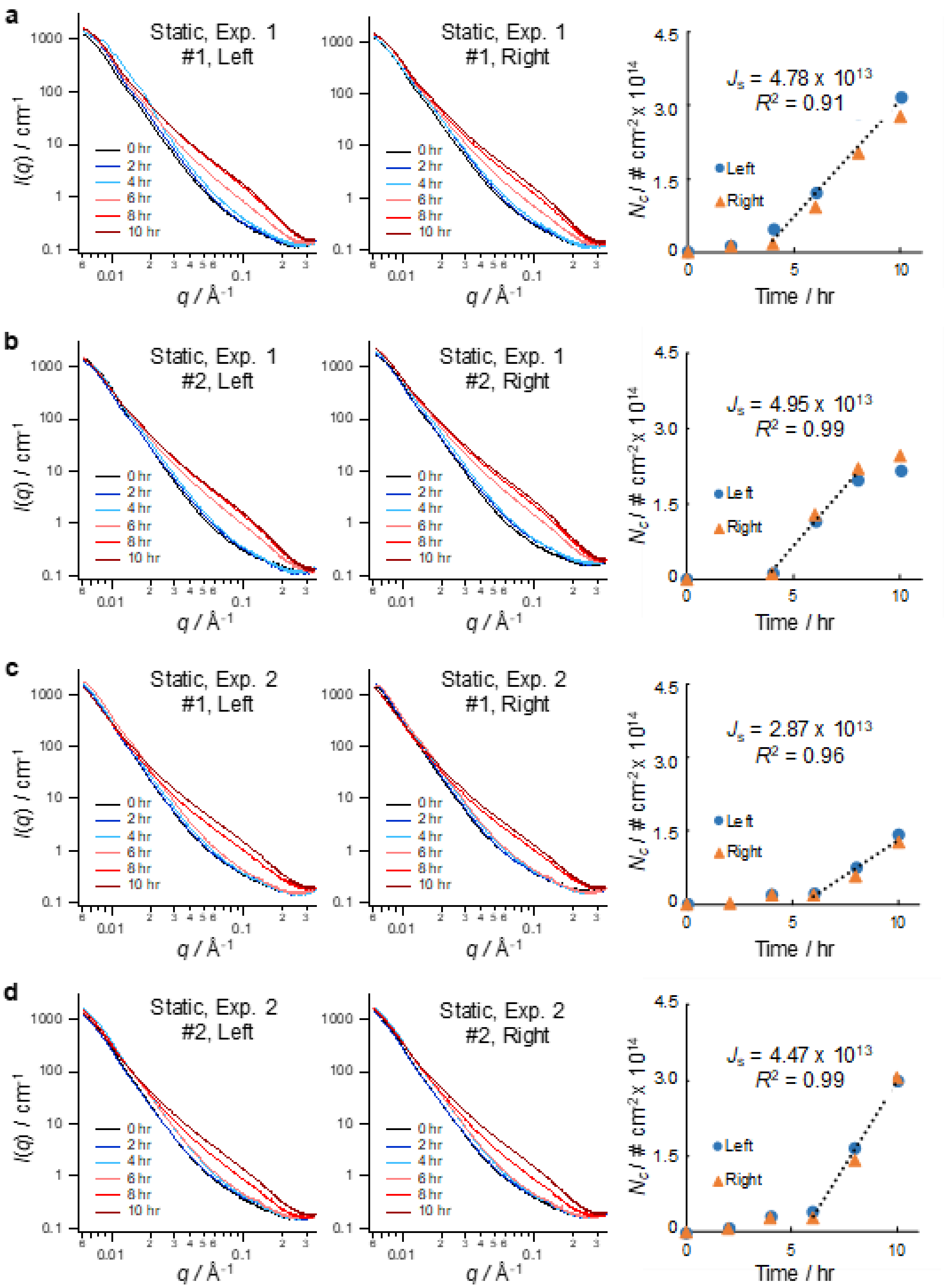
a
Static, Exp. 1 #1, Left
Static, Exp. 1 #1, Right
J_s = 4.78 x 10^{13}
R^2 = 0.91
b
Static, Exp. 1 #2, Left
Static, Exp. 1 #2, Right
J_s = 4.95 x 10^{13}
R^2 = 0.99
c
Static, Exp. 2 #1, Left
Static, Exp. 2 #1, Right
J_s = 2.87 x 10^{13}
R^2 = 0.96
d
Static, Exp. 2 #2, Left
Static, Exp. 2 #2, Right
J_s = 4.47 x 10^{13}
R^2 = 0.99
0 hr
2 hr
4 hr
6 hr
8 hr
10 hr
$I(q)$ / cm^{-1}
1000
100
10
1
0.1
q / $Å^{-1}$
0.01
0.1
N_c / # cm^{-2} x 10^{14}
4.5
3.0
1.5
0
Left
Right
Time / hr
0
5
10

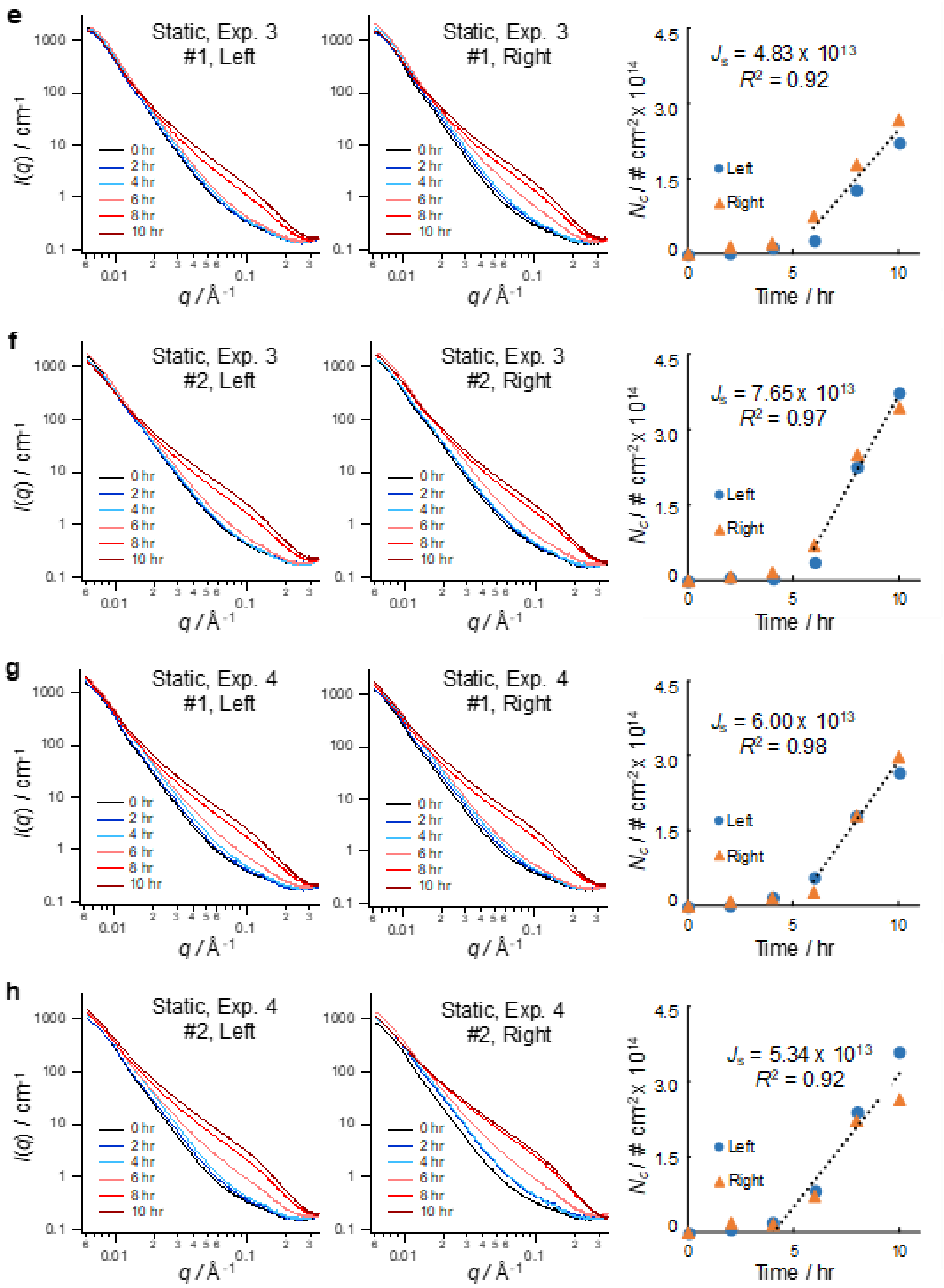

Figure 4–S5 *In situ* SAXS data for collagen mineralization under static strain. Four experiments were conducted. Two samples (#1 and #2) were analyzed per experiment, and two positions (left and right sides) were scanned per sample. The linear slopes of the number concentration vs. time plots indicate nucleation rates, J_s.

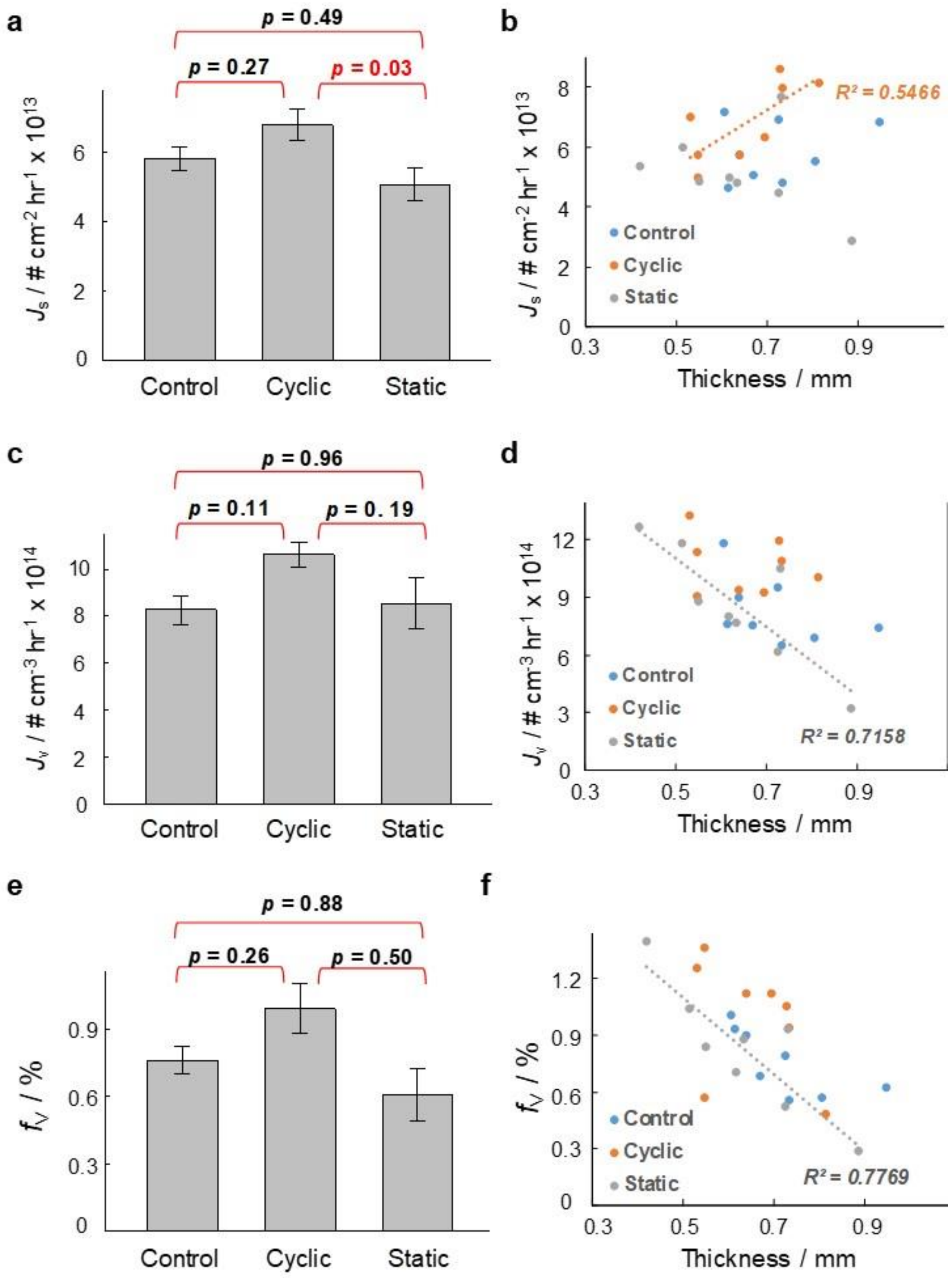

Figure 4–S6 Summary of in situ SAXS analysis. (a) Nucleation rate per scanning surface area (J_s). (b) Nucleation rate per scanning volume ($J_v = J_s$ × sample thickness). (c) Volume fraction of bioapatite in collagen matrix (f_V).

4.7.3. *Ex situ* SEM-EDX Analyses

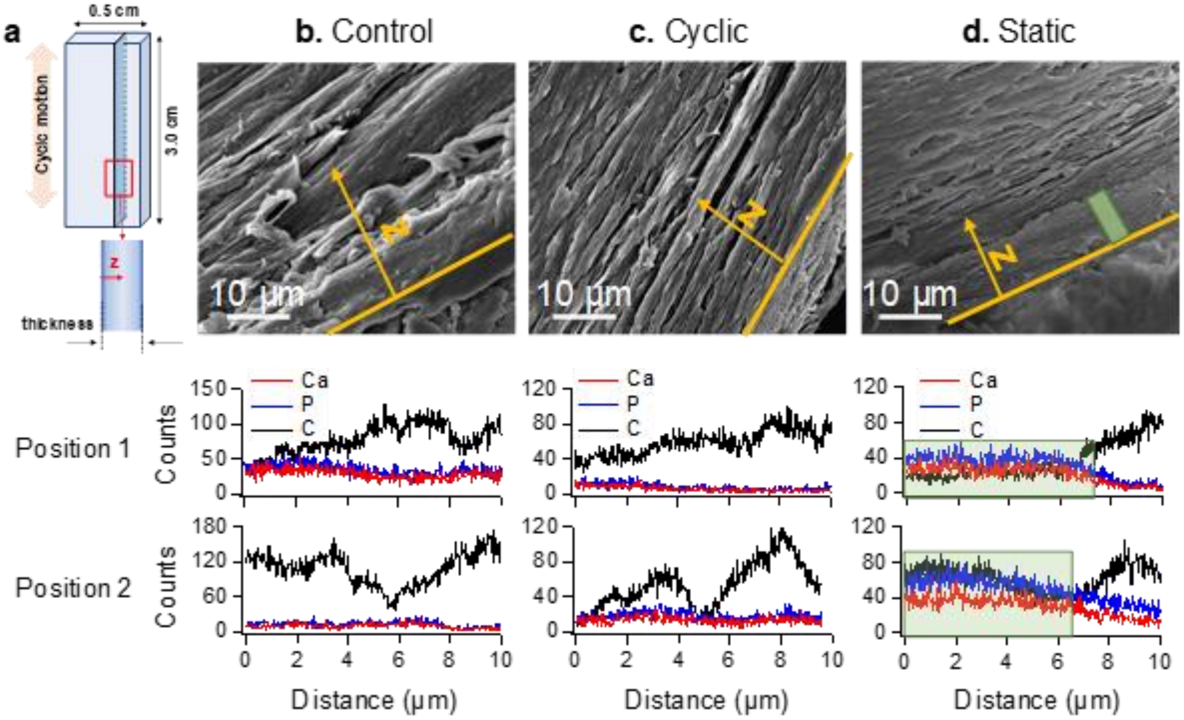

Figure 4–S7 Cross-sectional images of collagen matrices. a, Schematic of the sample geometry, showing the direction of the cyclic motion. The *z*-direction indicates the depth of collagen matrices from the outermost surface. b–c, Scanning electron microscope (SEM) images of cross sections. Line profiles of elemental composition along the z-direction were obtained from energy-dispersive X-ray spectroscopy (EDX).

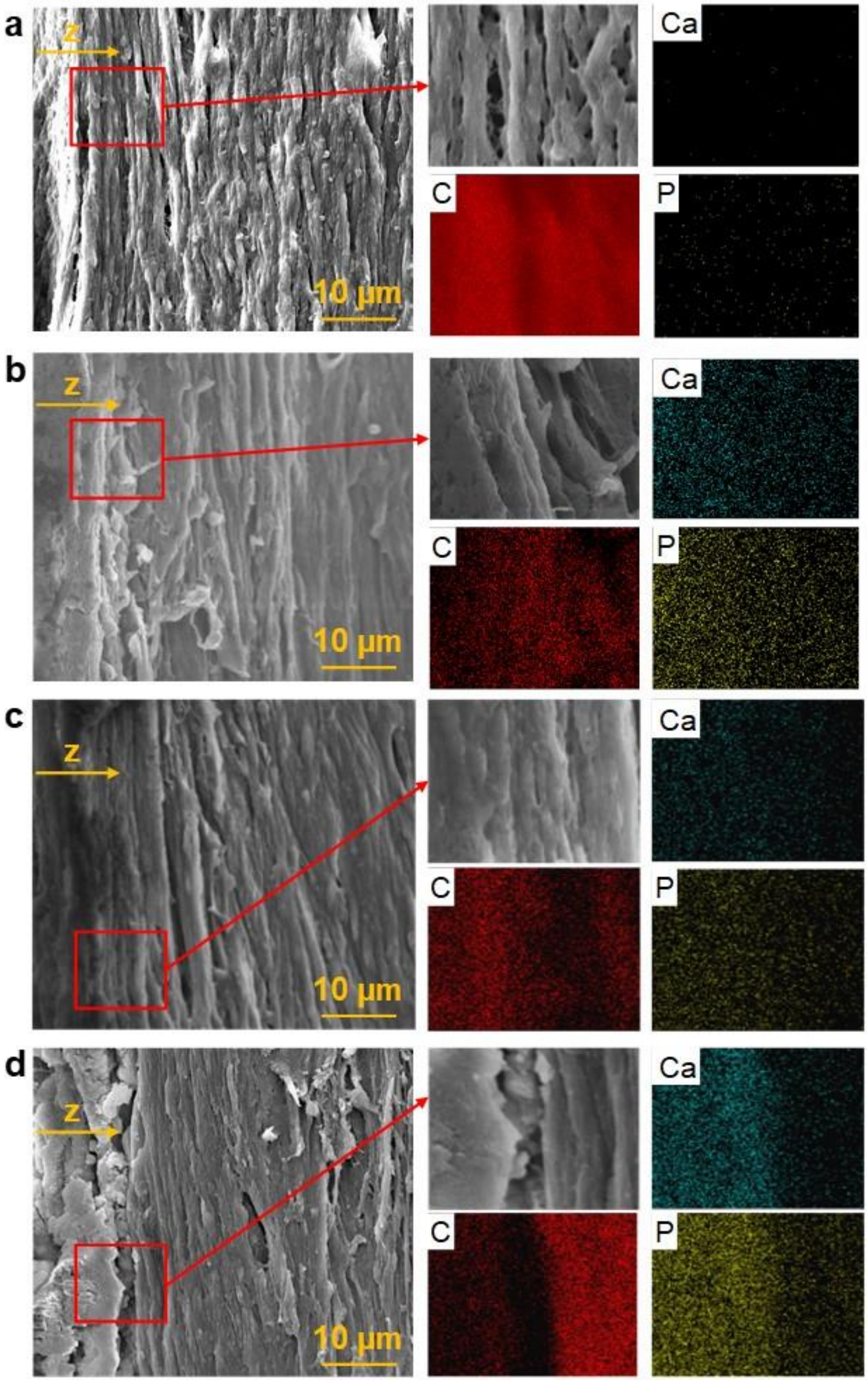

Figure 4–S8 SEM-EDX mapping of cross-sections of collagen matrices. (**a**) Unmineralized collagen. (**b**) Control. (**c**) Cyclic strain. (**d**) Static condition. The z-direction indicates depth direction of the matrix. Selected areas of SEM images (rectangles in the left panels) were analyzed for C, Ca, and P distribution maps (right panels).

4.7.4. Mechanical and Chemical Properties of Animal Bones

Table 4–S2 Mechanical and chemical properties of animal bones.

Species	**Bone**	***n****	***E_m**** (GPa)	***m_{Ca}**** (mg g^{-1})	**Porosity***	***f_V***** (%)
Alligator	Femur	9	13.0	253	0.057	40.1
Atlantic whale	Rib	7	8.4	253	0.31	29.4
Axis deer	Term fetus	4	13.2	242	-	36.5
	Mother	3	31.6	274	-	41.3
Bovine	Femur (9 yr)	10	24.5	271	0.044	45.4
	Tibia (1 yr)	8	20.4	252	-	38.0
Brown bear	Femur	3	16.9	255	-	38.4
Crane	T-metatarsus	2	23.1	240	-	36.2
	Tibiotarsus	5	17.6	224	-	33.8
	Ossified tendon	5	22.6	256	-	38.6
Donkey	Radius	7	16.2	255	0.066	40.2
Dugong	Scapula	6	5.5	258	-	38.9
	Radius	2	7.5	253	-	38.1
	Ulna	1	4.9	242	-	36.5
Fallow deer	Tibia	9	25.2	260	0.024	43.4
	Radius	4	25.0	249	-	37.5
Flamingo	Tibiotarsus	4	28.4	257	-	38.7
Galapagos tortoise	Femur	10	12.3	244	0.058	37.9
	Tibia	3	13.0	232	-	35.0
	Fibula	5	11.8	230	0.058	34.6
Man	Femur (3 yr)	7	7	227	-	34.2
	Femur (5 yr)	4	12.8	222	-	33.5
	Femur (35 yr)	4	16.7	249	-	37.5
Horse	Femur (7 yr)	7	23.7	263	0.033	43.8
King penguin	Humerus	4	22.2	266	0.089	42.0
	Radius	2	22.2	265	-	39.9
	Ulna	2	21.7	266	-	40.1
Leopard	Femur	4	21.5	254	-	38.3
Polar bear	Femur (Very Young)	5	8.1	244	-	36.8
	Femur (Young)	13	16.1	259	-	39.0
	Femur (Adult)	6	22.2	268	-	40.4
Red deer	Antler	42	7.1	213	0.134	28.5
Reindeer	Antler	14	7.0	217	0.176	27.8
Rhinoceros	Hmerus	9	13.1	253	-	38.1
Roe deer	Femur	5	17.2	259	0.047	42.1
Wallaby	Femur	3	22.0	274	0.032	46.8
	Tibia	4	25.4	268	-	40.4
Walrus	Humerus	5	14.2	245	-	36.9

* Number of samples (n), elastic modulus (E_m in GPa), and calcium contents (m_{Ca} in mg g^{-1}) were obtained from Currey *et al*. (2004)[65]. Porosity data were obtained from Currey et al. (1988).[64]

** Volume fraction of mineral, f_V were calculated based on Ca contents based on eq. 4–S1, if porosity data were given.

$$f_V = \left(\frac{V_{apatite}}{V_{apatite} + V_{collagen}}\right) \times (1 - porosity)$$

$$= \left(\frac{\mathrm{m}_{apatite}/\rho_{apatite}}{\mathrm{m}_{apatite}/\rho_{apatite} + m_{collagen}/\rho_{apatite}}\right) \times (1 - porosity) \qquad \text{eq. 4–S1}$$

Apatite mineral contents ($m_{apatite}$ in mg g^{-1}) were calculated by assuming all Ca exist as apatite ($Ca_5(PO_4)_3OH$) as written in eq. 4–S2.

$$m_{apatite} = m_{Ca} \times \frac{molecular\ weight\ of\ apatite}{5 \times molecular\ weight\ of\ calcium} \qquad \text{eq. 4–S2}$$

Collagen contents ($m_{collagen}$ in mg g^{-1}) were calculated to be 1 - $m_{apatite}$. 3.16 and 1.35 g cm^{-3} were used as densities of apatite and collagen ($\rho_{apatite}$ and $\rho_{collagen}$)[146].

When porosity data were not available, f_V were obtained from eq. 4–S3 using an approximate density of bone (ρ_{bone} = 1.9 g cm^{-3}), which is relatively constant for most of compact bones.[147]

$$f_V = m_{apatite} \times 10^{-3} \times \frac{\rho_{bone}}{\rho_{apatite}} \qquad \text{eq. 4–S3}$$

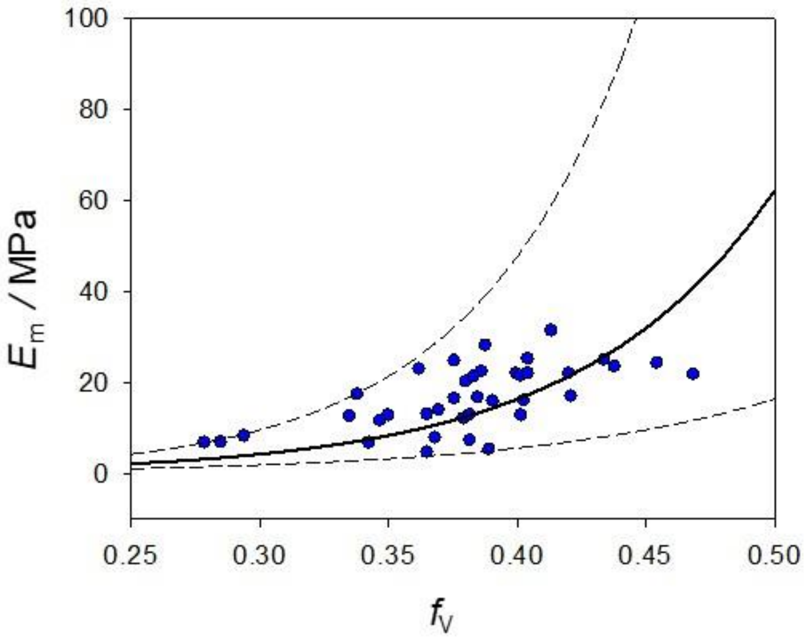

Figure 4–S9 The relationship between E_m vs. f_V in bones. Experimental data (blue dots) obtained from Table 4–S2. The data were fit to the equation $\frac{E_m}{E_{un}} = \exp(A\, f_V(1 - 2f_d))$, where A is a constant related to the ratio of the elastic moduli of apatite and collagen and f_d is the fraction of debonded particles. A = 15.98 and f_d = 0.083 were obtained from the least-square error method for fitting (solid line). All the data were within the range of ± 20% of A (dotted lines). The elastic modulus of unmineralized collagen, E_{un} = 79.6 MPa, was obtained from tensile test results of the PBS group in Figure 4.4a.

Chapter 5. Application I: Enhanced Collagen Mineralization using Pulsed Electrical Stimulation

5.1 Overview

In Chapter 2, we explored the kinetics of CaP nucleation pathways through (sub)nanoscale observation. We evaluated how the nano-confined collagen structure provides thermodynamically stable nucleation sites for CaP intrafibrillar mineralization in Chapter 3. Then, in Chapter 4, we examined the influence of nanoscale nucleation on microscale mineral distribution and macroscale mechanical properties. These findings apply to the chemical and mechanical properties of the collagen/CaP composite system at multiple-length scales. Utilizing the principles that we learned in Chapters 2–4, we suggest, in this chapter, a biomedical application to enhance bone mineralization utilizing bioelectricity.

In bones, bioelectricity is generated as a pulsed signal from mechanical loadings such as walking and running. It is known that bioelectricity contributes to bone mineralization by enhancing activities of bone-forming cells. However, little is known about the physicochemical response of collagen to bioelectricity in body fluids, and its consequent influence on mineralization. Here, we show that applying pulsed electrical stimulation significantly enhances the transport of ionic body fluid components through a narrow channel (~100–200 μm) between the inner surface of the tube-like collagen scaffold and the cathode placed inside the scaffolds. The enhanced transport of ionic precursors increases diffusion of the charged precursor molecules to the inner collagen surface, where bone mineralization is otherwise restricted without any stimulation. The results indicate that the pulsed electrical signals can locally speed up the nucleation of bioapatite, allowing us to better control the spatial distribution of bioapatite at the microscale. The findings from this study provide insights into the utilization of bioelectricity for clinical applications for facilitating bone-fracture healing and designing better biomaterials.

5.2 Introduction

Bones are hierarchical structures with organic matrices and inorganic minerals.[61] Triple-helix of type I collagen molecule is a major extracellular protein. Collagen molecules are assembled to form a fibrillar structure to serve as a skeletal template.[6,34] The deposition of the mineral component of bones, known as bioapatite, which is a biologically produced analog of HA,[2] increases mechanical strength of bones, while the collagen predominantly responds to deformation process.[10] During their development, bones actively respond to mechanical loading.[117] As a response to the mechanical loading, bioelectricity up to a hundred millivolts with short durations can be generated in many animal tissues including human tibia bones.[148-150] The generated pulsed electrical signals have been considered an important factor for controlling bone mineralization by stimulating the activities of bone-forming cells. Indeed, several *in vitro* studies have reported increased osteoblastic differentiation and consequently, more collagen synthesis and bone mineral formation by applying pulsed electrical stimulation.[151-153]

Despite the positive outcomes from several *in vitro* studies utilizing pulsed stimulation of cellular activities for the bone regeneration,[154-156] its clinical application has been limited owing to uncertainties in the supporting mechanisms.[157] The physicochemical responses of collagen to pulsed electrical stimulation, which are distinct from biological responses, should be further evaluated for a more precise control of the application. Furthermore, it is surprising that the importance of electrostatic interactions has been highly underestimated despite of critical roles of charged ionic molecules, such as Ca^{2+} or HPO_4^{2-}, as nucleation precursors in bone mineralization.

Recent findings of collagen mineralization have emphasized the electrostatic interactions between charged amino acid residues in collagen and precursor molecules in the mineralization solution.[27,68,158] Hence, the electrostatic interactions between the collagen surface and charged precursor molecules is expected to be highly influenced by the pulsed electric stimulations.

For the tissue-level fabrication of biomaterials or facilitated bone-fracture healing of collagen mineralization, the inhibited diffusion of nucleation precursors molecules into a deeper side of the collagen matrix is challenging.[120] In particular, this is a significant problem for collagen scaffolds with high collagen fibrillar density, such as ones extracted from native bones or tendons.[43,47] Not only does the denser collagen structure require a longer time for diffusion of precursors, but it may form an exterior mineral layer, which acts as an additional diffusion barrier,[99] more easily than loosely-packed collagen matrix or single collagen fibrils.

In this study, we investigated how pulsed electrical stimulation can enhance mineralization of the collagen scaffold. We used collagen scaffolds extracted from chicken fibular bones. The pulsed electric condition used here is mimicking a bioelectrical condition with moderate frequency and moderate magnitude, which can be generated by common mechanical loading such as walking or running.[127] To better understand how to apply electrodes to collagen, the samples were located either on the cathode or the anode. Utilizing *in situ* SAXS and WAXD, we identified the morphology and crystalline structure of the nuclei and quantified the extent of nucleated CaP crystals. We observed the enhanced transport of ionic precursor molecules into a narrow channel (~100–200 μm) between the inner surface of a tube-like collagen scaffold and the cathode placed inside the scaffold. As a consequence, more mineralization was achieved from the inner surface of the collagen, where mineralization was highly limited without pulsed stimulation. By successfully controlling spatial distribution of CaP crystals in dense collagen scaffolds, this study provides new insight into utilizing pulsed electric stimulation for bone fracture healing and development of better biomaterials.

5.3 Materials and Methods

5.3.1 Preparation of Collagen Samples

Fibular bones were separated from chicken legs fresh purchased from local grocery stores. Top heads and bottom tendons of the bones were cut out, and then soft tissues, bone marrow and blood in the inner side were carefully removed. The remaining tube-shaped bones were thoroughly demineralized in ethylenediaminetetraacetic acid (EDTA) solution (0.1 M, pH 7.4) for 2 days under magnetic stirring (130 rpm) at room temperature. After demineralization, tube-shaped soft collagen matrices were obtained and cut into 0.5 cm long pieces for further mineralization reactions.

5.3.2 Preparation of Mineralization Solution

Deionized water (18.2 MΩ-cm) obtained from Barnstead Ultrapure Water System (D11931, Thermo Scientific) and American Chemical Society grade chemicals were used to prepare a modified simulated body fluid (SBF) to mimic major ionic compounds in human body plasma[85,86,91]. In this study, to facilitate the reaction to be conducted within a reasonable time period for *in situ* beamtime experiments, an SBF solution with 2.5 times higher concentrations in Ca and P is used (2.5×SBF, Table 5.1). To prevent any precipitation prior to the experiment, we prepared two separate SBF solutions containing either Ca or P sources and these two solutions were separately fed to a reactor for mineralization. The pH of the solutions was adjusted to 7.4 using tris buffer and hydrochloric acid. In addition, pAsp (10 mg L^{-1}, sodium salt, Mw: 5,000 Da, LANXES) was added to aid intrafibrillar mineralization of collagen by inhibiting undesirable extrafibrillar mineralization or homogeneous calcium phosphate nucleation in solution.[99]

Table 5.1. Concentrations (mM) of ionic components of simulated body fluids and human blood plasma.

Solutions	Na^+	K^+	Mg^{2+}	Ca^{2+}	Cl^-	HCO_3^-	HPO_4^{2-}	SO_4^{2-}
1xSBF[86]	142.0	5.0	1.5	2.5	147.8	4.2	1.0	0.5
2.5xSBF	142.0	8.0	1.5	6.3	155.3	4.2	2.5	0.5
Human blood plasma[85]	142.0	5.0	1.5	2.5	103.0	27.0	1.0	0.5

*The pH of the 2.5xSBF was adjusted to 7.4 with 50 mM of Tris ($(CH_2OH)_3CNH_2$) and 1 N HCl.

5.3.3 *In situ* X-ray data Collection during Collagen Mineralization

Two separate SBF solutions were mixed in a flow-through reactor whose temperature was maintained at 37^oC using a hot plate during mineralization (Figure 5.1a). Once the temperature and flow-rate of the solution in the reactor was stabilized, a custom-designed sample holder containing two pieces of collagen tubes was placed in the reactor (Figure 5.1b). The holder was designed to equip two stainless electrodes (dimensions, two wires twisted), and one of them was used to penetrate the collagen tube to apply electric stimulation to the inner surface (Figure 5.1c). The electrode, holding two collagen samples, were connected to a pulse generator (Siglent Technologies SDG800) as either the cathode or anode, and another electrode without samples was used as a counterpart. This mineralization process was conducted at the APS at Argonne National Laboratory (Argonne, IL, USA) for *in situ* X-ray data collection.

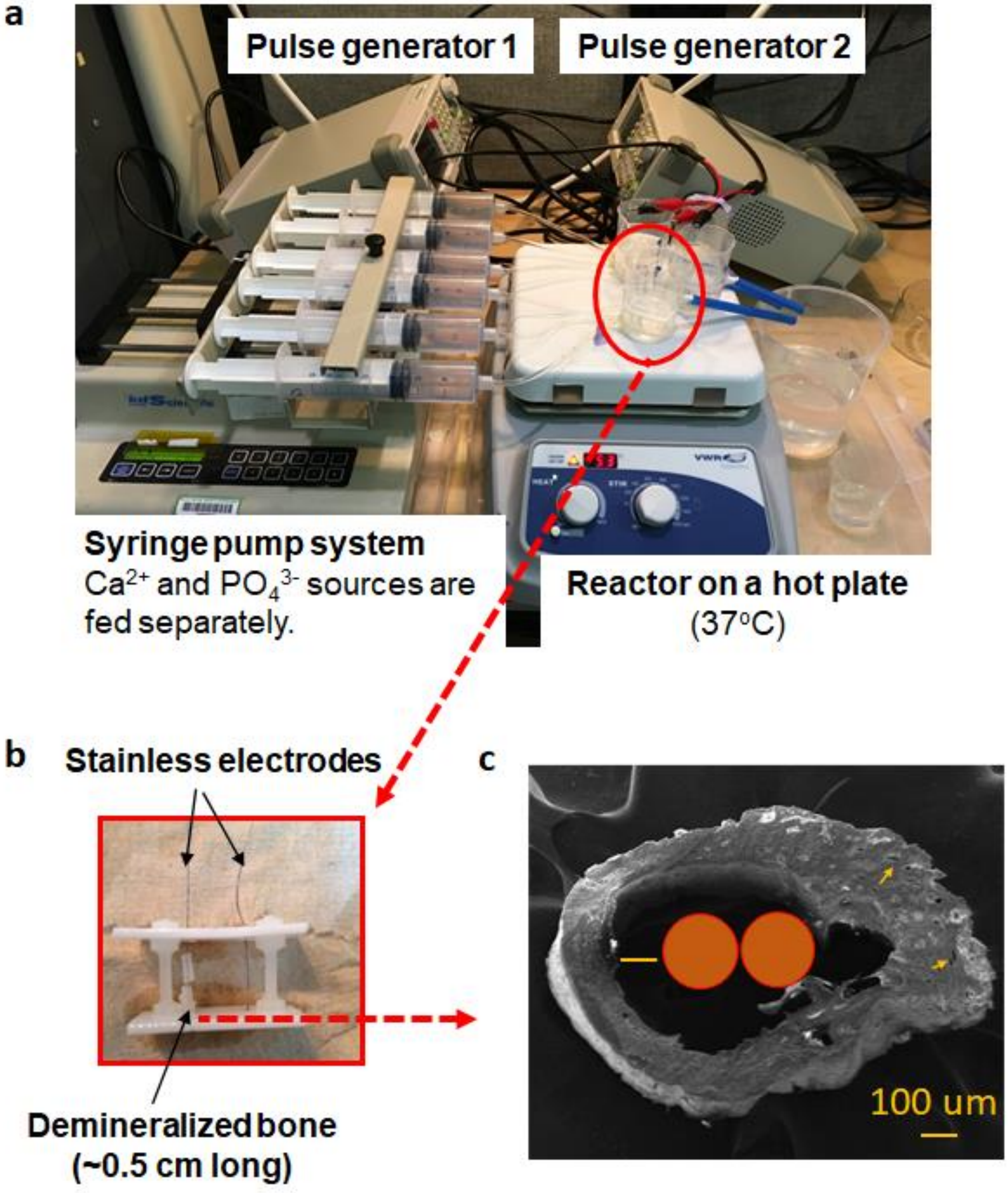

Figure 5.1 Experimental setup for collagen mineralization under electrical stimulation. (**a**) A photo of the flow-through reactor setup. (**b**) A frame with two electrodes. Two collagen scaffolds were placed one of the electrodes. (**c**) SEM images of cross-section of collagen. Two orange circles represent the electrode consists of two wires of stainless steel (200 μm in diameter).

For the SAXS measurements, samples were taken off from the electrode and then placed into a SAXS sample stage. For each SAXS scan, the sample was exposed to a 13.3 keV X-ray beam for 1 second. The size of the beam was 150 μm (horizontal dimension, parallel to the long direction of collagen) × 40 μm (vertical dimension, perpendicular to the long direction of collagen). To better represent the sample, it was scanned five times horizontally (along the fibrillar direction of collagen) by moving sample stage by 0.2 mm per scan (Figure 5.2). Then the average intensity value of five scans was taken to represent the sample. From the 2-dimenstional scattering intensity images obtained from the detector (2M Pilatus), 1-dimensional scattering intensities, $I(q)$, were extracted by averaging the sector along the vertical lines, which was perpendicular to the fibrillar direction (Figure 5.2). From the sector averaged 1-dimensional $I(q)$, we better quantify the increasing intensity from nucleation and better fit the morphology of newly formed particles without interference by peaks coming from the periodicity (~67 nm) of collagen gap and hole regions. The distance from the sample to the SAXS detector was 2 m, which provided a range of 0.0017–0.53 $Å^{-1}$ for the scattering vector, q. Silver behenate powder was used as the q calibration standard and $I(q)$ was normalized by the incident beam intensities and calibrated using a reference glassy carbon standard sample to compare absolute SAXS intensities collected from different measurements. The SAXS intensities were corrected by subtracting the intensity from air by scanning the empty sample holder.

Further SAXS data analyses were conducted using the 1-dimensional horizontal cut data. Total particle volume was estimated from the linear relationship with invariant values, $Q = \frac{1}{2\pi^2}\int q^2 I(q) dq$. Integration was conducted within a limited q range of 0.0017–0.3 $Å^{-1}$, due to the relatively high noise in larger q regions. This Q value indicates total scattering amount, thus could be considered to as proportional to particle number concentration, $N_c = \frac{Q}{r_e^2 \Delta\rho^2 V}$, when the particle morphology is uniform.[17,90] Here r_e, and V represent the classical electron radius (2.818 fm) and the volume a particle, respectively. $\Delta\rho$ is the difference in electron densities between particles and water ($\Delta\rho = 6.12\times10^{23}$ cm^{-3}, particles were assumed to be hydroxyapatite crystals and surrounded by water in collagen matrices).[99] The Modeling II tool of the IRENA package written in IGOR Pro (WaveMetrics Inc.) was provided by APS and used to fit the SAXS pattern to evaluate the particle morphology. From the morphology of individual particle, V, was calculated. Volume fraction of minerals in collagen were obtained by $f_V = V \times N_c$. Details about models used in the package is well described elsewhere.[94,99]

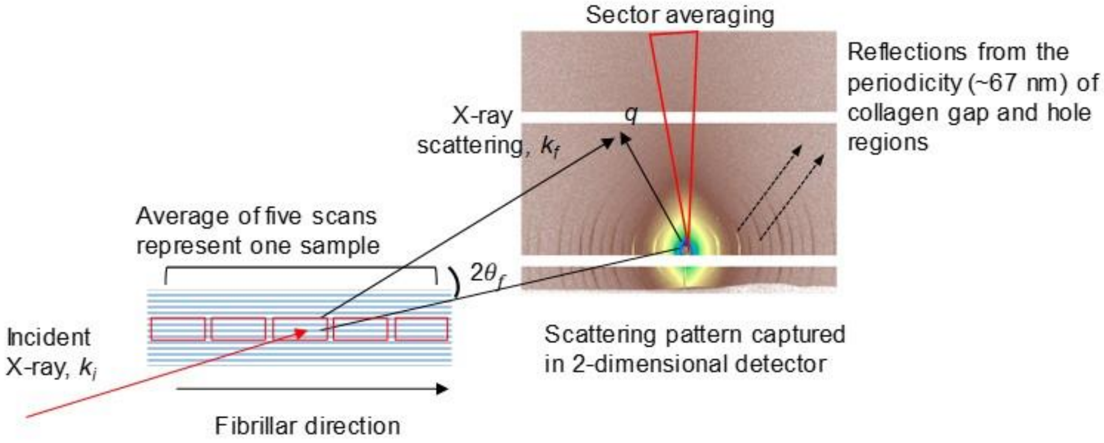

Figure 5.2 A schematic of SAXS data collection. k_i and k_f are the incident and scattered wave vectors, respectively, and $2\theta_f$ is the exit angle of the X-rays.

Similarly, *in situ* WAXD data was collected at APS sector 11-ID-B to identify the CaP phases during collagen mineralization. Every two hours during the mineralization, collagen samples were exposed to a 58.66 keV X-ray beam for 10 seconds at 95 cm distance between sample and detector (Perkin Elmer amorphous silicon detector). Due to the larger size of beam (500 μm × 500 μm) for WAXD than for SAXS, a one-time scan was used to collect the data for one spot. Then the 2D intensities were averaged over the q range along the radial direction to produce 1D intensities I(q), using GSAS-II.[159] Cerium dioxide was used as the calibration standard.

5.3.4 *Ex situ* Analyses

Cross-sections of mineralized collagen scaffolds were imaged using optical microscope and SEM. For the optical microscope imaging (Carl Zeiss Axio Scope A1m), methylmethacrylate embedded samples were cut into 5 µm sections followed by von Kossa and Goldner's trichrome staining. The embedding, sectioning, and staining processes were conducted at Musculoskeletal Research Center (Washington University in St. Louis, MO). For the SEM imaging, mineralized samples were fixed in 100 mM cacodylate buffer containing 2% paraformaldehyde and 2.5% glutaraldehyde, followed by dehydration in successive ethanol baths. Samples were sectioned in 20 µm on a freezing stage (Physitemp BFS-30MP) using sledge microtome (Leica 1400). EDX analyses were also conducted to obtained elemental compositions.

To evaluate the diffusion of Sirius Red molecule into collagen, samples were reacted under pulsed electric stimulation in phosphate buffer saline (PBS, no mineralization occurs) containing 2% of PicroSirius Red F3BA (Polysciences, Inc). The unreacted Sirius Red molecules were removed by storing samples in wet gauze. For the optical microscope imaging, 20 µm sections were prepared using freezing stage microtome without a fixing process.

To evaluate the collagen damage, collagen scaffolds experienced pulsed electric stimulation in PBS for 16 hr. For SEM images, samples were fixed and dehydrated as described above. Then, they were cut into halves along the long direction and placed on SEM stubs with the inner surface exposed for scanning. The Fourier-transform infrared spectroscopy (FTIR) absorption spectra were collected (Nicolet iS10, Thermo Scientific) without the fixing and dehydration processes.

5.4 Results & Discussion

5.4.1 Applying Pulsed Electrical Stimulation through an Electrode within Collagen Scaffolds

Pulsed electrical stimulation was applied to the tube-like collagen scaffolds prepared by demineralizing chicken fibular bones. The obtained scaffolds were chosen to best represent a dense and well-organized fibrillar type I collagen structure in compact bones.[135] Collagen was placed on either side of the cathode or anode, which penetrates inside the scaffold (Figures 5.3a–c). Then the pulsed stimulation (40 mV peak-to-peak amplitude, 1 Hz frequency, and 100 ms pulse width) was applied through the cathode to the inner surface. The re-mineralization of the collagen was conducted in a modified simulated body (SBF) fluid with 2.5 times higher Ca and P concentrations than body plasma (2.5×SBF, Table 5.1)[85,86,91] using a flow-through reaction system (Figure 5.1a). Considering the shapes and sizes of the tube-like collagen scaffold (approximately 500 µm inner diameter) and electrode (twist of two stainless wires of ~200 µm in diameter), inner surfaces were exposed to the SBF only through a narrow channel (~100–200 µm, Figure 5.1c). The size of this channel is at a scale comparable to a diameter of the central canal (~30 µm) in the Haversian system where blood travels through vessels.[4] On the other hand, the outer surfaces of collagen in our reaction system were fully exposed to the bulk SBF, allowing precursor molecules to diffuse more freely into the collagen than from the inner surfaces.

During the pulsed electrical stimulation, the pulse generator supplies electrons to the cathode (pulse on), negatively charging the vicinity of cathode for a short duration, attracting cationic precursors including Ca^{2+}. These attracted ions would diffuse back into the bulk solution when the cathode loses its negative charge (pulse off) (Figure 5.3a). During this process, anionic precursors move in the opposite direction. Therefore, the repetition of these processes by pulsed stimulation through the entire reaction time led to more active transport of these ionic precursor molecules into the narrow channel between the cathode and the inner surface of the collagen.

In typical electrolysis cells operated at >1.5 V, electron transfer at the anode occurred by the oxidation of metal components of the electrodes, or any other body fluid components.[160] However, the oxidation reactions at the anode is highly restricted at this low voltage condition (40 mV) in our experimental systems, leading to negligible changes of the anode surface. Therefore, the consequent transport of precursor molecules through the channel are expected to be less significant than at the cathode (Figure 5.3b). The anode could be stably operated during the entire set of mineralization experiments with 40 mV without significantly damaging the collagen or releasing metal components into the system.

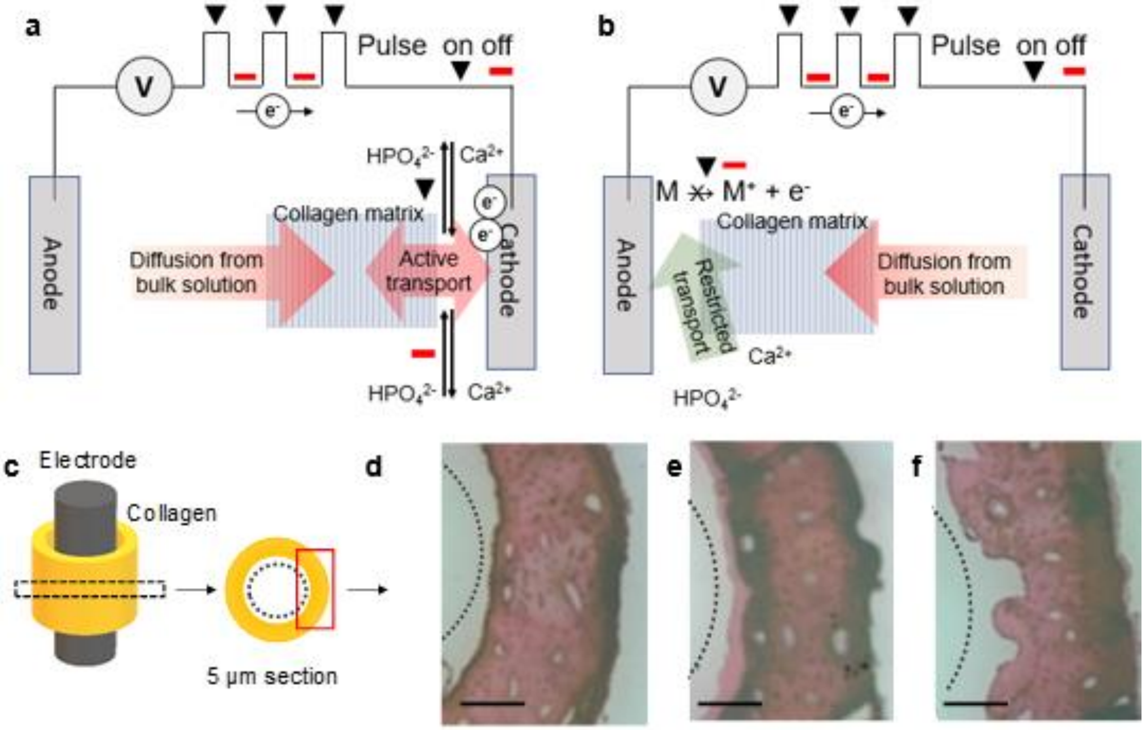

Figure 5.3 Collagen mineralization under pulsed electric stimulation. (**a–b**) Schematic illustration of collagen mineralization under pulsed electric stimulations applied on the cathode (**a**) or the anode (**b**). Oxidation of electrode ($M \rightarrow M^+ + e^-$, M represents the metal components) is limited at the anode due to the low pulse amplitude. (**c**) Illustration of collagen tube with electrode in the center. (**d–f**) 5 µm cross-sections of samples mineralized for 48 hours under the pulsed stimulation were imaged with optical microscope (**d**: control, **e**: cathode, **f**: anode control). Dotted lines indicate where electrodes were located. Scale bars are 100 µm.

5.4.2 Enhanced Inner Surface CaP mineralization of Collagen at the Cathode

Figures 5.3d–f are optical images of cross-sections of collagen after 48 hr of mineralization. More images are shown in Figure 5.4 in comparison with fresh fibular and fully demineralized bones. The sections were stained with von Kossa's and Goldner's Trichrome methods to indicate mineralized (in grey) and unmineralized collagen (in pink) regions, respectively. As suggested in Figure 5.3a, the effective inner surfaces mineralization by pulsed stimulation was achieved only when collagen scaffolds were placed at the cathode (Figure 5.3e). The inner surfaces were rarely mineralized before 48 hr without pulsed electrical stimulation (Figure 5.3d) and the inner surface mineralization was even weaker when collagen scaffolds were placed on the anode (Figure 5.3f). On the other hand, at the outer surfaces, where the diffusion of precursors from the bulk solution is freely allowed, a similar mineralization was apparent on all samples. The results indicate that restricted transport of precursors into the narrow channels between electrodes and the inner surfaces is a limiting factor of CaP mineralization. However, this limitation was effectively overcome by applying the pulsed electrical stimulation through the cathode.

To evaluate the spatial distribution of CaP minerals after 16 hr of electrical stimulation, SEM-EDX analyses were conducted. At this relatively early stage, overall mineral contents were relatively low (< 3 atomic %) except for the outermost surface, preventing us from evaluating the mineral distribution from images. Instead, EDX spectra were collected at 5 different positions from the innermost to outermost surfaces (A to E positions, Figure 5.5a). Ca and P signals at B and C positions (30 µm from A position and center position, respectively) were only detected from samples mineralized at the cathode, leading to a relatively even distribution of CaP minerals along the radial direction (Figures 5.5b–c). On the other hand, samples mineralized without pulsed stimulation (control), Ca and P were mostly concentrated only at the outer surfaces (D and E positions).

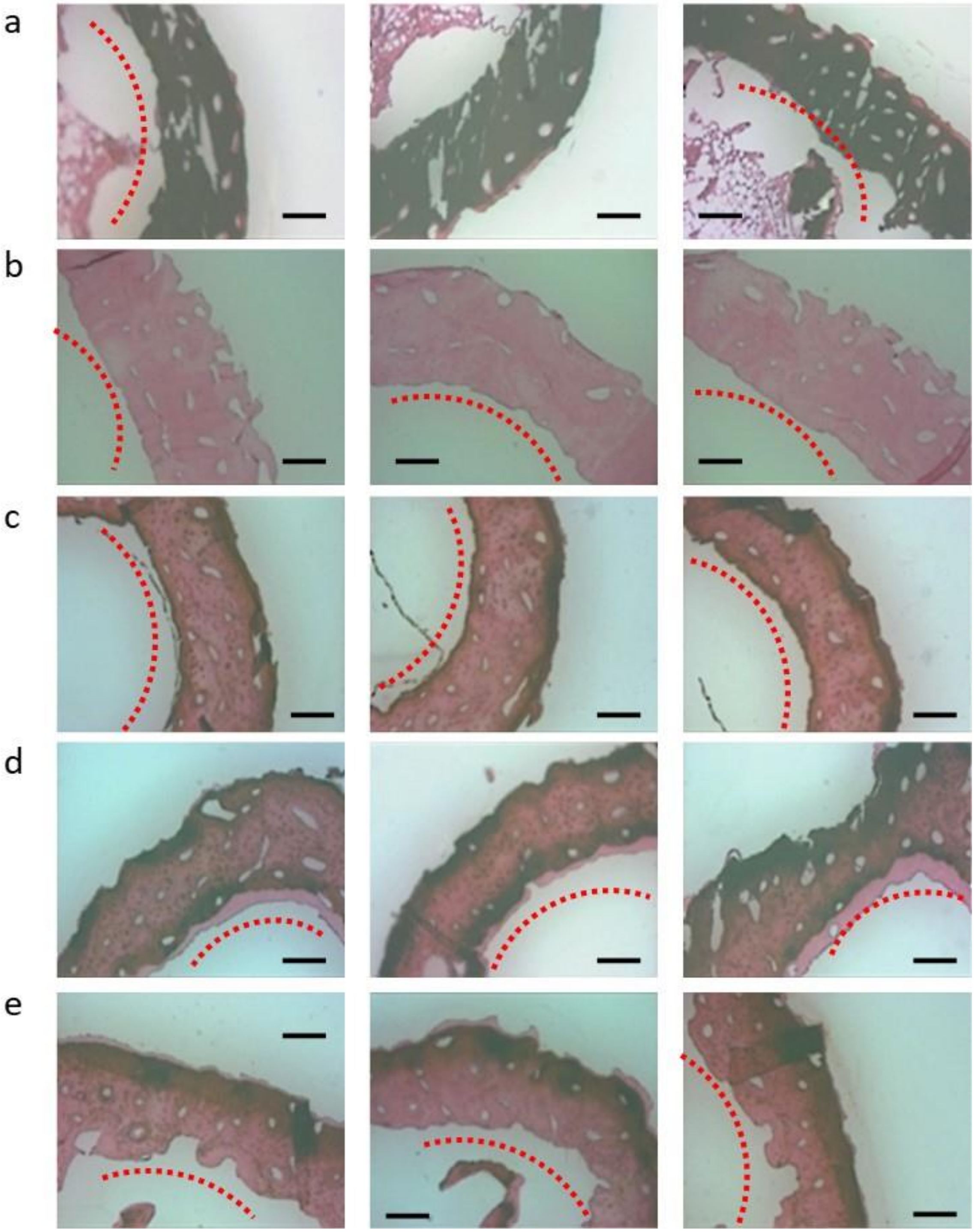

Figure 5.4 Optical images of cross-sections (5 µm) of collagen scaffold. Dotted lines indicate the outlines of innermost surfaces. Samples were stained with von Kossa's (dark: mineral) and Goldner's trichrome (pink: collagen) methods. (**a**) Fresh fibular bone (**b**) Demineralized fibular bone (**c**–**e**) Collagen mineralized for 48 hr under pulsed electrical stimulation. (**c**) Control without stimulation. (**d**) Cathode. (**e**) Anode. Scale bars are 100 µm.

Ca and P were detected at the innermost surface (A position) of the control samples, but the signals were not expanded to B position. The inner most surface mineralization was most inhibited for samples on the anode. A similar inhibited bioapatite nucleation was reported observed from a positively charged collagen under tensile stress.[161] Potentially, the slightly positively charged anode (but not sufficient to make active transport of ionic molecules in the solution) further inhibits the inner surface mineralization by not allowing initial Ca attachments at the nucleation sites on collagen surface.

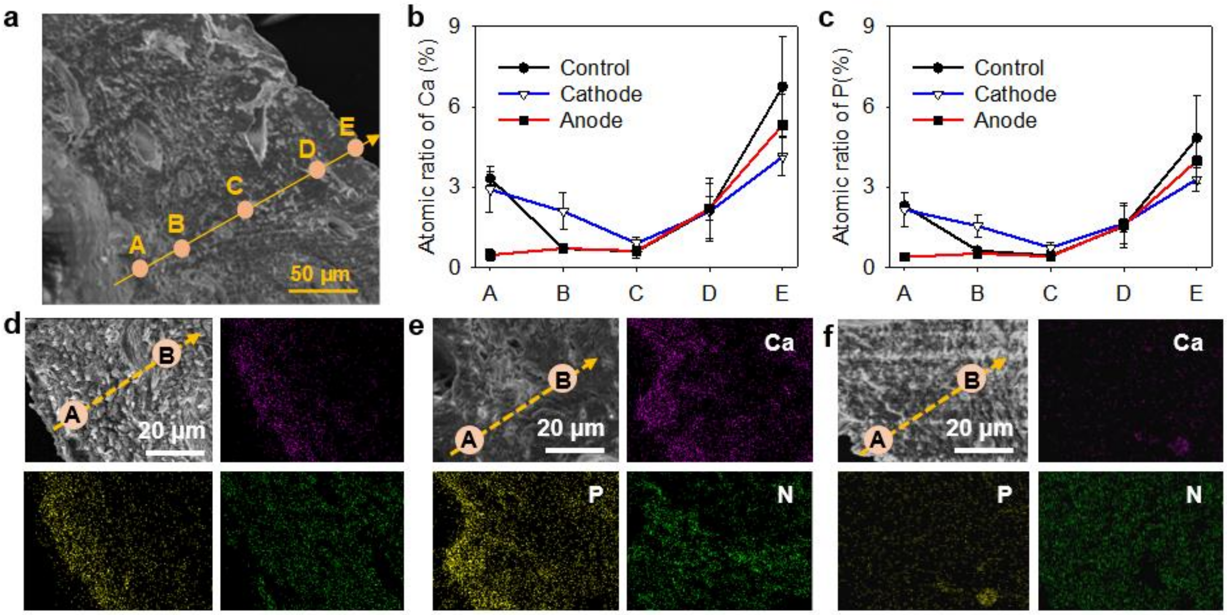

Figure 5.5 Spatial distribution of bioapatite minerals along the cross-sections of collagen. (**a**) SEM image of a collagen cross-section indicating Positions A–E for EDX spectral analyses. (**b–c**) Results from SEM-EDX spectral analysis of collagen mineralized after 16 hr. Scanning area of each position is ~8 µm × 8 µm. Error bars are standard errors from 3 different samples. (**d–f**) Elemental mappings of inner surface area of mineralized collagen: (**d**) Control with no pulsed stimulation, (**e**) cathode, and (**f**) anode.

Elemental mapping images of inner surfaces (covering A and B positions) also show the corresponding results with spectral analyses. Ca and P signals (indicated as pink and yellow dots, respectively) were evenly detected from the cathode sample (Figure 5.5e), while only a shallow layer near A position provided Ca and P signals from control samples (Figure 5.5d). No Ca and P signals were detected from the samples located at the anode where N signal from collagen was dominant (Figure 5.5f). The atomic ratio of Ca/P from all the spectra measurements were 1.32 ± 0.13, showing a typical value observable from poorly crystalline apatite during the biomineralization.[8,99]

5.4.3 Morphology and Crystalline Structure of CaP Nuclei

In situ SAXS/WAXD analyses are powerful tools to quantitatively evaluate nanocrystals embedded in organic templates without destroying the structure of both templates and nuclei.[11,99,108] Figure 5.3a shows examples of SAXS patterns of collagen after 48 hr mineralization under pulsed electrical stimulation. With mineralization, SAXS patterns show increased intensities, compared to unmineralized collagen, at scattering vector, q = 0.01–0.3 Å^{-1}. In general, higher intensities were observed from samples on the cathode than those from the other two sample groups (Figure 5.6a), indicating more CaP minerals nucleated within the scaffolds. The SAXS intensities from samples mineralized at the anode and without pulsed stimulation were within a similar range, thus two SAXS patterns were mostly overlapped in Figure 5.3a. By subtracting the unmineralized collagen SAXS pattern, we can better evaluate the morphology of CaP nuclei formed within the collagen (Figure 5.6b). All SAXS patterns after subtracting unmineralized collagen background fit well with a disc of ~1.7 nm thick and ~34 nm in diameter, which is comparable to the dimension of bioapatite plates observed in *in vitro* mineralization[8,99,126] or nature bone apatite crystals (~2 × 30 × 40 nm).[6,9,73] Collagen background subtracted WAXD patterns identified that the crystalline structure of nuclei formed in collagen scaffolds were, regardless of the location of the electrodes, all poorly crystalline HA (Figure 5.6c) which is typical of bioapatite from most animal bones.[6,136] Therefore, we concluded that bioapatite-like CaP minerals (in terms of morphology and crystalline structure) formed in the collagen scaffolds regardless of the pulsed electric conditions.

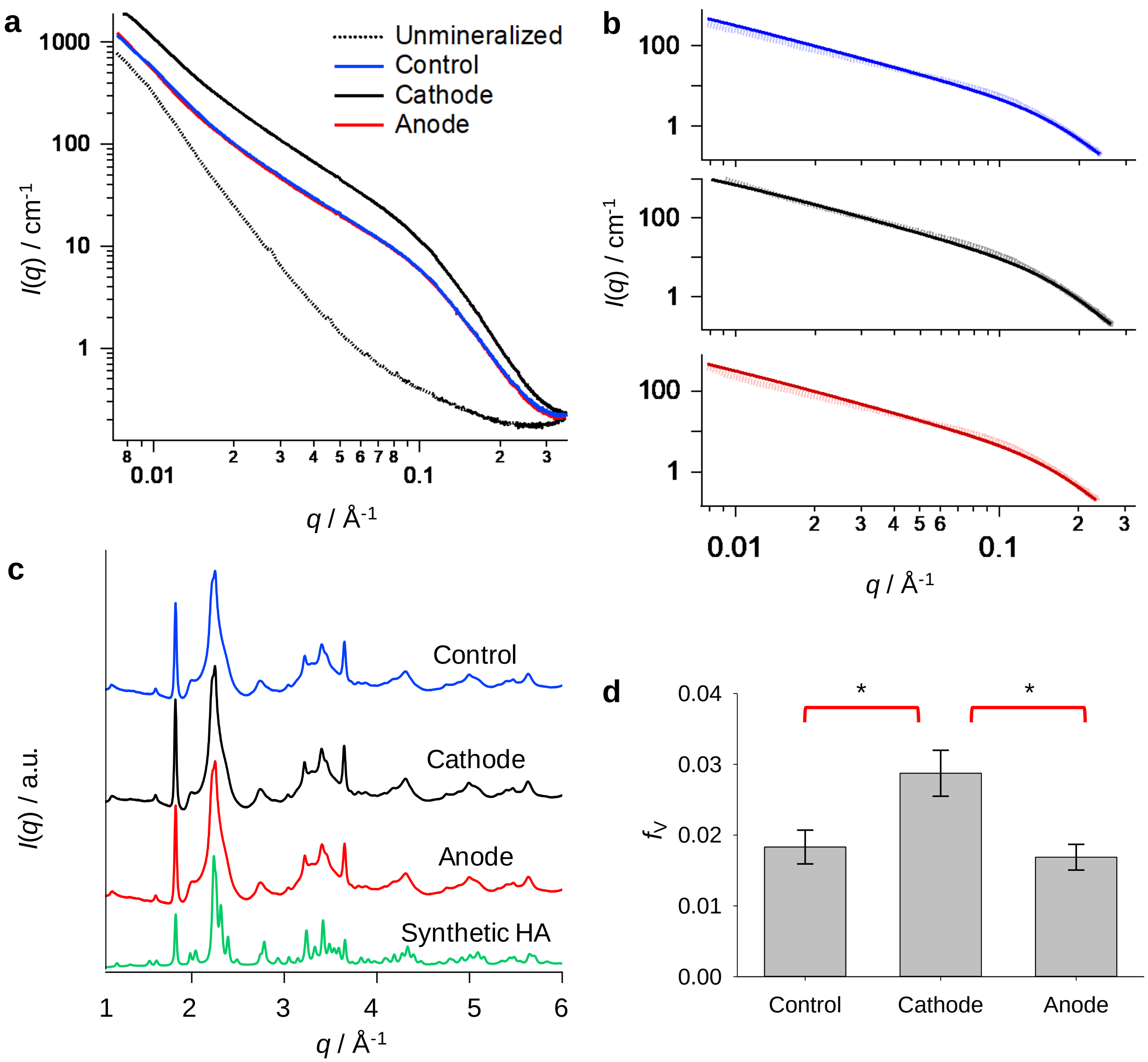

Figure 5.6 SAXS/WAXD data analysis. (**a**) Sector averaged 1-dimentional SAXS patterns of collagen mineralized for 48 hr. (**b**) Background subtracted SAXS patterns using unmineralized collagen intensity (thick dotted line). Data in (**a**) are processed. Thin solid lines show the fitting results indicating a disc-shape nucleus (1.7 nm thick and 34 nm in diameter). (**c**) WAXD patterns of collagen mineralized for 48 hr. (**d**) Volume fraction of minerals in collagen, f_V, after 48 hr CaP mineralization. Error bars are standard errors from 6 sample measurements.

The clear difference in SAXS analysis among the three groups was the absolute intensity which indicates the amounts of minerals formed in collagen. With the given morphology (from SAXS fitting) and crystalline structure (from WAXD), we can quantitatively provide the volume fractions of newly formed CaP minerals, f_V (Figure 5.6d)[11,83,99,133]. The f_V increased by about 57% from pulsed stimulation applied through the cathode compared to the control with a statistically significant difference ($p < 0.05$, TukeyHSD post-hoc test to ANOVA). On the other hand, the f_V of samples at the anode were slightly reduced (~8%) from the control group, but the difference was within the error range. The difference in f_V at the later time period (48 hr) is more significant than Ca and P contents detected from SEM-EDX at the early time period (16 hr, Figure 5.5b–c). A potential reason of the similar nucleation rates at the early stage is that the total amounts of precursors available in the reactors are the same for all conditions. However, for samples on the cathode, both inner and outer surfaces could be mineralized, providing about twice as many nucleation sites as under other conditions. Therefore, the increase in f_V by the cathode application mostly comes from inner surface mineralization after 16 hr, when the mineralization sites on the outer surfaces are almost saturated (Figure 5.3d–e).

5.4.4 Enhanced Transport of CaP Precursors by Pulsed Electrical Stimulation.

In Figure 5.3a, we suggested a mechanism of active transport of precursor molecules within the narrow channel between the cathode and the inner collagen surface by the pulsed electrical stimulation. To evaluate the actual transport of molecules into the channel, and their consequent diffusion into collagen matrices under different electric conditions, we traced the diffusion of Sirius Red (molecular weight, MW is 1,373 g mol^{-1}) in a phosphate buffer saline (PBS) at pH 7.4. This red fluorescent molecule would exist as a divalent anion in the PBS, based on its pK_a values ($pK_{a1\text{-}6} < 2$ and $pK_{a7,8} > 13$).[162] Because it is commonly used to stain collagen, we can easily trace the transport of these molecules within the collagen matrix by optically imaging the cross-section of samples.[144] Sirius Red staining of the inner surface of the collagen was achieved only by the pulse application through the cathode, while the staining of the outer surface was similar regardless of the electrode (Figure 5.7). The staining pattern under the pulsed stimulation is almost identical to the mineralization pattern shown in Figures 5.3d–f. The diffusion of Sirius Red from the innermost surface was also not as significant under the continuous electrical stimulation (40 ± 0.5 mV). The continuous stimulation would result in a permanent net negative surface charge at the cathode, as illustrated in Figure 5.8a. The low amplitude of the stimulation would not influence the charge distribution at the anode under the continuous stimulation (Figure 5.8b). As a consequence, almost no differences in f_V (Figure 5.8c) and crystallinity (Figure 5.8d) among different electrodes were observed under the continuous stimulation.

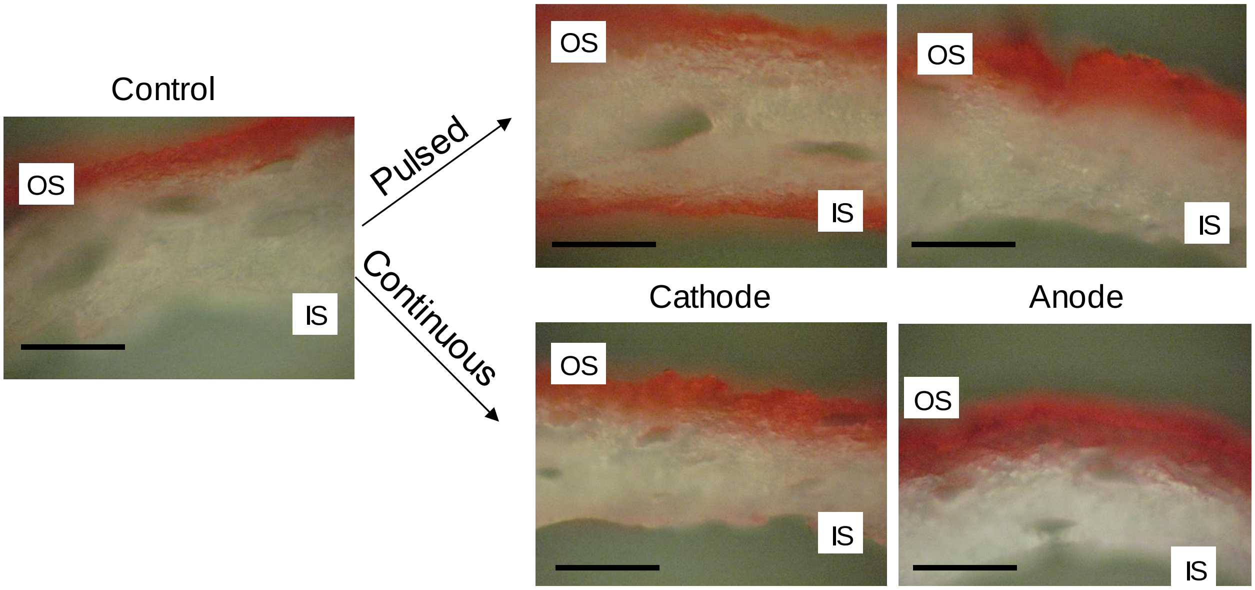

Figure 5.7 Optical microscope images of cross-sections of collagen after staining with Sirius Red. OS: outside and IS: inside collagen. Samples were reacted in PBS for 16 hr under different electric stimulation conditions. Scale bars 50 um.

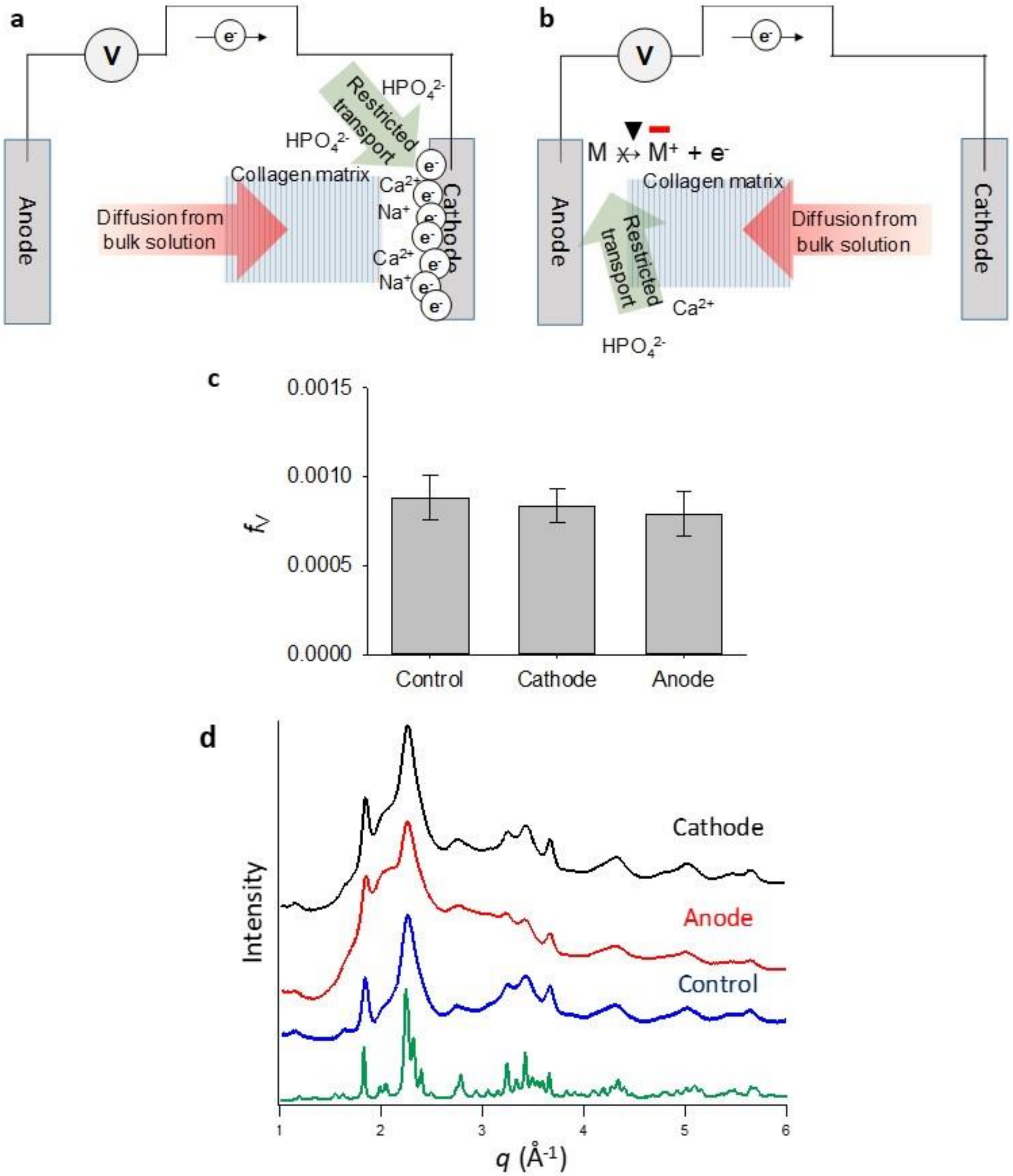

Figure 5.8 Collagen mineralization under continuous electrical stimulation (40 ± 0.5 mV). (**a,b**) Schematic illustration of suggested mechanisms for collagen mineralization at the cathode and the anode. (**c**) Volume fractions of minerals, f_V, were evaluated from SAXS measurements after 48 hr of mineralization. (**d**) WAXD patterns of mineral formed in collagen after 16 hr of mineralization.

Table 5.2 Aqueous Ca and P species in 2.5×SBF solution.

Charge	Species	Conc. (M)*	Ca fraction (%)	P fraction (%)
+2	**Ca^{2+}**	**5.69 x 10^{-3}**	**91.0**	**-**
+1	$CaHCO_3^+$	1.57 x 10^{-4}	2.5	-
	$CaOH^+$	3.14 x 10^{-8}	< 0.1	-
	$CaH_2PO_4^+$	1.19 x 10^{-5}	0.2	0.5
	$MgH_2PO_4^+$	6.31 x 10^{-6}	-	0.3
0	$CaHPO_4$	3.00 x 10^{-4}	4.8	12.0
	$MgHPO_4$	9.97 x 10^{-5}	-	4.0
	$CaSO_4$	4.59 x 10^{-5}	0.7	-
	$CaCO_3$	1.37 x 10^{-5}	0.2	-
	H_3PO_4	1.22 x 10^{-9}	-	< 0.1
	CaH_2-pAsp**	5.25 x 10^{-27}	< 0.1	-
-1	$NaHPO_4^-$	6.76 x 10^{-4}	-	27.0***
	$H_2PO_4^-$	2.62 x 10^{-4}	-	10.5
	$CaPO_4^-$	3.49 x 10^{-5}	0.6	1.4
	$KHPO_4^-$	2.46 x 10^{-5}	-	1.0
	$MgPO_4^-$	1.31 x 10^{-7}	-	< 0.1
	CaH-pAsp**	3.56 x 10^{-23}	< 0.1	-
-2	**HPO_4^{2-}**	**1.08 x 10^{-3}**	**-**	**43.2**
	Ca-pAsp**	4.44 x 10^{-20}	< 0.1	-

*Calculated by MINEQL+ (ver. 4.61).

**Ca-pAsp complexes were calculated based on the amount of aspartyl residue in pAsp (10 mg L^{-1} pAsp is equivalent to 0.072 mM aspartyl residue). Dissociation and calcium binding constants of pAsp were obtained from literature[102].

*** The fraction of $NaHPO_4^-$ among Na species is only 0.5%, while 99.4% is Na^+.

The findings indicate that a pulsed application successfully enhanced the transport of nucleation precursor molecules through the narrow channel without aid of any bone-forming cell activity, and this enhanced transport consequently led to increased mineralization of the inner collagen surface. As summarized in Table 5.2, most of the Ca and P species, which are important precursor molecules for bioapatite minerals, exist as divalent ions (91% Ca^{2+} and 43% HPO_4^{2-}) in our experimental condition. Only a small fraction of Ca was complexed with pAsp (MW is ~5,000 g mol^{-1}), which were added to prevent undesirable extrafibrillar mineralization.[99] Because the majority of the ionic precursors in the SBF have smaller sizes per charge compared to the Sirius Red molecule, these ionic Ca and P precursors would be more actively responsive to the pulsed stimulation in physiologically relevant conditions than we observed from the diffusion of Sirius Red as shown in Figure 5.7.

5.4.5 Increasing Pulse Amplitude and Collagen Stability

To better utilize the pulsed electrical stimulation through the cathode, we evaluated the influence of pulse amplitude (0–200 mV) on collagen mineralization. An increasing trend in f_V occurred along the amplitude at 8 hr, however the difference soon disappeared at around 12 hr (Figure 5.9a). Then, only 40 mV amplitude showed a noticeable increase in f_V compared to that from the control sample. Potential damage of collagen at a higher amplitude might be the reason for limited collagen mineralization. The inner surface of the collagen stored in PBS for 16 hr without stimulation shows rough fibers (Figure 5.9c) a few microns in diameter (Zoomed in image of Figure 5.9c). With the 40 mV pulsed stimulation, the rough surface was mostly maintained (Figure 5.9d). However, the surface was mostly flattened after applying 200 mV pulsed for 16 hr, indicating the fibers at the outer surface disappeared (Figure 5.9e), leaving residues of broken fibers (Zoomed in image of Figure 5.9e). Similar damage was observed in a previous study of skin collagen under photoirradiation,[163] indicating that there is a possibility that some portions of the inner surfaces mineralized were lost by the pulsed stimulations at 100 and 200 mV amplitudes. However, there was no discernable change in the molecular level structure as observed in FTIR spectra (Figure 5.9b) after 16 hr, so it is unclear yet that the electrical stimulation can change the properties of the collagen surface to inhibit the nucleation What we can conclude from these data sets is that 40 mV pulses increase nucleation rates without significant collagen damage.

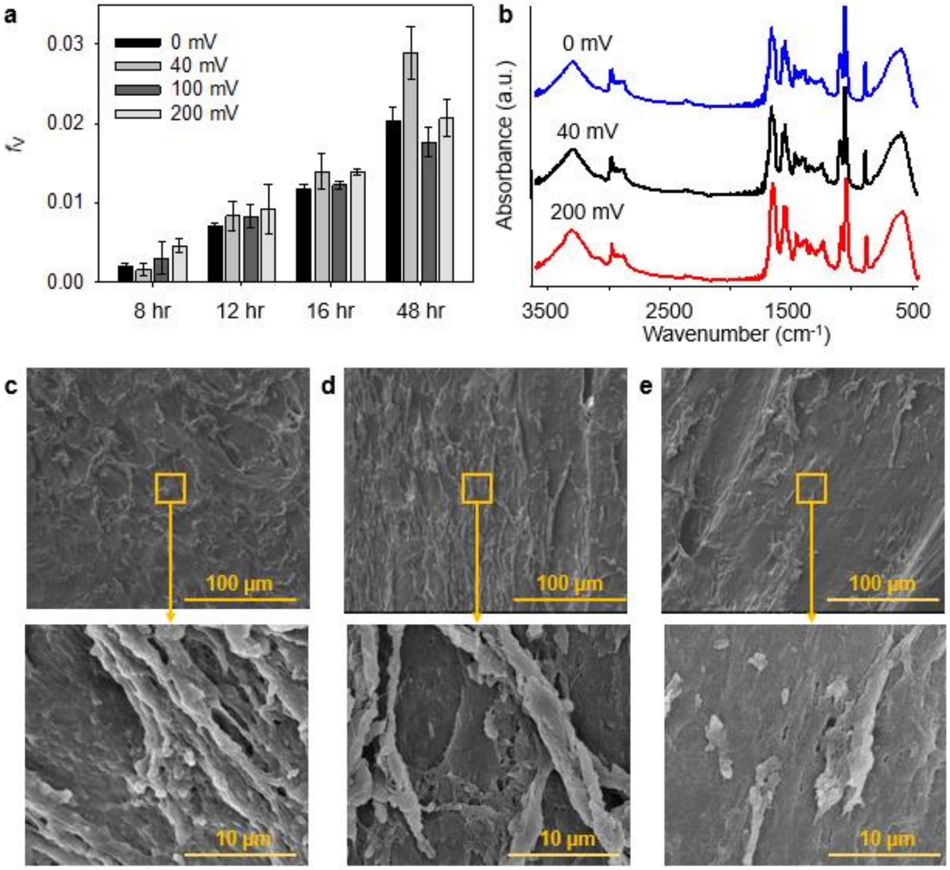

Figure 5.9 Influence of pulse amplitude on the mineralization kinetics and stability of collagen at the cathode. (**a**) Changes in volume fraction (f_V) of minerals in collagen evaluated from SAXS measurements. Up to 16 hr, same samples were measured repeatedly (*n* = 4 for 40 mV, n = 2 for 100–200 mV), while 48 hr samples were just measured once at the end of the experiments (*n* = 6 for 40 mV, *n* = 4 for 100–200 mV). Error bars are standard errors. (**b**) FTIR absorption spectra of collagen under the pulsed stimulation for 16 hr in PBS. (**c–e**) SEM images of inner surface of collagen for 16 hr in PBS with 0 (**c**), 40 (**d**), and 200 mV (**e**) pulse amplitudes.

5.5 Conclusions

In this study, we show how acellular pulsed electrical stimulation enhances collagen mineralization kinetics while maintaining the physical stability of the scaffold. By controlling the transport of ionic precursor molecules through the narrow channel, we were able to control the spatial distribution of CaP in collagen scaffolds. This provides new insights into utilization of electric signals for bone-fracture healing and improved biomaterials, and also emphasizes the localized application of pulsed stimulation for mineralization in a narrow space, where diffusion of precursor molecules is highly restricted.

By combining recent advances in engineering, the improved understanding of the influence of electrical stimulation on biomineralization is expected to increase less-invasive treatment options for bone fracture healing, while contributing to the development of better biomaterials. For example, application of medical microbots may accurately deliver well-controlled electrical stimulation to the targeted area at microscale-level.[164] Installing small piezoelectric or triboelectric devices[158,165-168] and injecting a conductive bio-scaffold[169-172] can be future options to utilize biologically generated pulsed electricity for tissue regeneration. Photoactivated materials can be alternatively used with pulsed irradiation to stimulate osteogenic differentiation by simulating bio-generated electric conditions in physiological systems.[173] In addition, by revealing the principles governing mineral arrangements within the fibrillar matrix, pulsed electrical stimulation can be used to synthesize highly compatible biomaterials, mimicking details of human tissues.[174-176] For instance, controlling spatial distribution of mineral to create a gradient in mineral density along the matrix can contribute to developing improved tendon-to-bone insertion replacement.[167,177,178]

5.6 Acknowledgments

The Nano Research Facility, the Institute of Materials Science & Engineering, and Musculoskeletal Research Center at Washington University in St. Louis provided their facilities for the experiments. We thank Prof. J. Ballard for carefully reviewing the manuscript. The project was supported by the National Science Foundation (DMR-1608545 and DMR-1608554). Use of the Advanced Photon Source (sectors 12-ID-B and 11-ID-B) at Argonne National Laboratory was supported by the U.S. Department of Energy, Office of Science, Office of Basic Energy Sciences, under Contract No. DE-AC02-06CH11357.

Reprinted with permission from [Doyoon Kim, Tong Wu, Melanie Cohen, Inhyeong Jeon, and Young-Shin Jun, Designing the crystalline structure of calcium phosphate seed minerals in organic templates for sustainable phosphorus management. *Green Chemistry*, 2018, 20, 534–543. DOI: 10.1039/C7GC02634J]. Copyright [2018] Royal Society of Chemistry.

Chapter 6. Application II: Bioinspired Environmental Remediation Strategy for Sustainable Phosphorus Management

Portions of this chapter have been published in *Green Chemistry* in 2018, DOI: 10.1039/C7GC02634J.

6.1 Overview

The purpose of this chapter is to extend the knowledge obtained from our biomineralization study to the realm of environmental remediation. In previous chapters, we discussed the nucleation behaviors of calcium phosphate (CaP) minerals in organic templates and considered how to control nucleation kinetics for engineering applications. Nucleation kinetics are highly influenced by aqueous chemistry, and by engineering the kinetics, we can manage aqueous environments. Just as bones effectively maintain the phosphorus (P) balance in the human body, we can develop a sustainable environmental P management plan utilizing these principles.

Global P should be managed more sustainably to secure food, energy, and water for a growing population. Despite the abundance of calcium in most environments, we have not fully utilized its thermodynamic stability to form CaP for aqueous P management. In this study, we showed that the energy barriers to CaP nucleation can be reduced by seeding reactive CaP nuclei in calcium alginate beads. The CaP nucleation kinetics enhanced by seeds effectively immobilized aqueous P into the macroscale beads, which can be reused as a slow-release fertilizer. Given that more developed CaP crystalline seeds have a lower solubility than does an amorphous structure, equilibrium P concentration was regulated successfully by the seed crystallinity during both the removal and release processes. A simultaneous seed nucleation during alginate gelation enabled control of the degree of the seeds' crystallinity without using any hazardous substance or additional energy input. Poorly crystalline hydroxyapatite CaP seeds effectively decreased aqueous P concentration from 200 to 22.7 µM within one day at a final pH 7.2 (96.4 mg P g^{-1} dry seed). After P recovery, the beads were moved to a P-deficient environment to be evaluated as a slow-release fertilizer. Utilizing the thermodynamic stability of CaP at neutral pH, this approach highlights a potential application of naturally abundant biomaterials for sustainable P management.

6.2 Introduction

Recent anthropogenic activities, such as deforestation and fertilization, have doubled natural dissolved P fluxes.[179,180] This increased release is turning P into a pollutant that poses significant threats, such as mass die-offs of aqueous organisms owing to significant eutrophication in local aquatic systems.[181,182] On the other hand, the sustainability of the global P cycle will also be significantly endangered by an increase in P mining from limited natural sources to supply fertilizers for agricultural production. Unfortunately, these mines are located in only a few countries, such as Western Sahara, which is the largest P rock exporter to Europe.[182,183]

Recycling P from wastewater streams or eutrophic water bodies can be an environmentally sustainable approach to mitigate the imbalance of the global P cycle, securing food and water for a growing population.[184-186] P recovery as struvite ($MgNH_4PO_4 \cdot 6H_2O$) is a promising strategy in enhanced biological P removal facilities with anaerobic digesters.[185,187,188] Where this centralized treatment option is not feasible, such as in the remediation of eutrophic reservoirs, then other approaches, including chemical precipitation,[185] constructed wetlands,[189] and column filtration,[190,191] can be used to prevent P pollution of aqueous environments. These strategies rely highly on chemical reactions, such as sorption and ion exchange between phosphate and cationic Ca, Fe, or Al species in solutions or on the surfaces of natural or engineered materials.[188,191] In particular, P removal efficiency has shown good correlations with the CaO and Ca contents in filter materials (R^2 = 0.51 and 0.43, respectively).[191] While many of these materials have shown effective P removal, challenges still handicap practical operations: For example, filtration materials can become clogged, thus reducing the interval between replacements.[187,191] The pH of effluents is another important concern, because many CaO or Ca-bearing materials often result in treated effluent pH higher than 10,[191-195] thus requiring secondary pH adjustment or buffering chemicals. Chemical precipitation using ferric or aluminum salts also needs to be operated at pH below 5 to prevent undesired hydroxide mineral formation.[185,196] Additionally, these approaches have some limitations for on-site restoration, such as of eutrophic lakes, because many sorption and precipitation reactions are easily reversible.[190,197] In other words, if the immobilized P is not totally separated from the environment, P can be released again when the water chemistry changes for natural or anthropogenic reasons.[198]

While evaluating the water quality of eutrophic environments in the USA,[199,200] we found that many groundwater samples in the Chesapeake Bay and the available data set from Louisiana area were indeed supersaturated with respect to hydroxyapatite (HA, $Ca_5(PO_4)_3OH$), which is the most thermodynamically stable calcium phosphate mineral (CaP) at neutral pH (More discussion of the saturation index (SI) and aquatic components in these areas is available in Section 6.7.1).[201] P concentrations in these areas remain higher than those at equilibrium condition, thus increasing the risk of eutrophication. Further, this risk can be significantly enhanced during summers in certain areas, where P-binding iron oxides are abundant because these minerals are reductively dissolved by the decreasing dissolved oxygen level with increasing temperature.[202] Interestingly, a similar situation involving maintaining an HA-supersaturated condition without precipitation can be found in physiological body fluid systems (pH 7.4).[2,6,85] Recent studies demonstrated that a combined structure of CaP nuclei and fibrillar collagen protein is a key to the bone mineralization, driving the deposition of aqueous Ca and P species in specific locations within the fibrillar structure.[26,47] This process can provide useful insights for regulating P levels in environmental aqueous systems with high nucleation energy barriers.

Here, we propose a new strategy to manage P in aqueous systems by recovering it from nutrient-rich aqueous solutions and reusing it as a slow-releasing fertilizer. We hypothesize that a composite material of biological substrates and embedded mineral seed nuclei can help overcome the nucleation energy barrier for CaP in aqueous environments supersaturated with HA. As a biological organic substrate, calcium alginate ($(C_{12}H_{14}CaO_{12})_n$) bead was chosen due to its abundance in nature and its benign properties.[203] Furthermore, its biodegradation in soil, which produces the most basic units of carbohydrates, such as uronic acids, makes it environmentally sustainable as a fertilizer.[204,205] Replacement of Na^+ by Ca^{2+} in the alginate structure naturally forms a spherical bead.[203] This form has been effectively used to encapsulate synthetic nanoparticles or minerals utilized for their catalytic[206-208] and adsorptive properties[209-211] in environmental applications. Unlike previous applications that simply embed pre-synthesized or stable natural minerals, in this study, we initiated the nucleation of reactive CaP seed mineral particulates directly from ionic precursors during the beads' formation. This straightforward preparation allowed a better control of the crystalline structures of seed minerals without using any hazardous substance or additional energy input.[212] To our knowledge, no previous studies have utilized the properties of calcium phosphate minerals with different crystallinities in alginate beads for P management in aqueous systems. For comparison with the CaP seed minerals, we also utilized calcium carbonate ($CaCO_3$),[17,175,213] which is another representative biomineral, to simulate potential substrates for CaP nucleation in natural systems.[214]

Therefore, the goal of this study was to investigate the feasibility of mineral–organic composites prepared from naturally abundant resources for P management in aqueous systems at neutral pH. The degree of CaP seed crystallization in the beads was evaluated as a critical factor governing the equilibrium P concentration during the removal and release processes. The findings suggest that engineering the thermodynamic driving force of CaP nucleation is a promising way to regulate P levels in both P-abundant and P-deficient environments as a green chemistry solution.

6.3 Materials and Methods

6.3.1 Preparation of Ca-alginate Beads

All chemicals used in this study were at least ACS grade, and solutions for the experiments were prepared using deionized water (> 18.2 MΩ-cm, Barnstead ultrapure water systems). Four different types beads were synthesized: calcium alginate beads without any seed mineral (Ca-Alg), and beads with CaP, $CaCO_3$, and both CaP and $CaCO_3$ (called Ca-Alg/CaP, Ca-Alg/$CaCO_3$, and Ca-Alg/CaP+$CaCO_3$, respectively). Ca-Alg beads were prepared by slowly adding 2 mL of sodium alginate solution (6 mg mL^{-1}, Spectrum Chemical SO106) dropwise into a 50 mL Ca bath (180 mM $CaCl_2$ and 20 mM NaOH) with mild stirring at room temperature. Each droplet of the solution immediately formed one spherical Ca-Alg bead (2.8 ± 0.2 mm in diameter, Table 6–S1). To seed CaP or $CaCO_3$ nuclei inside Ca-Alg beads, 35.2 mM Na_2HPO_4 or 119.0 mM $NaHCO_3$ were mixed into the sodium alginate solutions, respectively. CaP or $CaCO_3$ nuclei formed simultaneously with the formation of beads. The SI values of the reaction solutions, defined as the ion activity product (IAP) over the solubility product (K_{sp}) in log scale, were calculated using Visual MINTEQ (ver. 3.1). The SI values of solutions forming CaP and $CaCO_3$ nuclei were 27.6 for HA and 4.3 for calcite, respectively. Photographs of the four bead types are shown in Figure 6–S3, with particle size analyses and dry weight measurements in Table 6–S1.

Seeds of three different degrees of crystallinity in Ca-Alg/CaP beads were obtained by varying the OH^- concentrations (0, 10, and 20 mM NaOH) in Ca baths. Most CaP minerals, including HA, show lower solubility at higher pH.[201] We, therefore hypothesized that the addition of OH^- caused seed nuclei to form in a solution with higher SI with respect to HA, and that the higher SI provided a greater driving force for HA nucleation, leading to formation of seed minerals with higher crystallinity. All beads, after dropwise addition, were stored in the Ca bath for four hours, during which time they settled onto the bottom of the bath. The beads were rinsed with deionized water five times to remove unreacted phosphate or carbonate precursors before being used for batch experiments. For the reference samples used to compare the mineral crystallographies in systems, synthetic HA (purchased from ACROS Organics™) and octacalcium phosphate (OCP, synthesized as described by Arellano-Jiménez *et al*.[215]), and Iceland spar calcite crystals from Chihuahua, Mexico, (purchased from Ward's Science, USA) were used.

6.3.2 P removal and Release Experiments

To evaluate the P removal efficiencies of beads with different seed nuclei, batch experiments were conducted in both HA-supersaturated (2 mM $CaCl_2$, 10 mM NaCl, and 0.2 mM Na_2HPO_4) and HA-undersaturated (0 mM $CaCl_2$, 10 mM NaCl, and 0.2 mM Na_2HPO_4) solutions. The SI value for the HA-supersaturated condition was 11.8 at an initial pH of 7.8 ± 0.1. However, with respect to calcite, the system was undersaturated at pH < 8. (Detailed SI values at different pH values are available in the Supporting Information for this chapter). Beads prepared from a 2 mL volume of the sodium alginate solution were added to 100 mL of HA-supersaturated and undersaturated solutions with mild stirring. At 2, 5, and 22 hours of reaction time, 2 mL of solution from each batch was filtered (0.45 μm) and diluted with 1% trace metal HNO_3 for analyses of Ca and P concentrations, using inductively coupled plasma-optical emission spectrometry (ICP-OES, PerkinElmer Optima 7300DV). To evaluate the P removal efficiencies of different crystallinities of CaP seed nuclei prepared with varying OH^- concentrations in the Ca bath, similar batch experiments were conducted under the HA-supersaturated condition (SI = 11.0 at initial pH 7.6 ± 0.1).

To test the potential reuse of beads as a fertilizer, the release of P from beads was also evaluated. The beads were transferred to a fresh batch containing no phosphate ions (2 mM $CaCl_2$ and 10 mM NaCl, initial pH 6.8 ± 0.1) after P removal experiments. Changes in P concentrations were measured until equilibrium (up to 24 hours, called one cycle), then the beads were transferred to another P-free solution batch to repeat the experiments. In total, three cycles of batch experiments were conducted using same beads to evaluate how seed minerals control the equilibrium P concentrations over multiple cycles with a decreasing amount of available P from the beads. In addition, to evaluate P release kinetics in a soil-relevant condition, sand column experiments (cross-sectional dimension 2.5 × 2.5 cm) were conducted. The columns were packed with a 5 cm thickness of acid-rinsed sand on top of a 3 cm thick gravel layer, then beads prepared from 5 mL of sodium alginate solutions were applied on top of the column. Then, 10 mM NaCl solution was injected at a flow rate of 80 mL h^{-1} for 4 hours. Effluent was collected for every 30 minutes for P quantification. To quantify P during the releasing experiments, the colorimetric molybdenum blue method was used by measuring the maximum absorbance at 880 nm with a UV-visible spectrophotometer (Thermo Scientific Evolution 60S).[216] Duplicate batch experiments were conducted for both P removal and release experiments.

Because HA mineralization releases protons (e.g., $5Ca^{2+} + 3HPO_4^{2-} + OH^- \rightarrow Ca_5(PO_4)_3OH + 3H^+$),[8] the pH of the solutions slightly decreased during P removal and increased during P release.

To fairly compare the final P concentrations from different experiments at similar final pH ~7, the initial pH values for different experiments were adjusted to 6.8–7.8.

6.3.3 Characterization of Beads and Seed Minerals

SEM and X-ray diffraction (XRD) were used to identify the seed minerals in the beads. Ca-Alg/CaP beads prepared at different OH^- concentrations were further characterized by multiple synchrotron-based X-ray analyses: WAXD, X-ray pair distribution function (PDF), and ultra-small- and small-angle X-ray scattering (USAXS and SAXS). The characterization data was obtained at the APS at sectors 9-ID-C, 11-ID-B, and 12-ID-B. Detailed procedures can be found in Section 6.6.2 of the Supporting Information for this Chapter.

6.3.4 Thermodynamic Calculations

For the HA-supersaturated system, concentrations of Ca and P species in equilibrium with different minerals at pH 5–10 were calculated using a script written in MATLAB (Mathworks, USA) with the following input solubility products: $K_{sp}=10^{-58.5}$, $10^{-48.4}$, $10^{-6.62}$, and $10^{-8.48}$, respectively for HA ($Ca_5(PO_4)_3OH$),[104] OCP ($Ca_8H_2(PO_4)_6 \cdot 5H_2O$),[217] dicalcium phosphate dihydrate (DCP, $CaHPO_4 \cdot 2H_2O$),[218] and calcite (CC, $CaCO_3$).[219] SI values for these phosphate minerals were also calculated, and the procedures and results are detailed in Section 6.6.3 of the Supporting Information for this Chapter. A potential formation of struvite is also evaluated in Section 6.7.3 of the Supporting Information for this chapter.

6.4 Results & Discussion

6.4.1 Characterization of Beads with Different Seed Minerals

Ca-Alg beads with no seed mineral did not exhibit specific crystalline phases (Figure 6.1a), showing both relatively flatter alginate surfaces (circle in Figure 6.2a) compared to other systems and porous structures (inset of Figure 6.2a) in SEM images. A small sharp peak was observed in their XRD pattern at 2 theta = 29.5°, which corresponds to the strongest peak of calcite (Figure 1a). We postulated that a small fraction of calcite formed inside the Ca-Alg during the formation of beads in the Ca bath. In the Ca bath containing 20 mM of NaOH (pH above 12), calcite could form in the open carbonate system without any additional source of carbonate (Figure 6–S4a). Additions of phosphate precursors nucleated poorly crystalline HA-like CaP seed minerals. The XRD pattern of Ca-Alg/CaP was similar to that of the synthetic HA reference sample, but peaks from individual crystalline faces were not as fully developed (Figure 6.1b) as those from the synthetic HA. No individual crystal particles were apparent in the SEM images of the surface of Ca-Alg/CaP, but increased surface rippling was observed after seeding CaP nuclei in Ca-Alg (Figure 6.2b). CaP seed nuclei might be tightly bound or fully embedded in the alginate structure, presumably filling the porous structures. This structure can be achieved through our approach of forming seed nuclei simultaneously with the gelation of beads. In the Ca-Alg/$CaCO_3$ system, a clear calcite structure was observed in the XRD pattern (Figure 6.1c). Correspondingly, in Figure 2c, rhombohedral calcite crystals are visible on the surface of the beads.

The XRD patterns of Ca-Alg, Ca-Alg/CaP, and Ca-Alg/$CaCO_3$ did not change after 22 hours of reaction under the HA-supersaturated condition, indicating that no existing crystalline phase disappeared, and no noticeable crystalline phase was newly formed. A change in the XRD pattern was observed only for Ca-Alg/CaP+$CaCO_3$, which transformed the phase of nuclei from amorphous to poorly crystalline HA (Figure 6.1d). Because the broad XRD peak of amorphous nuclei corresponds to the strongest peak of calcite, the dominant phase of nuclei is expected to be amorphous calcium carbonate (ACC) containing a relatively large amount of phosphate. In the SEM images of Ca-Alg/CaP+$CaCO_3$, only scattered submicron spherical particles (yellow arrows in the top image of Figure 6.2d) initially formed on the surface of beads, while more planar crystals a few microns in diameter formed after the P removal reaction (circles in the bottom image of Figure 6.2d).

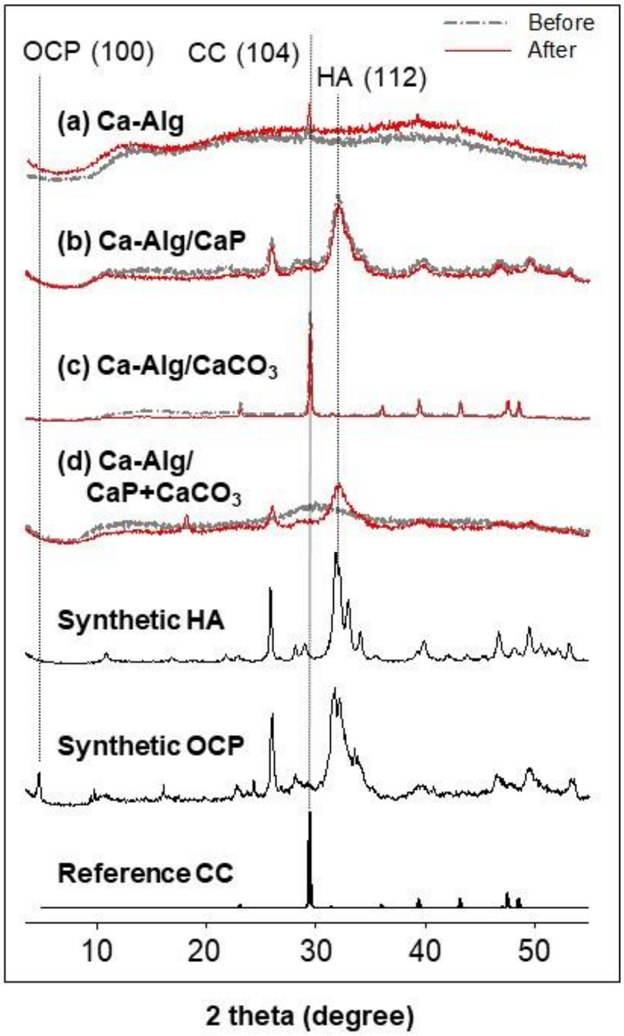

Figure 6.1 X-ray diffraction patterns of calcium alginate beads with different seed minerals (a–d) before and after 22 hours of P removal reaction under the hydroxyapatite (HA)-supersaturated condition. Synthetic HA and octacalcium phosphate samples (OCP) were analyzed for comparison. Reference calcite (CC) was prepared from Iceland spar crystal Chihuahua, Mexico (Ward's Science, USA).

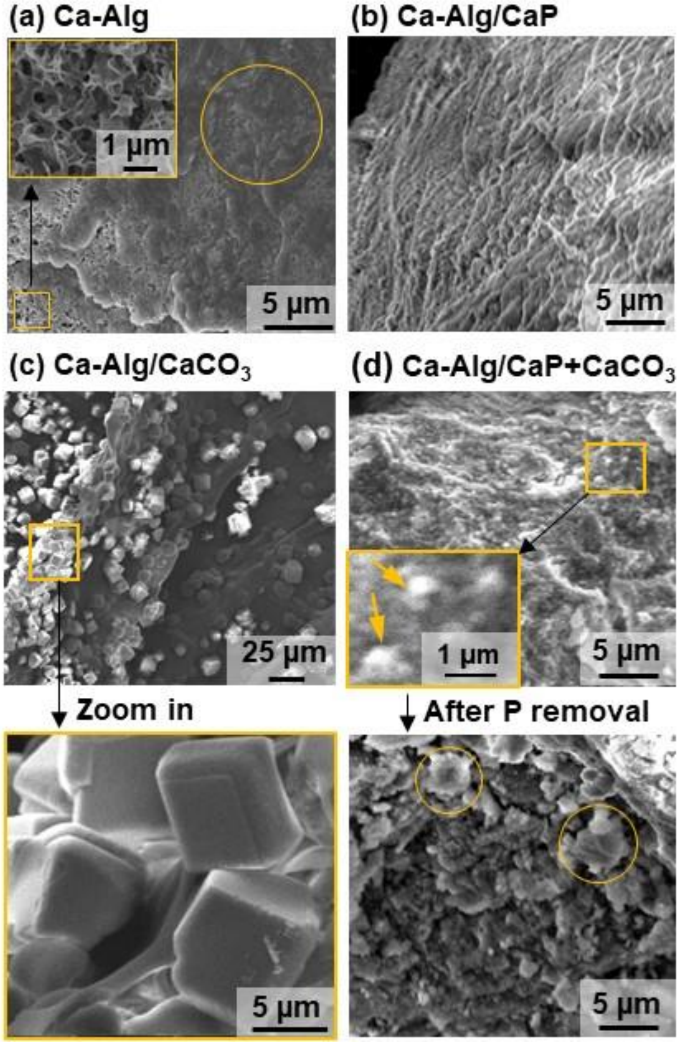

Figure 6.2 SEM images of (**a**) Ca-Alg, (**b**) Ca-Alg/CaP, (**c**) Ca-Alg/$CaCO_3$ with a zoomed in image showing faceted calcite crystals, and (**d**) Ca-Alg/CaP + $CaCO_3$ before and after P removal reaction.

6.4.2 P Removal by Calcium Alginate Beads with Different Seed Minerals

We evaluated the removal of P by beads with different seed minerals through batch experiments, monitoring P and Ca concentrations under both HA-supersaturated and HA-undersaturated conditions. In the control experiment (no beads) under the HA-supersaturated solution, both P and Ca (Figure 6.3a,c) concentrations remained constant during 22 hours of reaction. This observation confirms that there was no significant nucleation (i.e., there was a high energy barrier for HA nucleation). With Ca-Alg beads (no seed mineral), about 15% of P was removed from solutions during 22 hours. The role of a biological template in stimulating CaP nucleation has been previously reported.[8,26] However, no crystalline structural change was observed in the XRD data of the beads after the experiments (Figure 6.1a), indicating that the CaP nucleation and crystallization were not sufficiently enhanced by Ca-Alg within 22 hours. Instead, P species at prenucleation stages might be loosely bound to the alginate surface.[26]

P removal efficiencies increased with seed minerals in the beads under the HA-supersaturated condition (Figure 6.3a). The highest P removal efficiency was achieved by Ca-Alg/CaP, reducing P concentrations from an initial 200 µM to 22.7 µM in 22 hours (at final pH 7.2), which was close to or even below the typical P-levels in biologically or chemically treated effluents from wastewater treatment plants (~30–60 µM).[185] Because the XRD data showed no difference in patterns before and after the P removal process, it was concluded that P was sequestered in the beads as a form of calcium phosphate mineral with a crystalline structure similar to the seed mineral (Figure 6.1b). Therefore, as expected, the SI of the system also significantly decreased with Ca-Alg/CaP, from an initial value of 11.8 to 4.0 within 22 hours. The pH change of the solution did not contribute to the P removal, because the pH decreased slightly, from 7.8 to 7.2, during the experiments. With other types of beads, the final pH values were slightly higher (7.4–7.7) than with CaP seed, but their removal efficiencies were even lower.

Interestingly, even in the HA-undersaturated condition, up to 68% of initial P was removed by Ca-Alg/CaP (Figure 6.3b) by utilizing Ca-ions released from the beads. Thus, especially around the beads' surfaces, the batch environments become locally supersaturated with respect to HA, so CaP nucleation could be stimulated by the seed minerals. As a matter of fact, after P removal using Ca-Alg, Ca-Alg/$CaCO_3$, and Ca-Alg/CaP+$CaCO_3$, the Ca concentrations released into the undersaturated solutions became higher than 0.3 mM after 5 hours (Figure 6.3d). The SI of this environment was 8.1 (0.3 mM Ca, 0.2 mM P, and 10 mM NaCl at pH 7.8). On the other hand, the release of Ca from Ca-Alg/CaP remained lower (~0.1 mM Ca) than those from other beads until 22 hours, while the P concentration decreased from 200 µM to 66 µM. Therefore, we can estimate that the released Ca ions were reversely consumed by formation of new CaP phases. However, the loss of Ca^{2+} from the beads visibly destroyed the beads' gelated state and spherical shape under the HA-undersaturated condition (Figure 6–S3e,f). Hence, the existence of sufficient Ca^{2+}, as in the HA-supersaturated condition, would be an important factor for stable operation.

Although P removal was less efficient with carbonate seed mineral than phosphate seed, Ca-Alg/$CaCO_3$ beads removed about 35% of P from the HA-supersaturated condition (Figure 6.3a). The higher removal efficiency by Ca-Alg/$CaCO_3$ than by Ca-Alg with no seed minerals indicates the contribution of $CaCO_3$ seeds to the P removal. No phosphate mineral phases were observed from the XRD pattern of Ca-Alg/$CaCO_3$ after P removal (Figure 6.1c). Therefore, adsorption on surfaces of Ca-Alg and calcite seed are the most probable P removal mechanisms.[214,220] A similar removal efficiency was achieved by Ca-Alg/CaP+$CaCO_3$ beads, whose ACC-like seed transformed to HA-like platy particles at the outer surface of the beads after P removal under the HA-supersaturated condition (Figure 6.1d and 6.2d). This transformation indicated that ionic Ca and P species were dissolved from seeds and then secondarily precipitated. Indeed, in the HA-undersaturated condition with Ca-Alg/CaP+$CaCO_3$ beads, P concentrations increased over time due to the dissolution of seed minerals (Figure 6.3b). The XRD pattern of the final CaP products on the Ca-Alg/CaP+$CaCO_3$ surface after P removal (Figure 6.1d, red line) was comparable to that of seed minerals in Ca-Alg/CaP (Figure 6.1b). However, the P removal efficiency of Ca-Alg/CaP+$CaCO_3$ was much lower than that of the Ca-Alg/CaP system. Therefore, CaP seeds can be more effectively used for P removal when they form simultaneously with the beads (Ca-Alg/CaP) than when they are transformed from the amorphous phase during the P removal process (Ca-Alg/CaP+$CaCO_3$). Therefore, the later part of this study further evaluates the roles of seed minerals in Ca-Alg/CaP beads in aqueous P management.

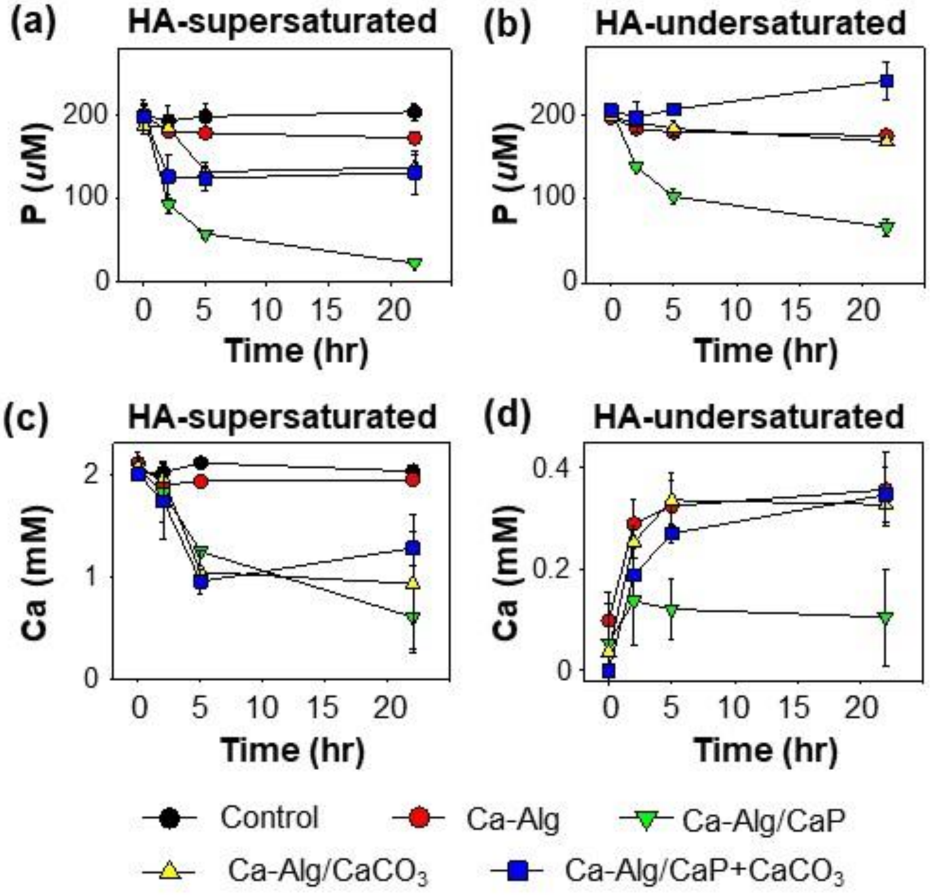

Figure 6.3 P and Ca concentrations during P removal reactions using Ca-Alg with different seed minerals in solutions initially supersaturated (**a, c**) and undersaturated (**b, d**) with hydroxyapatite. Initial conditions: 10 mM NaCl, 0.2 mM Na2HPO$_4$, pH = 7.8; for the HA-supersaturated condition, 2 mM $CaCl_2$ was added.

6.4.3 Aqueous P Concentrations Controlled by the Crystalline Degree of CaP Seed Minerals

Based on our evaluations of different types of seed minerals, we found that seeding HA-like particles within the beads (Ca-Alg/CaP) was most effective for P removal. The crystalline structure of newly precipitated CaP from the aqueous solution during P removal was the same as that of the initial seed mineral. Therefore, if the aqueous P concentration reaches an equilibrium with CaP seed, the solubility of the seed mineral governs the equilibrium P concentration. Given that the solubility of amorphous calcium phosphate is much higher than that of HA,[74] the equilibrium P concentration after P removal may be engineered by controlling the crystallinity of seed nuclei.

To prove this hypothesis, we prepared Ca-Alg/CaP in the Ca bath with lower OH^- concentrations of 0 and 10 mM, and then compared them with original samples prepared with 20 mM OH^-. Higher OH^- concentrations in the nucleating solution increased the PO_4^{3-} species fraction, and consequently, the *IAP* of calcium phosphate minerals, such as HA ($IAP_{HA} = [Ca^{2+}]^5[PO_4^{3-}]^3[OH^-]$). As we hypothesized in the experimental section, the increased *IAP* enhances the thermodynamic driving force for HA nucleation, which decreases the free energy of nucleation quickly,[19] forming stable CaP seed mineral with low solubility and high crystallinity.

WAXD patterns of Ca-Alg/CaP beads clearly confirmed that seed minerals prepared with 20 mM OH^- have a more HA-like structure than those prepared with 0 or 10 mM OH^- (Figure 6.4a). In the WAXD pattern of Ca-Alg/CaP prepared in 0 mM, only a few broad peaks appear, such as at q = 1.83, 2.23, 3.41, and 3.58 $Å^{-1}$, which correspond to the (002), (211), (213), and (402) faces of HA. However, with 20 mM OH^-, most peaks observed from synthetic HA also appeared identically. The influence of OH^- concentrations on the crystalline structures of Ca-Alg/CaP was further analyzed by X-ray PDF (Figure 6.4b). Ca-Alg/CaP samples prepared with 0 and 20 mM of OH^- both showed their first two peaks at the same interatomic distances, r, in their PDF functions, $G(r)$. The first peak, at r = 2.4 Å, corresponds to the nearest-neighbor Ca–O, which is evidence of calcium phosphate nuclei formation.[31] The second peak, at r = 2.8 Å, indicates an O–O interatomic distance typically observed in liquid water.[221] This peak at $r = 2.8$ Å was strong because the beads were all analyzed in a hydrated condition to prevent potential alteration of the seed nuclei's crystalline structures by dehydration. Compared to the PDF of synthetic HA, which showed a clear long-range order (interatomic distance, $r > 12$ Å), that for Ca-Alg/CaP prepared with 20 mM OH^- was weaker, but the correlation still extended for over 10 Å. Any comparable correlation essentially disappeared for samples prepared with 0 mM OH^-. Therefore, we concluded that seed mineral in Ca-Alg/CaP became structurally ordered more like HA when prepared with 20 mM OH^- than that with 0 mM OH^-.

During the phase transformation of CaP particles from amorphous to crystalline apatite in biologically relevant aqueous systems, the size of particles often decreases because the particles form via aggregation and subsequent condensation of nucleation precursors.[8,26,99] However, the size of CaP seeds embedded in beads could not be easily evaluated using conventional surface characterization tools. In this study, USAXS analysis of the Ca-Alg/CaP, we determined the grain size of the nuclei as a radius of gyration, R_g (Figure 6.4c).[94,95,222] The R_g of CaP nuclei decreased significantly with increasing crystallinity, from 522 nm (with 0 mM OH^-) to 232 nm (with 20 mM OH^-). No discernible features of smaller size particles, such as apatite plates (40 nm × 30 nm × 2 nm) in bones,[73] were observed by using either USAXS or SAXS (with an adjusted q range to better analyze particles smaller than 70 nm).[11,83] With a limited amount of calcium and phosphate precursors, the crystallization of seed nuclei might not proceed further during the Ca-Alg beads formation. Therefore, Ca-Alg/CaP beads prepared under different OH^- conditions could maintain specific seed nuclei crystalline structures and grain sizes, as introduced in this study.

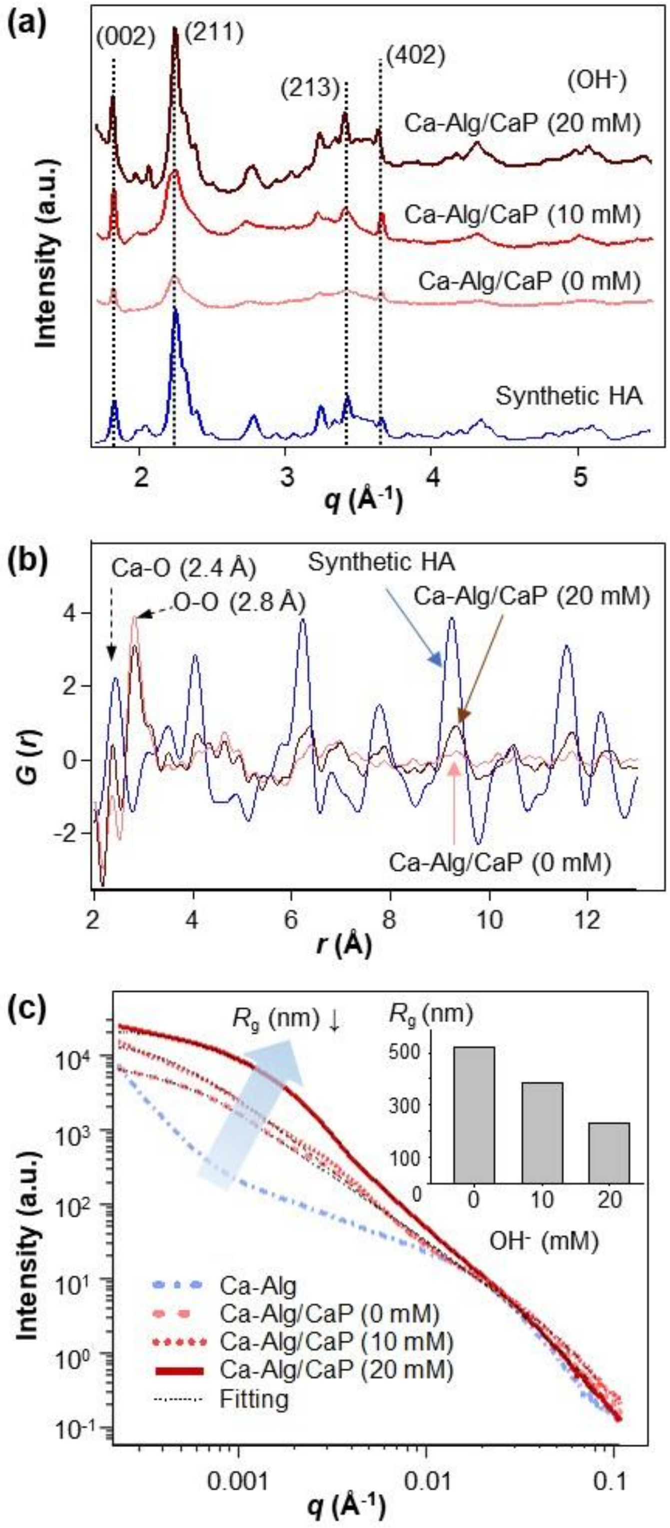

Figure 6.4 Crystalline structure of CaP seed nuclei and equilibrium P concentrations. (**a**) WAXD patterns, (**b**) X-ray PDF analyses, and (**c**) USAXS patterns of Ca-Alg/CaP prepared with different OH− concentrations (0–20 mM).

We confirmed that higher OH^- concentrations in the Ca bath for the beads' preparation resulted in a more ordered crystalline structure of HA-like seed minerals (Figure 6.4a,b). The higher crystallinity of the seed minerals made them less soluble, lowering the P concentrations at the end of the removal experiments (Figure 6.5a). From this clear trend, we can conclude that the equilibrium P concentration is highly governed by the degree of crystallinity of the seed mineral. After the P removal experiments, to evaluate whether the beads could release P into the aqueous system as a potential fertilizer, the beads were recovered from the batch and then placed in P-free solutions. P released from Ca-Alg/CaP reached equilibrium within five hours. This time to reach equilibrium was nearly constant over three cycles of the release experiments, although the P concentration was slightly higher in the 1st cycle than in the 2nd and 3rd cycles (Figure 6.5b). The equilibrium P concentrations in the 2nd and 3rd cycles with Ca-Alg/CaP prepared with 20 mM OH^- were 9.4 ± 2.0 µM, which was about 28% lower than with Ca-Alg/CaP prepared with 0 mM OH^- ($p < 0.1$ by Student's t-test, final pH values for both systems were equal to 7.0). This result indicates that the crystallinity of the seed nuclei also governs the P concentrations during the P release process, supporting the potential application of P-loaded Ca-Alg/CaP beads as a slow-release fertilizer. Over the three cycles, only 20 % of the total immobilized P was released from the beads.

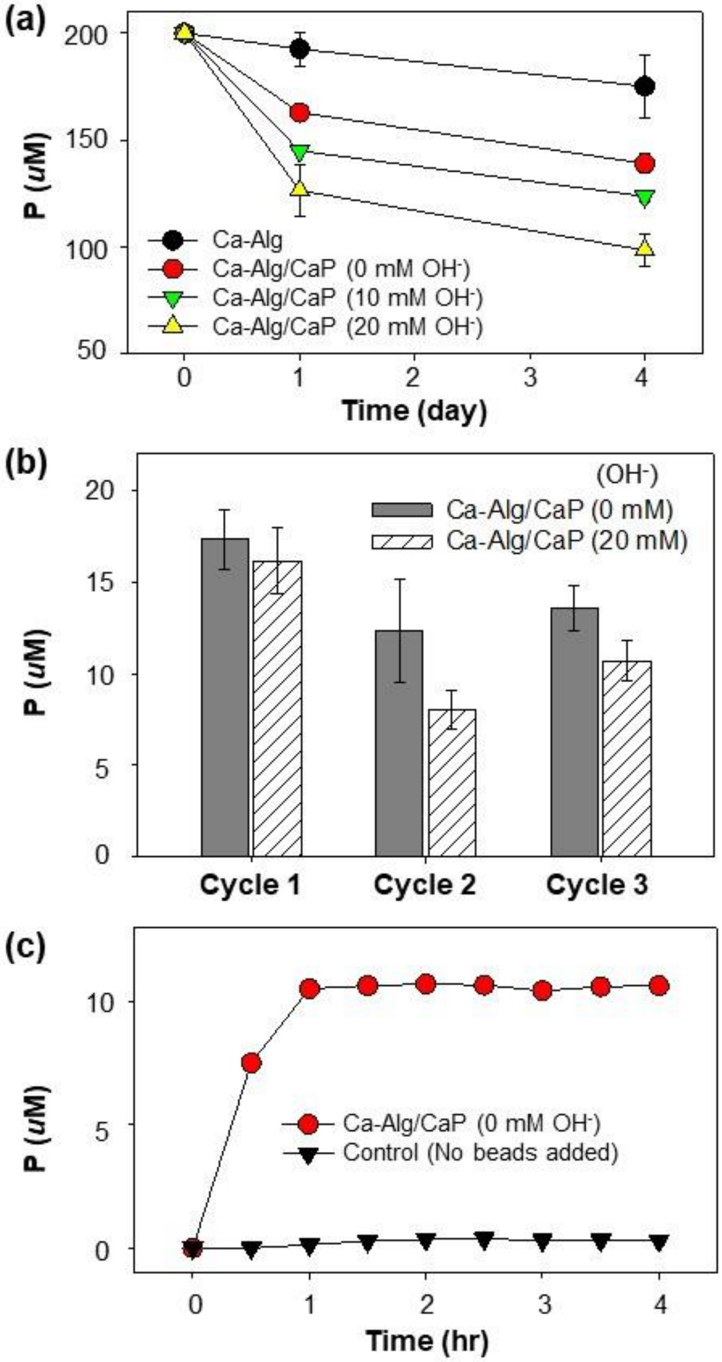

Figure 6.5 (**a**) Equilibrium aqueous P concentrations in the presence of Ca-Alg/CaP during P removal. Initial conditions: 10 mM NaCl, 0.2 mM Na_2HPO_4, pH = 7.6, and 2 mM $CaCl_2$. (**b**) Equilibrium aqueous P concentrations in the presence of Ca-Alg/CaP during three cycles of P release experiments. (**c**) P release kinetics from Ca-Alg/CaP beads (0 mM OH^-) in sand columns.

The beads' ability to maintain the P equilibrium concentration was also validated by sand column experiments. After the Ca-Alg/CaP beads (prepared in 0 mM OH^-) were placed on top of the 5 cm thick sand layer, P concentration in the effluent reached ~10 µM at pH ~7 within an hour (Figure 6.5c). Although the column experiments simulated a simplified soil system, the tests demonstrated that, within a relatively short time period, the P-captured beads can release P into the soil pore-water. The released P concentration was 10 times higher than the minimum P required in a rhizosphere soil solution (~1 µM) for crop production,[223] suggesting that P can be released sufficiently fast for plant growth. Furthermore, the P level in the effluent from the column remained constant for an extended time, without excessive release of P, thus working as a slow-release fertilizer. This release pattern is clearly distinct from that of other, much more soluble phosphate fertilizer, such as triple superphosphate ($CaH_4P_2O_8$, solubility in water is about 20 g L^{-1}, releasing up to 0.17 M of P).[224,225] These findings provide an insight into the engineered control of steady P transport from fertilizer to plants.

Figure 6.6 presents the final P concentrations (near equilibrium) obtained from the removal and release experiments, together with their final pH values, for comparison with the P solubility curves of reference CaP minerals (HA and OCP). At a final pH range 6.6–6.8, the data points from seed minerals with higher crystallinity are closer to the HA solubility curve, despite the slightly lower pH values. At this range of final pH values, the difference in equilibrium P concentrations for the different seed minerals most obviously appears as expected from the largest difference between the solubility curves for HA and OCP. The apparent solubility products, pK'_{sp}, of HA calculated based on the experimental data of CaP seed with 20 mM and 0 mM were 54.2 and 52.5, respectively, indicating that P solubility was controlled by the seed minerals' crystallinity over approximately two orders of magnitude.

Although the pK'_{sp} of CaP seeds prepared in 20 mM OH^- was lower than that of synthetic HA (pK_{sp} = 58.5),[104] the seeds effectively decreased P concentrations from an initial 200 µM to ~20 µM at the end of release experiments (final pH 7.0–7.2). This P range is below the level allowed for typical wastewater effluents (~30–60 µM).[185] Therefore, the beads can be effectively utilized to treat aqueous systems contaminated by various P pollution sources, such as wastewater and landfill leachate (240–880 µM P, pH 7.5–8.5),[226] without the need for secondary pH adjustments. Similar equilibrium P concentrations with the CaP seed minerals (~10 µM P at pH 7.0–7.2) were also achieved during the P release experiments, highlighting the potential use of recovered P as a slow-release fertilizer. This level of P is sufficient to maintain the growth of crops,[223] without excessive P release into the environment.

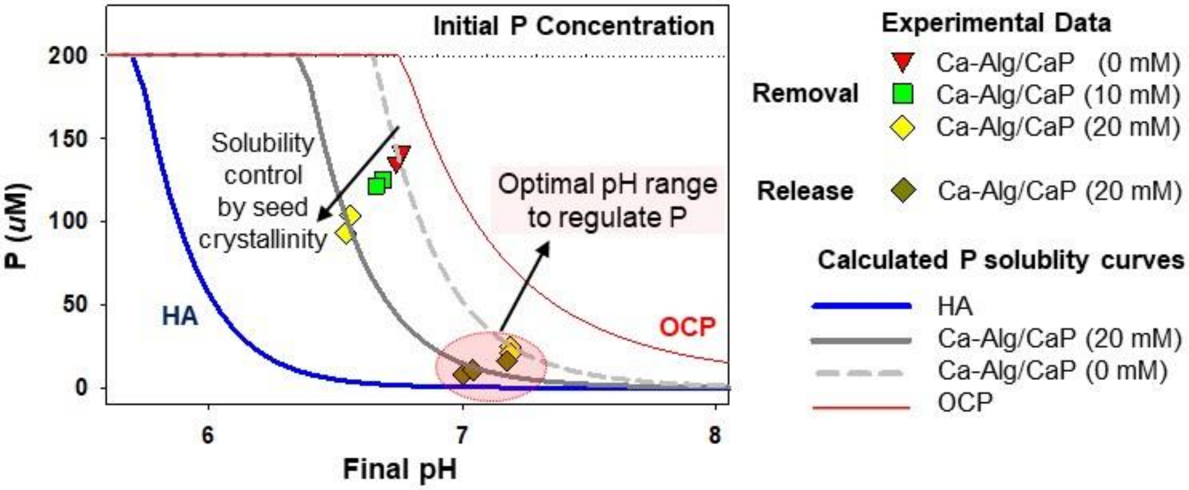

Figure 6.6 P concentrations at final pH values obtained from the P removal and release experiments (data from Figure 6.3a and 6.5a, b). Blue and red solid lines are drawn based on thermodynamic calculations using the solubility products of hydroxyapatite (HA, pK_{sp} = 58.5) and octacalcium phosphate (OCP, pK_{sp} = 48.4). Grey solid and dotted lines show apparent P solubility curves for HA calculated based on the experimental data of Ca-Alg/CaP prepared with 20 mM OH^- (pK'_{sp} = 54.2) and 0 mM OH^- (pK'_{sp} = 52.5), respectively.

6.4.4 Potential Field Applications of Ca-Alg/CaP

In this study, the aqueous P concentrations were controlled by the solubility of seed minerals, and the CaP seeded beads could remove almost 90% of P in the HA-supersaturated system within a day at pH 7.2 (from initial 200 µM to ~20 µM, Figure 6.3a). Therefore, the suggested approach can be successfully operated for the P removal at neutral pH, avoiding expensive secondary pH adjustment of the effluent. The same principle for reaching equilibrium with poorly crystalline HA-like seed mineral can also be applied for P release (Figure 6.5c), highlighting the potential use of recovered P as a fertilizer. The use of a macroscale organic template of calcium alginate beads provided a practical benefit of easier recovery for reuse as a fertilizer without the need for further processes, such as filtration or centrifugation. In addition, the large volume of the beads (compared to the amount of alginate and seed mineral) can store a large amount of P. In our experiments under the HA-saturated condition, 96.4 mg of P was captured per g of dry seed mineral (Figure 6.3a and Table 6–S1). In our additional experiments, the beads captured additional P over two more cycles, showing removal of up to 186 mg g^{-1} (Figure 6.7). This value was significantly higher than for other recently reported P adsorbents, such as commercial HFO-201 (an Fe(III) oxide-based nanocomposite, ~35 mg g^{-1} at pH 6–7), hydrated La(III) oxide nanoclusters (~60 mg g^{-1} at pH 6–7),[227] or zirconium oxide nanoparticles (99 mg g^{-1} at pH 6.2).[228] However, more accurate comparisons with these materials can be made by evaluating P removal efficiency under the same experimental conditions and with the same dose of adsorbents in the future. Especially, the competition among phosphate and other oxyanions, such as arsenic and nitrate, needs to be evaluated because these oxyanions potentially affect the P removal efficiency of beads and their environmental safety when applied as a clean fertilizer. Although struvite formation in our experimental condition was not plausible (Figure 6–S5), when the beads are used for effluents from wastewater treatment plants with anaerobic digestion,[225] the influence of NH_4^+ should be considered because it may compete with HA by forming struvite in the presence of Mg^{2+}.

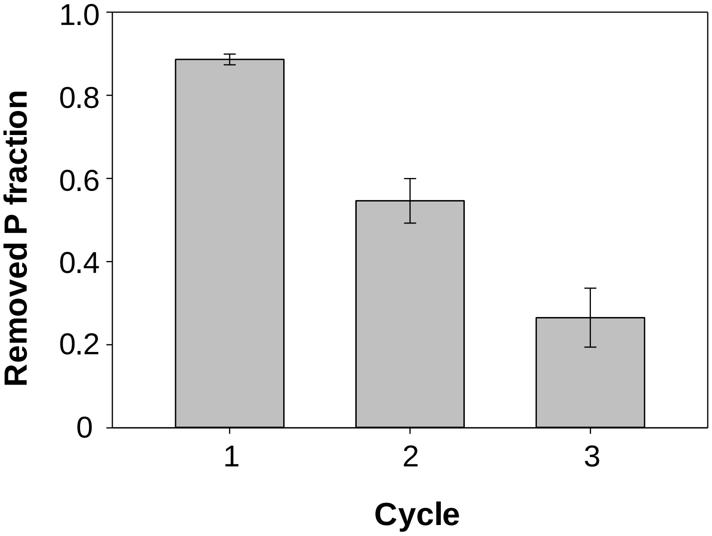

Figure 6.7 Removed P fractions in solutions (initial conditions were 10 mM NaCl, 0.2 mM Na_2HPO_4, and 2 mM $CaCl_2$, pH = 7.8) using Ca-Alg/CaP. Experiments were conducted by adding beads prepared by addition of 2 mL sodium alginate solution (equivalent to 5.7 mg of dry CaP seed mineral, see Section 6.7.2) into a batch containing 100 mL solution (first cycle). After 24 hours of reactions, beads were collected and then transferred to a fresh batch (second cycle). Three batches were used for removal with the same beads.

As discussed, Ca-Alg/CaP performed best under the HA-supersaturated condition (2 mM Ca and 0.2 mM P) at circumneutral pH, and this condition is highly comparable to Ca-rich and/or P-rich aqueous environments. According to the USGS National Water-Quality Assessment, about 60 percent of sampled wells provide hard water (>120 mg/L as $CaCO_3$). Moreover, many of them have hardness levels even higher than 180 mg L^{-1} (equivalent to 1.8 mM of Ca^{2+}, generally classified as very hard water).[200] These aqueous systems with high Ca^{2+} concentrations can be easily HA-supersaturated when exposed to P-abundant streams. For example, even without significant commercial or industrial loads, the concentration of total phosphorus in wastewater treatment effluent may exceed 6 mg L^{-1} as P (~0.2 mM).[229,230] Indeed, our evaluation of the saturation of groundwater using USGS National Groundwater Monitoring Network data showed that most of samples in the Chesapeake Bay and Louisiana areas (pH 7.7 ± 0.9 and 7.7 ± 0.7, respectively) were HA-supersaturated (Figure 6–S1). This analysis strongly supports our approach as a potential P management strategy by showing that many aqueous environments at neutral pH are already supersaturated with respect to HA.

The current options for chemical precipitations using ferric salts or calcium (hydr)oxide are known to be effective, but they have limited applicability for on-site operations due to their significant pH alteration.[185] Moreover, although phosphate minerals are generally formed during these chemical processes, they turn into other mineral forms, such as ferric oxide, coloring water orange. Indeed, hematite (Fe_2O_3) is thermodynamically more stable than strengite ($FePO_4 \cdot 2H_2O$) at a wide pH range, as shown in an example of a system containing 1 mM $FeCl_3$ and 0.1 mM Na_3PO_3 (Figure 6–S6). Thus, the consumption of ferric ions by hematite precipitation would inhibit P immobilization in certain environments. In addition, pH must be maintained around 5 during chemical precipitation using ferric chloride, because iron hydroxide minerals, which compete with iron phosphate minerals, can form at a higher pH range.[185] During treatments using CaO or Ca bearing materials, calcium hydroxide or calcium carbonate may form instead of CaP minerals (pH > 8.5, Figure 6–S4a), which can release P into the aqueous environments again. This adverse effect significantly weakens the capacities of these processes as effective treatment methodologies.

6.5 Conclusions

In this study, we developed a new approach for P management of aqueous environments at neutral pH using naturally abundant biomineral (CaP) and a biodegradable organic template (alginate beads). A green synthesis approach at room temperature for the composites that does not use hazardous substances provides an opportunity for ‘greening’ the global phosphorus cycle for the security of food, energy, and water.[186] By utilizing CaP seed minerals with a poorly crystalline HA-like structure in calcium alginate beads, we successfully enhanced the kinetics for aqueous P concentration to reach near equilibrium solubility of HA. In addition, we also explored the potential application of the beads as a slow-release fertilizer. The performance of the beads in controlling P concentrations in both P-deficient and P-abundant aqueous systems was regulated by the engineered manipulation of the CaP crystallinity. By linking biomineralization to P management strategy, our study also expands applications of biomaterials to environmental issues.

6.6 Acknowledgments

The project was mainly supported by Y.S.J.'s faculty startup fund and was partially supported by the National Science Foundation (DMR-1608545 and DMR-1608554). The undergraduate researchers received fellowships from Washington University's Office of Undergraduate Research (T.W.) and from the McDonnell Academy Global Energy and Environmental Partnership (I.J.). The Nano Research Facility and Earth and Planetary Sciences X-ray Diffraction Laboratory at Washington University in St. Louis provided their facilities for the experiments. Use of the Advanced Photon Source at Argonne National Laboratory was supported by the U.S. Department of Energy (DE-AC02-06CH11357). We thank beamline scientists at sectors 9-ID-C (Dr. Jan Ilavsky), 11-ID-B (Dr. Karena Chapman, Dr. Olaf Borkiewicz, and Mr. Kevin Beyer), and 12-ID-B (Dr. Byeongdu Lee) for assisting with data acquisition and analyses. We also thank Prof. J. Ballard for carefully reviewing the manuscript.

6.7 Supporting Information for Chapter 6

6.7.1. A Case Study: Hydroxyapatite Saturation index (SI) Mapping of Groundwater in the Chesapeake Bay, Louisiana, and Northern Illinois Areas

A. Procedures. This study was conducted to test our hypothesis that many nutrient-rich environments are already supersaturated with respect to hydroxyapatite (HA). If we are able to cause such aqueous systems to reach equilibrium quickly (e.g., by adding calcium phosphate (CaP) seed nuclei in calcium alginate beads, as used in this study), we can easily regulate the P concentration at a lower level, reducing the risk of eutrophication. In this case study, we investigated the actual SI values (the log of the ion activity product, *IAP*, divided by the solubility product, K_{sp}) of groundwater samples from three areas in the USA. The Chesapeake Bay area (C. Bay) was chosen because of the frequent occurrence of eutrophication in this region due to inflows from natural and anthropogenic sources.[231,232] Similarly, the coastal Louisiana area (LA) has also faced issues associated with eutrophication and high P levels in the water.[233] Contrarily, an area in northern Illinois area (IL) near Lake Michigan was chosen because of this region's reputation for low P levels,[234] but this area may show relatively high Ca levels due to its calcareous soils.[235]

Groundwater monitoring data (1970–2007) were collected from the USGS National Groundwater Monitoring Network (NGWMN),[199] then processed to determine whether environments were actually supersaturated with respect to HA (HA-supersaturated). The latest data from groundwater samples, including pH, total P (assumed to be equal to total phosphate) concentration, hardness, and total dissolved solid values, were selected as input parameters for Visual MINTEQ (Ver. 3.1), which calculates the SI using its built-in database. Hardness data (as $CaCO_3$) were used as input parameters of Ca^{2+}, unless Ca^{2+} concentration was given specifically.

The concentrations of Ca^{2+}, aqueous carbonate species, Na^+, and Cl^- were considered to calculate the ionic strength. By assuming that the amount of total dissolved solids is the sum of the hardness and NaCl, we estimated the concentrations of NaCl. Organic molecules, such as natural organic matter and extracellular matrix proteins from microorganisms, may influence the saturation condition or nucleation energy barrier by complexation with Ca^{2+} or other aqueous species.[71,236] However, in this proof of concept calculation, we limited the input parameters to the inorganic compounds listed above. The SI values for HA, as the output parameters of the software, were placed on SI maps (Figure 6–S1a-c) created by ArcGIS (Esri, USA), using longitude and latitude information from the NGWMN database.[199]

B. Analyses of SI of three areas. Based on our thermodynamic calculations of the SI values for HA, interestingly, 36 out of 48 groundwater samples (75%) in the C. Bay area were HA-supersaturated (Figure 6–S1a). Most of the HA-supersaturated sampling points were close to the Bay, indicating that significant Ca and P concentrations have been introduced into the ocean through the groundwater. Two sampling sites were studied from LA, and the SI values of both sites were higher than 4 (Figure 6–S1b). Because of the limited data available, the result may not represent the entire LA area. However, this result also shows that multiple aqueous environments are HA-supersaturated. In contrast, only two out of five sites were slightly HA-supersaturated ($0 < SI < 2$) in northern IL, and other three sites were undersaturated with respect to HA ($SI < 0$, Figure 6–S1c).

The SI values in the three studied areas show correlations in the order pH > P > Ca (Figure S2a–c). P concentrations in C. Bay and LA are obviously higher than in northern IL (Figure 6–S2d), suggesting the influence of increasing P levels on eutrophication. Due to the calcareous soils, Ca concentrations in the northern IL are relatively higher than in the other two areas (Figure 6–

S2e). However, due to the region's low P concentrations and pH, SI values are relatively low (Figure 6–S1c). The pH values for the HA-supersaturated sites are typically higher than 7 (Figure 6–S2f), and HA is the most stable of calcium phosphate minerals in this pH range.[201] Our study shows that Ca-Alg/CaP can effectively decrease P concentrations close to the equilibrium level with HA at pH around 7 (Figure 6.6). Therefore, this strategy can contribute to maintaining the P level in the stable range (e.g., equilibrium with seed mineral in beads), preventing a sudden increase of P in the aqueous systems.

Based on the evaluation of SI for HA in areas with high eutrophication risks (C. Bay and LA) and the comparison with an area relatively free from the risk (IL), we suggested that utilizing the thermodynamic property of HA (i.e., its low solubility at neutral pH) can advantageously regulate P concentrations in most aqueous systems. In addition, to select other possible application sites, we can refer to the USGS database.

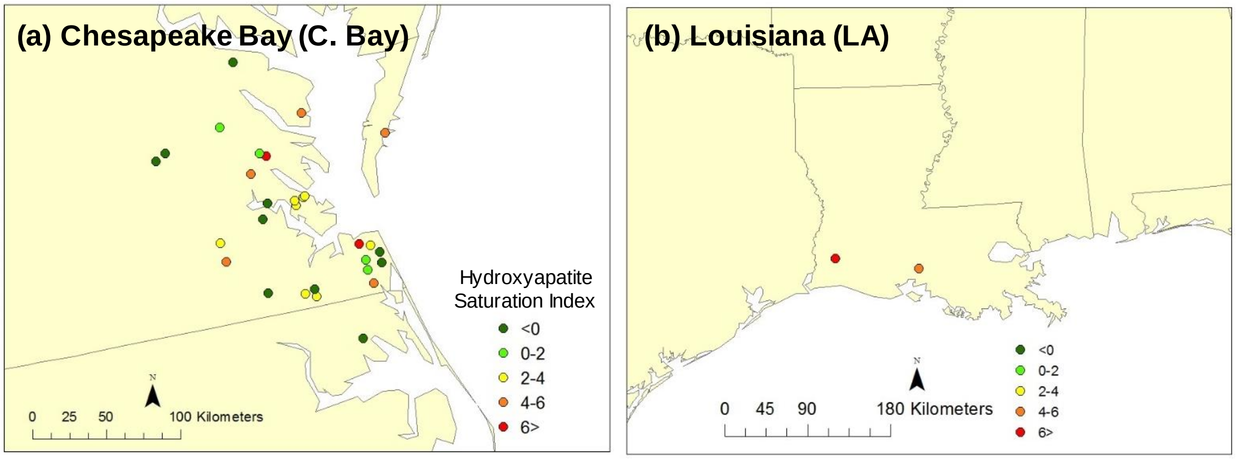

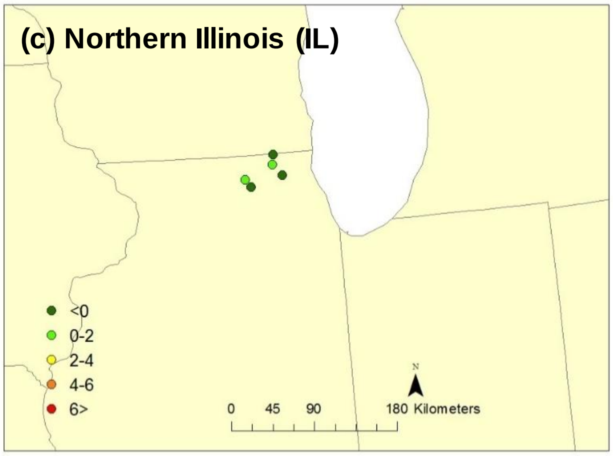

SI	C. Bay	LA	IL
< 0	12	0	3
0-2	9	0	2
2-4	17	0	0
4-6	6	1	0
> 6	4	1	0
total	48	2	5
% saturated	75	100	40

Figure 6–S1 Hydroxyapatite SI maps of the (**a**) Chesapeake Bay (C. Bay), (**b**) Louisiana (LA), and (**c**) northern Illinois (IL) areas. The SI values were calculated using Visual MINTEQ. The table at the bottom right corner summarizes the number of sampling sites categorized into different SI values.

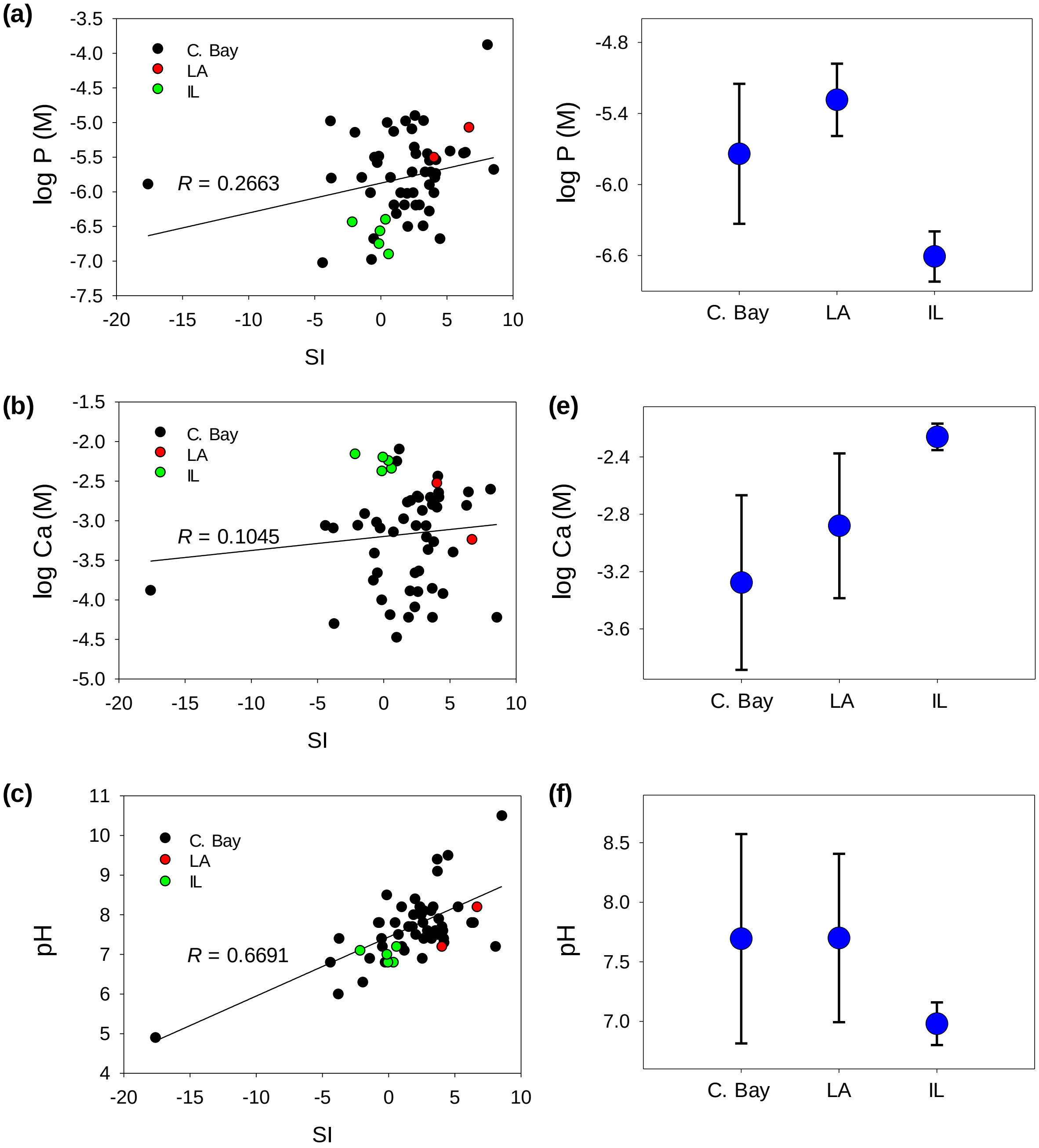

Figure 6–S2 (**a-c**) Relationships between the SI for HA and concentrations of P, Ca, and pH in three areas studied (C. Bay, Chesapeake Bay; LA, Louisiana; IL, northern Illinois). *R* is the correlation coefficient from the linear relationship. (**d-f**) Average and standard deviation values of P, Ca, and pH in these three areas are shown separately in the right column figures.

6.7.2 Characterizations of Beads

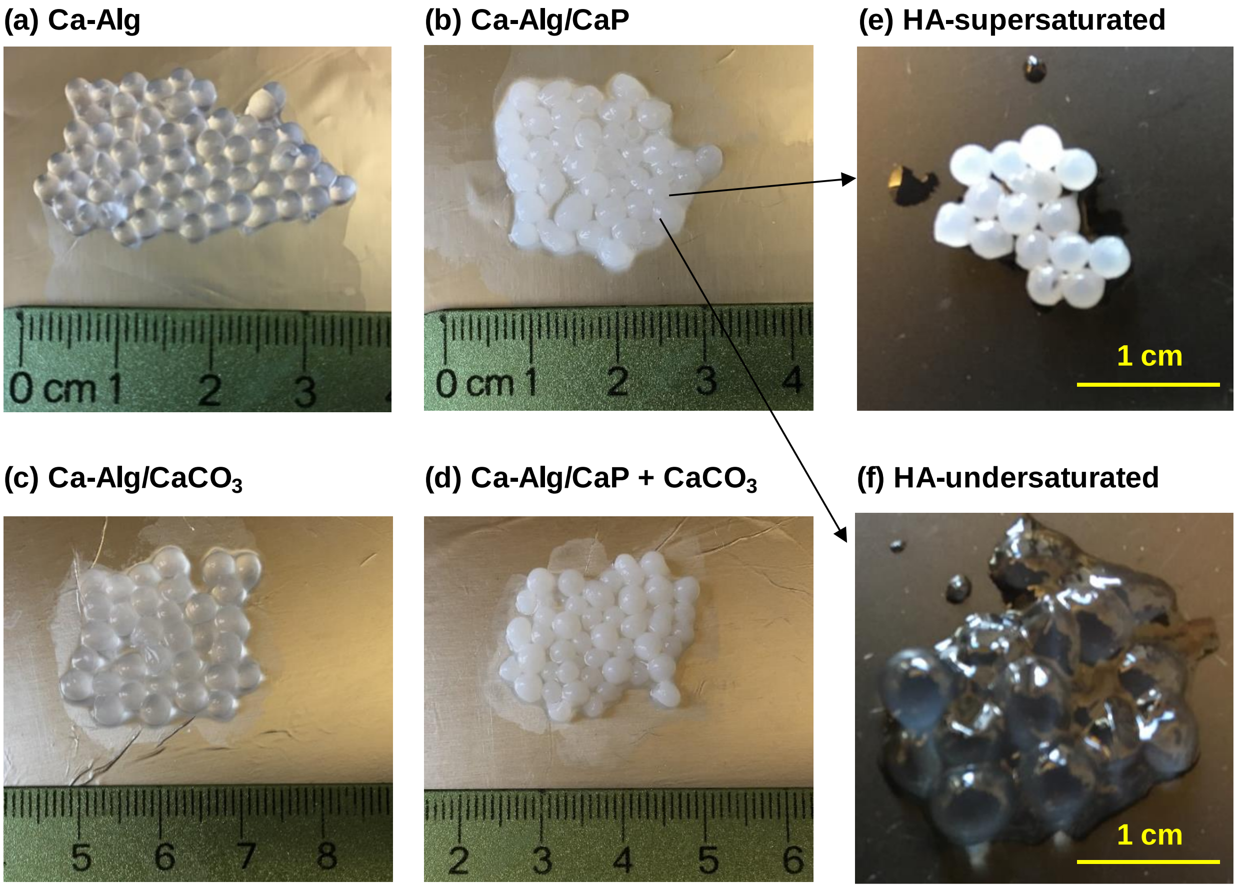

Figure 6–S3 (**a-d**) Photographs of the four different types of beads used in this study. (**e-f**) Ca-Alg/CaP after three cycles of P removal experiments (24 hours for one cycle) under HA-supersaturated and HA-undersaturated conditions.

Table 6–S1. Bead sizes and dry weights of beads and seed minerals.

	Ca-Alg	Ca-Alg/CaP	Ca-Alg/$CaCO_3$	Ca-Alg/CaP+$CaCO_3$
Bead size (mm)	2.8 ± 0.2	3.3 ± 0.4	3.8 ± 0.2	3.2 ± 0.4
Dry weight (mg)*	14.0 ± 3.9	19.7 ± 1.7	19.4 ± 1.3	24.7 ± 2.0
Seed weight (mg)	-	5.7	5.5	10.7

*Drying procedure is described below.

To analyze the particle sizes, ImageJ 1.47v (National Institutes of Health, USA) was used. The average and standard deviation values for each bead type were obtained by measuring 15 samples. For the batch experiments for P removal, 2 mL of sodium alginate solution (6 mg L^{-1}) was added dropwise to form beads. The average and standard deviation of the dry weight were obtained from triplicate bead preparation procedures. Beads were fully dried in a 105°C oven for 24 hours before the measurements. The dry weights of Ca-Alg beads were slightly higher than the amount of initially added sodium alginate (12 mg) because of calcium replacement and structural water inside the composites. The dry weights of seed minerals were calculated by subtracting that of Ca-Alg beads.

A. Procedures for other characterizations of beads and seed minerals. Before and after the P removal experiments, to characterize the crystalline structure of seed minerals and to image the surfaces of beads, X-ray diffraction (XRD, Bruker D8 Advance) data and SEM (FEI Nova NanoSEM 230) images of beads were used, respectively. To prepare samples for XRD and SEM analyses, beads were air-dried and gently ground with ethanol in an agate mortar. For XRD analysis, ground samples were placed on a zero diffraction Si plate (MTI Corporation), then the XRD patterns were collected using Cu Kα radiation (40 kV and 40 mA). For SEM analysis, ground samples were placed on adhesive carbon tapes attached on SEM stubs, sputter-coated with Au-Pd under Ar gas at 0.2 mbar (Cressington 108) to increase conductivity, then imaged with a 10 kV electron accelerating voltage at 5−6 mm working distances.

To characterize the particle size and crystallinity of CaP seed nuclei prepared with different OH^- concentrations, X-ray scattering data were collected at the Advanced Photon Source (APS) at Argonne National Laboratory (Argonne, IL, USA). Beads were packed in Kapton polyimide capillaries (Cole-Parmer, inner diameter 1.46 mm) without any dehydration procedures. Analyses of samples under hydrated conditions maintained the particle sizes and phases of CaP nuclei. WAXD and X-ray PDF data were collected at sector 11-ID-B using a 58.66 keV X-ray beam.[237] For the WAXD data collection, samples were exposed to the beam for 25 sec at a sample-to-detector distance (SDD) of 95 cm. For the X-ray PDF, data was collected during 3 min of beam exposure using a 20 cm SDD. Then one-dimensional data were produced by using FIT2D software provided by European Synchrotron Radiation. The PDF function, G(r), was obtained by PDFgetX2 software to provide the atomic number density as a function of atomic separation distances, r.[238] We evaluated particle size (d) over a wide range of the scattering vector, q = 0.0001–0.1 Å^{-1}, using USAXS. Because $d = 2\pi / q$, the corresponding particle size range was 6.3 nm–6.3 µm. USAXS data was collected at sector 9-ID-C using a 21.0 keV X-ray beam.[239] Data analyses, including one-dimensional data reduction and fitting scattering patterns, were conducted using a series of macro programs in the IRENA package written in IGOR Pro (WaveMetrics Inc.), which was provided by sector 9-ID-C.[94,95,222] In addition, SAXS measurements of samples were conducted at sector 12-ID-B (14.0 keV) to better evaluate the features of small particles appearing at q = 0.009–0.3 Å^{-1} (d = 2–70 nm). The WAXD, USAXS, and SAXS patterns of an empty Kapton capillary were also collected for background subtraction.

6.7.3 Thermodynamic Calculations of Ca and P Concentrations in Equilibrium with Different Calcium Phosphate Minerals

The concentrations of Ca and P species equilibrated with different calcium phosphate minerals at pH 5–10 were calculated based on the equilibrium constants among calcium, phosphate, and carbonate species. To simulate the calcium phosphate saturated condition used in this study, 10 mM NaCl, 2 mM $CaCl_2$, and 0.2 mM Na_2HPO_4 were added as initial aqueous components, and an open carbonate system (p_{CO_2} = $10^{-3.5}$, p_{CO_2}/[H_2CO_3(aq)] = 31.6 atm/M) was assumed. The association/dissociation reactions listed in eqs. 6–S1–11 were considered for the calculation of the activities of carbonate, phosphate, and calcium species in the system.[100,240]

$$K_{\mathrm{A1,CO3}} = \frac{(\mathrm{H^+})(\mathrm{HCO_3{}^-})}{(\mathrm{H_2CO_3(aq)})} = 10^{-6.35} \qquad \text{eq. 6–S1}$$

$$K_{\mathrm{A2,CO3}} = \frac{(\mathrm{H^+})(\mathrm{CO_3{}^{2-}})}{(\mathrm{HCO_3{}^-})} = 10^{-10.33} \qquad \text{eq. 6–S2}$$

$$K_{\mathrm{A1,PO4}} = \frac{(\mathrm{H^+})(\mathrm{H_2PO_4{}^-})}{(\mathrm{H_3PO_4(aq)})} = 10^{-2.12} \qquad \text{eq. 6–S3}$$

$$K_{\mathrm{A2,PO4}} = \frac{(\mathrm{H^+})(\mathrm{HPO_4{}^{2-}})}{(\mathrm{H_2PO_4{}^-})} = 10^{-7.21} \qquad \text{eq. 6–S4}$$

$$K_{\mathrm{A3,PO4}} = \frac{(\mathrm{H^+})(\mathrm{PO_4{}^{3-}})}{(\mathrm{HPO_4{}^{2-}})} = 10^{-12.32} \qquad \text{eq. 6–S5}$$

$$K_{\mathrm{CaHCO_3^+}} = \frac{(\mathrm{CaHCO_3^+})}{(\mathrm{Ca^{2+}})(\mathrm{HCO_3{}^-})} = 10^{1.16} \qquad \text{eq. 6–S6}$$

$$K_{\mathrm{CaCO_3(aq)}} = \frac{(\mathrm{CaCO_3(aq)})}{(\mathrm{Ca^{2+}})(\mathrm{CO_3{}^{2-}})} = 10^{3.38} \qquad \text{eq. 6–S7}$$

$$K_{\mathrm{CaOH^+}} = \frac{(\mathrm{CaOH^+})}{(\mathrm{Ca^{2+}})(\mathrm{OH^-})} = 25.12 \qquad \text{eq. 6–S8}$$

$$K_{\mathrm{CaH_2PO_4^+}} = \frac{(\mathrm{CaH_2PO_4^+})}{(\mathrm{Ca^{2+}})(\mathrm{H_2PO_4{}^-})} = 31.9 \qquad \text{eq. 6–S9}$$

$$K_{\mathrm{CaHPO_4(aq.)}} = \frac{(\mathrm{CaHPO_4(aq)})}{(\mathrm{Ca^{2+}})(\mathrm{HPO_4{}^{2-}})} = 6.81 \times 10^2 \qquad \text{eq. 6–S10}$$

$$K_{\mathrm{CaPO_4{}^-}} = \frac{(\mathrm{CaPO_4{}^-})}{(\mathrm{Ca^{2+}})(\mathrm{PO_4{}^{3-}})} = 3.46 \times 10^6 \qquad \text{eq. 6–S11}$$

The activity of each ionic component, *i*, in parentheses was the product of its concentration, C_i, and the activity coefficient of the component, γ_i by the Davies equation (eq. 6–S12). I is the ionic strength of the solution (eq. 6–S13) and Z is the charge of the component.[240]

$$\log\gamma_i = -0.5{z_i}^2\left[\frac{I^{\frac{1}{2}}}{1+I^{\frac{1}{2}}} - 0.2I\right] \qquad \text{eq. 6–S12}$$

$$I = \frac{1}{2}\sum_i c_i{z_i}^2 \qquad \text{eq. 6–S13}$$

By applying eqs. 6–S1–13 to mass balance equations with respect to Ca, PO_4^{3-}, and CO_3^{2-}, we calculated the activities of all components and the *IAP* of three different calcium phosphate minerals: HA (eq. 6–S14), octacalcium phosphate (OCP, eq. 6–S15), and dicalcium phosphate (DCP, eq. 6–S16). In addition to these calcium phosphate minerals, the most stable calcium carbonate mineral, calcite (CC, eq. 6–S17), was considered as well, due to the higher possibility of its formation in an aqueous system with sufficient Ca in a high pH range.

$$IAP_{\mathrm{HA}} = (\mathrm{Ca^{2+}})^5(\mathrm{PO_4{}^{3-}})^3(\mathrm{OH^-}) \qquad \text{eq. 6–S14}$$

$$IAP_{\mathrm{OCP}} = (\mathrm{Ca^{2+}})^4(\mathrm{H^+})(\mathrm{PO_4{}^{3-}})^3 \qquad \text{eq. 6–S15}$$

$$IAP_{\mathrm{DCP}} = (\mathrm{Ca^{2+}})(\mathrm{HPO_4{}^{2-}}) \qquad \text{eq. 6–S16}$$

$$IAP_{\mathrm{CC}} = (\mathrm{Ca}^{2+})(\mathrm{CO_3}^{2-}) \qquad \text{eq. 6–S17}$$

The SI for each mineral can be calculated by IAP over K_{sp} in log scale (SI = $\log \frac{IAP}{K_{sp}}$). The experimentally determined K_{sp} values were obtained from different literature sources: $K_{\mathrm{sp,HA}} = 10^{-58.5}$ at 25°C,[104] $K_{\mathrm{sp,OCP}} = 10^{-48.4}$ at 23.5°C,[217] $K_{\mathrm{sp,DCP}} = 10^{-6.62}$ at 25°C,[218] and $K_{\mathrm{sp,CC}} = 10^{-8.48}$ at 25°C.[219] SI values were evaluated for each mineral at each pH, from 5 to 10 with 0.05 steps. When SI > 0, we assumed that phosphate (or carbonate for CC) species were governed by K_{sp} reaching an equilibrium. Thus, concentrations of all the species were recalculated until the sum of Ca precipitated as a mineral and all the aqueous Ca species equaled the initial Ca amount in the system. The computational work was done using a script written in MATLAB R2013 (Mathworks, USA).

Figure 6–S4a,b show the total aqueous Ca and P concentrations, equilibrated with different calcium phosphate and carbonate minerals at pH 5–10. Figure 6–S4c shows the SI with respect to different calcium phosphate minerals. Among the minerals studied, HA shows the lowest solubility above pH 6. Aqueous P concentration starts to decrease at pH 7, when equilibrium with OCP is reached. However, the system is undersaturated with respect to dicalcium phosphate within the pH range evaluated. Calcite formation becomes significant above pH 8, and therefore, carbonate may compete with phosphate for Ca above that pH. However, the equilibrium pH values of the solution after the experiments in this study were all below pH 8, thus the possibility of CC formation was considered insignificant.

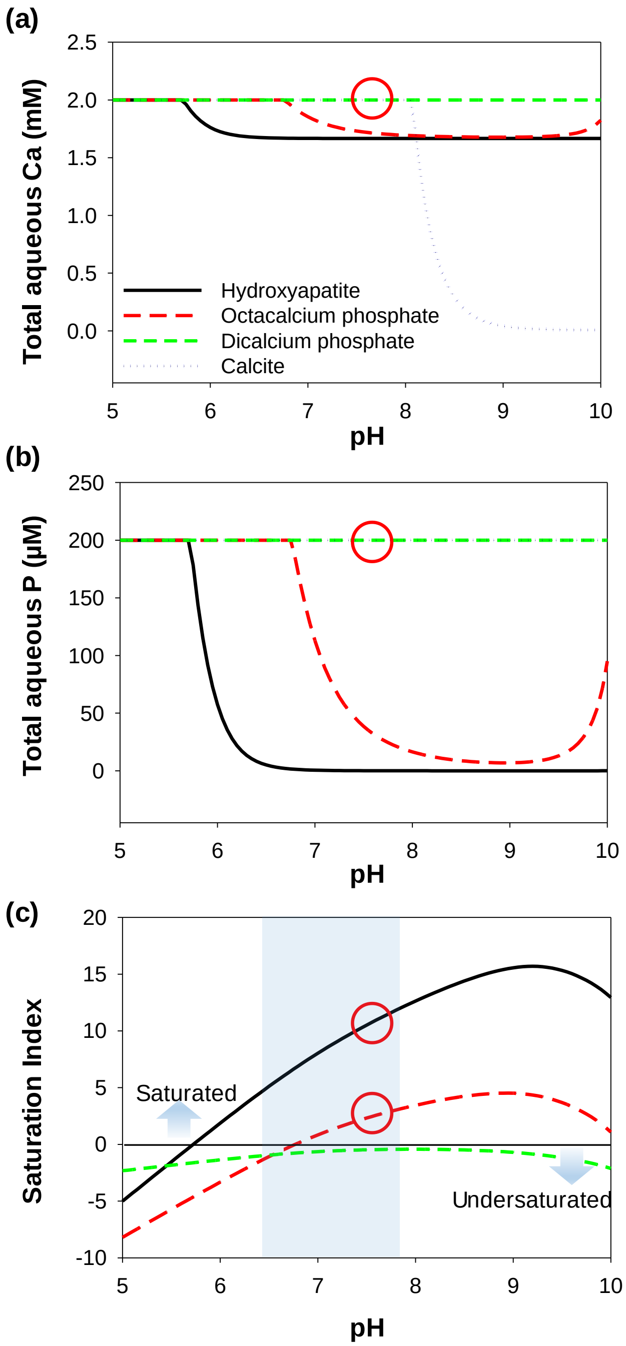

Figure 6–S4 Ca and P concentrations in equilibrium with different calcium phosphate and carbonate minerals at pH 5–10 (**a-b**). Initial conditions of the system: 10 mM NaCl, 2 mM $CaCl_2$, and 0.2 mM Na_2HPO_4. Open carbonate system. Plotted saturation indices for calcium phosphate minerals under the initial condition in the pH range (**c**). The blue box in (**c**) highlights the experimental regime used in this study. Red circles in (**a-c**) indicate the initial experimental condition for P removal experiments in the saturated system.

6.7.4 Potential Formation of Struvite in the HA-Supersaturated Condition

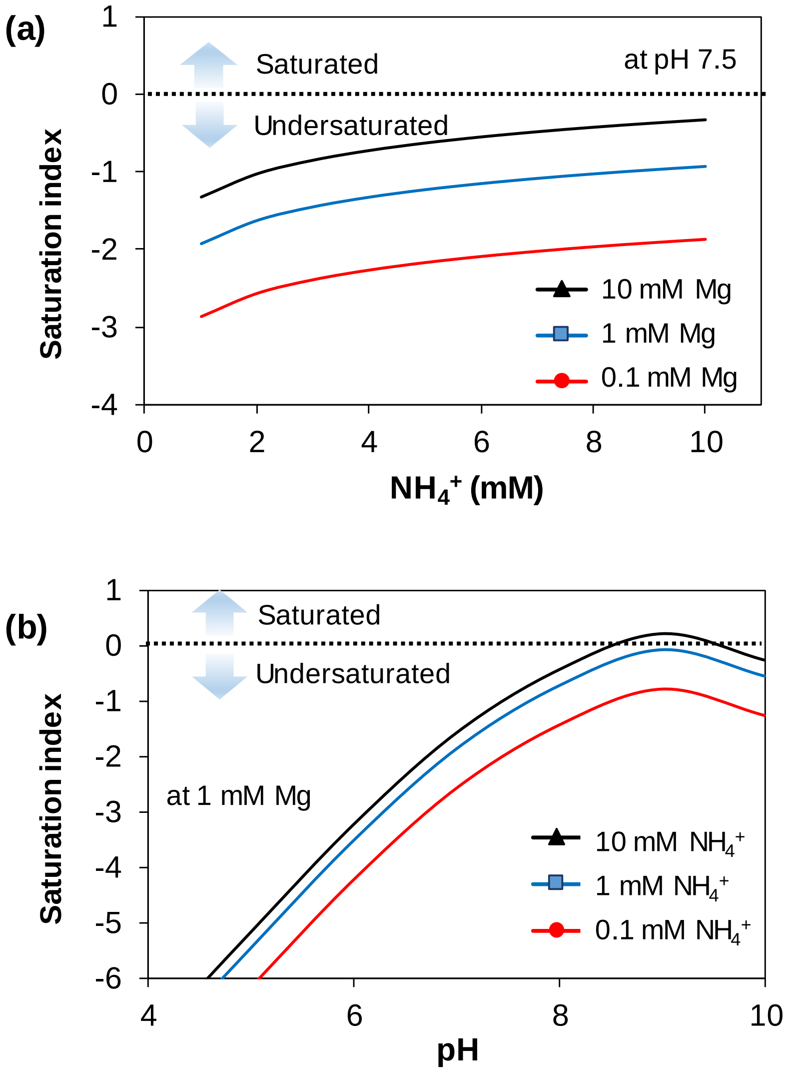

Figure 6–S5 Supersaturation index with respect to struvite in the HA-supersaturated condition. (**a**) The influence of NH_4^+ at 0.1–10 mM Mg in the system. (**b**) The influence of pH at 0.1–10 mM NH_4^+. Thermodynamic equilibrium calculations were conducted by Visual MINTEQ (Ver. 3.1). Our simulation result shows that in most cases, even at high Mg^{2+} and NH_4^+ concentrations up to 10 mM, the HA-supersaturated solution was undersaturated with respect to struvite at neutral pH. For comparison, typical levels of NH_4^+ in toilet water[160] and Mg^{2+} in fresh urine[241] are around 5 and 4 mM, respectively.

6.7.5 Aqueous Fe and P concentrations equilibrated with hematite and strengite

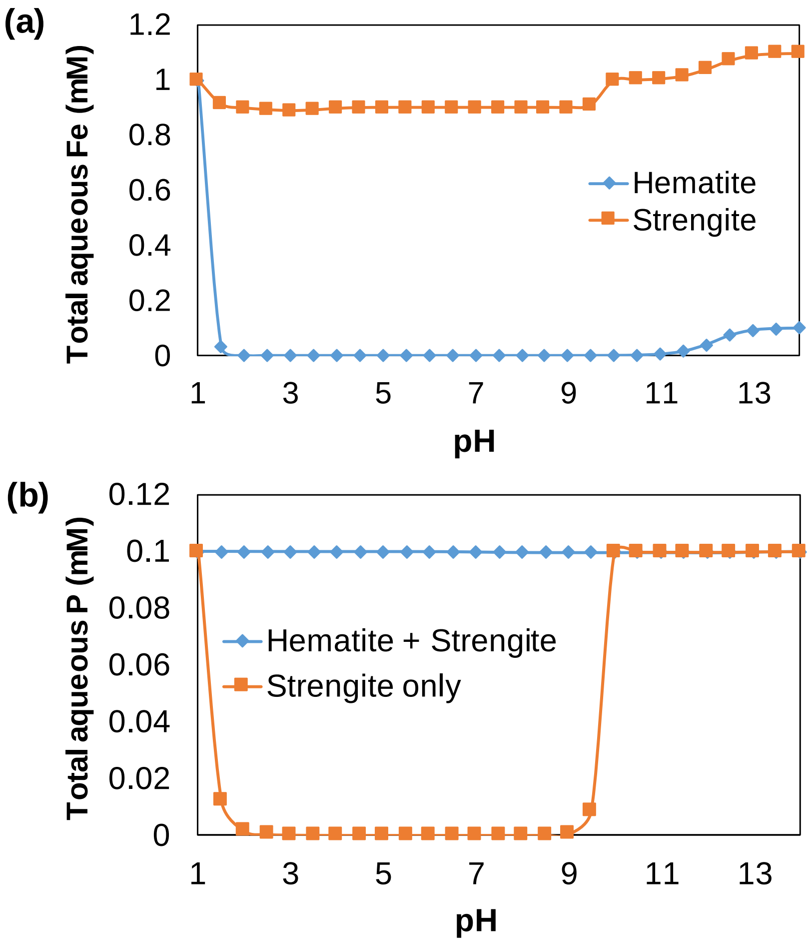

Figure 6–S6 Aqueous Fe and P concentrations equilibrated with hematite (Fe_2O_3) and strengite ($FePO_4 \cdot 2H_2O$). Thermodynamic equilibrium calculations were conducted by Visual MINTEQ (Ver. 3.1). Initial conditions of the system were 1 mM $FeCl_3$ and 0.1 mM Na_3PO_4. A lower Fe concentration equilibrated with hematite than with strengite indicates that iron oxide is more thermodynamically stable than iron phosphate minerals (**a**). If hematite precipitation occurs (**b**), the immobilization of P as a strengite mineral is inhibited. At higher pH, iron hydroxide formation dominates, therefore P immobilization is also inhibited.

Chapter 7. Conclusions and Future Directions

7.1 Conclusions

The nucleation, growth, and crystallization of CaP minerals in collagen are important in the initial stages of bone mineralization. Utilizing synchrotron-based *in situ* observation techniques, we successfully provided new kinetic and thermodynamic insights into collagen mineralization. With an advanced understanding of the interfacial chemistry between collagen and CaP nuclei, we were able to better control the nucleation kinetics and pathways of CaP nuclei (nanoscale), the spatial distribution of CaP minerals within the organic matrix (macroscale), and the mechanical properties of the composite structure (macroscale). Furthermore, we achieved enhanced mineralization of densely-packed and highly-organized collagen matrix by utilizing external mechanical loading and electrical stimulation. Applying the principles from CaP biomineralization studies, we engineered the thermodynamic properties of CaP minerals using alginate beads as organic templates for solid nucleation. By utilizing alginate beads embedding CaP minerals with different levels of solubility, we successfully managed P concentrations to prevent eutrophication and recover P as a renewable source.

The work of the dissertation was conducted through five different tasks, each summarized below.

In **Task 1**, using *in situ* SAXS, we examined the nucleation and growth of CaP within collagen matrices and elucidated how a nucleation inhibitor, pAsp, governs mineralization kinetics and pathways. Mineralization without pAsp led initially to spherical aggregates of CaP in the entire extrafibrillar space, which later transformed into extrafibrillar plates at the outermost surface of the collagen matrix. However, mineralization with pAsp led directly to the formation of intrafibrillar CaP plates with a spatial distribution gradient through the depth of the matrix. The results showed that nucleation kinetics and mineral distributions within organic matrices could be controlled by aqueous chemistry.

In **Task 2**, we combined *in situ* X-ray scattering observations and classical nucleation theory to report on experimentally obtained nucleation energy barriers to EM and IM. With the addition of pAsp, interfacial energies between nuclei and mineralization fluids increased. However, the confined gap spaces inside collagen fibrils lowered the energy barrier by reducing the reactive surface area of nuclei, thus decreasing the surface energy penalty. The confined gap geometry of collagen changed the nucleation pathway and guided the 2D morphology and structure of bioapatite.

In **Task 3**, we showed that cyclic strain increased acellular nucleation rates in highly-organized fibrillar collagen matrices by 33% compared to the static strain condition. The enhanced transport of mineralization fluids by the cyclic strain delivered nucleation precursors into the inner surface of the matrix more effectively. The enhancement of inner matrix bioapatite by cyclic strain led to increases in the elastic modulus, strength, and resilience. The results suggested that the spatial distribution of mineral determines tissue-level mechanical properties more critically than total mineral contents, and the distribution could be effectively engineered by utilizing cyclic strain.

In **Task 4**, we found that the applying pulsed electric stimulation significantly enhanced the transport of body fluid components through a microscale channel between the cathode and collagen surfaces. The enhanced transport increased the diffusion of nucleation precursor molecules to the inner surface of tube-like collagen scaffolds. Our findings indicated that applying proper pulsed electrical signals through a cathode can locally speed up the nucleation of bioapatite, allowing us to control the spatial distribution of bioapatite in microscale.

In **Task 5**, we demonstrated that bioinspired biomineralization principles can be applied to environmental remediation of P-rich aquatic environments. By seeding reactive CaP nuclei in calcium alginate beads, we reduced the energy barriers to CaP nucleation. The CaP nucleation kinetics enhanced by seeds effectively immobilized aqueous P in the macroscale beads, which could be reused as a slow-release fertilizer. Given that the CaP crystalline seed with a higher degree of crystallinity has a lower solubility than does an amorphous structure, the equilibrium P concentration was regulated successfully by the seed crystallinity during both the removal and release processes. Simultaneous seed nucleation during alginate gelation enabled control of the degree of the seeds' crystallization, without requiring any hazardous substance or additional energy input.

7.2 Future Research Directions

We evaluated different aspects of CaP mineralization in the complex hierarchical organic structure using *in situ* and surface characterization tools at multiple-length scales. A highly interdisciplinary approach was utilized for this study, providing insights into future research directions in various fields of research.

In the aspect of interfacial chemistry, we need to better understand CaP nucleation pathways for bone mineralization. In our studies, we simplified the experimental system into EM- and IM-dominant systems. However, there would be different nucleation sites in the physiological systems, including outer surfaces of collagen microfibrils. Different nucleation sites might involve different nucleation pathways. If the pathways follow non-classical nucleation pathways, a new model or another modification of CNT will be required. In addition, the dynamics in aqueous environments caused by cellular activities in physiological systems should be considered in the future studies. For example, the excretion of NCPs from osteoblast cells will be a step function, changing the local environments where nucleation occurs temporarily.[63,242]

Confined nucleation in collagen gap regions can be further evaluated from the perspectives of physical chemistry and geochemistry. In addition to the 2D model developed in this study, a 3D constructed collagen gap model needs to be considered to better predict nucleation behaviors during bone mineralization. The thermodynamic properties of CaP nuclei in confined space need to be further explored, especially considering the affinity between collagen side walls and the nucleus' surface. The functional groups of amino acid residues in collagen would play a significant role in determining the surface affinity.

For biomedical applications, we need to clearly distinguish the contributions of the cellular and acellular activities to bone formation. Currently, many studies evaluate various biomaterials' ability to increase osteoblast cell differentiation *in vivo* and *in vitro*. However, relatively few studies have been conducted on how osteoblast cell activity results in transport of inorganic precursor molecules and their transformation into mineral phases. The outcomes will contribute to developing an abiotic synthesis of bone-like materials for bone grafts and tissue-replacement.

In this dissertation, we elucidated how we can control nanoscale nucleation and macroscale CaP distribution in collagen, employing cyclic mechanical loading and pulsed electrical stimulation. These controls can eventually lead to tuning the macroscale mechanical properties of biomaterials. The lessons learned from this study can also be applied to other nano/organic composite materials requiring different functionality. As an example, in Task 5, we engineered the solubility of CaP minerals using alginate beads as an organic template for an environmental remediation strategy. The utilization of the reactive functional nanomaterials whose properties are controlled by organic templates will open more research opportunities for different engineering applications, such as drug and gene release for cancer therapy.

In conclusion, this dissertation explores chemistry at organic–mineral interfaces to seek engineering applications of the composite system with hierarchical structures. By linking nanoscale reactions to macroscale properties, we can design the functionality of composite materials at multiple length scales. The obtained knowledge and interdisciplinary approach utilized in this study can be extended to various fields of study and to developing different engineering applications.

References

1 Butusov, M. & Jernelöv, A. *Phosphorus: an element that could have been called Lucifer*. Vol. 9 (Springer, 2013).

2 Pasteris, J. D., Wopenka, B. & Valsami-Jones, E. Bone and tooth mineralization: Why apatite? *Elements* **4**, 97-104 (2008).

3 Glimcher, M. J. Molecular Biology of Mineralized Tissues with Particular Reference to Bone. *Reviews of Modern Physics* **31**, 359-393 (1959).

4 Reznikov, N., Shahar, R. & Weiner, S. Bone hierarchical structure in three dimensions. *Acta Biomaterialia* **10**, 3815-3826 (2014).

5 Reznikov, N., Bilton, M., Lari, L., Stevens, M. M. & Kröger, R. Fractal-like hierarchical organization of bone begins at the nanoscale. *Science* **360** (2018).

6 Glimcher, M. J. Bone: Nature of the calcium phosphate crystals and cellular, structural, and physical chemical mechanisms in their formation. *Rev. Mineral. Geochem.* **64**, 223-282 (2006).

7 Dove, P. M. The Rise of Skeletal Biominerals. *Elements* **6**, 37-42 (2010).

8 Habraken, W. J. E. M. *et al.* Ion-association complexes unite classical and non-classical theories for the biomimetic nucleation of calcium phosphate. *Nat. Commun.* **4** (2013).

9 Liu, Y. *et al.* Modelling the mechanics of partially mineralized collagen fibrils, fibres and tissue. *Journal of The Royal Society Interface* **11** (2014).

10 Nair, A. K., Gautieri, A., Chang, S.-W. & Buehler, M. J. Molecular mechanics of mineralized collagen fibrils in bone. *Nat Commun* **4**, 1724, doi:10.1038/ncomms2720 (2013).

11 Jun, Y.-S., Kim, D. & Neil, C. W. Heterogeneous nucleation and growth of nanoparticles at environmental interfaces. *Acc. Chem. Res.* **49**, 1681-1690 (2016).

12 Gebauer, D., Kellermeier, M., Gale, J. D., Bergstrom, L. & Colfen, H. Pre-nucleation clusters as solute precursors in crystallisation. *Chem. Soc. Rev.* **43**, 2348-2371 (2014).

13 De Yoreo, J. J. & Vekilov, P. G. Principles of Crystal Nucleation and Growth. *Rev. Mineral. Geochem.* **54**, 57-93 (2003).

14 Gebauer, D. & Cölfen, H. Prenucleation clusters and non-classical nucleation. *Nano Today* **6**, 564-584 (2011).

15 Becker, R. R. Becker and W. Döring, Ann. Phys.(Leipzig) 24, 719 (1935). *Ann. Phys.(Leipzig)* **24**, 719 (1935).

16 Li, Q. & Jun, Y.-S. The apparent activation energy and pre-exponential kinetic factor for heterogeneous calcium carbonate nucleation on quartz. *Communications Chemistry* **1**, 56 (2018).

17 Li, Q., Fernandez-Martinez, A., Lee, B., Waychunas, G. A. & Jun, Y.-S. Interfacial energies for heterogeneous nucleation of calcium carbonate on mica and quartz. *Environ. Sci. Technol.* **48**, 5745-5753 (2014).

18 Fernandez-Martinez, A., Hu, Y., Lee, B., Jun, Y.-S. & Waychunas, G. A. In Situ Determination of Interfacial Energies between Heterogeneously Nucleated $CaCO_3$ and Quartz Substrates: Thermodynamics of CO2 Mineral Trapping. *Environmental Science & Technology* **47**, 102-109 (2013).

19 De Yoreo, J. J., Waychunas, G. A., Jun, Y.-S. & Fernandez-Martinez, A. In situ investigations of carbonate nucleation on mineral and organic surfaces. *Rev. Mineral. Geochem.* **77**, 229-257 (2013).

20 Gebauer, D., Völkel, A. & Cölfen, H. Stable Prenucleation Calcium Carbonate Clusters. *Science* **322**, 1819-1822 (2008).

21 Meldrum, F. C. & Sear, R. P. Now you see them. *Science* **322**, 1802-1803 (2008).

22 Betts, F., Blumenthal, N. C., Posner, A. S., Becker, G. L. & Lehninger, A. L. Atomic structure of intracellular amorphous calcium phosphate deposits. *Proceedings of the National Academy of Sciences* **72**, 2088-2090 (1975).

23 Betts, F. & Posner, A. S. An X-ray radial distribution study of amorphous calcium phosphate. *Mater. Res. Bull.* **9**, 353-360 (1974).

24 Onuma, K. & Ito, A. Cluster Growth Model for Hydroxyapatite. *Chemistry of Materials* **10**, 3346-3351 (1998).

25 Oyane, A. *et al.* Formation and growth of clusters in conventional and new kinds of simulated body fluids. *Journal of Biomedical Materials Research Part A* **64A**, 339-348 (2003).

26 Dey, A. *et al.* The role of prenucleation clusters in surface-induced calcium phosphate crystallization. *Nat. Mater.* **9**, 1010-1014 (2010).

27 Nudelman, F. *et al.* The role of collagen in bone apatite formation in the presence of hydroxyapatite nucleation inhibitors. *Nat. Mater.* **9**, 1004-1009 (2010).

28 Mahamid, J. *et al.* Mapping amorphous calcium phosphate transformation into crystalline mineral from the cell to the bone in zebrafish fin rays. *Proc. Natl. Acad. Sci. U.S.A.* **107**, 6316-6321 (2010).

29 Yang, Y., Mkhonto, D., Cui, Q. & Sahai, N. Theoretical Study of Bone Sialoprotein in Bone Biomineralization. *Cells Tissues Organs* **194**, 182-187 (2011).

30 Xu, Z. *et al.* Small molecule-mediated control of hydroxyapatite growth: Free energy calculations benchmarked to density functional theory. *J. Comput. Chem.* **35**, 70-81 (2014).

31 Delgado-López, J. M. *et al.* Crystal size, morphology, and growth mechanism in bio-inspired apatite nanocrystals. *Adv. Funct. Mater.* **24**, 1090–1099 (2013).

32 Deymier, A. C. *et al.* Protein-free formation of bone-like apatite: New insights into the key role of carbonation. *Biomaterials* **127**, 75-88 (2017).

33 Alexander, B. *et al.* The nanometre-scale physiology of bone: steric modelling and scanning transmission electron microscopy of collagen–mineral structure. *J. R. Soc., Interface* **9**, 1774-1786 (2012).

34 Hodge, A. J. & Petruska, J. A. *In Aspects of protein structure (ed. G. N. Ramachandran)*. (Academic Press, 1963).

35 Orgel, J. P. R. O., Irving, T. C., Miller, A. & Wess, T. J. Microfibrillar Structure of Type I Collagen In Situ. *Proc. Natl. Acad. Sci. U.S.A.* **103**, 9001-9005 (2006).

36 Orgel, J. P. R. O. *et al.* The In Situ Supermolecular Structure of Type I Collagen. *Structure* **9**, 1061-1069 (2001).

37 Jung, H., Lee, B. & Jun, Y.-S. Structural Match of Heterogeneously Nucleated Mn(OH)2(s) Nanoparticles on Quartz under Various pH Conditions. *Langmuir* **32**, 10735-10743 (2016).

38 Ito, S., Saito, T. & Amano, K. In vitro apatite induction by osteopontin: interfacial energy for hydroxyapatite nucleation on osteopontin. *J. Biomed. Mater. Res., Part A* **69**, 11-16 (2004).

39 Koutsopoulos, S., Paschalakis, P. C. & Dalas, E. The calcification of elastin in vitro. *Langmuir* **10**, 2423-2428 (1994).

40 Koutsoukos, P. G. & Nancollas, G. H. The mineralization of collagen in vitro. *Colloids Surf.* **28**, 95-108 (1987).

41 Nielsen, A. E. & Söhnel, O. Interfacial tensions electrolyte crystal-aqueous solution, from nucleation data. *Journal of Crystal Growth* **11**, 233-242 (1971).

42 Olszta, M. J., Douglas, E. P. & Gower, L. B. Scanning Electron Microscopic Analysis of the Mineralization of Type I Collagen via a Polymer-Induced Liquid-Precursor (PILP) Process. *Calcif Tissue Int* **72**, 583-591 (2003).

43 Jee, S. S., Culver, L., Li, Y., Douglas, E. P. & Gower, L. B. Biomimetic mineralization of collagen via an enzyme-aided PILP process. *Journal of Crystal Growth* **312**, 1249-1256 (2010).

44 Jee, S.-S., Thula, T. T. & Gower, L. B. Development of bone-like composites via the polymer-induced liquid-precursor (PILP) process. Part 1: Influence of polymer molecular weight. *Acta Biomater.* **6**, 3676-3686 (2010).

45 Li, Y. *et al.* Biomimetic Mineralization of Woven Bone-Like Nanocomposites: Role of Collagen Cross-Links. *Biomacromolecules* **13**, 49-59 (2011).

46 Toroian, D., Lim, J. E. & Price, P. A. The Size Exclusion Characteristics of Type I Collagen: Implications for the Role of Noncollageneous Bone Constituents in Mineralization. *Journal of Biological Chemistry* **282**, 22437-22447 (2007).
47 Wang, Y. *et al.* The predominant role of collagen in the nucleation, growth, structure and orientation of bone apatite. *Nat. Mater.* **11**, 724 (2012).
48 Chen, L., Jacquet, R., Lowder, E. & Landis, W. J. Refinement of collagen–mineral interaction: A possible role for osteocalcin in apatite crystal nucleation, growth and development. *Bone* **71**, 7-16 (2015).
49 Landis, W. J. *et al.* Mineralization of collagen may occur on fibril surfaces: Evidence from conventional and high-voltage electron microscopy and three-dimensional Imaging. *J. Struct. Biol.* **117**, 24-35 (1996).
50 Emmanuel, S., Anovitz, L. M. & Day-Stirrat, R. J. Effects of coupled chemo-mechanical processes on the evolution of pore-size distributions in geological media. *Rev. Mineral. Geochem.* **80**, 45-60 (2015).
51 Hedges, L. O. & Whitelam, S. Patterning a surface so as to speed nucleation from solution. *Soft Matter* **8**, 8624-8635 (2012).
52 Jiang, Q. & Ward, M. D. Crystallization under nanoscale confinement. *Chem. Soc. Rev.* **43**, 2066-2079 (2014).
53 Page, A. J. & Sear, R. P. Heterogeneous Nucleation in and out of Pores. *Physical Review Letters* **97**, 065701 (2006).
54 Hamilton, B. D., Ha, J.-M., Hillmyer, M. A. & Ward, M. D. Manipulating Crystal Growth and Polymorphism by Confinement in Nanoscale Crystallization Chambers. *Accounts of Chemical Research* **45**, 414-423 (2012).
55 Wang, Y. Nanogeochemistry: Nanostructures, emergent properties and their control on geochemical reactions and mass transfers. *Chem. Geol.* **378–379**, 1-23 (2014).
56 Buckton, G. & Beezer, A. E. The relationship between particle size and solubility. *International Journal of Pharmaceutics* **82**, R7-R10 (1992).
57 Anduix-Canto, C. *et al.* Effect of Nanoscale Confinement on the Crystallization of Potassium Ferrocyanide. *Crystal Growth & Design* **16**, 5403-5411 (2016).
58 Shahroosvand, H. & Ghorbani-asl, M. Understanding the thermal decomposition effects in TOPO capped ZnO nanocrystals. *CrystEngComm* **14**, 8199-8207 (2012).
59 Cantaert, B., Beniash, E. & Meldrum, F. C. Nanoscale confinement controls the crystallization of calcium phosphate: relevance to bone formation. *Chem. - Eur. J.* **19**, 14918-14924 (2013).
60 Cantaert, B., Beniash, E. & Meldrum, F. C. The role of poly(aspartic acid) in the precipitation of calcium phosphate in confinement. *J. Mater. Chem. B* **1**, 6586-6595 (2013).
61 Boskey, A. L. Mineralization of bones and teeth. *Elements* **3**, 385-391 (2007).
62 Liu, Y., Luo, D. & Wang, T. Hierarchical Structures of Bone and Bioinspired Bone Tissue Engineering. *Small* **12**, 4611-4632 (2016).
63 Simon, P. *et al.* First evidence of octacalcium phosphate@osteocalcin nanocomplex as skeletal bone component directing collagen triple–helix nanofibril mineralization. *Scientific Reports* **8**, 13696 (2018).
64 Currey, J. D. The effect of porosity and mineral content on the Young's modulus of elasticity of compact bone. *Journal of Biomechanics* **21**, 131-139 (1988).
65 Currey, J. D. Tensile yield in compact bone is determined by strain, post-yield behaviour by mineral content. *Journal of Biomechanics* **37**, 549-556 (2004).
66 Smith, L. *et al.* Graded control of collagen matrix stiffness using extrafilbrillar and intra fibrillar mineralization. *In preparation*.
67 Li, X. *et al.* Nanofiber Scaffolds with Gradations in Mineral Content for Mimicking the Tendon-to-Bone Insertion Site. *Nano Letters* **9**, 2763-2768 (2009).
68 Landis, W. J. & Jacquet, R. Association of calcium and phosphate Ions with collagen in the mineralization of vertebrate tissues. *Calcif. Tissue International* **93**, 329-337 (2013).

69 Schwartz, A. G., Pasteris, J. D., Genin, G. M., Daulton, T. L. & Thomopoulos, S. Mineral Distributions at the Developing Tendon Enthesis. *PLoS ONE* **7**, e48630 (2012).

70 Wopenka, B., Kent, A., Pasteris, J. D., Yoon, Y. & Thomopoulos, S. The Tendon-to-Bone Transition of the Rotator Cuff: A Preliminary Raman Spectroscopic Study Documenting the Gradual Mineralization Across the Insertion in Rat Tissue Samples. *Appl. Spectrosc.* **62**, 1285-1294 (2008).

71 Olszta, M. J. *et al.* Bone structure and formation: A new perspective. *Mater. Sci. Eng. R* **58**, 77-116 (2007).

72 Heiss, A. *et al.* Structural Basis of Calcification Inhibition by α2-HS Glycoprotein/Fetuin-A: Formation of Colloidal Calciprotein Particles. *Journal of Biological Chemistry* **278**, 13333-13341 (2003).

73 Landis, W. J., Song, M. J., Leith, A., McEwen, L. & McEwen, B. F. Mineral and organic matrix interaction in normally calcifying tendon visualized in three dimensions by high-voltage electron microscopic tomography and graphic image reconstruction. *J. Struct. Biol.* **110**, 39-54 (1993).

74 Combes, C. & Rey, C. Amorphous calcium phosphates: Synthesis, properties and uses in biomaterials. *Acta Biomater.* **6**, 3362-3378 (2010).

75 Posner, A. S. & Betts, F. Synthetic amorphous calcium phosphate and its relation to bone mineral structure. *Acc. Chem. Res.* **8**, 273-281 (1975).

76 Campi, G. *et al.* Imaging collagen packing dynamics during mineralization of engineered bone tissue. *Acta biomaterialia* **23**, 309-316 (2015).

77 Campi, G. *et al.* Early stage mineralization in tissue engineering mapped by high resolution X-ray microdiffraction. *Acta Biomaterialia* **8**, 3411-3418 (2012).

78 Fratzl, P., Fratzl-Zelman, N., Klaushofer, K., Vogl, G. & Koller, K. Nucleation and growth of mineral crystals in bone studied by small-angle X-ray scattering. *Calcif Tissue Int* **48**, 407-413 (1991).

79 Fratzl, P. *et al.* Mineral crystals in calcified tissues: A comparative study by SAXS. *Journal of Bone and Mineral Research* **7**, 329-334 (1992).

80 Fratzl, P., Schreiber, S. & Klaushofer, K. Bone Mineralization as Studied by Small-Angle X-Ray Scattering. *Connective Tissue Research* **34**, 247-254 (1996).

81 Liebi, M. *et al.* Nanostructure surveys of macroscopic specimens by small-angle scattering tensor tomography. *Nature* **527**, 349-352 (2015).

82 Schaff, F. *et al.* Six-dimensional real and reciprocal space small-angle X-ray scattering tomography. *Nature* **527**, 353-356 (2015).

83 Jun, Y.-S., Lee, B. & Waychunas, G. A. In situ observations of nanoparticle early development kinetics at mineral−water interfaces. *Environ. Sci. Technol.* **44**, 8182-8189, (2010).

84 Boyle, J. J. *et al.* Simple and accurate methods for quantifying deformation, disruption, and development in biological tissues. *J. R. Soc., Interface* **11** (2014).

85 Gamble, J. L. *Chemical anatomy physiology and pathology of extracellular fluid: A lecture syllabus*. Sixth edition edn, Vol. Cambridge, MA (Harvard University Press, 1967).

86 Ohtsuki, C., Kokubo, T. & Yamamuro, T. Mechanism of apatite formation on CaOSiO2P2O5 glasses in a simulated body fluid. *J. Non-Cryst. Solids* **143**, 84-92 (1992).

87 Kihara, T., Ito, J. & Miyake, J. Measurement of Biomolecular Diffusion in Extracellular Matrix Condensed by Fibroblasts Using Fluorescence Correlation Spectroscopy. *PloS one* **8**, e82382 (2013).

88 Rigler, R., Mets, Ü., Widengren, J. & Kask, P. Fluorescence correlation spectroscopy with high count rate and low background: analysis of translational diffusion. *Eur Biophys J* **22**, 169-175 (1993).

89 Liu, J. *et al.* Evaluation of the Particle Growth of Amorphous Calcium Carbonate in Water by Means of the Porod Invariant from SAXS. *Langmuir* **26**, 17405-17412 (2010).

90 Beaucage, G., Kammler, H. K. & Pratsinis, S. E. Particle size distributions from small-angle scattering using global scattering functions. *J. Appl. Crystallogr.* **37**, 523-535 (2004).

91 Tas, A. C. The use of physiological solutions or media in calcium phosphate synthesis and processing. *Acta Biomater.* **10**, 1771-1792 (2014).

92 Fratzl, P. Small-angle scattering in materials science - a short review of applications in alloys, ceramics and composite materials. *J. Appl. Crystallogr.* **36**, 397-404 (2003).

93 Eppell, S. J., Tong, W., Lawrence Katz, J., Kuhn, L. & Glimcher, M. J. Shape and size of isolated bone mineralites measured using atomic force microscopy. *Journal of Orthopaedic Research* **19**, 1027-1034 (2001).

94 Ilavsky, J. & Jemian, P. R. Irena: tool suite for modeling and analysis of small-angle scattering. *J. Appl. Crystallogr.* **42**, 347-353 (2009).

95 Zhang, F. *et al.* Glassy carbon as an absolute intensity calibration standard for small-angle scattering. *Metall. Mater. Trans. A* **41**, 1151-1158 (2010).

96 Beaucage, G. Approximations Leading to a Unified Exponential/Power-Law Approach to Small-Angle Scattering. *Journal of Applied Crystallography* **28**, 717-728 (1995).

97 Masic, A. *et al.* Osmotic pressure induced tensile forces in tendon collagen. *Nat. Commun.* **6**, 5942 (2015).

98 Omelon, S. *et al.* Control of Vertebrate Skeletal Mineralization by Polyphosphates. *PLoS ONE* **4**, e5634 (2009).

99 Kim, D., Lee, B., Thomopoulos, S. & Jun, Y.-S. In situ evaluation of calcium phosphate nucleation kinetics and pathways during intra and extrafibrillar mineralization of collagen matrices. *Cryst. Growth Des.* **16**, 5359-5366 (2016).

100 Lu, X. & Leng, Y. Theoretical analysis of calcium phosphate precipitation in simulated body fluid. *Biomaterials* **26**, 1097-1108 (2005).

101 CW, D. *Ion association*. 41 (Butterworths, 1962).

102 Wu, Y.-T. & Grant, C. Effect of Chelation Chemistry of Sodium Polyaspartate on the Dissolution of Calcite. *Langmuir* **18**, 6813-6820 (2002).

103 Boistelle, R. & Lopez-Valero, I. Growth units and nucleation: The case of calcium phosphates. *J. Cryst Growth* **102**, 609-617 (1990).

104 McDowell, H., Gregory, T. & Brown, W. Solubility of Ca5 (PO4) 3OH in the System Ca (OH) 2-H3PO4-H2O at 5, 15, 25, and 37 C. *J. Res. Nat. Bur. Stand. A* **81**, 273-281 (1977).

105 De Yoreo, J. J. *et al.* Crystallization by particle attachment in synthetic, biogenic, and geologic environments. *Science* **349** (2015).

106 Na, H. G. *et al.* One-to-one correspondence growth mechanism of gourd-like SiOx nanotubes. *Cryst Growth Des.* **16** (2016).

107 Xu, Z. *et al.* Molecular mechanisms for intrafibrillar collagen mineralization in skeletal tissues. *Biomaterials* **39**, 59-66 (2015).

108 Li, T., Senesi, A. J. & Lee, B. Small angle X-ray scattering for nanoparticle research. *Chem. Rev.* **116**, 11128-11180 (2016).

109 Grynpas, M. D., Bonar, L. C. & Glimcher, M. J. Failure to detect an amorphous calcium-phosphate solid phase in bone mineral: A radial distribution function study. *Calcif. Tissue International* **36**, 291-301 (1984).

110 Jäger, C., Welzel, T., Meyer-Zaika, W. & Epple, M. A solid-state NMR investigation of the structure of nanocrystalline hydroxyapatite. *Magnetic Resonance in Chemistry* **44**, 573-580 (2006).

111 Kerschnitzki, M. *et al.* Bone mineralization pathways during the rapid growth of embryonic chicken long bones. *J. Struct. Biol.* **195**, 82-92 (2016).

112 Scherer, G. W. Crystallization in pores. *Cement and Concrete Research* **29**, 1347-1358 (1999).

113 Boskey, A. L. Noncollagenous matrix proteins and their role in mineralization. *Bone and Mineral* **6**, 111-123 (1989).

114 Zhang, H., Gilbert, B., Huang, F. & Banfield, J. F. Water-driven structure transformation in nanoparticles at room temperature. *Nature* **424**, 1025-1029 (2003).

115 McKee, M. D., Addison, W. N. & Kaartinen, M. T. Hierarchies of Extracellular Matrix and Mineral Organization in Bone of the Craniofacial Complex and Skeleton. *Cells Tissues Organs* **181**, 176-188 (2005).

116 Rogers, K. D. & Zioupos, P. The Bone Tissue of the Rostrum of a Mesoplodon Densirostris Whale: a Mammalian Biomineral Demonstrating Extreme Texture. *Journal of Materials Science Letters* **18**, 651-654 (1999).

117 Tanck, E. *et al.* Cortical bone development under the growth plate is regulated by mechanical load transfer. *Journal of Anatomy* **208**, 73-79 (2006).

118 Bailey, D. A., Mckay, H. A., Mirwald, R. L., Crocker, P. R. E. & Faulkner, R. A. A Six-Year Longitudinal Study of the Relationship of Physical Activity to Bone Mineral Accrual in Growing Children: The University of Saskatchewan Bone Mineral Accrual Study. *Journal of Bone and Mineral Research* **14**, 1672-1679 (1999).

119 Collet, P. *et al.* Effects of 1- and 6-month spaceflight on bone mass and biochemistry in two humans. *Bone* **20**, 547-551 (1997).

120 Fritton, S. P. & Weinbaum, S. Fluid and Solute Transport in Bone: Flow-Induced Mechanotransduction. *Annual Review of Fluid Mechanics* **41**, 347-374 (2009).

121 Benjamin, M. & Ralphs, J. R. Fibrocartilage in tendons and ligaments — an adaptation to compressive load. *Journal of Anatomy* **193**, 481-494 (1998).

122 Burr, D. B., Robling, A. G. & Turner, C. H. Effects of biomechanical stress on bones in animals. *Bone* **30**, 781-786 (2002).

123 PJ, D., EU, P. & DR, P. Turneaureite, a new member of the apatite group from Franklin, New Jersey, Balmant, New York and Laangban, Sweden. (1985).

124 Donahue, S. W., Jacobs, C. R. & Donahue, H. J. Flow-induced calcium oscillations in rat osteoblasts are age, loading frequency, and shear stress dependent. *American Journal of Physiology-Cell Physiology* **281**, C1635-C1641 (2001).

125 Tan, S. D. *et al.* Osteocytes subjected to fluid flow inhibit osteoclast formation and bone resorption. *Bone* **41**, 745-75 (2007).

126 Kim, D., Lee, B., Thomopoulos, S. & Jun, Y.-S. The role of confined collagen geometry in decreasing nucleation energy barriers to intrafibrillar mineralization. *Nature Communications* **9**, 962 (2018).

127 Hart, N. H. *et al.* Mechanical basis of bone strength: influence of bone material, bone structure and muscle action. *Journal of Musculoskeletal & Neuronal Interactions* **17**, 114-139 (2017).

128 Piekarski, K. & Munro, M. Transport mechanism operating between blood supply and osteocytes in long bones. *Nature* **269**, 80 (1977).

129 Ehrlich, P. & Lanyon, L. Mechanical strain and bone cell function: a review. *Osteoporos Int* **13**, 688-700 (2002).

130 Fritton, S. & Rubin, C. In vivo measurement of bone deformations using strain gauges. *Bone mechanics handbook* **1**, 8-34 (2001).

131 Liu, Y., Schwartz, A. G., Birman, V., Thomopoulos, S. & Genin, G. M. Stress amplification during development of the tendon-to-bone attachment. *Biomechanics and modeling in mechanobiology* **13**, 973-983 (2014).

132 Wozniak, M., Fausto, A., Carron, C. P., Meyer, D. M. & Hruska, K. A. Mechanically Strained Cells of the Osteoblast Lineage Organize Their Extracellular Matrix Through Unique Sites of αVβ3-Integrin Expression. *Journal of Bone and Mineral Research* **15**, 1731-1745 (2000).

133 Jun, Y. S. & Lee, B. Total X-Ray Scattering and Small-Angle X-ray Scattering for Determining the Structures, Sizes, Shapes, and Aggregation Extents of Iron (Hydr) oxide Nanoparticles. *Iron Oxides: From Nature to Applications*, 371-396 (2016).

134 P., M. S. *et al.* Differential strain patterns of the human gastrocnemius aponeurosis and free tendon, in vivo. *Acta Physiologica Scandinavica* **177**, 185-195 (2003).

135 Chen, J. *et al.* In Vitro Mineralization of Collagen in Demineralized Fish Bone. *Macromolecular Chemistry and Physics* **206**, 43-51 (2005).

136 Rey, C., Combes, C., Drouet, C. & Glimcher, M. J. Bone mineral: update on chemical composition and structure. *Osteoporos Int* **20**, 1013-1021 (2009).
137 Genin, G. M. & Thomopoulos, S. Unification through disarray. *Nature Materials* **16**, 607, (2017).
138 Rossetti, L. *et al.* The microstructure and micromechanics of the tendon–bone insertion. *Nature Materials* **16**, 664 (2017).
139 Smith, L. J. *et al.* Tunability of collagen matrix mechanical properties via multiple modes of mineralization. *Interface Focus* **6** (2016).
140 Teng, H. Stiffness properties of particulate composites containing debonded particles. *International Journal of Solids and Structures* **47**, 2191-2200 (2010).
141 Cowin, S. C., Moss-Salentijn, L. & Moss, M. L. Candidates for the Mechanosensory System in Bone. *Journal of Biomechanical Engineering* **113**, 191-197 (1991).
142 M., R. K., V., G. C. & A., F. J. Fluid shear stress as a mediator of osteoblast cyclic adenosine monophosphate production. *Journal of Cellular Physiology* **143**, 100-104 (1990).
143 A., H. J. & P., A. S. Effect of cyclic and static tensile loading on water content and solute diffusion in canine flexor tendons: An in Vitro study. *Journal of Orthopaedic Research* **12**, 350-356 (1994).
144 Junqueira, L. C. U., Bignolas, G. & Brentani, R. R. Picrosirius staining plus polarization microscopy, a specific method for collagen detection in tissue sections. *The Histochemical Journal* **11**, 447-455 (1979).
145 H., T. B. & B., V. D. R. GSAS-II: the genesis of a modern open-source all purpose crystallography software package. *Journal of Applied Crystallography* **46**, 544-549 (2013).
146 Yu, X. *et al.* Controlling the structural organization of regenerated bone by tailoring tissue engineering scaffold architecture. *Journal of Materials Chemistry* **22**, 9721-9730 (2012).
147 Cameron, J. R., Skofronick, J. G. & Grant, R. M. (1997).
148 Gandhi, R. B. & Robinson, J. R. Permselective characteristics of rabbit buccal mucosa. *Pharmaceutical research* **8**, 1199-1202 (1991).
149 Spadaro, J. A. Mechanical and electrical interactions in bone remodeling. *Bioelectromagnetics* **18**, 193-202 (1997).
150 Friedenberg, Z. & Brighton, C. T. Bioelectric potentials in bone. *J Bone Joint Surg Am* **48**, 915-923 (1966).
151 Hartig, M., Joos, U. & Wiesmann, H.-P. Capacitively coupled electric fields accelerate proliferation of osteoblast-like primary cells and increase bone extracellular matrix formation in vitro. *Eur Biophys J* **29**, 499-506 (2000).
152 Lohmann, C. H. *et al.* Pulsed electromagnetic field stimulation of MG63 osteoblast-like cells affects differentiation and local factor production. *Journal of Orthopaedic Research* **18**, 637-646 (2000).
153 Wiesmann, H.-P., Hartig, M., Stratmann, U., Meyer, U. & Joos, U. Electrical stimulation influences mineral formation of osteoblast-like cells in vitro. *Biochimica et Biophysica Acta (BBA) - Molecular Cell Research* **1538**, 28-37 (2001).
154 Yuan, X., Arkonac, D. E., Chao, P.-h. G. & Vunjak-Novakovic, G. Electrical stimulation enhances cell migration and integrative repair in the meniscus. *Scientific Reports* **4**, 3674, d (2014).
155 Gupta, H. S. *et al.* Cooperative deformation of mineral and collagen in bone at the nanoscale. *Proceedings of the National Academy of Sciences* **103**, 17741-17746 (2006).
156 Ciombor, D. M. The Role of Electrical Stimulation in Bone Repair. *Foot and ankle clinics* **10**, 579-593 (2005).
157 Assiotis, A., Sachinis, N. & Chalidis, B. Pulsed electromagnetic fields for the treatment of tibial delayed unions and nonunions. A prospective clinical study and review of the literature. *Journal of Orthopaedic Surgery and Research* **7**, 24 (2012).

158 Minary-Jolandan, M. & Yu, M.-F. Uncovering Nanoscale Electromechanical Heterogeneity in the Subfibrillar Structure of Collagen Fibrils Responsible for the Piezoelectricity of Bone. *ACS Nano* **3**, 1859-1863 (2009).

159 H., T. B. & B., V. D. R. GSAS-II: the genesis of a modern open-source all purpose crystallography software package. *Journal of Applied Crystallography* **46**, 544-549 (2013).

160 Huang, X. *et al.* Electrochemical disinfection of toilet wastewater using wastewater electrolysis cell. *Water Research* **92**, 164-172 (2016).

161 Noris-Suárez, K. *et al.* In Vitro Deposition of Hydroxyapatite on Cortical Bone Collagen Stimulated by Deformation-Induced Piezoelectricity. *Biomacromolecules* **8**, 941-948 (2007).

162 chemicalbook.com. *DIRECT RED 80*, https://www.chemicalbook.com/ChemicalProductProperty_EN_CB3126376.htm.

163 Fligiel, S. E. G. *et al.* Collagen Degradation in Aged/Photodamaged Skin In Vivo and After Exposure to Matrix Metalloproteinase-1 In Vitro. *Journal of Investigative Dermatology* **120**, 842-848 (2003).

164 Sanchez, S., Solovev, A. A., Schulze, S. & Schmidt, O. G. Controlled manipulation of multiple cells using catalytic microbots. *Chemical Communications* **47**, 698-700 (2011).

165 Halperin, C. *et al.* Piezoelectric Effect in Human Bones Studied in Nanometer Scale. *Nano Letters* **4**, 1253-1256 (2004).

166 Lee, B. Y. *et al.* Virus-based piezoelectric energy generation. *Nat Nano* **7**, 351-356 (2012).

167 Zhai, J. *et al.* Spatial charge manipulated set-selective apatite deposition on micropatterned piezoceramic. *RSC Advances* **7**, 32974-32981 (2017).

168 Tang, W. *et al.* Implantable Self-Powered Low-Level Laser Cure System for Mouse Embryonic Osteoblasts' Proliferation and Differentiation. *ACS Nano* **9**, 7867-7873 (2015).

169 Kumar, M. R. & Freund, M. S. Electrically conducting collagen and collagen-mineral composites for current stimulation. *RSC Advances* **5**, 57318-57327 (2015).

170 Meng, S., Zhang, Z. & Rouabhia, M. Accelerated osteoblast mineralization on a conductive substrate by multiple electrical stimulation. *J Bone Miner Metab* **29**, 535-544 (2011).

171 Yazdimamaghani, M. *et al.* Biomineralization and biocompatibility studies of bone conductive scaffolds containing poly(3,4-ethylenedioxythiophene):poly(4-styrene sulfonate) (PEDOT:PSS). *J Mater Sci: Mater Med* **26**, 1-11 (2015).

172 Chen, Z. *et al.* Recent progress in injectable bone repair materials research. *Front. Mater. Sci.* **9**, 332-345 (2015).

173 Tiwari, J. N. *et al.* Accelerated Bone Regeneration by Two-Photon Photoactivated Carbon Nitride Nanosheets. *ACS Nano* **11**, 742-751 (2017).

174 Pasteris Jill, D. in *Am. Mineral.* Vol. 101 2594 (2016).

175 Bhushan, B. Biomimetics: lessons from nature–an overview. *Philos. Trans. R. Soc., A* **367**, 1445-1486 (2009).

176 Cüneyt Tas, A. Synthesis of biomimetic Ca-hydroxyapatite powders at 37°C in synthetic body fluids. *Biomaterials* **21**, 1429-1438 (2000).

177 Liu, W. *et al.* Nanofiber Scaffolds with Gradients in Mineral Content for Spatial Control of Osteogenesis. *ACS Applied Materials & Interfaces* **6**, 2842-2849 (2014).

178 Eser, P. *et al.* Effect of electrical stimulation-induced cycling on bone mineral density in spinal cord-injured patients. *European Journal of Clinical Investigation* **33**, 412-419 (2003).

179 Filippelli, G. M. The global phosphorus cycle. *Rev. Mineral. Geochem.* **48**, 391-425 (2002).

180 Powers, S. M. *et al.* Long-term accumulation and transport of anthropogenic phosphorus in three river basins. *Nat. Geosci.* **9**, 353-356 (2016).

DOYOON KIM

Department of Energy, Environmental & Chemical Engineering, Washington University in St. Louis
One Brookings Drive, Campus Box 1180 St. Louis, MO 63130
Cell phone: (314)761-7049 | Email: doyoon@wustl.edu

EDUCATION

Washington University in St. Louis, MO, USA
Ph.D. in Energy, Environmental & Chemical Engineering ***2012 – 2018***
Dissertation: Mechanisms of Calcium Phosphate Mineralization on Biological Interfaces and their Engineering Applications (Advisor: Professor Young-Shin Jun)

Hanyang University, Seoul, Korea
M.S. in Environmental Engineering ***2009 – 2011***
Thesis: Modification of Activated Carbon Surface for the Stabilization of Contaminated Sediments (Advisor: Professor Jae-Woo Park)
B.S. in Civil Engineering, Summa Cum Laude ***2002 – 2009***

PUBLICATIONS (Google Scholar Profile)

16 Published

1. Min, Y., ***Kim, D***., and Jun, YS. (**2018**) Effects of Na^+ and K^+ Exchange in Interlayers on Biotite Dissolution under Geologic CO_2 Sequestration Conditions, ***Environmental Science & Technology***, DOI: 10.1021/acs.est.8b04623.
2. Wu, X., Neil, C., ***Kim, D.,*** Jung, H., Newville, M., and Jun, YS. **(2018)** Co-effects of UV/H_2O_2 and Natural Organic Matter on the Surface Chemistry of Cerium Oxide Nanoparticles, ***Environmental Science: Nano,*** DOI: 10.1039/C8EN00435H.
3. Zhang, L., ***Kim, D***., and Jun, YS. (**2018**) Effects of Phosphonate Structures on Brine−Biotite Interactions under Subsurface Relevant Conditions, ***ACS Earth and Space Chemistry***, DOI: 10.1021/acsearthspacechem.8b00075.
4. Zhang, L., ***Kim, D***., and Jun, YS. (**2018**) The Effects of Phosphonate-Based Scale Inhibitor on Brine−Biotite Interactions under Subsurface Conditions, ***Environmental Science & Technology***, DOI: 10.1021/acs.est.7b05785.
5. ***Kim, D.***, Lee, B., Thomopoulos, S., and Jun, YS. (**2018**) The Role of Confined Collagen Geometry in Decreasing Nucleation Energy Barriers to Intrafibrillar Mineralization, ***Nature Communications***, DOI: 10.1038/s41467-018-03041-1. Open Access Link
6. ***Kim, D.***, Wu, T., Cohen M., Jeon, I., and Jun, YS. (**2018**) Designing the Crystalline Structure of Calcium Phosphate Seed Minerals in Organic Templates for Sustainable Phosphorus, ***Green Chemistry***, DOI: 10.1039/C7GC02634J.

7. Zhang, L., ***Kim, D***., Kim, Y., Wen, J., and Jun, YS. (**2017**) Effect of Phosphate on Biotite Dissolution and Secondary Precipitation under conditions relevant to engineered subsurface processes, ***Physical Chemistry Chemical Physics***, DOI: 10.1039/C7CP05158A.
8. Hui, Y., Jung, H., ***Kim, D.,*** and Jun, YS. (**2017**) Kinetics of α-MnOOH Nanoparticle Formation through Enzymatically-catalyzed Bio-mineralization inside Apoferritin, ***Crystal Growth & Design***, DOI: 10.1021/acs.cgd.7b00568.
9. Jung, H., Chandha, T.S., ***Kim, D.,*** Biswas, P., and Jun, YS., (**2017**) Photochemically-Assisted Fast Oxidation of Manganese and Formation of δ-MnO$_2$ Nanosheet in Nitrate Solution, ***Chemical Communications***, DOI: 10.1039/C7CC00754J**.**
10. ***Kim, D.***, Lee, B., Thomopoulos, S., and Jun, YS. (**2016**) *In situ* Evaluation of Calcium Phosphate Nucleation Kinetics and Pathways during Intra-and Extrafibrillar Mineralization of Collagen Matrices. ***Crystal Growth & Design***, DOI: 10.1021/acs.cgd.6b00864.
11. Jun, YS., ***Kim, D***., and Neil, CW. (**2016**) Heterogeneous Nucleation and Growth of Nanoparticles at Environmental Interfaces, ***Accounts of Chemical Research***, DOI: 10.1039/C7CC00754J. Open Access Link
12. ***Kim, D.***, Min, J., Yoo, Y., and Park, J. -W. (**2014**) *Eisenia fetida* Growth Inhibition by Amended Activated Carbon Causes Less Bioaccumulation of Heavy Metals. ***Journal of Soils and Sediments***, DOI: 10.1007/s11368-014-0934-0
13. ***Kim, D.***, Kim, C. -K., Chun, B., and Park, J. -W. (**2012**) Enhanced Heavy Metal Sorption by Surface-Oxidized Activated Carbon Does Not Affect the PAH Sequestration in Sediments, ***Water, Air, & Soil Pollution***, DOI: 10.1007/s11270-012-1101-0.
14. ***Kim, D.***, Jung, Y. -W., Kwon, S. -J., and Park, J. -W. (**2011**) Adsorption of Cadmium (II) from Aqueous Solutions by Thiol-functionalized Activated Carbon, ***Water Science and Technology: Water Supply***, DOI: 10.2166/ws.2011.009.
15. Lee, J., ***Kim, D.***, Park, J. –W. (**2011**) Long-Term Effect of Consolidation on Contaminant Transport, ***Journal of the Korean Geotechnical Society***, DOI: 10.7843/kgs.2011.27.1.035.
16. Yeo, I. H., ***Kim, D.***, Paik, J. H., Lee, Y. J., Shin, M. C., and Park, J. –W. (**2010**) Modeling of Blades to Enhance Self-power Generation in Pipe Flow, ***Journal of the Korean Society of Water and Wastewater***, 24(3): 277-285.

3 Submitted/In preparation

1. ***Kim, D.***, Lee, B., Thomopoulos, S., and Jun, YS. The Interfacial Reaction between Collagen and Bioapatite Under Cyclic Loading Condition, ***In preparation.***
2. ***Kim, D.***, Lee, B., Thomopoulos, S., and Jun, YS. The Effect of Pulsed Electric Stimulation on Spatial Distribution and Crystallinity of Calcium Phosphate Minerals in Collagen, ***In preparation.***
3. Wu, X., Bower, B., ***Kim, D***., Lee, B., and Jun, YS. Effects of Organic Matter on Arsenopyrite Dissolution and Secondary Mineral Precipitation during Managed Aquifer Recharge, ***In preparation.***

RESEARCH & TEACHING EXPERIENCE

Washington University in St. Louis, MO

Graduate Research Assistant (PI: Professor Young-Shin Jun) ***2012 – 2018***

"Nucleation of calcium phosphate biomaterials," Collaborative Research, Biomaterials Program, Division of Materials Research, the National Science Foundation, (September 1, 2016-August 31, 2019. Total cost: $390,000) ***- Significant contributor to a funding proposal***

Guest Lecturer (EECE 505, Aquatic Chemistry)

- Thermodynamic simulations using MINEQL+ and Visual MINTEQ ***2013 – 2018***
- Thermodynamics with non-ideal effects and kinetic reactions ***2017 – 2018***

Guest Lecturer for Lab Class (EECE 534, Environmental Nanochemistry)

- Synthesis and analysis of magnetite nanoparticles ***2016 – 2018***

Graduate Teaching Assistant ***2013 – 2014***

- Aquatic Chemistry (EECE 505, Fall 2013)
- Atmospheric Science and Climate (EECE 547, Spring 2014)
- Engineering Economics, Analytics, and Policy Analysis Tools (EECE 382, Fall 2014)

Research mentoring

- Eunyoung Jang, Research rotation with doctoral student researcher ***2018***
- Albern Tan and Weiyi Pan, Research rotation with doctoral student researchers ***2017***
- Samantha Burnell, Undergraduate summer researcher from MIT ***2017***
- Anushree Ghosh, Research rotation with doctoral student researcher ***2016***
- Inhyeong Jeon from Seoul National University, McDonnell Academy Global Energy and Environment Partnership undergraduate fellowship student ***2016***
- Mujia Gu, Master's student researcher in EECE ***2015***
- Melanie Cohen, Undergraduate student researcher in EECE ***2015 – 2016***
- Vanessa Wu, Undergraduate student researcher in EECE, Summer Research Fellowship recipient ***2014 – 2015***
- Yusef Rahaman, Master's student researcher in EECE ***2014***
- Claire Dang, High school student researcher, Student and Teachers as Research Scientists (STARS) program ***2013***

National Institute of Environmental Research, Incheon, Korea

Research assistant, Soil and Groundwater Research Division ***2011 – 2012***

Hanyang University, Seoul, Korea

Graduate Research Assistant (PI: Professor Jae-Woo Park) ***2009 – 2019***

SELECTED CONFERENCE PRESENTATIONS (* oral presenter)

1. ***Kim, D***., Lee, B., Thomopoulos, S., and Jun, YS*****. (2018) Exploring Energetics of Confined Nucleation for Bioapatite Formation, Special symposium on "Energy landscapes in

biomineralization, geochemistry, and materials science: A celebration of Alex Navrotsky's 75th birthday", ***Goldschmidt 2018***, Boston, MA, USA.

2. ***Kim, D***., Lee, B., Thomopoulos, S., and Jun, YS*. (2018) Nucleation of Calcium Phosphate in Nano-scale Confinement, ***The 256th ACS National Meeting***, Boston, MA, USA.
3. ***Kim, D.****, Lee, B., Thomopoulos, S., and Jun, YS. (2018) Thermodynamics of Confined Calcium Phosphate Nucleation in Collagen Fibrils, Special symposium on "Biomineralization & Bio-compatible Minerals," ***The 255th ACS National Meeting***, New Orleans, LA, USA.
4. ***Kim, D.***, Cohen, M., Jeon, IH., Burnell, S., and Jun, YS. (2017) Utilization of Poorly Crystalline Calcium Phosphate Minerals for Selective Phosphate Recovery and Recycling, ***the 2017 Association of Environmental Engineering and Science Professors Conference***, Ann Arbor, Michigan, USA.
5. ***Kim, D.****, Cohen, M., Gu, M., Jeon, IH., and Jun, YS. (2017) Calcium Phosphate Seed Nuclei for Selective Phosphorus Recovery at Neutral pH, ***The 253rd ACS National Meeting***, San Francisco, California, USA.
6. ***Kim, D.****, Lee, B., Thomopoulos, S., and Jun, YS. (2017) Nucleation, Growth, and Transformation of Calcium Phosphate Minerals in Multi-scale Nucleation Sites of Collagen Fibrils, ***The 253rd ACS National Meeting***, San Francisco, California, USA.
7. ***Kim, D.****, Wu, T., Cohen, M. and Jun, YS. (2016) Calcium Phosphate-Organic Composites for a more Sustainable P Cycle: Learning from Biomineralization, ***The 251st ACS National Meeting***, San Diego, California, USA.
8. ***Kim, D.****, Lee, B., Thomopoulos, S., and Jun, YS. (2016) Influence of Biological Interfaces on Nucleation Pathways and Kinetics of Calcium Phosphate Minerals, ***The 251st ACS National Meeting***, San Diego, California, USA.
9. ***Kim, D.****, Wu, T., Cohen, M. and Jun, YS. (2015) Remediation Strategy for Phosphorous-rich Aqueous Environments Inspired by Biominerals, ***The 21st Annual Mid-America Environmental Engineering Conference***, Columbia, Missouri, USA.
10. ***Kim, D.****, Lee, B., Thomopoulos, S and Jun, YS. (2015) Nucleation and Crystallization Kinetics of Initial Apatite Nanocrystal Formation within Biological Templates, ***The 249th ACS National Meeting,*** Denver, Colorado, USA.
11. ***Kim, D.****, Kwon, S. -J., and Park, J. -W. (2010) Effects of Surface Oxygen Group of Activated Carbon on Heavy Metal and PAH Adsorption, ***The International Chemical Congress of Pacific Basin Societies***, Honolulu, Hawaii, USA.
12. ***Kim, D.****, Kwon, S. -J., and Park, J. -W. (2010) Evaluation of Oxidized Activated Carbon as a Stabilization Agent for Sediments Contaminated with Hydrophobic Organic Chemicals and Heavy Metals, ***8th International Symposium On Ecohydraulics***, Seoul, Korea.
13. ***Kim, D.****, Jung, Y. -W., Kwon, S. -J., and Park, J. -W. (2009) Adsorption of Cadmium (II) from Aqueous Solutions by Thiol-Functionalized Activated Carbon, ***The 3rd IWA-ASPIRE Conference***, Taipei, Taiwan.

PEER-REVIEWED BEAMTIME PROPOSALS (Advanced Photon Source, Argonne National Lab)

1. ***Kim, D.*** and Jun, YS. Phase transformation of calcium bearing minerals, from amorphous to crystalline, in the confined space, APS 11-ID-B, 2018-2 cycle for X-ray PDF experiments.
2. ***Kim, D.***, Zhu, Y. and Jun, YS. Nano-confinement effects on the phase transformation of calcium bearing minerals, APS 11-ID-B, 2018-2 cycle for X-ray PDF experiments.
3. ***Kim, D.*** and Jun, YS. Evaluation of calcium phosphate mineralization in various collagen fibrillar structures using *in situ* SAXS, APS 12-ID-B, 2018-1 cycle for GISAXS/SAXS experiments.
4. ***Kim, D.*** and Jun, YS. Application of electric stimulation for the enhanced bioapatite crystallization in demineralized bones, APS 11-ID-B, 2017-1,2,3 cycles for X-ray PDF experiments.
5. ***Kim, D.*** and Jun, YS. Enhanced recovery of crystalline bioapatite in demineralized bones by pulse electric stimulation, APS 11-ID-B, 2017-1 and 2018-1 cycles for X-ray PDF experiments.
6. ***Kim, D.*** and Jun, YS. The influence of collagen fibrillar structure on the nucleation kinetics of calcium phosphate nanocrystals, APS 9-ID-B,C, 2016-3 cycle for USAXS experiments.
7. ***Kim, D.*** and Jun, YS. Evaluation of the *in situ* kinetics of bioapatite crystallization determined by fibrillar collagen structures, APS 11-ID-B, 2016-2,3 cycles for X-ray PDF experiments.
8. ***Kim, D.*** and Jun, YS. In situ observation of calcium phosphate mineralization within the fibrillar collagen structures, APS 9-ID-B,C, 2016-1,2 cycles for USAXS experiments.
9. ***Kim, D.*** and Jun, YS. The effects of extrafibrillar spaces of collagen matrices on the kinetics of bioapatite crystallization, APS 11-ID-B, 2016-1 cycle for X-ray PDF experiments.
10. ***Kim, D.*** and Jun, YS. In situ observation of intrafibrillar mineralization of collagen under controlled solution chemistry, APS 12-ID-B, 2015-3 cycle for GISAXS/SAXS experiments.
11. ***Kim, D.*** and Jun, YS. Evaluation of the phase distribution of calcium phosphate minerals within collagen matrix, APS 11-ID-B, 2015-1 cycle for X-ray PDF experiments.
12. ***Kim, D.*** and Jun, YS. The effects of non-collagenous proteins and small acidic molecules on the crystal structures of calcium phosphate mineralized collagen, APS 11-ID-B, 2014-3 cycle for X-ray PDF experiments.
13. Jun, YS., ***Kim, D.***, and Lee, B. Evaluation of thermodynamic factors controlling bone formation: Heterogeneous nucleation of calcium phosphate on collagen substrates, APS 12-ID-B, 2014-2 cycle for GISAXS/SAXS experiments.
14. Jun, YS. and ***Kim, D.*** Kinetics of phase transformation of bone minerals: From amorphous calcium phosphate to hydroxylapatite within collagen matrix, APS 11-ID-B, 2014-2 cycle for X-ray PDF experiments.

HONORS AND AWARDS

Doh Won Suk Memorial Award	***2018***
Certificate of Merit, Division of Environmental Chemistry, 253rd American Chemical Society meeting	***2017***
Student travel award, Division of Geochemistry, 251th American Chemical Society meeting	***2016***
Study-abroad scholarship from Hanyang University	***2012***
Science and technology scholarship from Hanyang University	***2009 – 2011***
Korean Society of Environmental Engineers Spring Conference – Outstanding Paper Award	***2010***

Daewoo Engineering funded scholarship ***2010***

Academic scholarship from Hanyang University (4 semesters) ***2003 – 2009***

PROFESSIONAL MEMBERSHIP

American Institute of Chemical Engineers ***2018 –***

American Chemical Society ***2015 – 2018***

WORKSHOPS

Transmission Electron Microscopy Workshop of the Institute of Materials Science & Engineering ***2017***

- Washington University in St. Louis, MO. November 6–10
- Presented a poster titled "Transmission Electron Microscopy for Studying Mineral-Water Interfaces"

The Chemical Life Cycle Collaborative (CLiCC) Workshop ***2016***

- University of California at Santa Barbara, CA. June 25–26
- Received a travel award

NSF-Sponsored Workshop on Atom Probe Tomography for Earth Sciences ***2016***

- The University of Alabama, AL. January 29–30

Small-Angle Scattering Short Course: Beyond R_g ***2013***

- Advanced Photon Source, Argonne National Laboratory, IL. October 26–31

SERVICE AND OUTREACH

Student committee for interviewing faculty candidates, Washington University in St. Louis ***2018***

Women in STEM Day ***2013 – 2018***

- Education for more than 100 high school girls, sponsored by the Washington University Chapter of the Society of Women Engineers

Moving and Shaking: An Introduction to Engineering ***2013 – 2018***

- Education for students in grade 6-8, supported by the St. Louis Area Gifted Resource Council
- Program leader for 2017 and 2018

Hot Topic Workshops with Middle School Teachers in St. Louis Area. ***2015 – 2017***

- The Institute for School Partnership at Washington University in St. Louis.

President of Korean-American Scientists and Engineers Association in St. Louis ***2014 – 2016***

Vice President of Korean-American Scientists and Engineers Association in St. Louis ***2013 – 2014***

Military service in the Division of Rescue and First Aid, Ulsan Fire Department, Korea ***2004 – 2006***

SKILLS

Advanced Photon Source (synchrotron-based X-ray facility) in Argonne National Laboratory, IL

- On-site experience in grazing-incident small-angle X-ray scattering/small-angle X-ray scattering analysis at sector 12-ID-B ***2013 – 2018***
- On-site experience in X-ray PDF analysis at sector 11-ID-B ***2014 – 2018***

- On-site experience in Ultra-small-angle X-ray scattering at sector 9-ID ***2015 – 2018***
- Mail in experiment for HRXRD at sector 11-BM ***2013 – 2018***

Washington University in St. Louis

- High Resolution Transmission Electron Microscopy with Electron Diffraction and Energy-Dispersive X-ray analysis. Experienced in treating biological tissues – staining and section cutting.
- Contact angle analyzer (Instrument manger)
- Atomic Force Microscopy
- Scanning Electron Microscopy with Energy-Dispersive X-ray Spectroscopy
- X-ray Diffraction
- Inductively Coupled Plasma - Mass Spectrometry and Atomic Emission Spectroscopy
- Dynamic Light Scattering and UV-Visible Spectroscopy
- Raman spectroscopy
- Fluorescence correlation spectroscopy
- Thermogravimetric analysis

Other experimental skills

- Liquid Chromatography-Tandem Mass Spectrometry
- Ion Chromatography
- Atomic absorption spectroscopy

Software

- Programming Languages: MATLAB, R
- Chemical Equilibrium Modeling: MINEQ+, Visual MINTEQ, GWB
- X-ray data analysis: IRENA package (written in IGOR Pro), GISAXS shop (written in IGOR Pro), GSAXS-II (written in python), PDFgetX2, FIT2D